
THE UNIVERSITY *of* EDINBURGH

# Search for right-handed $W$ bosons and heavy neutrinos with the ATLAS experiment

Xanthe Hoad


Doctor of Philosophy
The University of Edinburgh
August 2018

# Abstract

A search for heavy right-handed Majorana or Dirac neutrinos ($N_R$) and heavy right-handed $W$ gauge bosons ($W_R$) participating in the Keung-Senjanović process has been performed in events with a pair of energetic electrons or muons, with opposite-sign charges, and two energetic jets. Events were selected from $pp$ collision data with an integrated luminosity of $36.1\,\text{fb}^{-1}$ collected by the ATLAS detector at $\sqrt{s} = 13\,\text{TeV}$. No significant deviations from the Standard Model expectation were observed. The results were interpreted within the theoretical frameworks of two forms of Left-Right Symmetric Model and lower limits were set on masses in the heavy right-handed $W$ and neutrino mass plane, as well as upper limits on the Keung-Senjanović process cross section multiplied by the branching fraction to $eejj$ or $\mu\mu jj$. The excluded region extends to $m_{W_R} = 4.7\,\text{TeV}$ for both Majorana and Dirac $N_R$ neutrinos. The $m_{N_R} > m_{W_R}$ region is explored for the first time by a search for the Keung-Senjanović process at the LHC.

# Lay Summary

Science's current best description of particle physics, the Standard Model, agrees with nature to a high degree of accuracy in almost all ways that humanity has been able to test it. However, the Standard Model does not, for historical reasons, correctly describe a group of particles called the neutrinos. When the Standard Model was formulated, it was thought that neutrinos had no mass, but subsequent experiments have shown that they do have small masses. There are various ways that the Standard Model could be extended to include a description of neutrino mass. This thesis is concerned with one type of extension, the Left-Right Symmetric Model extensions to the Standard Model. The Left-Right Symmetric Models contain a mechanism which gives mass to the neutrinos, by making their masses be inversely proportional to the masses of some new, as-yet undiscovered, neutrinos. By making these new neutrinos very heavy, the known neutrinos can have small masses.

In the Standard Model, forces act between particles by the exchange of force-carrying particles called 'bosons'. One of the fundamental forces described by particle physics, the weak nuclear force, has an interesting characteristic, which is, unlike the other fundamental forces, it doesn't act the same way on a system as it would on the mirror image of that system. This happens because the weak force only acts on particles which are 'left-handed' (this classification refers to the particle's 'chirality', a particular quantum mechanical property of a particle). The weak force only acts on left-handed particles because its bosons are left-handed, and only particles of the same handedness can interact. Reflecting a left-handed particle in a mirror turns it into a right-handed particle, so the weak force would no longer act on that particle. For this reason, we say the weak force is left-handed.

Left-Right Symmetric Models, as well as describing how neutrinos can have small masses, extend the weak force to have a right-handed component. In order to

explain why we don't see right-handed weak interactions happening in nature, the right-handed bosons introduced within Left-Right Symmetric Models must be very heavy compared to the left-handed weak bosons. As previously stated, the new neutrinos also predicted by Left-Right Symmetric Models must also be heavy. Creating such heavy particles requires a lot of energy, due to the equivalence of mass and energy. The Large Hadron Collider, the world's most powerful particle accelerator and collider, has the capability to produce these heavy particles, if they exist.

In this thesis, data collected by the ATLAS detector, one of the multipurpose particle detectors at the Large Hadron Collider, was analysed to try to find evidence that one type of Left-Right Symmetric Model right-handed boson, $W_R$, and the new heavy neutrinos, $N_R$, had been produced. The energy at which collisions at the Large Hadron Collider occur sets a limit on the range of masses of $W_R$ and $N_R$ that the collisions would be able to create. No evidence that the particles were created on collisions at the Large Hadron Collider during 2015 and 2016 was found. The non-observation of $W_R$ and $N_R$ allows us to say, with some degree of confidence, that the particles must be heavier than the range of $W_R$ and $N_R$ masses that could be created with the current collision energy of the Large Hadron Collider, if they exist.

# Declaration

I declare that this thesis was composed by myself, that the work contained herein is my own except where explicitly stated otherwise in the text, and that this work has not been submitted for any other degree or professional qualification except as specified.

Parts of this work have been published in [1, 2].

(*Xanthe Hoad, August 2018*)

# Acknowledgements

As a tiny cog in a giant physics machine, I am indebted to all the other members of the ATLAS collaboration, especially to my supervisor, Christos, and the rest of our analysis team, without whom this work would not have been possible.

My time spent at CERN was one of the most enjoyable periods during my PhD, thanks to the sense of community within the LTA and the welcome distractions provided by the Department of Mysteries - I hope none of you ever have to sacrifice your exploratory natures. I have loved living in Edinburgh and my friends here have been a big part of that.

I am grateful for my family's love and support, and to the Hewletts for taking me in like one of their own. And mostly, thanks to Tim, for being superlatively great and for convincing me that I'm alright too.

# Contents

# List of Figures

# List of Tables

# Chapter 1

# Introduction

One of the major goals of the ATLAS experiment at the Large Hadron Collider (LHC) is to search for signs of new physics. One group of beyond the Standard Model (BSM) theories that can be investigated with ATLAS are the Left-Right Symmetric Models (LRSMs). These models are attractive for a number of reasons, including that they restore parity to the Standard Model (SM) by introducing a right-handed component to the left-handed weak force, and can offer a plausible explanation to the smallness of the masses of the known neutrinos. New particles predicted by LRSMs include heavy right-handed $W$ bosons ($W_R$) and heavy right-handed neutrinos ($N_R$). Depending on the form of the LRSM, the heavy right-handed neutrinos can be Majorana or Dirac particles.

In this thesis, an analysis searching for evidence of $W_R$ and $N_R$ using data collected by the ATLAS experiment is presented. The search focuses on the Keung-Senjanović process, in which an initial $W_R$ is produced during a proton-proton collision and then decays to an $N_R$ and a charged lepton, with the $N_R$ then decaying to a second $W_R$ and a second charged lepton. Final states containing an electron–positron pair or a muon–anti-muon pair are considered. The situation where the second $W_R$ decays to a quark pair is considered, resulting in a two lepton plus two jet experimental signature for the process. Either the first or second $W_R$ must be off mass shell, depending on the mass hierarchy of the LRSM particles. The situation where $m_{N_R} > m_{W_R}$ is studied in this thesis for the first time by an LHC analysis. The analysis was performed by myself and other members of a small analysis team within the ATLAS collaboration.

More details regarding the motivation and theoretical background to the analysis

described in this thesis can be found in Chapter 2. The dataset used in the analysis consists of $36.1\,\text{fb}^{-1}$ of proton-proton collision data collected at $\sqrt{s} = 13\,\text{TeV}$ with the ATLAS detector (described in Chapter 3) during 2015–2016. Data collection and data quality monitoring for the ATLAS experiment is described in Sections 4.1 and 4.2, including work I performed to improve the data quality monitoring capabilities of the ATLAS Trigger Group in Section 4.2.1. Simulated datasets were used to model the Keung-Senjanović process and SM processes, described in Section 5.2. Data collected by ATLAS and simulated data alike were reconstructed using the methods described in Section 4.4.

The analysis strategy, which I designed in conjunction with the rest of the analysis team, is detailed in Chapter 5. The statistical analysis, which I performed, is described in Chapter 6. The final results, which consist of exclusion limits in $m_{W_R}$–$m_{N_R}$ space and upper limits on the Keung-Senjanović process cross section multiplied by the branching fraction to $eejj$ or $\mu\mu jj$, can be found in Chapter 7. No evidence for the existence of $W_R$ and $N_R$ was found.

Natural units ($\hbar = c = 1$) are used throughout this thesis.

# Chapter 2

# Theoretical Background

> With so much misery, inequality and human-exploitation in the world, why would anyone invest precious resources in studying hypothetical (i.e. imaginary) particles because some theorist (let's face it, probably some old white guy) came up with a crazy idea while in the shower?
>
> *XH by CL*

In this chapter, the theoretical motivation for the work described in this thesis is outlined. First, in Section 2.1, the Standard Model (SM) is briefly discussed, before some issues with the SM are covered in Section 2.2. In Section 2.3, Left-Right Symmetric Models (LRSMs) are discussed, focussing on how they can address the highlighted issues in the SM. These models, depending on the model variant, can restore parity to the SM, provide a mechanism for the generation of neutrino masses, and explain why neutrino masses are so different in scale to the other lepton masses. The chapter concludes with a description of the Keung-Senjanović process, an interaction predicted by LRSMs, which is of interest in this thesis.

## 2.1 The Standard Model

The Standard Model of particle physics consists of the theories of the electroweak [3, 4, 5, 6, 7, 8, 9] and strong [10, 11, 12] interactions. The particles within the SM

are divided into fermions, matter particles with spin $\frac{1}{2}$, and bosons, force carrying particles with spin 1. The fermions are further divided into the six quarks and the six leptons, both of which are grouped into three families of increasing mass. The bosons that mediate the electromagnetic, weak and strong interactions are the photon, $W$ and $Z$ bosons and the eight gluons, respectively. The gauge group of the SM is $SU(3)_c \times SU(2)_L \times U(1)_Y$, where $SU(3)_c$ is the strong gauge group and $SU(2)_L \times U(1)_Y$ is the electroweak group. Spontaneous symmetry breaking via the Higgs mechanism breaks the $SU(2)_L \times U(1)_Y$ part down to $U(1)_{EM}$, the electromagnetic gauge group, during which the weak bosons and the charged fermions become massive particles. A schematic of the SM, including its particle content, the interactions that occur between those particles, and the effect of spontaneous symmetry breaking within the SM is shown in Figure 2.1.

The SM is a very successful theory, which accurately predicts the cross sections of many particle physics processes across many orders of magnitude, as shown in Figure 2.2. A recent validation of the SM, and a triumph of the LHC, was the discovery of the Higgs boson, generator of mass for the weak bosons and charged fermions, in 2012 [13, 14]. However, there are issues with the SM which necessitate movement to Beyond the Standard Model (BSM) theories. Section 2.2 focusses on two such issues, the non-existence of neutrino mass within the theory and the fact that the weak force is parity violating.

It is important to briefly define parity, helicity and chirality. The parity transformation switches the sign of spatial coordinates, and so describes a reflection through the origin. The parity of a variable is defined as either even $(+1)$ or odd $(-1)$ depending on whether the system or variable changes sign after the parity transformation. For example, the momentum of a particle changes under reflection as momentum is a vector quantity, so momentum has odd parity. The parity of a particle is the parity of its quantum mechanical state (or wavefunction). By Noether's theorem [17], if a system is symmetric (behaves the same way) before and after a parity transformation, then parity is conserved within that system. In other words, if the universe behaves the same way when reflected, then parity would be a conserved quantity. A force is parity violating if it affects a system differently when the system is reflected, and the result would be that parity would not be conserved by that force.

The helicity of a particle is affected by the parity operator (so is a variable with odd parity), as helicity (a pseudoscalar) is defined as the projection of a particle's spin onto its momentum, and momentum (a vector) is affected by the

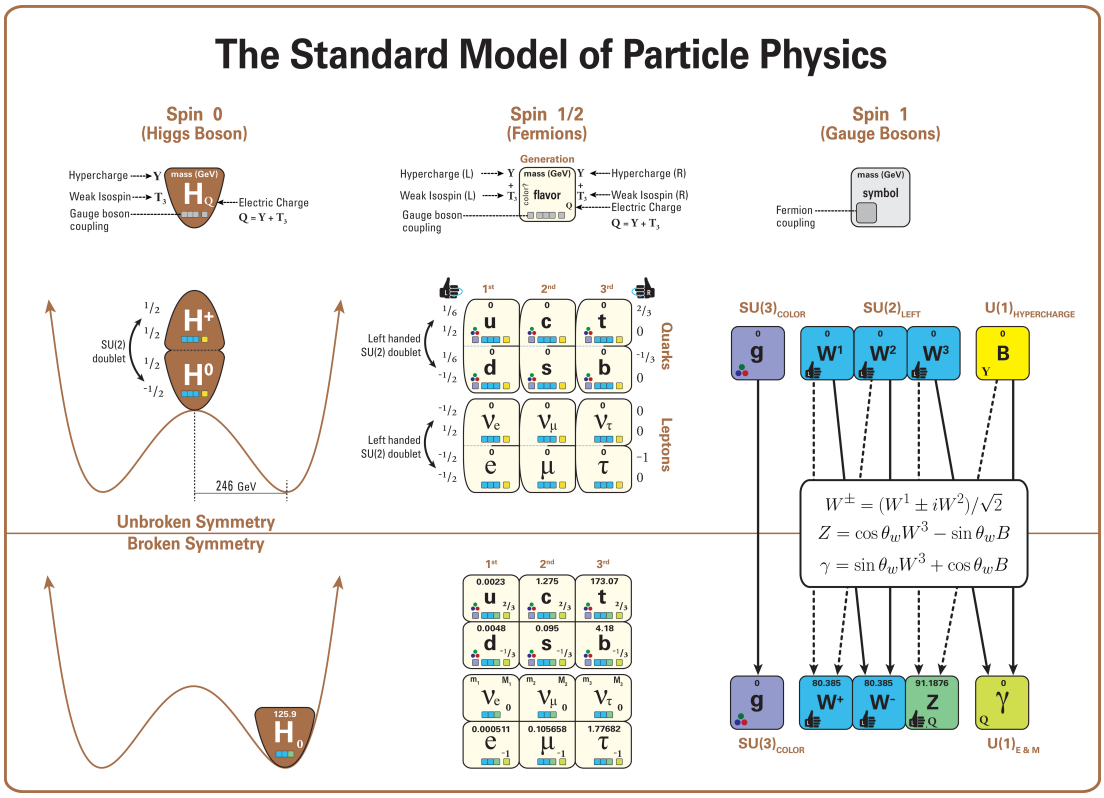


**Figure 2.1** A summary of the Standard Model, including particle contents, quantum numbers and interactions before and after spontaneous symmetry breaking (SSB) [15] (CC-SA 4.0). Key features with respect to this thesis are that right-handed neutrinos do not exist within the SM (indicated by the fact they have no associated hypercharge ($Y$) or weak isospin ($T_3$), and that the weak force is left-handed (indicated by $SU(2)_{\text{LEFT}}$, written as $SU(2)_L$ in this thesis). These features are described in more detail in the text.

parity operator, whilst spin (a pseudovector) is not. If a particle's momentum and spin are aligned, the particle is right-handed, whilst if they are anti-aligned, the particle is left-handed. In the massless particle limit, helicity is equivalent to chirality. Chirality is a frame independent intrinsic property of a particle, unlike helicity, and relates to the direction that a particle's wavefunction shifts when the particle is rotated. When a spin $\frac{1}{2}$ particle is rotated through $2\pi$, the quantum mechanical state of the particle gains a minus sign. The chirality of this spin half particle defines the manner is which this minus sign is obtained: either by passing through $i$ or $-i$ in the complex plane. In the rest of this thesis, right-handed and left-handed will be used to refer to chirality states, unless otherwise stated.

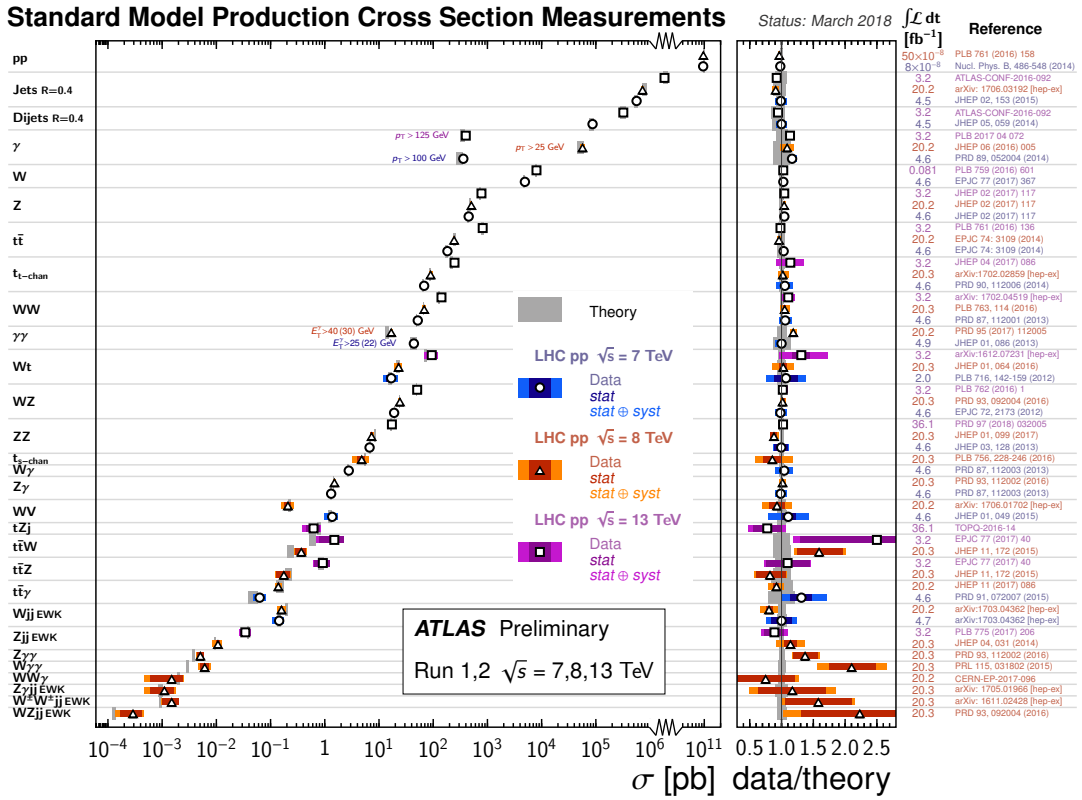


**Figure 2.2** Summary of Standard Model production cross section measurements by the ATLAS collaboration, compared to theory predictions. Excellent agreement can be seen for the vast majority of measurements. The reference is shown for each measurement, along with the integrated luminosity[1], the number of collisions per area in the time for which data was collected to produce each measurement. Taken from [16].

## 2.2 Selected issues within the Standard Model

### 2.2.1 Parity violation in weak interactions

The first hint that parity might not be conserved by the weak force came with the discovery of the $\tau^+$ and $\theta^+$ particles in the 1950s, which decayed as:

$$\tau^+ \rightarrow \pi^+ + \pi^+ + \pi^-$$
$$\theta^+ \rightarrow \pi^+ + \pi^0$$

[1]Luminosity is defined as $\mathcal{L} = \frac{1}{\sigma}\frac{dN}{dt}$, where $N$ is number of events and $\sigma$ is the interaction cross section.

As pions have intrinsic parity $-1$ [18] (due to the fact that quarks have parity $+1$ and antiquarks have parity $-1$) and parity is multiplicative, the $\tau^+$ and $\theta^+$ were therefore known to decay to systems with different intrinsic parity states. However, as the two particles had the same masses and lifetimes as each other, there was speculation that they could be the same particle. In response to this, Lee and Yang [19] pointed out that it had not be experimentally demonstrated that the weak force conserved parity, so if one of the decays proceeded via the weak force and the other not, this could be a solution. They therefore proposed experiments to further test the nature of the weak force. This led to the first definitive evidence of parity violation in weak interactions in the observation of an asymmetry in the direction of emission of electrons from the decay of Cobalt-60 atoms [20] and in the angular distribution of electrons from muon decays originating from pions decaying in a cyclotron [21]. The discovery of parity violation confirmed that the $\tau^+$ and $\theta^+$ particles were one particle, now referred to as the $K^+$, where the decay to two pions is the parity violating decay mode of the two, as the $K^+$ has intrinsic parity $-1$ [22].

The parity violating nature of the SM is explicit, through its gauge group structure of $SU(3)_c \times SU(2)_L \times U(1)_Y$, where $SU(2)_L$ is the left-handed weak gauge group. Only particles with a left-handed component experience the weak force for this reason. Left-handed particles have weak isospin ($T_3$, the quantum number relating to weak interactions) values of $\pm 1/2$ and consequently form doublets, whilst right-handed particles have $T_3 = 0$ and form weak isospin singlets, as shown in Figure 2.1.

Though it is clear that the weak force is parity violating, it is not explained within the SM why this should be the case. As parity is conserved during strong and electromagnetic interactions, the weak force is the clear odd one out within the SM. If there were a theory which included non-conservation of parity at low energies, conservation of parity at high energies, and provided testable predictions at accessible energies, this would provide a reason for the observed behaviour of the weak force.

### 2.2.2 Lack of neutrino masses

Fermions that are massive within the SM (all fermions except the neutrinos) have mixed helicity states, reflecting that they have right- and left-handed chirality components. Once antiparticle components are accounted for, these massive

fermions have four components. Right-handed components have corresponding left-handed antiparticle components, and left-handed components have corresponding right-handed antiparticle components. Mass terms for four component particles take the form of Yukawa couplings [23]:

$$m\bar{\psi}\psi = m(\bar{\psi}_L\psi_R + \bar{\psi}_R\psi_L)$$

The Yukawa coupling allows a right-handed chiral component to convert to a left-handed chiral component, and vice versa. As the fermion components that take part in the Yukawa coupling are massless, and chirality and helicity are equivalent in the massless limit, chirality and helicity are equivalent for these components. Therefore, the Yukawa coupling allows a component with right-handed helicity to switch to one with left-handed helicity. To switch from right-handed to left-handed helicity is to switch direction of motion. This means that switch helicity is to travel slower than the speed of light, and therefore, to have mass. Fermions that gain mass in this way are referred to as a Dirac fermions, in reference to the fact that their behaviour is described by the Dirac equation [24], and the mass they gain as a Dirac mass. The SM Yukawa couplings between the left- and right-handed components of the massive fermions are facilitated by the Higgs field [7, 8, 9], which has the correct quantum numbers, relative to those of the massive fermions, to conserve all quantum numbers that must be conserved by such interactions.

Following from experiments demonstrating the parity violating nature of the weak force (see Section 2.2.1), it was suggested that the neutrinos may have only two components [25, 26, 27], either a right-handed component and a left-handed antiparticle component, or left-handed component and a right-handed antiparticle component. Evidence for this was found in 1958, when it was shown that electron neutrinos have negative (left-handed) helicity [28], one of the two possibilities from the two-component theory. Two-component neutrinos can not generate Dirac masses. However, an alternative way to generate mass, which is available to two-component particles, is the Majorana mechanism [29]. Majorana particles are their own antiparticles, meaning they have the property:

$$\psi^c = \psi \quad \text{where} \quad \psi^c = \hat{C}\bar{\psi}^T$$

where $\hat{C}$ is the charge conjugation operator. Only uncharged particles such as neutrinos can be Majorana particles. The Majorana mechanism allows particles

with two components to have mass, with terms of form:

$$m\bar{\psi}_L^c\psi_L \quad \text{or} \quad m\bar{\psi}_R^c\psi_R$$

At the time when the SM was developed, no evidence for neutrino mass had yet been found, so it was not desirable for terms like this to be present in the SM Lagrangian. This resulted in the SM being formulated without a field that would allow the two neutrino components to couple in this way whilst conserving all required quantum numbers.

To summarise, the fermions fields in the SM are:

$$\psi_L = \begin{pmatrix} \nu_{\ell_L} \\ \ell_L \end{pmatrix} \qquad \psi_R = (\ell_R)$$

where $\ell = e, \mu, \tau$, and the Higgs doublet is:

$$\phi = \begin{pmatrix} \phi^+ \\ \phi^0 \end{pmatrix}$$

The part of the SM Lagrangian that concerns the interaction of the Higgs field with the lepton fields is:

$$\begin{aligned} \mathcal{L}_{\text{mass}}^{\text{SM}} &= h_D \left[\bar{\psi}_L \phi \psi_R + \bar{\psi}_R \bar{\phi} \psi_L\right] \\ &= h_D \left[(\bar{\nu}_{\ell_L}, \bar{\ell}_L) \begin{pmatrix} \phi^+ \\ \phi^0 \end{pmatrix} \ell_R + \bar{\ell}_R (\phi^+, \phi^0) \begin{pmatrix} \nu_{\ell_L} \\ \ell_L \end{pmatrix}\right] \end{aligned}$$

where $h_D$ is the coupling strength. When spontaneous symmetry breaking occurs, and the neutral component of the Higgs field gains a vacuum expectation value (VEV):

$$\phi = \begin{pmatrix} 0 \\ v \end{pmatrix}$$

which results in Dirac mass terms for the charged leptons, and no mass terms for the neutrinos:

$$\mathcal{L}_{\text{mass}}^{\text{SM}} = h_D v \left[\bar{\ell}_L \ell_R + \bar{\ell}_R \ell_L\right]$$

That neutrinos may be massive and oscillate between flavours was first suggested

by Pontecorvo in 1957 [30, 31], and later expanded upon by Maki, Nakagawa and Sakata [32], and by Pontecorvo again in 1967 [33]. The central idea is that the neutrino flavour eigenstates that participate in weak interactions ($\nu_e$, $\nu_\mu$, $\nu_\tau$) are superpositions of neutrino mass eigenstates ($\nu_1$, $\nu_2$ and $\nu_3$). A neutrino with a particular flavour emitted during a weak interaction is therefore formed of a mixture of the mass eigenstates. The flavour eigenstates and mass eigenstates are related through the Pontecorvo–Maki–Nakagawa–Sakata (PMNS) mixing matrix, which specifies the mixing angles between the eigenstates:

$$\begin{aligned}\begin{pmatrix}\nu_e\\ \nu_\mu\\ \nu_\tau\end{pmatrix} &= \begin{pmatrix}U_{e1} & U_{e2} & U_{e3}\\ U_{\mu1} & U_{\mu2} & U_{\mu3}\\ U_{\tau1} & U_{\tau2} & U_{\tau3}\end{pmatrix}\begin{pmatrix}\nu_1\\ \nu_2\\ \nu_3\end{pmatrix}\\ &= \begin{pmatrix}1 & 0 & 0\\ 0 & c_{23} & s_{23}\\ 0 & -s_{23} & c_{23}\end{pmatrix}\begin{pmatrix}c_{13} & 0 & s_{13}e^{-i\delta_{CP}}\\ 0 & 1 & 0\\ -s_{13}e^{i\delta_{CP}} & 0 & c_{13}\end{pmatrix}\begin{pmatrix}c_{12} & s_{12} & 0\\ -s_{12} & c_{12} & 0\\ 0 & 0 & 1\end{pmatrix}\begin{pmatrix}\nu_1\\ \nu_2\\ \nu_3\end{pmatrix}\end{aligned}$$

The matrix is shown parametrised into three mixing angles $\theta_{ij}$ where $i, j = 1, 2, 3$ and $\delta_{CP}$, a CP violating phase. $c_{ij} = \cos\theta_{ij}$ and $s_{ij} = \sin\theta_{ij}$. $|U_{\ell i}|^2$ gives the probability for a neutrino with flavour $\ell$ to be found with mass $m_i$. A neutrino flavour eigenstate is a weighted sum of mass eigenstates:

$$|\nu_\ell\rangle = \sum_i U_{\ell i}\,|\nu_i\rangle$$

A neutrino emitted in a weak interaction is a weak eigenstate, but the mass eigenstates are the ones that propagate through space. The time evolution of the neutrino flavour eigenstate is given by:

$$|\nu_\ell(t)\rangle = \sum_i e^{-iE_i t}U_{\ell i}\,|\nu_i\rangle$$

Therefore, if the mass eigenstates are non-degenerate in mass, they will pick up different phases (because of their different energies $E_i$, due to their different masses) as they propagate through space, resulting in a different mixture of mass eigenstates that may correspond to a different flavour eigenstate. Thus, having at least one non-zero mass eigenstates is necessary in order for neutrino oscillations to occur, or at least two non-zero mass eigenstates for neutrino oscillations between all three pairings of flavour eigenstates.

The first evidence for neutrino oscillations came when the Homestake experiment,

which ran from the late 1960s, reported fewer neutrinos arriving at Earth from the Sun than were expected from solar models at the time [34]. Neutrino oscillations were suggested as a solution to this problem by Pontecorvo and Bilenky [35]. As the Homestake experiment was only sensitive to one flavour of neutrino, the electron neutrino, if neutrinos could change flavour en route from Sun, this would result in an apparent deficit in detected yield. The SNO Collaboration conclusively demonstrated in 2001, with an experiment sensitive to multiple solar neutrino types, that neutrino oscillations were indeed responsible for the deficit in electron neutrinos seen at Homestake [36]. Today, from various atmospheric, reactor and beam neutrino oscillation experiments, the difference-squared between all combinations of neutrino masses, and the mixing angles in the PMNS matrix, are known to be non-zero [22].

Direct measurements of neutrino mass have provided only upper bounds so far. For electron (anti-)neutrinos, the most stringent limits come from tritium beta decay measurements ($^3_1\mathrm{H} \rightarrow {}^3_2\mathrm{He} + e^- + \bar{\nu_e}$), where the mass of the $\bar{\nu_e}$ is determined from the shape of tail of the measured electron energy distribution, giving a limit of $m_{\bar{\nu_e}} < 2.05\,\mathrm{eV}$ [37]. For muon neutrinos, the limit is obtained from pion decays at rest ($\pi^+ \rightarrow \mu^+ + \nu_\mu$) by measuring the momentum of the resultant muon, which gives a limit of $m_{\nu_\mu} < 170\,\mathrm{keV}$ [38]. The limit on tau neutrino mass is the highest at $m_{\nu_\tau} < 18.2\,\mathrm{MeV}$, and comes from the ALEPH Collaboration, from analysis of tau decays to pions and a tau neutrino ($\tau^- \rightarrow 2\pi^- + \pi^+ + \nu_\tau$, $\tau^- \rightarrow 3\pi^- + 2\pi^+ + \nu_\tau$ and $\tau^- \rightarrow 3\pi^- + 2\pi^+ + \pi^0 + \nu_\tau$) [39].

It is clear then, that the neutrinos have small, but non-zero masses. Neutrino mass needs to be incorporated into the SM, in such a way as to preserve the degree of parity violation that is observed within the SM at low energies. It is possible to introduce Dirac masses for neutrinos to the SM by introducing right-handed $SU(2)$ singlet neutrino components [40]. Neutrino masses would then be generated via the Higgs mechanism, through mixing between the left- and right-handed components. This is not the ideal solution because the smallness of the known neutrino masses is not naturally explained, as the coupling constants between the right- and left-handed components would be arbitrary [40]. It would also be possible to introduce extra Higgs fields to allow two-component neutrino Majorana mass terms. However, a more attractive option is available if the need to introduce neutrino masses is seen as an opportunity to restore parity to the SM overall. This is the approach taken by Left-Right Symmetric Models, which are the focus of Section 2.3. Within the forms of LRSM considered in this thesis,

neutrino masses are generated by so-called 'Seesaw Mechanisms'. Very simply, these Seesaw Mechanisms describe a situation where the known neutrino masses are inversely proportional to the masses of some as-yet undiscovered neutrinos, and therefore the known neutrinos can be very light, if the new neutrinos are made to be heavy. These Seesaw Mechanisms are described in more detail in Sections 2.3.1 and 2.3.2.

## 2.3 Left-Right Symmetric Models (LRSMs)

LRSMs are a class of models that can restore parity to the SM, and can introduce a mechanism for the generation of neutrino masses. A key feature of LRSMs is that they introduce a right-handed component to the weak force, allowing left- and right-handed fermions to take part in weak interactions.

Pati and Salam first suggested the idea of left-right symmetry in 1974, as part of the Pati–Salam partial unification theory that attempted to unify the quarks and leptons under a set of four colour charges [41]. This idea of left-right symmetry was developed into the first Left-Right Symmetric Model in 1975 [42, 43, 44, 45]. This was then developed into a variant featuring the Type-I Seesaw Mechanism [46, 47, 48, 49], referred to in this thesis as the Type-I LRSM and discussed in Section 2.3.1, and a variant featuring the Inverse Seesaw Mechanism [50, 51], referred to in this thesis as the Inverse LRSM [52, 53, 54] and discussed in Section 2.3.2, among others. All of the the above LRSM variants predict heavy, right-handed $W$ bosons ($W_R$), and the Type-I and Inverse LRSMs predict heavy, right-handed neutrinos ($N_R$). The Keung-Senjanović process, involving $W_R$ and $N_R$, is discussed in Section 2.4, and is the focus of the analysis described in this thesis.

Though it is possible to introduce neutrino mass via a Seesaw Mechanism without embedding it in an LRSM [40, 55], LRSMs have the advantage of also explaining the parity violating nature of the weak force. It is also possible to formulate an LRSM that does not include a Seesaw Mechanism, but instead adds right-handed $SU(2)$ singlet neutrino components so that neutrino masses are obtained via the Higgs mechanism. In fact, this is how neutrino masses were included in the LRSM during its early development [42, 43, 44, 45]. Modern versions of LRSMs including Seesaw Mechanisms are preferred because they can explain the smallness of the known neutrino masses in a way that this setup cannot, as the coupling constants between the right- and left-handed neutrino components would be arbitrary [40].

Heavy neutrinos are sometimes postulated as dark matter candidates [56]. However, in the Type-I and Inverse LRSMs, the $N_R$ can decay, as discussed in Section 2.4. As dark matter must be stable on timescales comparable to the age of the Universe [57], LRSM $N_R$ do not seem to be a good candidate. But, if there were to exist a very light $N_R$ compared to the mass of the $W_R$, the decay of the $N_R$ could be highly suppressed, resulting in a long lifetime for the $N_R$ [58]. Therefore, it is possible that there could be one or more light, long-lifetime $N_R$ coexisting with heavy, short-lifetime $N_R$. Long-lifetime $N_R$ are not the focus of this thesis, but the discovery of a heavy $N_R$ participating in the Keung-Senjanović process would allow for the possibility that long-lifetime $N_R$ may also exist.

Features common to the Type-I and Inverse LRSMs will now be described. Both LRSMs introduce the $SU(2)_R$ gauge group, a right-handed analogue to the left-handed weak gauge group $SU(2)_L$. $U(1)_Y$ is also exchanged for $U(1)_{B-L}$, where $Y$ is the SM $U(1)$ hypercharge, $B$ is baryon number and $L$ is lepton number. The electric charge formula is redefined as follows:

$$Q = T_3 + \frac{Y}{2} \longrightarrow T_{3_L} + T_{3_R} + \frac{B-L}{2}$$

where $T_{3_L} = T_3$, weak isospin under $SU(2)_L$, and $T_{3_R}$ is the weak isospin under $SU(2)_R$.

Right-handed neutrino components are introduced, forming doublets with the existing right-handed lepton components:

$$\psi_L = \begin{pmatrix} \nu_{\ell_L} \\ \ell_L \end{pmatrix} \qquad \psi_R = (\ell_R) \longrightarrow \begin{pmatrix} \nu_{\ell_R} \\ \ell_R \end{pmatrix}$$

where $\ell = e, \mu, \tau$. The right-handed lepton doublet has $T_{3_R} = \pm\frac{1}{2}$ and $T_{3_L} = 0$, whilst the left-handed lepton doublet has $T_{3_R} = 0$, $T_{3_L} = \pm\frac{1}{2}$. Both doublets have $B - L = -1$.

The gauge fields associated with $SU(2)_L$ and $SU(2)_R$ are $\vec{W}_L$ and $\vec{W}_R$ respectively, where:

$$\vec{W}_{L,R} = \begin{pmatrix} W_1 \\ W_2 \\ W_3 \end{pmatrix}_{L,R}$$

$\vec{W}_L$ is identical to the SM $\vec{W}$ with elements $W_1$, $W_2$ and $W_3$, and $B$ is associated

with $U(1)_{B-L}$ in the same way it is for the SM $U(1)_Y$. The gauge coupling constants between the respective gauge fields and lepton fields are $g_L$ for $SU(2)_L$, $g_R$ for $SU(2)_R$, and $g'$ for $U(1)_{B-L}$.

The part of the LRSM Lagrangian that concerns the interaction of the LRSM gauge bosons with fermions is [40, 42]:

$$\begin{aligned}\mathcal{L}^{\text{LRSM}}_{\text{gauge}} = & g_L \left[\bar{q}_L \gamma_i \frac{\vec{\sigma}}{2} q_L + \bar{\psi}_L \gamma_i \frac{\vec{\sigma}}{2} \psi_L\right] \cdot \vec{W}^i_L \\ & + g_R \left[\bar{q}_R \gamma_i \frac{\vec{\sigma}}{2} q_R + \bar{\psi}_R \gamma_i \frac{\vec{\sigma}}{2} \psi_R\right] \cdot \vec{W}^i_R \\ & + g' \left[\frac{1}{6} \bar{q} \gamma_i q - \frac{1}{2} \bar{\psi} \gamma_i \psi\right] B\end{aligned}$$

where $q_L$ and $q_R$ are the SM left- and right-handed quark doublets, $\gamma_i$ are the Dirac matrices and $\sigma$ are the Pauli matrices. In order to ensure the model is parity conserving the Lagrangian is required to be invariant under:

$$\psi_L \longleftrightarrow \psi_R \qquad q_L \longleftrightarrow q_R \qquad \vec{W}_L \longleftrightarrow \vec{W}_R$$

This requires that the $SU(2)$ coupling constants are set to be equal ($g_R = g_L$).

Spontaneous symmetry breaking then occurs to break the LRSM gauge group down to the SM pre-spontaneous symmetry breaking group:

$$SU(2)_L \times SU(2)_R \times U(1)_{B-L} \longrightarrow SU(2)_L \times U(1)_Y$$

Following this, the usual SM spontaneous symmetry breaking occurs, which ensures that the LRSM looks like the SM at low energy scales:

$$SU(2)_L \times U(1)_Y \longrightarrow U(1)_{EM}$$

Different Higgs multiplets are introduced in different LRSM versions, and will be described in the following sections. The nature of the first SSB stage is dependent on the Higgs multiplets introduced.

### 2.3.1 ... with Type-I Seesaw Mechanism

In the Type-I LRSM, the SM Higgs doublet is replaced with a bidoublet $\phi$ and a triplet $\Delta$ with forms:

$$\phi = \begin{pmatrix} \phi_1^0 & \phi_1^+ \\ \phi_2^- & \phi_2^0 \end{pmatrix} \qquad \Delta_{L,R} = \begin{pmatrix} \frac{1}{\sqrt{2}}\Delta^+ & \Delta^{++} \\ \Delta^0 & -\frac{1}{\sqrt{2}}\Delta^+ \end{pmatrix}_{L,R}$$

This set of Higgs fields is left-right symmetric, as can be seen from the fields' $T_{3_R}$ and $T_{3_L}$ values. $\phi$ has $T_{3_R} = \pm\frac{1}{2}$, $T_{3_L} = \pm\frac{1}{2}$ and $B - L = 0$. $\Delta_R$ has $T_{3_R} = \pm 1$, $T_{3_L} = 0$, whilst $\Delta_L$ has $T_{3_R} = 0$, $T_{3_L} = \pm 1$. Both have $B - L = 2$.

The Higgs fields spontaneously gain VEVs [49]:

$$\langle\phi\rangle = \begin{pmatrix} \kappa & 0 \\ 0 & \kappa' \end{pmatrix} \qquad \langle\Delta_R\rangle = \begin{pmatrix} 0 & 0 \\ v_R & 0 \end{pmatrix}_R \qquad \langle\Delta_L\rangle = \begin{pmatrix} 0 & 0 \\ 0 & 0 \end{pmatrix}_L$$

The introduction of a VEV for the neutral $\Delta_R$ component ($\Delta_R^0$) breaks the LRSM gauge group to $SU(2)_L \times U(1)_Y$. It is important that $\Delta_L$ does not have a similarly induced VEV in order to prevent possibly large corrections to the light neutrino mass [59, 60]. The VEVs for $\phi$ take care of breaking $SU(2)_L \times U(1)_Y$ to $U(1)_{EM}$.

New LRSM gauge bosons $W_R^\pm$ (referred to as $W_R$ throughout this thesis) and $Z_R$ are formed post-SSB, along with the familiar SM gauge bosons, from the mixing of the pre-SSB gauge fields [40, 45, 59]. In general, the mass states of the charged bosons are a mixture of the $W_L$ and $W_R$ states, and the $\kappa'$ controls the degree of mixing. By choosing $\kappa \gg \kappa'$, mixing between $W_L$ and $W_R$ states is suppressed [40, 45] and the $W_L$ and $W_R$ can be treated as the mass states. A similar effect occurs whereby the mass states of the heavy neutral gauge bosons are mixtures of the $Z$ and $Z_R$ states, but as $v_R \to \infty$ this mixing is suppressed and $Z$ and $Z_R$ can be treated as mass states [40]. The set of gauge boson states are therefore,

in the limit $v_R \gg \kappa \gg \kappa'$:

$$\begin{aligned}
W_L^{\pm} &= \frac{1}{\sqrt{2}}(W_L^1 \pm W_L^2) \\
W_R^{\pm} &= \frac{1}{\sqrt{2}}(W_R^1 \pm W_R^2) \\
Z &= W_L^3 \cos\theta_W - W_R^3 \sin\theta_W \tan\theta_W - B \tan\theta_W \sqrt{\cos 2\theta_W} \\
Z_R &= W_R^3 \frac{\sqrt{\cos 2\theta_W}}{\cos\theta_W} - B \tan\theta_W \\
\gamma &= (W_L^3 + W_R^3)\sin\theta_W + B\sqrt{\cos 2\theta_W}
\end{aligned}$$

where $\theta_W$ is the SM Weinberg angle defined by $\sin\theta_W = e/g$, where $g = g_L = g_R$. In the limit $v_R^2 \gg \kappa^2 + \kappa'^2$ [47, 59], the masses of the bosons are given by:

$$\begin{aligned}
m_{W_L}^2 &\simeq \frac{g^2}{2}(\kappa^2 + \kappa'^2) \\
m_{W_R}^2 &\simeq \frac{g^2}{2}(\kappa^2 + \kappa'^2 + 2v_R^2) \\
m_Z^2 &\simeq \frac{1}{\cos^2\theta_W} m_{W_L}^2 \\
m_{Z_R}^2 &\simeq \frac{\cos^2\theta_W}{2\cos 2\theta_W} m_{W_R}^2 \\
m_\gamma &\simeq 0
\end{aligned}$$

By choosing $v_R \gg \kappa, \kappa'$, it is ensured that the LRSM gauge bosons are heavier than the SM gauge bosons.

The part of the Type-I LRSM Lagrangian that concerns the interaction of the LRSM Higgs fields with leptons is [59, 61] (shown for one generation for simplicity):

$$\begin{aligned}
\mathcal{L}_{\text{mass}}^{\text{LRSM}} &= h_{D_1}\bar{\psi}_L \phi \psi_R + h_{D_2}\bar{\psi}_L \tilde{\phi}\psi_R \\
&\quad + h_M(\bar{\psi}_L^c \Delta_L \psi_L + \bar{\psi}_R^c \Delta_R \psi_R) + \text{H.c.}
\end{aligned}$$

where $\tilde{\phi} = \sigma_2 \phi^* \sigma_2$ and '+ H.c.' indicates Hermitian conjugate terms have been omitted. The terms in the Lagrangian preceded by $h_{D_{1,2}}$ are Dirac mass terms, and $h_{D_{1,2}}$ are the coupling strengths. Terms preceded by $h_M$ can be identified as Majorana mass terms, with $h_M$ as the coupling strength. Following the two SSB stages, once the VEVs $\langle\phi\rangle$ and $\langle\Delta_R\rangle$ have been substituted into the Lagrangian,

the lepton mass is given by:

$$m_\ell = h_{D_1}\kappa' + h_{D_2}\kappa$$

For the neutrinos, a mass matrix for the $\nu_L$ and $\nu_R$ is obtained:

$$\begin{array}{c} \\ \nu_L \\ \nu_R \end{array} \begin{array}{c} \begin{array}{cc} \nu_L & \nu_R \end{array} \\ \begin{pmatrix} 0 & m_\ell \\ m_\ell & m_R \end{pmatrix} \end{array}$$

where $m_R = h_M v_R$. This matrix has eigenvalues of:

$$m_{\nu_{L,R}} = \frac{m_R \pm \sqrt{m_R^2 + 4m_\ell^2}}{2}$$

which in the limit $m_R \gg m_\ell$ (from $v_R \gg \kappa, \kappa'$), and expanding via a Taylor series, gives two masses:

$$m_{\nu_L} \simeq \frac{m_\ell^2}{m_R}$$
$$m_{\nu_R} \simeq m_R$$

This is where the name 'Seesaw Mechanism' originates: as $m_R$ increases, $m_{\nu_R}$ increases whilst $m_{\nu_L}$ decreases. In this way, the Type-I LRSM contains a natural reason for the small masses of the known neutrinos, and the LRSM gauge bosons and right-handed neutrinos could have masses that are within the reach of the LHC, assuming they exist. As a reminder that $\nu_R$ are heavy in the context of this model, $N_R$ will be used to refer to them in the rest of this thesis. Because $h_M$ is a free parameter, the mass hierarchies $m_{W_R} > m_{N_R}$ and $m_{N_R} > m_{W_R}$ are both possible. As the $\nu_L$ and $N_R$ resulting from the Type-I Seesaw Mechanism are Majorana particles, lepton number violating processes are predicted to occur involving them. One process involving Majorana $N_R$, the Keung-Senjanović process, is discussed in Section 2.4.

### 2.3.2 ... with Inverse Seesaw Mechanism

The Inverse Seesaw Mechanism, like the Type-I Seesaw Mechanism, provides a way to naturally explain the small masses of the known neutrinos. The Inverse Seesaw Mechanism was originally implemented in the context of superstring

theories [50, 51], but can also arise within an LRSM [52, 53, 54].

There are several ways to implement the Inverse Seesaw Mechanism in an LRSM, with different choices of Higgs multiplets. One way is to introduce a pair of Higgs doublets $\chi_{L,R}$, alongside $\phi$ and $\Delta_{L,R}$:

$$\chi_{L,R} = \begin{pmatrix} \chi^+ \\ \chi^0 \end{pmatrix}_{L,R}$$

$\chi_R$ has $T_{3_R} = \pm\frac{1}{2}$, $T_{3_L} = 0$, whilst $\chi_L$ has $T_{3_R} = 0$, $T_{3_L} = \pm\frac{1}{2}$. Both have $B - L = 1$. A set of singlet fermions $S$, with $T_{3_{L,R}} = 0$ and $B - L = 0$ are also introduced.

$\phi$ and $\Delta_R$ gain the same VEVs as in the Type-I LRSM, and $\chi_R$ gains a VEV:

$$\chi_R = \begin{pmatrix} 0 \\ \lambda_R \end{pmatrix}_R \quad \chi_L = \begin{pmatrix} 0 \\ 0 \end{pmatrix}_L$$

The part of the Lagrangian that concerns the interaction of the Higgs fields with leptons is (shown for one generation for simplicity):

$$\begin{aligned} \mathcal{L}_{\text{mass}}^{\text{LRSM}} &= h_{D_1}\bar{\psi}_L\phi\psi_R + h_{D_2}\bar{\psi}_L\tilde{\phi}\psi_R \\ &+ h_{N_1}\bar{\psi}_L\chi_L S + h_{N_2}\bar{\psi}_R\chi_R S + h_S S^c S \\ &+ h_M(\bar{\psi}_L^c\Delta_L\psi_L + \bar{\psi}_R^c\Delta_R\psi_R) + \text{H.c.} \end{aligned}$$

where $h_{N_{1,2}}$ are the couplings between $\phi_{L,R}^-$ and $S$, and $h_S$ is the $S$ self coupling.

Following the substitution of the VEVs $\langle\phi\rangle$, $\langle\Delta_R\rangle$ and $\langle\chi_R\rangle$, the lepton mass is given by:

$$m_\ell = h_{D_1}\kappa' + h_{D_2}\kappa$$

as in the Type-I LRSM. A mass matrix is formed for the $\nu_L$, $\nu_R$ and S:

$$\begin{array}{c} \\ \nu_L \\ \nu_R \\ S \end{array} \begin{array}{c} \begin{array}{ccc} \nu_L & \nu_R & S \end{array} \\ \begin{pmatrix} 0 & m_\ell & 0 \\ m_\ell & m_R & m_N \\ 0 & m_N & m_S \end{pmatrix} \end{array}$$

where $m_R = h_M v_R$, $m_N = h_N\lambda_R$ and $m_S = 2h_S$.

From this matrix, two mass eigenstates are formed from $\nu_R$ and $S$:

$$m_{N_{R_{1,2}}} = \frac{m_R \pm \sqrt{m_R^2 + 4m_N^2}}{2}$$

In the limit $m_R \to 0$, there are two equal magnitude, opposite sign solutions:

$$|m_{N_{R_1}}| = |m_{N_{R_2}}| = m_N.$$

In this situation, a pseudo-Dirac $N_R$ [62] is formed from the combination of the Majorana $N_{R_{1,2}}$. For a pseudo-Dirac $N_R$ formed in this way, as $m_R \to 0$, the amount of lepton number violation also tends to zero [52, 63]. The simplest way to ensure $m_R = 0$ is to remove the $\Delta_{L,R}$ entirely. As $m_R \to 0$, the light neutrino mass is given by:

$$m_{\nu_L} = \frac{m_S m_\ell^2}{m_N^2}$$

so, like in the Type-I Seesaw Mechanism, $m_{\nu_L}$ decreases as $m_{N_R}$ increases. The pseudo-Dirac $N_R$ will be referred to as a Dirac $N_R$ throughout the rest of this thesis.

## 2.4 The Keung-Senjanović Process

In LRSMs containing $W_R$ and $N_R$, $N_R$ can be produced via a $W_R$ and decay via a second $W_R$. This is known as the Keung-Senjanović process [64]. The $N_R$ must decay via a second $W_R$, if there is no mixing between the $W_L$ and $W_R$. When $m_{W_R} > m_{N_R}$, the second $W_R$ in the decay chain must be produced off mass shell, whilst in the $m_{N_R} > m_{W_R}$ case, the first $W_R$ is off shell. This results in suppressed cross sections for the $m_{N_R} > m_{W_R}$ case compared to the $m_{W_R} > m_{N_R}$ case, as shown in Section 4.3.1. The situation where the second $W_R$ decays to a quark pair is the focus of the analysis described in this thesis. Free quarks are not observed due to the approximately linear increase in the strong coupling strength when increasing the distance between colour-charged interacting objects. This characteristic of the strong force means that, as the two quarks travel apart, it is energetically favourable for additional colour-charged particles to be produced, and these additional colour-charged particles produce further colour-charged particles as they travel apart, and so on. The result of this process is a collimated spray of colour neutral hadrons - a jet. The Keung-

Senjanović process therefore has a two charged lepton plus two jets ($\ell\ell jj$) final state, as shown in Figure 2.3. When $m_{W_R} > m_{N_R}$ ($m_{N_R} > m_{W_R}$), the on-shell $W_R$ mass can be reconstructed from the invariant mass of the $\ell\ell jj$ ($jj$) system, while the $N_R$ mass can be found from the $\ell_2 jj$ system in both cases.

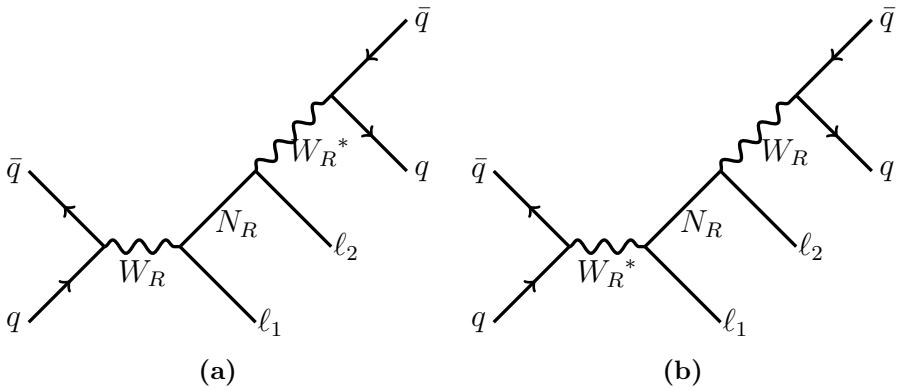


**Figure 2.3** The leading Feynman diagram for the Keung-Senjanović process, for (a) the $m_{W_R} > m_{N_R}$ case and (b) the $m_{N_R} > m_{W_R}$ case.

Dirac and Majorana $N_R$ can both participate in the Keung-Senjanović process, with the same production cross section [52]. The Majorana nature of the $N_R$ would be evident from the Keung-Senjanović process, from the ratio of events containing opposite-sign charged (OS) leptons to those containing same-sign charged (SS) leptons. In the version of the Type-I LRSM outlined in Section 2.3.1, lepton number violating processes can occur, due to the Majorana nature of the $N_R$. The result of this would be that the leptons in the $\ell\ell jj$ final state will have the same-sign charges half the time and opposite-sign charges the other half the time. If CP violating phase effects are included and some of the Type-I LRSM Majorana $N_R$ are degenerate in mass, the same-sign final state can be suppressed [52, 63], however this situation is not considered in this thesis. In the version of the Inverse LRSM described in Section 2.3.2, $N_R$ are pseudo-Dirac particles, and the final state leptons will have opposite-sign charges 100% of the time. As the $\ell\ell jj$ final state with opposite-sign leptons is sensitive to both Majorana and Dirac $N_R$, this final state is the focus of this thesis. Any possible mixing between $N_e$, $N_\mu$ and $N_\tau$ is not considered in this thesis, so only final states with same flavour leptons are considered. Final states with two electrons ($eejj$) or two muons ($\mu\mu jj$) are considered, referred to as the electron and muon channels respectively.

### 2.4.1 Existing limits

The Keung-Senjanović process in the $eejj$ and $\mu\mu jj$ final state has been studied by both ATLAS and CMS collaborations using $\sqrt{s} = 7\,\text{TeV}$ [65, 66], $\sqrt{s} = 8\,\text{TeV}$ [67, 68] and $\sqrt{s} = 13\,\text{TeV}$ [69] collision data. CMS also has published results for the hadronic $\tau\tau jj$ final state at $\sqrt{s} = 13\,\text{TeV}$ [70, 71], in which only leptonic $\tau$ decays are considered. No evidence for LRSM $W_R$ or $N_R$ has emerged from these studies. The current most stringent exclusion limits on LRSM $W_R$ and Majorana $N_R$ masses are derived by the CMS experiment [69] at $\sqrt{s} = 13\,\text{TeV}$, shown in Figure 2.4. In both electron and muon channels, the CMS collaboration excluded regions extending to $m_{W_R} \sim 4.4\,\text{TeV}$ (for a range of $m_{N_R}$ values), whilst the $m_{N_R}$ limits reach $\sim 2.9\,\text{TeV}$ in the electron channel (for $m_{W_R} \sim 3.8\,\text{TeV}$) and $\sim 3\,\text{TeV}$ in the muon channel (for $m_{W_R} \sim 3.6\,\text{TeV}$). The most stringent limits for the Dirac $N_R$ case, assuming the total $N_R$ production cross section is unchanged from the Majorana $N_R$ case, come from ATLAS at $\sqrt{s} = 7\,\text{TeV}$ [65], shown in Figure 2.5. The ATLAS Dirac $N_R$ results are presented for decays to either two electrons or two muons combined, rather than the two channels seperately, and the limits reach $m_{W_R} \sim 2.45\,\text{TeV}$ (for $m_{N_R} \sim 800\,\text{GeV}$), whilst the $m_{N_R}$ limits reach $\sim 1.5\,\text{TeV}$ (for $m_{W_R} \sim 1.8\,\text{TeV}$). The $m_{N_R} > m_{W_R}$ case has not been studied by LHC experiments, for either Majorana or Dirac $N_R$, until now.

Other bounds on $W_R$ and $N_R$ exist from double beta decay [72, 73] and from $W' \to jj$ searches [74], where $W'$ is a generic heavy $W$. Figure 2.6 presents combined limits from these searches in the electron channel, with the addition of recasted ATLAS limits in the $e + E_{\text{T}}^{\text{miss}}$ final state [75, 76], represented as limits on $m_{W_R}$ and $m_{N_R}$ [77]. $\ell + E_{\text{T}}^{\text{miss}}$ final states can occur from the Keung-Senjanović process at the LHC if the $N_R$ has a long enough lifetime to exit the detector. Of these, only the $W' \to jj$ limit is in a relevant section of the parameter space to this thesis, at $m_{W_R} \sim 3.7\,\text{TeV}$.

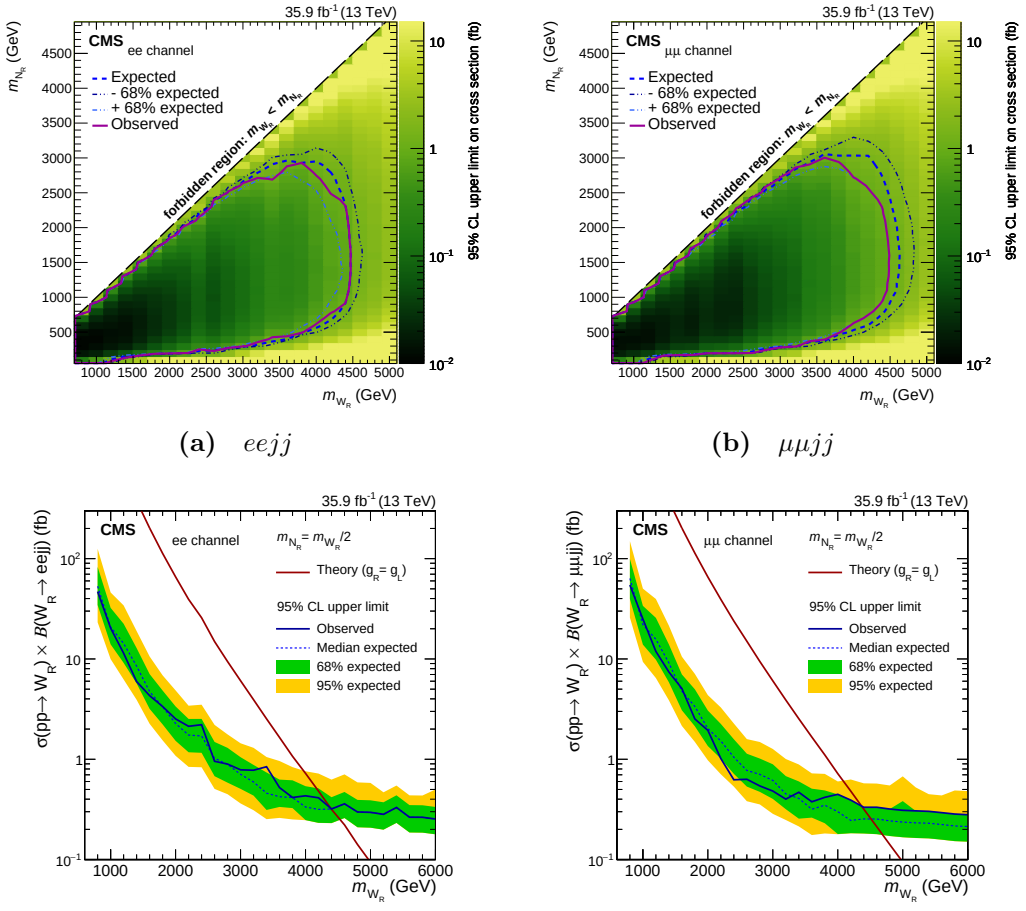


**(a)** $eejj$ **(b)** $\mu\mu jj$

**(c)** $eejj$ **(d)** $\mu\mu jj$

**Figure 2.4** The strongest current LHC limits on $W_R$–$N_R$ mass in the (a) $eejj$ and (b) $\mu\mu jj$ final states, by the CMS Collaboration at $\sqrt{s} = 13\,\text{TeV}$, for the Majorana $N_R$ case. (c) and (d) show limits for the $m_{W_R} = 2 \times m_{N_R}$ hypothesis. The cross section multiplied by branching fraction values shown in (a) and (b) are not consistent with the values shown in (c) and (d), and it is likely that the $z$-axes of (a) and (b) are mislabelled. No lepton charge requirement is applied and the $m_{N_R} > m_{W_R}$ mass hierarchy is not considered. Taken from [69].

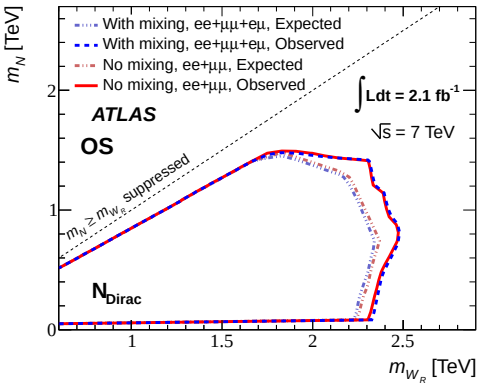


**Figure 2.5** The strongest current LHC limits on $W_R$–$N_R$ mass in the $eejj$ or $\mu\mu jj$ final states (combined), by the ATLAS collaboration at $\sqrt{s} = 7\,\text{TeV}$, for the Dirac $N_R$ case. Leptons are required to have opposite charges. Limits are also shown for the case where mixing between $N_R$ flavours is allowed, which is not considered in this thesis. The $m_{N_R} > m_{W_R}$ mass hierarchy is not considered. Taken from [65].

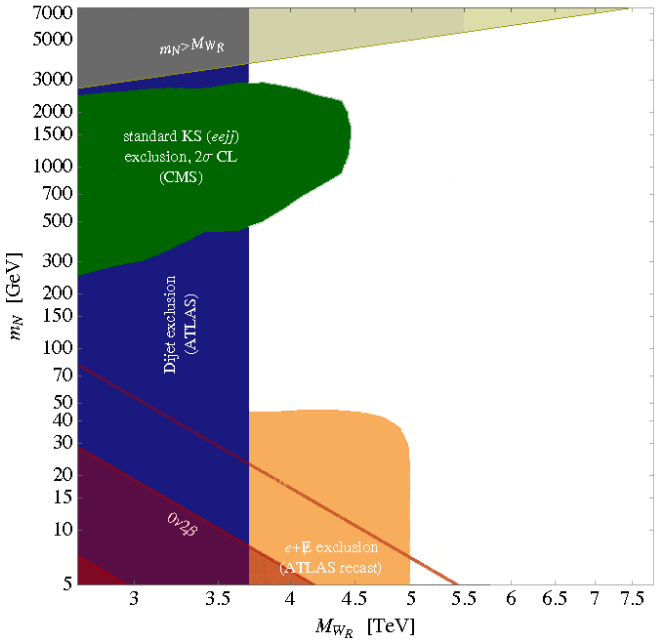


**Figure 2.6** The strongest current limits on $W_R$–$N_R$ mass in the electron channel. $\not{E}$ represents missing transverse energy, typeset as $E_{\text{T}}^{\text{miss}}$ throughout this thesis. Adapted from [77].

# Chapter 3

# The LHC and the ATLAS Experiment

The Large Hadron Collider (LHC) [78, 79, 80] is a 26.7 km circumference circular accelerator and collider, the largest particle accelerator in the world. Within the LHC, bunches of particles are accelerated and circulated in opposite directions, before being brought together in collisions with centre of mass energies ($\sqrt{s}$) up to 13 TeV (for proton-proton collisions to date). To reach these energies, particles are pre-accelerated in a number of smaller accelerators (shown in Figure 3.1), many of which used to be the main accelerators on the CERN site. This set of smaller accelerators are referred to as the LHC injector chain. Proton-proton collisions take place at the LHC as standard, and are the collision type of interest in this thesis, though lead and xenon ions are also occasionally collided. The LHC has 4 collision points, at which 7 detector experiments are positioned: ATLAS (A Toroidal LHC Apparatus), CMS (Compact Muon Solenoid), ALICE (A Large Ion Collider Experiment), LHCb (LHC beauty), LHCf (LHC forward), TOTEM (Total Elastic and Diffractive Cross Section Measurement), and MoEDAL (Monopole and Exotics Detector at the LHC). ATLAS is one of two 'general purpose' detectors on the CERN site, along with CMS, with a broad physics programme including Higgs boson physics, exotic particle searches and Standard Model precision measurements. Material in this chapter is drawn from [78, 79, 80] for the LHC and [81] for ATLAS, unless otherwise referenced.

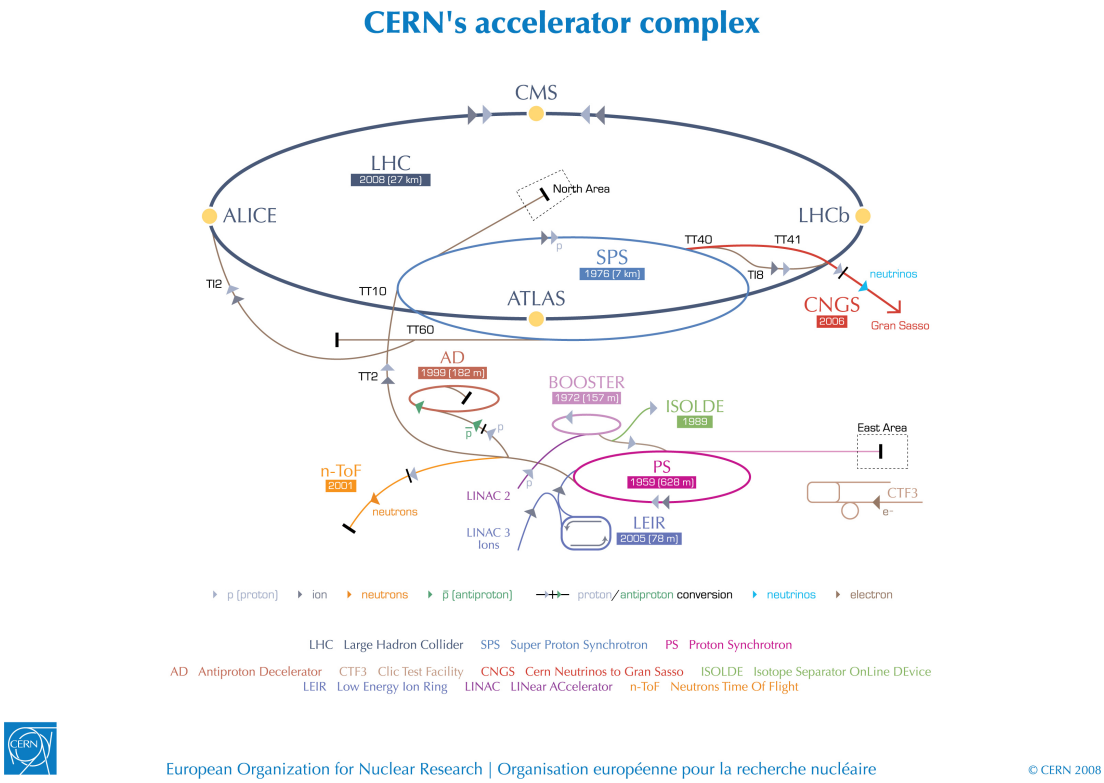


**Figure 3.1** A schematic of the CERN accelerator complex and many of the experiments on the CERN site [82].

## 3.1 The Large Hadron Collider

The LHC accelerates particles using radio frequency (RF) accelerating cavities. The shape of the RF cavities at the LHC is such that electromagnetic waves resonate at a particular frequency within the cavities when an external voltage is applied. Particles experience a Lorentz force when subject to an electromagnetic field, causing the particles to accelerate as they travel through the RF cavity. The applied voltage switches direction with a frequency appropriate to the target velocity of the particles. This causes particles that are travelling slower than the target velocity to accelerate, those travelling faster than the target velocity to decelerate, and those travelling at the target velocity to feel no net force. Particles travel through each RF cavity within a small tube, referred to as a 'beampipe'. The LHC can accelerate a maximum of 2556 bunches of $\mathcal{O}(10^{11})$ particles in this way.

As the LHC is a particle-particle collider, two beampipes are required so that particles can be accelerated in opposite directions. The beampipes are kept a high vacuum of $10^{-13}$ atmospheres in order to avoid particle interactions with gas

molecules. The LHC and the ATLAS detector are situated underground (45–170 m below surface level for different parts of the ring) for radiation shielding purposes. The circular nature of the accelerator allows for particles to be continuously accelerated for long periods of time. The maximum energy they can reach is therefore not constrained by having a beampipe of fixed length, like in a linear collider. In this way, the LHC can accelerate protons from 450 GeV, the energy they have when entering the LHC from the injector chain, up to 14 TeV. As the LHC makes extensive use of superconducting technology, it is kept cooled to 1.9 K by a cryogenic system.

The LHC uses 1232 superconducting dipole magnets to curve the paths of the particles as they accelerate. These superconducting dipole magnets consist of niobium-titanium coils, which produce an 8.33 T magnetic field when a current of 11 850 A is passed through them, when cooled to 1.9 K. The shape of the 8.33 T magnetic field produced by these magnets results in an equal strength but opposite direction field across each beampipe. The resultant force of this magnetic field on particles travelling in either direction acts towards the centre of the LHC ring, and keeps the particle trajectories correctly altered to keep them travelling around the ring. Figure 3.2 shows a cut-through of an LHC dipole magnet along with the two beampipes.

At each of the four LHC interaction points, the two particle beams can be brought together, resulting in collisions between particles within the two beams. These collisions reduce the number of particles in each bunch, decreasing the likelihood of collisions occurring when the beams are brought together in the future. 'Luminosity' is a measurement of the number of collisions that can be produced in the detector per area and per second, so as bunches circulate, the luminosity decreases. Bunches are kept circulating around the LHC until they have been sufficiently depleted that it is more efficient to 'dump' the bunches and inject new beams from the injector chain. A 'fill' is defined as the period for which a set of bunches circulate within the LHC between their injection into the main ring and when they are dumped. The LHC uses quadrupole magnets to bring the beams into paths where they will collide and to narrow them to increase the likelihood of head-on proton-proton collisions. Other magnets, including other types such as sextopole and octopole magnets, are used to keep the beams vertically and horizontally focussed and to perform tunes of beam other parameters.

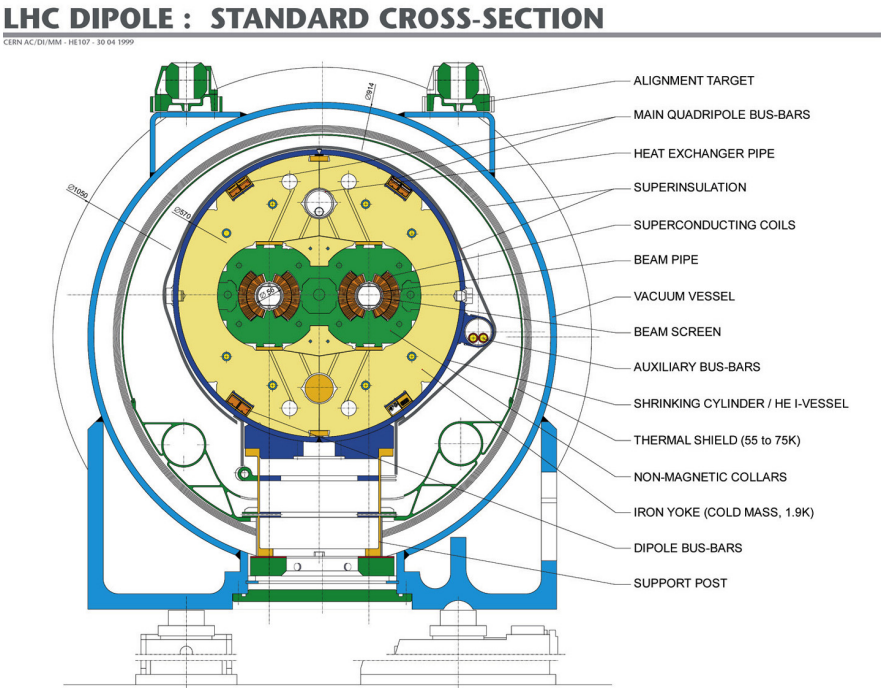


**Figure 3.2** A schematic of an LHC dipole magnet [83].

## 3.2 The ATLAS Detector

The ATLAS detector is one of the four main detectors situated at the LHC collision points. As a general purpose detector, it has been designed to track, identify, and characterise many types of particles arising out of collisions. Moving from the LHC beampipe outwards, the ATLAS detector can be divided into three sections: the Inner Detector, the Calorimeters, and the Muon Spectrometer. Figure 3.3 shows these different detector sections, and which sections are sensitive to which types of particle. The only known elementary particle type not detected by ATLAS are neutrinos. Their presence is instead inferred through imbalances in the detected energy or momentum distribution in the detector during collisions.

With respect to the ATLAS detector, some commonly used coordinates are defined as follows, where the interaction point is the origin: $x$ towards the centre of the LHC ring, $y$ upwards, $z$ along the beam axis (right-handed with respect to $x$ and $y$), $R$ the radius from the beampipe, $\phi$ the azimuthal axis around the beam axis, $\theta$ the polar angle from the beam axis, and the pseudorapidity $\eta = -\ln(\tan\theta/2)$, commonly used instead of $\theta$. ATLAS can not cover the whole solid angle around the collision point as this would require the detector be positioned within the beam line. Any particles produced with trajectories that

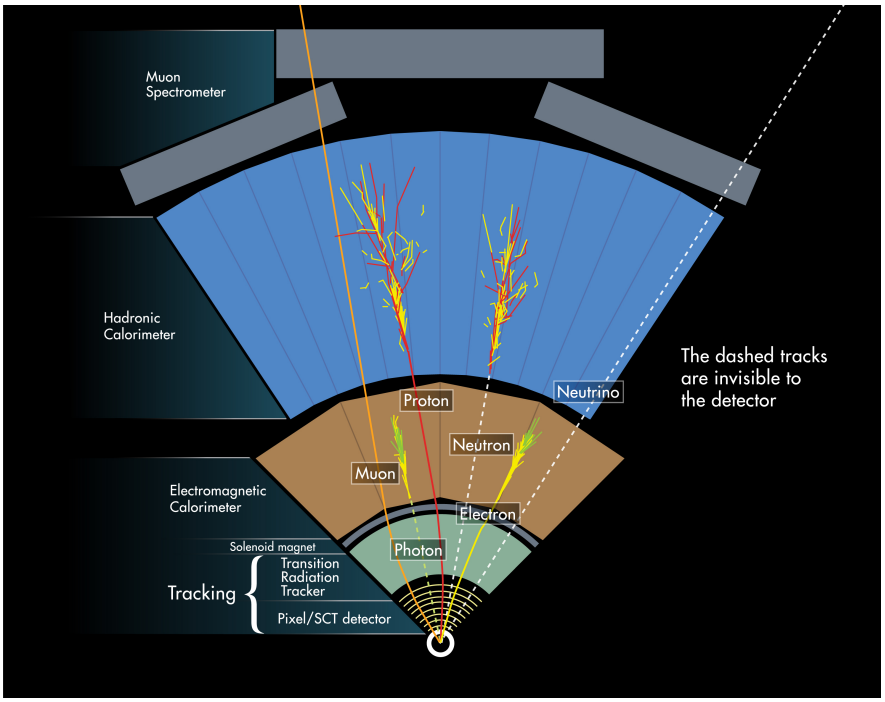


**Figure 3.3** A schematic of how ATLAS detects particles. The diagram shows a transverse slice through the detector with the beampipe as the small white circle at the bottom of the image. From [84].

carry them along the beam pipe can therefore not be detected. The quality of a detector which describes the percentage of events that it can detect for geometrical reasons is called the 'acceptance' of the detector. To make the acceptance of ATLAS as high as possible, the detector starts at $R = 3.3\,\text{cm}$ from the beam pipe and extends $\pm 22\,\text{m}$ along the beam pipe, with some detector segments orientated perpendicular to the beampipe, as can be seen in Figure 3.4. The region of the ATLAS detector where detecting elements are mounted parallel to and encircling the beampipe is referred to as the 'barrel' region, whilst the end sections that are mounted perpendicular to the beampipe are referred to as the 'endcap' regions.

A single event recorded by the ATLAS detector usually consists of multiple interaction vertices. The multiple interactions that occur are referred to as 'pile-up'. There are multiple sources of pile-up, including the fact that proton bunches are collided rather than single protons, the readout frequency of some detector components being such that collisions in adjacent bunch crossings can be overlaid, and effects due to the interaction of the beam and the beampipe [86]. A visualisation, or 'event display', of a bunch crossing occurring within the ATLAS detector featuring pile-up is shown in Figure 3.5. The average number of interactions per $pp$ bunch crossing in 2015 and 2016 combined was 24.

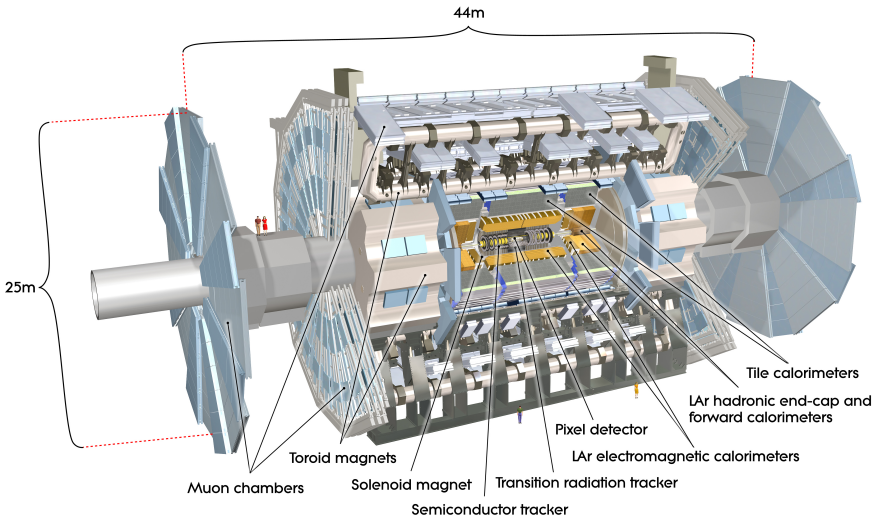


**Figure 3.4** A computer generated image of the ATLAS detector [85].

Very large amounts of data is created by the readout from all the ATLAS detector subsystems. The physics processes of interest to analysers often also have low cross sections and therefore occur rarely. The ATLAS trigger system reduces the amount of data sent to storage, in a way that enhances the proportion of interesting events in the stored data, by making fast assessments of events as they occur. The trigger system is described in more detail in Section 4.1. If an event is triggered on, the event data is processed with the aim of reconstructing what particle interactions occurred to produce the observed signals in the detector. This process, referred to as reconstruction, is described in Section 4.4.

### 3.2.1 The Inner Detector

The Inner Detector, shown in Figures 3.6 and 3.7, is designed to track charged particles by measuring their trajectories, momenta and charge as they leave the collision point. The Inner Detector consists of the three subdetectors: the Pixel Detector, the Semiconductor Tracker (SCT) and the Transition Radiation Tracker (TRT) and a 2 T solenoid magnet, as indicated in Figure 3.3. The Pixel Detector has been modified since construction of the ATLAS detector with the addition of the Insertable B-Layer (IBL) [88] in 2014. The insertion of the Inner Detector in the 2 T magnetic field allows positively and negatively charged particles to be discriminated, as their tracks bend in opposite directions in the field. Their momenta can also be determined, as the radius of curvature of the path taken by

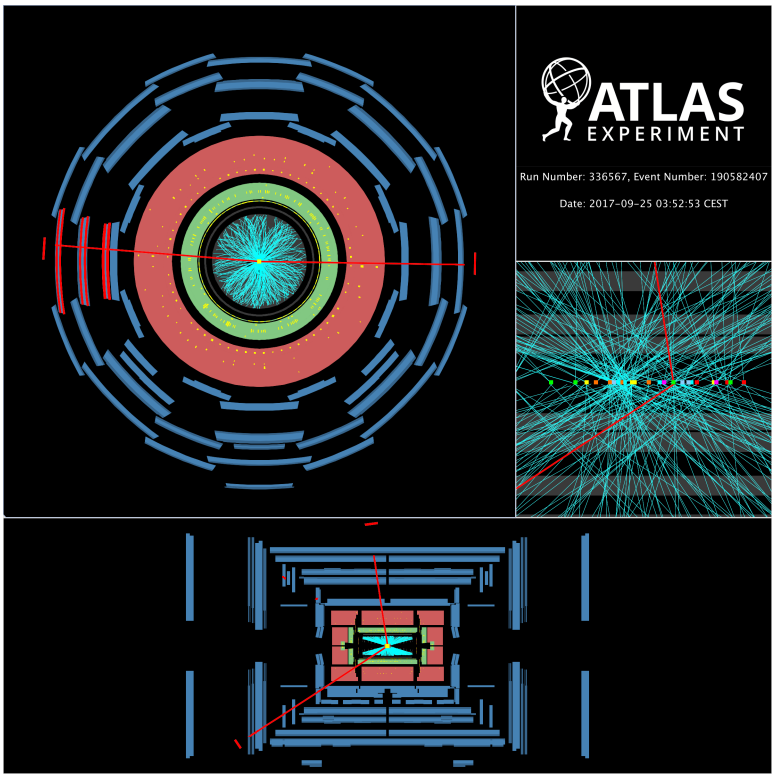


**Figure 3.5** An ATLAS event display of an event containing two muon candidates (red), along with multiple other interaction vertices. In the right panel, the 25 interaction vertices are marked by coloured squares. The reconstructed mass of the two muons is 91.1 GeV, indicating an $Z \to \mu\mu$ event. Taken from [87].

a particle in a magnetic field is proportional to the momentum of the particle. Tracking is also important for establishing which particles have emerged from which interaction point (or vertex), as many proton-proton collisions occur each time the two proton beams are brought together. The production of some particles, such as bottom quarks, can also result in a displaced vertex, where a short lived particle travels a short distance before decaying. The decay products will then originate from a distinct vertex some distance from the primary interaction vertex.

The Pixel and Semiconductor Tracker subdetectors both use silicon as their detecting material. When charged particles pass through silicon, electron and hole pairs are produced as the particle ionises the material. Though photons can also liberate electrons from atoms, photons produced in collisions within the ATLAS detector have high enough energies and the amount of material in the Inner Detector is low enough that photons are likely to pass through the Inner Detector without interacting. Charged particles do ionise the silicon as they pass through, by emitting lower energy photons as they pass through the

material, resulting in detectable signals. More details about how the Pixel and SCT subdetectors do this will be given in the next two sections, Sections 3.2.1.1 and 3.2.1.2. The Transition Radiation Tracker subdetector consists of small gas-containing tubes that act as proportional counters and will be discussed further in Section 3.2.1.3.

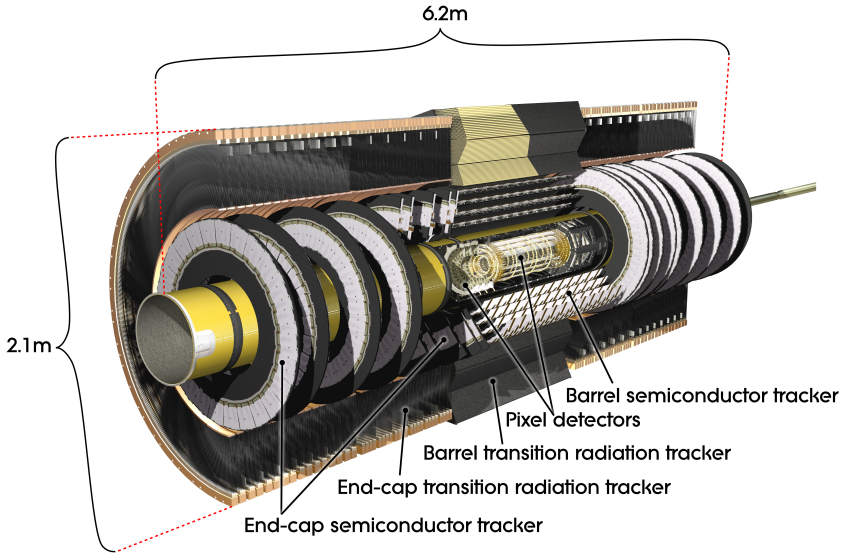


**Figure 3.6** A computer generated image of the ATLAS Inner Detector [89].

#### 3.2.1.1 The Pixel Detector

The original parts of the Pixel Detector, pre addition of the IBL, consists of 1774 silicon sensors connected to readout chips to form modules. The modules are mounted in different configurations in the barrel and endcap regions. In the barrel region, the straight section of the detector nearest the collision point, the modules are positioned on three cylindrical layers, concentric on the beampipe. The closest Pixel layer to the beampipe is positioned 5 cm away, as shown in Figure 3.7. The IBL was added at 3.3 cm from the beampipe, improving the resolution of the Pixel Detector. In the endcap regions, either end of the detector, two discs of sensors are positioned perpendicular to the beampipe. This layout gives coverage to $\eta = 2.5$, and full coverage in $\phi$ from 0 to $2\pi$, with resolution in $R - \phi \times z$ ($R - \phi \times R$ in the endcaps) of $10 \times 115\,\mu m^2$. Charged particles pass through an average of 3 sensors when passing through the Pixel Detector. When a particle passes through a sensor, this is referred to as a 'hit'. The modules are glued to staves (long, straight mounts) in the barrel region and sectors (segments of the disc) in the endcap region. The staves and sectors are then mounted on

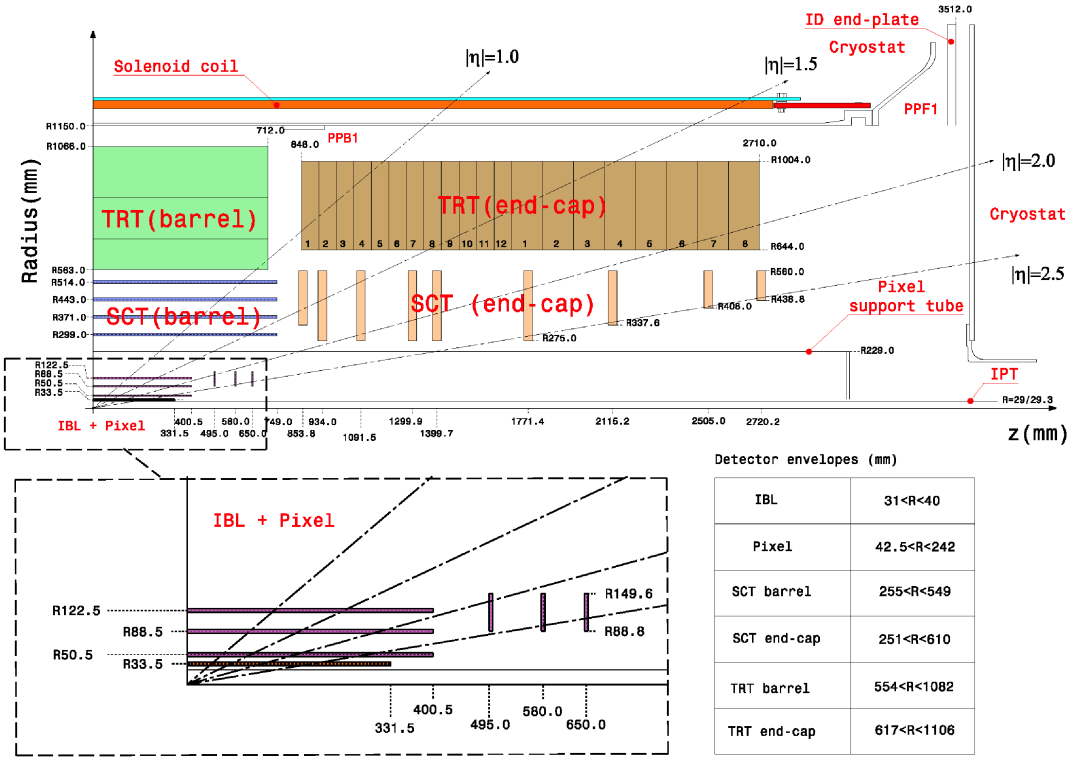


| | |
|---|---|
| IBL | 31<R<40 |
| Pixel | 42.5<R<242 |
| SCT barrel | 255<R<549 |
| SCT end-cap | 251<R<610 |
| TRT barrel | 554<R<1082 |
| TRT end-cap | 617<R<1106 |

**Figure 3.7** The arrangement and dimensions of the Pixel, SCT and TRT subdetectors [88].

carbon fibre structures (the Pixel Support Tube) in order to keep them accurately positioned.

The Pixel sensors are $n^+$-in-n type sensors: oxygenated n-type (negative-type: electrons are the majority charge carrier) silicon chips with p-type (positive-type: holes are the majority charge carrier) and $n^+$-type (enhanced negative type) doped regions, with the readout chips attached to the $n^+$ side. The silicon chips are doped on both sides to allow continued operation even when radiation damage has inverted the n-type bulk to form a p-type bulk. The nominal Pixel sensor size ($\sim$ 90% of the Pixel sensors) in $R-\phi\times z$ is $50\times 400\,\mu m^2$, with a thickness of 250 µm. The IBL also uses 75% $n^+$-in-n type silicon sensors however they have a nominal size in $R-\phi\times z$ is $50\times 250\,\mu m^2$. When particles pass through the Pixel and IBL sensors, a current is created as electron-hole pairs are formed, which are then swept to opposite sides of the depletion region created by the doping. The sensors are oxygenated to make them more radiation hard, which is crucial as they are mounted close to the beampipe. The readout chips record information relating to the rate of energy deposited in the detector ($dE/dx$) by particles by recording the time for which the charge deposited in each sensor

is over a set threshold value. This is referred to as the 'Time over Threshold' (ToT) measurement. By setting the minimum charge at which the readout chips register a hit to a set threshold value, the total energy deposited in that time can be found. $\mathrm{d}E/\mathrm{d}x$ for a track can then be found by looking at the amount of energy loss the particle suffers whilst passing through different pixel sensors and amounts of detector material. The linear relationship between ToT and injected charge and how $\mathrm{d}E/\mathrm{d}x$ information can be used for particle identification are shown in Figure 3.8.

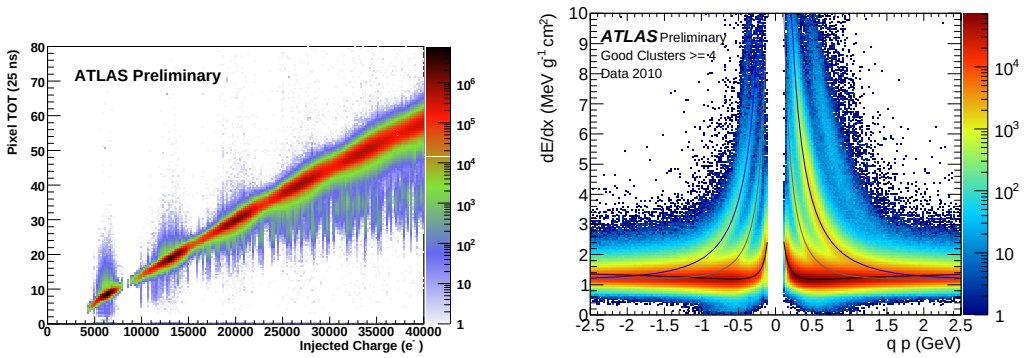


**(a)** **(b)**

**Figure 3.8** (a): the linear relationship beween ToT and charge, and (b): the relationship between $\mathrm{d}E/\mathrm{d}x$ and momentum for pions (black), kaons (gray) and protons (blue) for charged particles passing through the ATLAS Pixel Detector [90, 91].

#### 3.2.1.2 The Semiconductor Tracker (SCT)

The Semiconductor Tracker is the second of the ATLAS high-precision tracking devices, along with the Pixel Detector. It consists of 15 912 p-in-n silicon sensors with associated readout strips, forming 4088 modules. The SCT silicon sensors work in a similar way to the Pixel sensors and have a thickness of 285 µm. The SCT modules have several layouts to accomplish different goals, and are arranged in 4 layers in the barrel region and 9 disks in the endcaps. Modules in the barrel layers are mounted so as to be rotated from each other by a stereo angle of 40 mrad so as to provide information in the $z$ direction. Sufficiently energetic particles traversing the SCT from the interaction point pass through at least 4 SCT layers. The SCT has a resolution in $R - \phi \times z$ ($R - \phi \times R$ in the endcaps) of $17 \times 580\,\mu\mathrm{m}^2$, with coverage out to $\eta = 2.5$.

#### 3.2.1.3 The Transition Radiation Tracker (TRT)

The TRT consists of bundles of drift tubes (referred to as straws) containing predominately (70%) xenon as well as carbon dioxide and oxygen, with a thin (31 µm) gold-plated tungsten wire running through the centre of each straw. A potential difference of 1.5 kV is present between the wire and the polyimide walls of the straws, so that they can act as small proportional counters. The straws are surrounded by polymer fibres which cause transition radiation to be emitted, which is an effect whereby relativistic charged particles emit radiation as they pass from one material to another, due to the different magnetic and dielectric properties of the media. The charged particles accompanied by these photons then pass through the straws, ionising the gas inside, causing a current to flow as freed electrons are attracted to the central wire. The transition radiation enhances the amount of ionisation that occurs within the straws. The amount of transmission radiation emitted depends of the relativistic $\gamma$ factor of the particle in question, with the effect being strongest for electrons. The amount of transition radiation affects the time that the recorded charge exceeds a set threshold (ToT), allowing charged particles to be discriminated. The drift time (the time taken for a signal to travel from the point in a straw where a particle has passed through to the central wire), which is determined from the arrival time and the collision time by calibration [92], allows the distance between a particle track and the central wire distance to be determined. Relationships between ToT and particle identification and drift time and track-to-wire distance are shown in Figure 3.9.

Each TRT straw has a diameter of 4 mm and they are 144 cm long in the barrel region (37 cm in the endcaps). The straw walls have a thickness of 70 µm in order to keep the amount of material in the detector low. The ∼300 000 straws are aligned parallel to the beampipe in the barrel and fanned radially in the endcaps, and provide ∼30 hits per track. Due to the orientation of the straws, they provide 2D spatial information rather than 3D with an accuracy of in terms of $R - \phi$ of 130 µm in the barrel. The gas in the TRT straws is constantly circulated and the gas quality is monitored in order to maintain stable conditions in the detector. After the discovery of irreparable leaks in the gas system, some straws have subsequently been modified to use an argon gas based mixture, rather than the xenon mixture, as the argon mixture is cheaper but performance between the two mixtures is comparable [93].

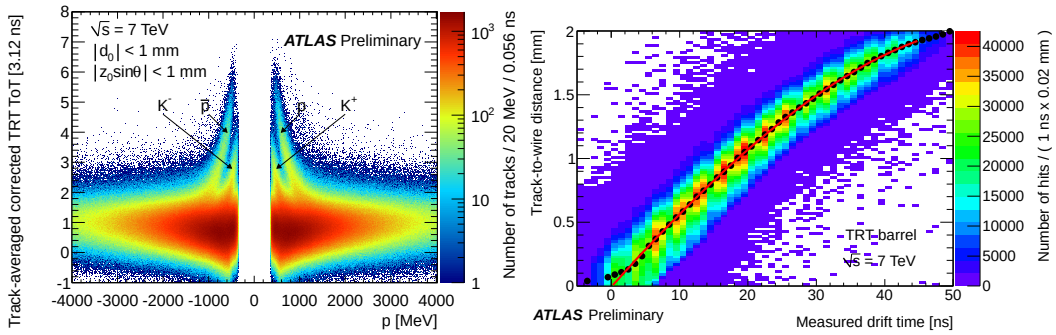


**(a)** **(b)**

**Figure 3.9** (a): the linear relationship beween ToT and momentum in data and (b): the relationship between drift time and track-to-wire distance for particles passing through the TRT [92, 94].

### 3.2.2 The Calorimeters

After leaving the Inner Detector, particles enter the ATLAS calorimeters. The calorimeters are designed to absorb incident electrons, photons and hadrons and output a signal that is proportional to the energy of the incident particles. They are constructed of alternating layers of absorbing and scintillating materials in order to achieve this. In terms of design, the calorimeters are divided into the Tile Calorimeter (TileCal) and the Liquid Argon (LAr) Calorimeters, however here we will divide them by functionality. The inner calorimeter section is designed to absorb electrons and photons and their associated electromagnetic showers and therefore is referred to as the electromagnetic calorimeter, whilst the outer calorimeter section's primary purpose is to absorb hadronic showers originating from hadrons, and is referred to as the hadronic calorimeter. The electromagnetic calorimeter uses liquid argon as the scintillating material in the barrel (LAr barrel) and endcap (LAr electromagnetic endcap, EMEC) regions, and lead and steel as absorbers. The hadronic calorimeter uses plastic scintillating tiles and steel as an absorber (TileCal), as well as LAr as a scintillator and copper as an absorber in the endcap regions (LAr hadronic endcap, HEC). The Forward Calorimeter (FCal) covers the very high $\eta$ region near the beampipe. The layout of the calorimeters is shown in Figure 3.10.

Though the calorimeters work by the same general principle, absorbing particles in order to determine their energy, there are distinctions due to the differences in the types of showers they are designed to measure. Hadronic showers, or jets, are in generally wider and longer than purely electromagnetic showers, so the

hadronic calorimeters extend deeper in $R$ than the electromagnetic calorimeters. The electromagnetic calorimeter has a total thickness between 14–40 radiation lengths ($X_0$, the distance travelled by a high energy electron through a material in which it loses $1 - 1/e$ of its energy, or 7/9 of the mean free path for a photon), meaning that it is highly likely that electromagnetic showers will be contained within this section of the detector. However, for hadronic showers the electromagnetic calorimeter is not as significant, with a maximum thickness of 4 nuclear interaction lengths (the mean path length to reduce the number of hadrons in a shower by $1/e$), whilst the hadronic calorimeter extends to between 10–19 nuclear interaction lengths. The thickness of all electromagnetic calorimeter and hadronic calorimeter sections are shown in Figure 3.11.

The ATLAS calorimeters have an unequal response to electromagnetic and hadronic showers. Electromagnetic showers usually result in all the energy of the incident particle being deposited in the detector, while for hadronic showers this is not the case. Electromagnetic showers are formed of bremsstrahlung (braking radiation) and pair production, as described in Section 3.2.2.1, whilst hadronic showers are more complicated, including strong interactions between hadrons (in the shower) and nuclei (in the detector material). Some of the energy of hadronic showers is not fully captured by the detector, and is for example lost to nuclear recoil in the absorbing material, before reaching the scintillating material. Hadronic showers also contain an electromagnetic shower component, as neutral pions produced via nuclear interactions decay to two photons 99% of the time [22].

#### 3.2.2.1 The Electromagnetic Calorimeter

In the electromagnetic calorimeter, accordion shaped (see Figure 3.12) layers of lead and steel act as absorbers to slow incident particles down, sandwiching 2 mm thick layers of liquid argon, with a copper electrode layer within each layer of liquid. Incident particles cause showers of electron-positron pairs and photons to be produced as they pass through the absorbers. These showers occur when high energy particles emit high levels of bremsstrahlung when they accelerate or decelerate due to magnetic fields around the nuclei in the absorbing material. High energy photons lose most of their energy through pair production, causing a chain reaction of electron, positron and photon production. Low energy electron-positron pairs and photons produced in the absorbers then go on to ionise the

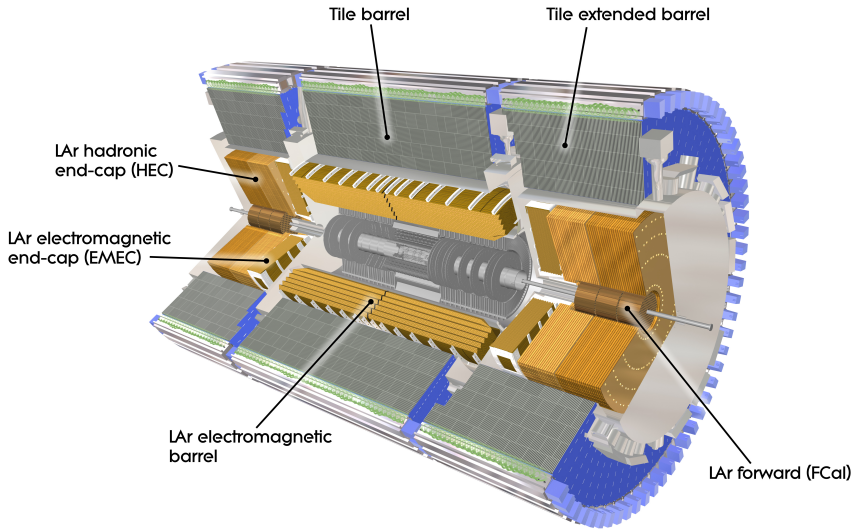


**Figure 3.10** A computer generated image of the ATLAS Calorimeters [95]. The electromagnetic calorimeter consists of the LAr electromagnetic barrel, the EMEC, and the FCal, whilst the hadronic calorimeter consists of the TileCal sections and the HEC.

liquid argon, producing a detectable current as electrons are drawn to the copper electrodes. The energy of the particle absorbed by the calorimeter is established from the magnitude of the signal produced. An advantage of using liquid argon as the scintillating material is that it is naturally radiation hard as it is a noble element.

The barrel electromagnetic calorimeter is segmented into 3 sections in $R$, so provides 3 energy deposition measurements if a particle radially traverses the full body of the electromagnetic calorimeter. In the central barrel regions ($\eta < 1.8$), and in front of the endcap wheels, presamplers are present to record the energy of incident particles before they enter they calorimeter. This is so that accurate readings of the energy loss by particles within the calorimeter can be recorded with reference to the energy they had when entering the calorimeter. Each section of the barrel electromagnetic calorimeter has a different granularity in terms of readout area, as show in Figure 3.12a. The granularity of the electromagnetic calorimeter is similar in the endcap regions, but instead of the folds of accordion geometry encircling the beampipe, the folds emanate outwards from the beampipe. The first layer of the FCal also acts as an electromagnetic calorimeter, with copper used as the absorber. Here, the structure is one consisting of tubes filled with liquid argon with electrode rods running through the centre, as opposed to the accordion structure in the barrel region.

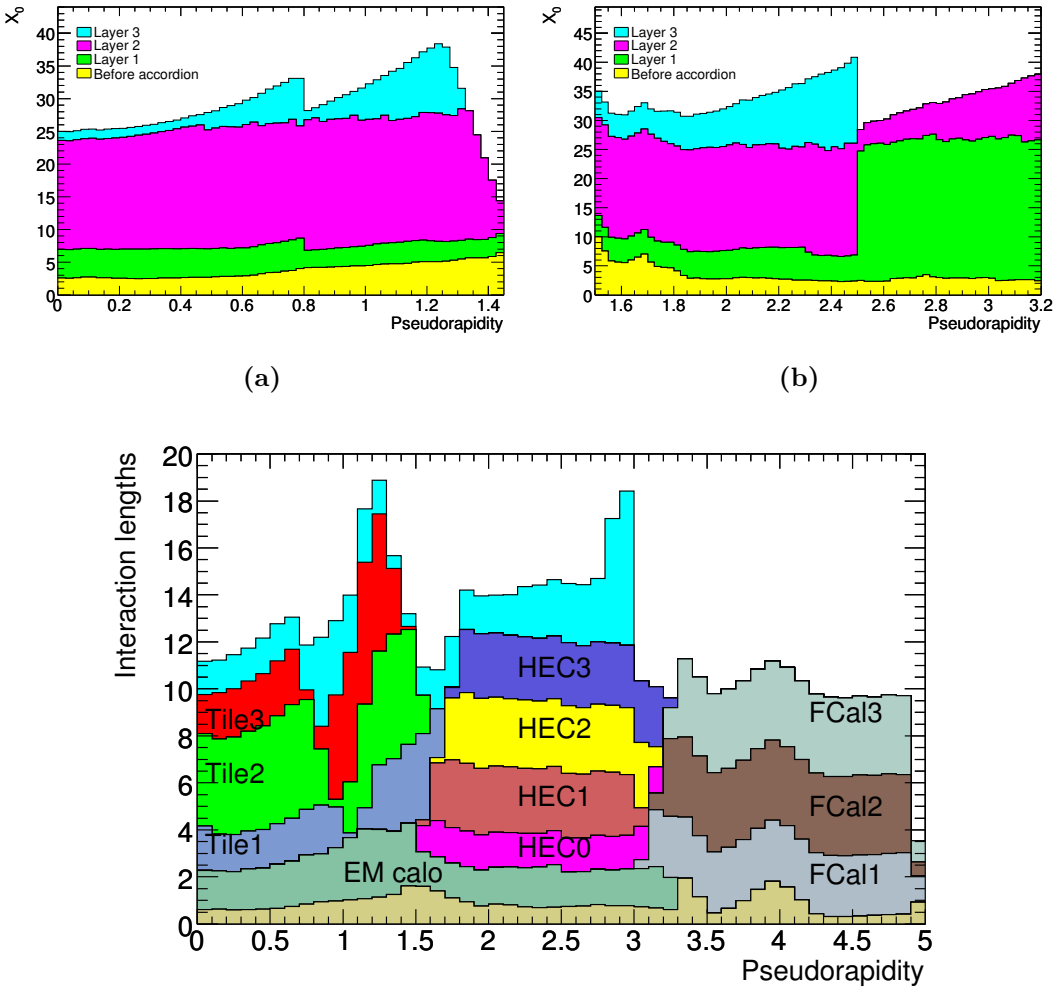


**Figure 3.11** The amount of material (in terms of radiation length $X_0$) in the electromagnetic calorimeter (a) barrel and (b) endcap layers. 'Before accordion' indicates the material in the inner regions of the detector. Additionally, (c) shows the amount of material (in terms of interaction length) in the 3 barrel Tile layers, the 4 hadronic endcap (HEC) layers and the 3 forward calorimeter (FCal) layers. The light brown region shows the material in the inner regions of the detector and the cyan region shows the additional material proceeding the Muon Spectrometer. From [81].

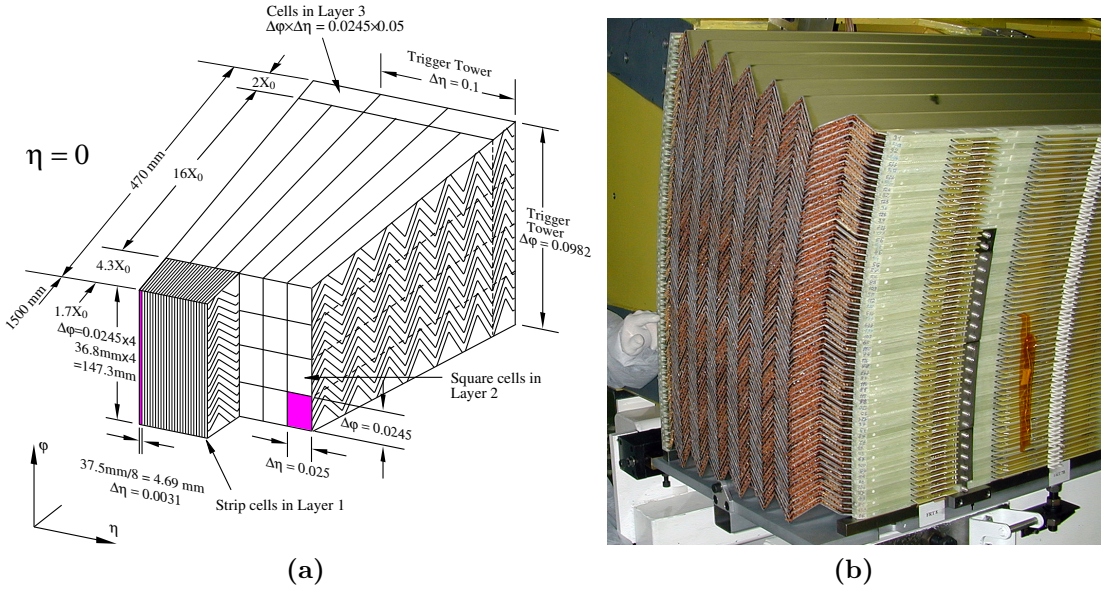


(a) (b)

**Figure 3.12** (a): the geometry of the LAr electromagnetic calorimeter barrel region at $\eta = 0$, from [81], and (b): the first constructed ATLAS electromagnetic calorimeter module, showing the distinctive accordion geometry of the layers of absorbing and scintillating material [96]. The sensor granularity varies by layer and is stated on the plot, as well as the depth of each section of the electromagnetic calorimeter in radiation lengths ($X_0$). The labelled 'trigger towers' refer to the regions that are read out by the ATLAS L1 trigger system, which is described in more detail in Section 4.1.1.

#### 3.2.2.2 The Hadronic Calorimeter

The barrel and extended barrel of the hadronic calorimeter, the TileCal, uses plastic scintillating tiles and steel absorbers, as already stated. The scintillating tiles are made of polystyrene doped with ∼1.5% fluorescent compounds. Ultraviolet light is produced within the scintillator when ionising particles pass through the plastic tiles, which is shifted to the visible range by the fluorescent compounds. Wavelength shifting fibres are attached to the edges of the plastic tiles which shift the light to a longer wavelength and guide it to photomultiplier tubes. The intensity of the light detected by the photomultiplier tubes is then used as a measure of the energy of the initial incident particle. The structure of the TileCal modules is shown in Figure 3.13a. There are 3 layers of TileCal modules in the barrel region, resulting in 3 energy samplings. The LAr hadronic endcap and the two hadronic FCal layers instead use liquid argon as the scintillating material, like the electromagnetic calorimeter, as these areas need higher resistance to radiation, which LAr provides. The endcap uses copper as an absorber, whilst the hadronic FCal uses tungsten. The hadronic FCal has the same basic structure

as the electromagnetic FCal, and is shown in Figure 3.13b.

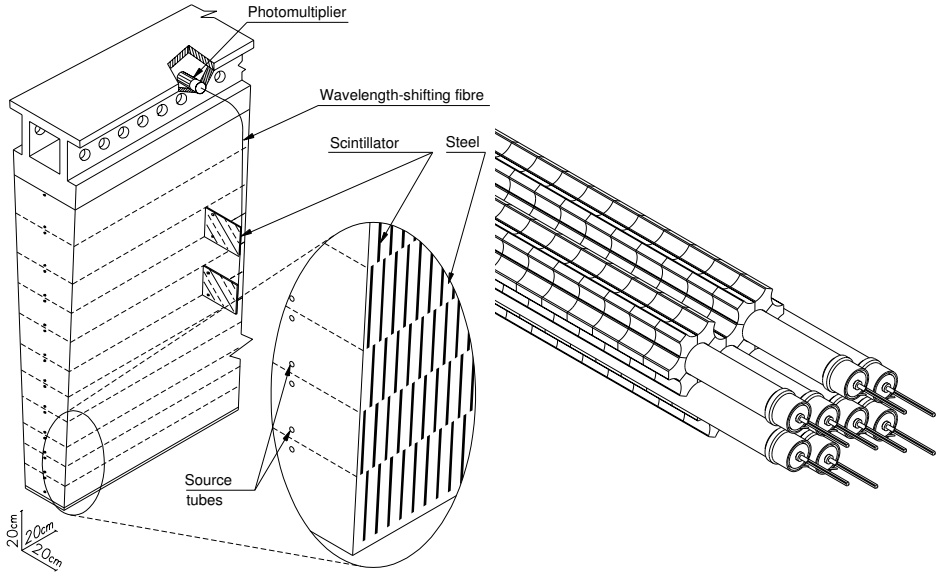


**Figure 3.13** (a): a TileCal module showing the plastic scintillator and steel absorber plates, the wavelength shifting fibres, and the photomultiplier tubes. Particles are incident from the bottom of the module. Also, (b): an illustration of the hadronic FCal tungsten rods, copper tubes (containing LAr), and tungsten absorber matrix. Both from [81].

### 3.2.3 The Muon Spectrometer

Muons pass through the inner subdetectors of ATLAS without being absorbed as their greater mass (compared to electrons) means they do not lose as much energy when passing through matter. They therefore pass through the whole of ATLAS, leaving tracks within all sections of the detector. The final section of the detector, the Muon Spectrometer, is inserted in a large magnetic field which allows measurements of muon momenta to be made, as the trajectories of the muons bend under the influence of the field. The magnetic field is supplied by 3 large air-core superconducting toroidal magnets, one in the barrel section (with strength up to 2.5 T) and two at the endcaps (with strength up to 3.5 T). The magnetic field is so constructed that muons bend in the $\eta$ plane, but not in the $\phi$ plane, with the exception of the $1.3 \leq |\eta| \leq 1.65$ region where the transition between fields created by barrel and endcap magents creates a complex field geometry. By this point, all other particles that are visible to the detector will have been stopped within the other subdetectors, meaning that this momentum measurement is enough to establish the energy of the muons, as their mass is known. There are

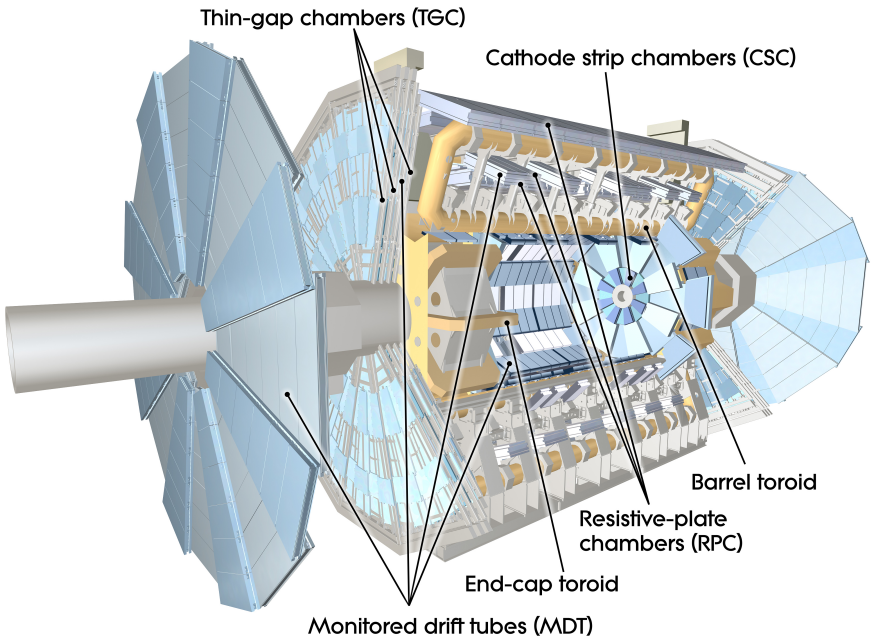


**Figure 3.14** A computer generated image of the ATLAS Muon Spectrometer, showing the 4 types of muon chambers [97].

4 different types of muon chambers within the Muon Spectrometer, as shown as Figure 3.14. The Monitored Drift Tubes (MDTs) and Cathode Strip Chambers (CSCs) are used for precision tracking, whilst the Thin Gap Chambers (TGCs) and Resistive Plate Chambers (RPCs) are used for momentum measurement and triggering. The RPCs and TGCs are suitable for triggering as they provide fast and coarse muon momentum measurements.

#### 3.2.3.1 Monitored Drift Tubes (MDTs)

The ∼30 mm diameter Monitored Drift Tubes are proportional drift tubes containing 93% Argon gas and 7% carbon dioxide, with a 50 µm central anode wire, made of tungsten-rhenium. There is a 3080 V potential difference between the aluminium drift tube walls and the anode wire. When a muon passes through, the gas is ionised, with electrons and the ions drifting towards the central wire and edges of the tube, depending on whether they are positively or negatively charged. The time taken for the electrons to drift to the central allows their starting locations within the tube to be found, and therefore the path of the muon to be tracked. In a similar way to the TRT straws (see Section 3.2.1.3), the drift time is calculated from the time when a signal is detected, and the collision time using a calibration constant that includes factors relating to the time of

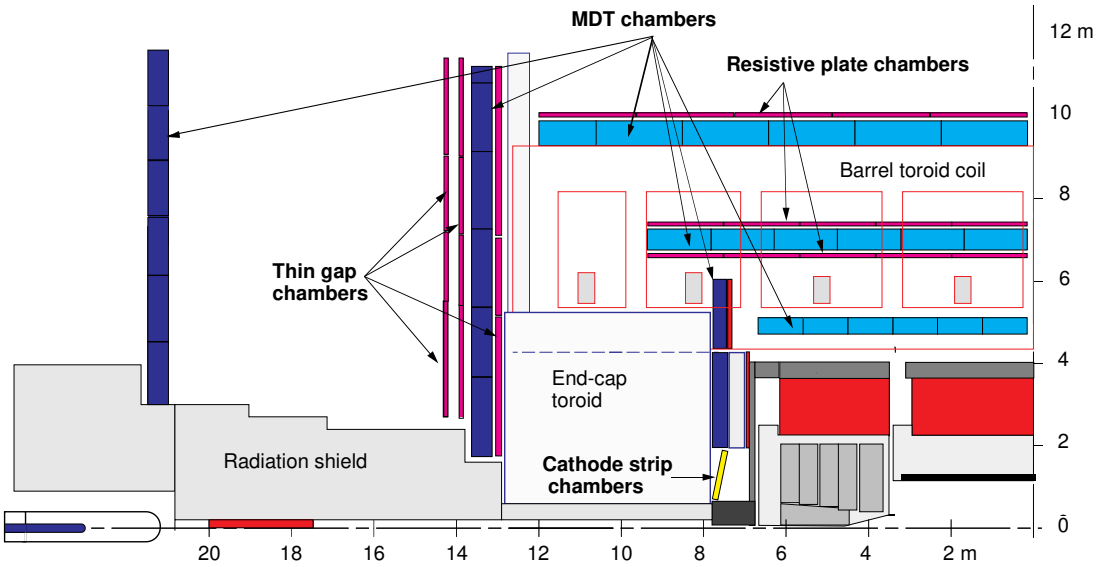


**Figure 3.15** The position of the muon subdetectors in the $y - z$ plane. The interaction point is at the bottom right corner of the figure. From [98].

flight of particles from the interaction point and cable delays [99]. This drift time is then related to the radius (see Figure 3.16a) travelled by the drift electrons. The average spatial resolution obtained by the MDTs is ∼80 µm. The MDTs are referred to as 'monitored' because of the existence of a gas monitoring system that continuously measures the composition of the gas that is cycled through the MDTs at a rate of one detector volume per day [100]. The composition of the gas can cause significant changes to drift times so is important to measure. There are 656 MDT chambers in the barrel region and 494 in the endcaps, each containing between 192–432 individual tubes. Each muon passes through an average of 20 MDTs in both the barrel and the endcaps.

#### 3.2.3.2 Cathode Strip Chambers (CSCs)

In the high $2 < \eta < 2.7$ region, MDTs are replaced by Cathode Strip Chambers, that can handle the higher counting rates present in this region. MDTs can handle counting rates up to 150 Hz/cm$^2$, whilst CSCs can operate at up to 1000 Hz/cm$^2$. The Cathode Strip Chambers are multiwire proportional chambers containing an 80% Argon and 20% carbon dioxide gas mix. Each CSC contains multiple 30 µm gold-plated tungsten anode wires orientated with the central wire radial from the beampipe, with the other wires parallel to this wire. When muons pass through the gas, ionisation electrons are drawn to these wires due a potential difference of 1900 V within the chambers. The current in the anode wires induces a charge on

cathode strips, which are positioned either parallel or perpendicular to the anode wires, as shown in Figure 3.16b, to provide 2D spatial information. A signal is usually induced in 3–5 cathode strips per incident particle, and the measurement of the relative signals to the cathode strips allows a resolution of 60 µm in each plane to be reached. Each chamber includes 4 planes of anode wires and cathode strips (two in each orientation). There are two discs of CSC chambers containing 8 chambers each.

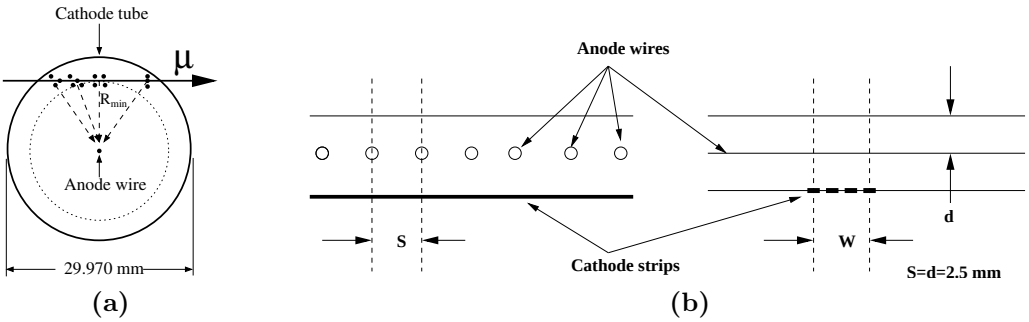


**Figure 3.16** (a): a cross section of an MDT, showing the path taken by electrons ionised from the gas inside the tubes and the radius of closest approach ($R_{\min}$). So as to prevent multiple signals from the same muon in the same tube being recorded, a deadtime is applied after a signal is detected during which no signals are read out. The circle around the anode wire with radius $R_{\min}$ is referred to as a 'drift circle'. Also, (b): the structure of a CSC viewed down the anode wires (left) and perpendicular to the wires (right). The cathode strips are arranged either parallel or perpendicular to the anode wires. Both from [81].

#### 3.2.3.3 Resistive Plate Chambers (RPCs)

The Resistive Plate Chambers are positioned in 3 concentric layers around the beampipe in the barrel region. The chambers consist of parallel phenolic-melaminic plastic laminate plates at a distance of 2 mm from each other, filled with a $C_2H_2F_4$/Iso-$C_4H_10$/$SF_6$ gas mixture in 94.7%:5%:0.3% proportions. An electric field with strength 4.9 kV/mm is present between the plates. A charged particle crossing this gap will create an avalanche of electrons, and therefore a detectable signal, which is read out through metallic strips that are capacitively coupled to the plates. Two layers of readout strips are positioned perpendicular to each other per gas layer to measure in the $\eta$ and $\phi$ directions. Each barrel RPC layer consists of two gas layers, so 6 $\eta$ vs. $\phi$ measurements are made for a muon passing through all three layers. The spatial location of muons passing

through the RPC layers allows their momentum to be determined as their tracks curve in the barrel toroid magnetic field.

#### 3.2.3.4 Thin Gap Chambers (TGCs)

Thin Gap Chambers are multiwire proportional chambers which work in a very similar way to the CSCs. They consist of strips containing multiple anode wires containing a 55% carbon dioxide, 45% n-pentane gas mixture. The TGCs are used in the endcap regions where, compared to the barrel region, greater and $\eta$ dependant sensor granularity is required. This is because muon momentum strongly increases with $\eta$, for a given $p_{\mathrm{T}}$. Radiation levels in the endcap regions are also around 10 times higher than in the barrel region, which the TGCs can handle. Figure 3.15 shows the position of the RPC and TGC layers relative to the MDT layers.

# Chapter 4

# Data Collection, Event Simulation and Reconstruction

This chapter describes how data is collected with the ATLAS experiment, how events are simulated for use in analyses, and how data and simulated events are both reconstructed from their raw types into 'physics object' candidates: data objects that are designed to represent the real physical particles detected as accurately as possible.

There is a distinction within ATLAS data processing which it is important to define. 'Online' refers to processing of data from the detector that occurs at the detector site (LHC Point 1, P1), within a specialised software environment (the ATLAS online software environment). 'Offline' refers to processing that occurs across the ATLAS computing grid. Reconstruction of data from the detector occurs almost exclusively at the Tier-0 computing centre, the first level of the ATLAS computing grid, whilst event simulation and reconstruction occurs at lower tiers [101]. As they have different functions and goals, different software releases are used online and offline, with different schedules for new software releases. This use of different software releases can create issues for the ATLAS offline monitoring system, most frequently for the trigger system. A particular example of one issue caused by this setup, and a solution to this problem I was involved in developing, is described in Section 4.2.1.

## 4.1 The ATLAS Trigger System

The ATLAS trigger system is designed to accept "interesting" (i.e. with high physics or calibration value) events for reconstruction and storage, and to reject others. There are two reasons to do this. Firstly, the maximum rate at which data can be written out from the detector to disk (1 kHz) is lower than the maximum event (or bunch crossing) rate (40 MHz) [102], and to increase the writeout rate would be very costly. Secondly, the physics processes of interest tend to occur rarely, so it is preferable to prioritise the use of data storage resources for this very small fraction of events. The ATLAS trigger system performs this task by making fast decisions on whether to store events during data taking. After data has been collected, it is reconstructed into physics object candidates for further analysis.

The ATLAS trigger system [81, 103] is divided into two parts, the custom hardware-based Level 1 (L1) [104] and the software-based High Level Trigger (HLT), which runs on a commercial, off-the-shelf, computing farm [105]. At L1, fast decisions are made on whether to pass an event to the HLT for further processing, resulting in a L1 output rate of 100 kHz. At HLT level, some event reconstruction occurs, in a similar way to the full reconstruction described in Section 4.4. Algorithms are then applied to determine whether to pass the event at HLT level, resulting in a final data readout rate of 1 kHz. HLT algorithms use data from the full detector, or from a 'Region of Interest' (RoI) within the detector, depending on the algorithm. A RoI is an area (in $\eta$ vs. $\phi$) of the detector within which the L1 algorithms have located an interesting physics object candidate. A schematic of the trigger and data acquisition systems is shown in Figure 4.1.

A 'trigger chain' is a series of algorithms that run in sequence. An event must pass at least one trigger chain selection in order to be permanently stored for offline analysis. Sets of related trigger chains which concern specific physics objects are devised and managed by ATLAS trigger signature groups (so named because the physics objects leave similar experimental 'signatures' in the detector). Trigger chains have an associated 'prescale', which defines the fraction of events satisfying the online selection to be stored for offline analysis. Prescales are set for different chains with a view to ATLAS analysis needs. As the bunches circulating in the LHC are depleted over time, prescales may change (commonly in steps) to retain the same number of accepted events in the face of decreasing collision rates. The

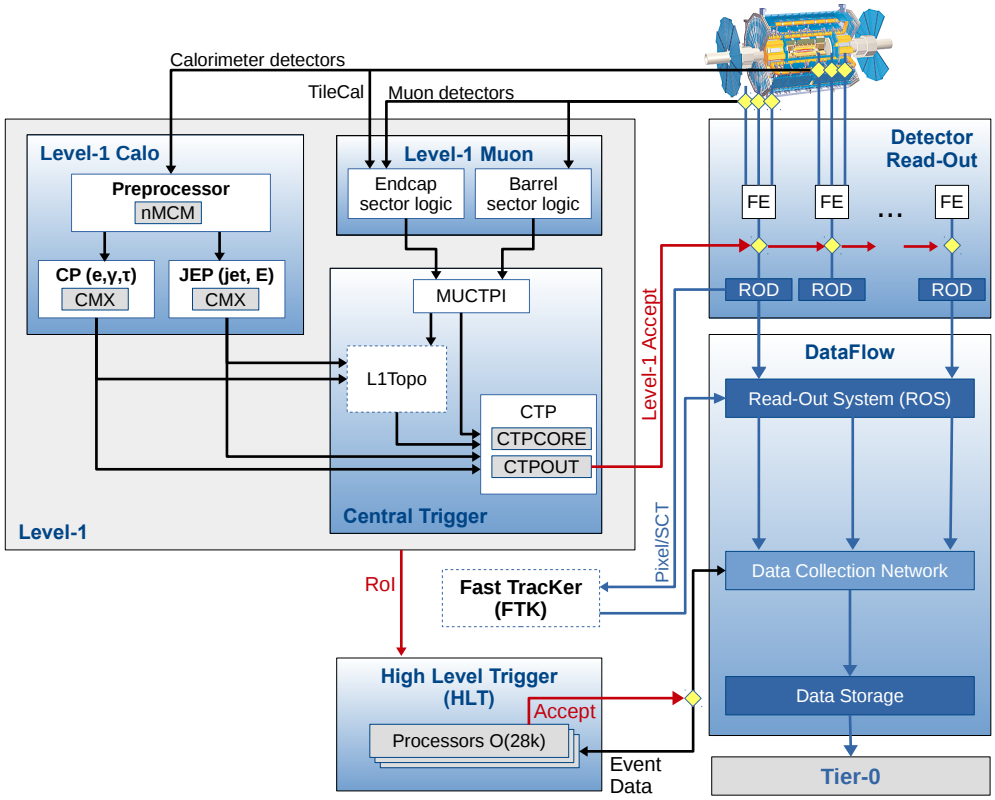


**Figure 4.1** Schematic of the ATLAS trigger and data acquisition system. 'CP' refers to the Cluster Processor and 'JEP' to the Jet/Energy-sum Processor. 'MuCTPI' refers to the Muon to CTP Interface, where 'CTP' is the Central Trigger Processor. L1Topo (L1 Topological Trigger) and Fast Tracker (FTK) were in commissioning during 2015–2016 so are not described in this thesis. Taken from [103].

pattern of decrease in event rates through a fill and increases in event rates due to prescale changes can be seen in Figure 4.2.

The set of trigger chains that are deployed during a data-taking run are defined in a trigger 'menu' [102] and are curated so as to provide algorithmic selections to meet the large variety of physics goals at the ATLAS experiment. As a trigger menu needs to provide an output data rate that is compatible with the maximum data readout rate, the choice of trigger chains in a trigger menu is also dependant on the collision rate, which depends on the luminosity. In practice, a set of trigger menus is defined for each year. Switches between trigger menus then occur when the luminosity exceeds or falls below set thresholds, rather than constantly modifying the menu. A typical trigger menu contains several hundreds of trigger chains. An entire unique online trigger configuration (including the trigger menu and other online software related parameters) is identified by a

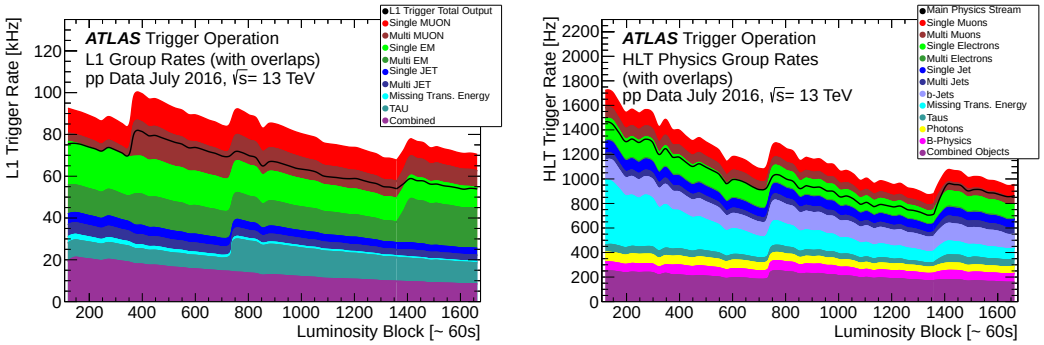


**(a)** **(b)**

**Figure 4.2** Example trigger rates at (a) L1 and (b) HLT for an LHC fill in July 2016. The total output rate is less than the sum of group rates for both L1 and HLT because events may pass triggers in multiple groups. Increases in rates are due to changes in prescale to counter the decrease in luminosity during fills, which causes the exponential decay. Other fluctuations in rates are due to detector deadtime (periods where no data can be read out due to bandwidth limitations and other reasons) and detector/electronics noise. A luminosity block is a short period of time (commonly ∼60 s) where the luminosity can be considered constant. In (a), rates are grouped by the type of L1 algorithms accepting the event, whilst in (b) rates are grouped by the stream the event is assigned to by the HLT. The 'Main Physics Stream' is the total HLT output for physics purposes. Both taken from [106].

'Super Master Key' (SMK). The online trigger configuration sets are stored in the 'trigger database', an SQL (Structured Query Language) database that stores trigger-related information. Every data-taking run has an associated SMK. The trigger menu and the online software change less frequently than the length of a run, so one SMK is usually used for a number of runs.

### 4.1.1 The First Level Trigger (L1)

The L1 trigger makes decisions regarding whether to store events using information from the ATLAS calorimeters and the RPC and TGC muon subdetectors. These detector subsystems are described in Sections 3.2.2 and 3.2.3. High $E_{\mathrm{T}}$ (transverse energy) electromagnetic (EM) clusters (the experimental signature of electrons and photons), jets and hadronically decaying $\tau$-leptons, and events with high total $E_{\mathrm{T}}^{\mathrm{miss}}$ (missing transverse momentum) or $E_{\mathrm{T}}$ are the focus of the L1 Calorimeter Trigger (L1Calo), whilst the L1 Muon Trigger (L1Muon) aims to identify high $p_{\mathrm{T}}$ (transverse momentum) muons. Information and results from L1Calo and L1Muon are combined and a decision on whether to accept

the event at L1 is made by the Central Trigger Processor (CTP). The L1 trigger system makes decisions about events within 2.5 µs, during which time all detector information is stored in temporary memory.

#### 4.1.1.1 The First Level Calorimeter Trigger (L1Calo)

L1Calo uses makes decisions based on information from $0.1 \times 0.1$ in $\eta$ vs. $\phi$ (larger at higher $|\eta|$) 'trigger towers', as shown in Figure 3.12a. The sum of signals (currents created by particles passing through the calorimeter segments, see Section 3.2.2) within a trigger tower is calculated by the preprocesser (see Figure 4.1) to provide energy deposition values within the towers. Candidate physics objects are then identified by the Cluster Processor (CP) and Jet/Energy-sum Processor (JEP). The CP identifies electron, photon and tau candidates whilst the JEP identifies jet candidates. The CP and JEP achieve this by searching for local energy maxima within groups of trigger towers, as shown in Figure 4.3. The EM cluster and tau algorithms require the summed energy deposit in at least a pair of towers in a $2 \times 2$ window in the electromagnetic calorimeter to exceed a predefined threshold. The jet algorithm requires that the summed deposit in $2 \times 2$, $3 \times 3$ or $4 \times 4$ window in the electromagnetic and hadronic calorimeters exceed a threshold, with a $2 \times 2$ local maxima within the region (in the centre of the region for the $4 \times 4$ case, to avoid the possibility of there being two jets in the window). Energy deposits above threshold are required to be isolated, with deposits in 'isolation rings' (and in the $2 \times 2$ window behind in the hadronic calorimeter in the case of the EM cluster algorithm) below a separate threshold. $E_{\mathrm{T}}$ and $E_{\mathrm{T}}^{\mathrm{miss}}$ candidate quantities are also computed by the JEP by summing over the full set of trigger towers within the calorimeters.

#### 4.1.1.2 The First Level Muon Trigger (L1Muon)

L1Muon uses information from the RPC and TGC subdetectors, the parts of the muon system directed towards triggering. The muon trigger algorithm performs simple tracking to coarsely determine muon momenta. The tracking algorithm requires hits (energy deposits left by particles) in the RPC (in the barrel regions) and TGC (in the endcaps) stations to be coincident with each other and the interaction point within a level tolerance. Figure 4.4 shows a schematic of this. The algorithm has 6 possible $p_{\mathrm{T}}$ windows (from 5–35 GeV) which the candidate

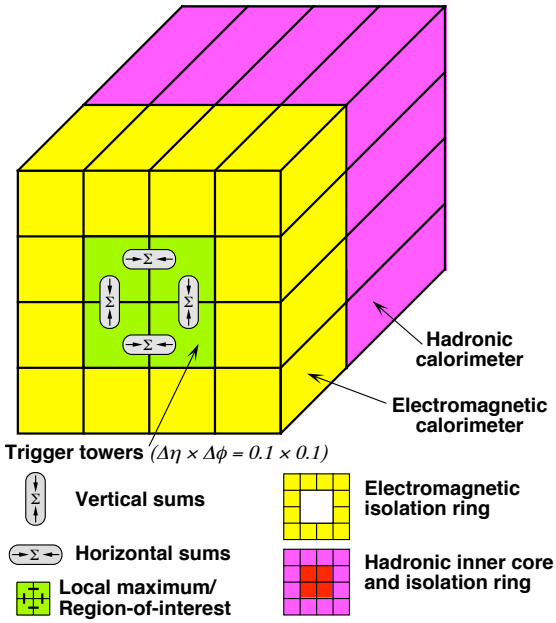


**Figure 4.3** Schematic of the trigger tower combinations used by L1Calo algorithms when identifying candidate EM clusters, taus and jets. Taken from [103].

muons can be assigned to. High $p_{\mathrm{T}}$ muons have tracks with lower curvature, so to be assigned to higher $p_{\mathrm{T}}$ categories, the hits must be coincident within a smaller level of tolerance. In the endcap region, the algorithm uses information from the two stations furthest from the interaction point for the low $p_{\mathrm{T}}$ thresholds, and additionally includes the next nearest layer for the high $p_{\mathrm{T}}$ thresholds. For the $1.3 < |\eta| < 1.9$ region, coincidence is also required in the nearest TGC layer to prevent triggering on particles that originate far from the interaction point. In the barrel regions, the two stations nearest the interaction point are used for the low $p_{\mathrm{T}}$ thresholds, along with the furthest layer for the high $p_{\mathrm{T}}$ thresholds.

#### 4.1.1.3 The Central Trigger Processor (CTP)

The Central Trigger Processor (CTP) makes the overall decision on whether to accept an event at L1 based on the L1 trigger menu. Items in the L1 menu consist of combinations of $E_{\mathrm{T}}/p_{\mathrm{T}}$ thresholds and object multiplicities. The degree of isolation EM cluster and tau candidates and the size of jet candidates can also be specified. If the L1 item is prescaled, the CTP will only accept a fraction of the events (1/prescale) that pass the item. Primary RoIs (that contributed directly to the acceptance of the event) and secondary RoIs (other, usually lower $p_{\mathrm{T}}$ regions) are passed to the HLT (in the form of the $\eta$–$\phi$ position, type of RoI

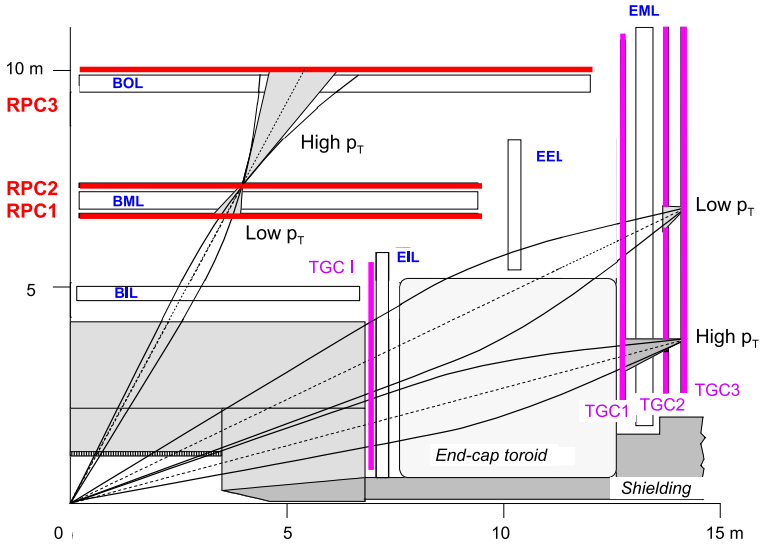


**Figure 4.4** Schematic of the curvature of high and low $p_T$ muons in the barrel and endcap magnetic fields and the tolerance regions (in grey) that hits must be coincident within in the RPC and TGC layers to pass low and high $p_T$ muon triggers. Taken from [81].

(EM cluster, tau, jet, etc) along with the threshold passed by the RoI) along with the CTP trigger decision.

### 4.1.2 The High Level Trigger (HLT)

The ATLAS HLT decision-making process consists of two stages: first, decisions are made within the RoIs identified at L1, but using the full information from the detector subsystems within those regions, including data from subsystems that do not participate in L1 decision making, rather than the coarser information used at L1. This means more precise $E_T$, $p_T$ and tracking information is available to the HLT with respect to L1. Feature extraction (FEX) and hypothesis (HYPO) algorithms are used in sequence on each event. FEX algorithms take information from RoIs, combine it with data from other subdetectors in the same $\eta$–$\phi$ region, and look for additional features, for example, a track in the inner detector that matches to an EM cluster, indicating an electron has been detected. HYPO algorithms make decisions regarding whether the features extracted meet set criteria, for example, have features been found which suggest the presence of a particular object above a $p_T/E_T$ threshold, with a certain isolation, etc.

If the event passes this first stage, the event data from the full ATLAS detector is combined and reconstruction is performed by the algorithms that are the same as,

or very similar to, those used offine (see Section 4.4), with some adaptations for the online software environment. Some calibrations are also applied at this point. Further decisions are made by more sophisticated algorithms at this stage and if an event passes, it is stored for further reconstruction and analysis. If an event is not passed by the HLT, the event is not stored. Events are also categorised here into 'streams' depending on what types of objects have been found within each event. Figure 4.2b shows the respected trigger rates for various streams for an example run in July 2016. In 2015, the average HLT processing time for an event (at a luminosity of $5.3 \times 10^{33}\,\mathrm{cm^2 s^{-1}}$) was $\sim$235 ms [103].

## 4.2 Data quality monitoring

Data quality monitoring at the ATLAS experiment is performed both online [107] and offline [108] in order to check for data irregularities that might indicate issues within the detector, trigger system or reconstruction software. It is important to do this so that the data used in analysis is known to be of high quality and physically accurate. The online and offline monitoring systems, though they have similar goals, have different approaches, as they have access to different resources and types of event information. Online data quality monitoring occurs during data taking, whilst offline data quality monitoring occurs during ATLAS offline event reconstruction.

Both the online and offline monitoring systems produce as their output histograms, which often have algorithmic checks applied (for example, a check that a distribution is consistent within a set tolerance to a reference distribution). These histograms and the check results are checked by experts within signature groups and decisions about the data quality are then made. These decisions are collated and lists of runs, and the lumiblocks within, that are deemed to be of good quality are produced, referred to as Good Run Lists. These lists detail the data which is then used for analysis within the collaboration. The analysis detailed in this thesis uses $36.1\,\mathrm{fb^{-1}}$ of good quality of $pp$ collision data recorded in 2015–2016 at $\sqrt{s} = 13\,\mathrm{TeV}$.

### 4.2.1 Offline data quality monitoring for the ATLAS Trigger Group

ATLAS offline trigger monitoring is designed to check the characteristics of the recorded events after they have been reconstructed offline. This is important for checking data quality, driving the development of new triggers, and evaluating new trigger software. Each trigger signature group maintains their own offline monitoring tools, which are contained in the ATLAS offline software release. While the tools differ between the various groups, they have a common aspect, which is that they are configured via Python configuration files. These configuration files include a list of trigger chains to monitor, as well as other parameters that can be configured depending on the trigger signature. The offline monitoring system takes, as input, information from particular triggers, and outputs histograms of signature specific quantities and distributions.

If the chains in the trigger menu change, changes to the offline monitoring configurations might be required, if the change affects the trigger chains used for monitoring. For example, there could be a trigger chain 'A' in the trigger menu, and an offline trigger monitoring tool could be configured to produce a plot of a quantity relating to this trigger. If trigger chain 'A' is then removed from the menu, the plots will be empty, motivating an update to the monitoring configurations. The offline monitoring configuration therefore needs to be updated because of this change to the menu. It is important that updates to offline monitoring are made promptly so that the monitoring output can be as useful as possible.

During LHC startup and commissioning phases, when the luminosity delivered to ATLAS can increase rapidly, the trigger menu often changes more frequently than new offline software releases are released. This mean the ATLAS offline software release cycle may not be in sync with updates to the trigger menu. 'Menu-aware Monitoring' (MaM) [1], a tool described in the follow section, has provided a solution to this particular problem. It allows offline trigger monitoring configurations to be updated, when needed, in a way that is independent from the software release cycles and does not require distribution throughout the software grid. Before the introduction of MaM, any configuration updates needed go into a new offline software release, which had to be compiled and distributed. This resulted in delays in updating offline trigger monitoring configurations. As the offline software release used at Tier-0 includes all ATLAS reconstruction

software, it is also not desirable to have to change the offline software release every time there is an online trigger menu change. The use of Python configuration files means that it would, in principle, be possible to make changes to the configurations without having to recompile the offline software release. However, distributing new Python configuration files throughout Tier-0 would incur a similar delay to distributing a new software release, even though it would not require recompilation of the software release.

#### 4.2.1.1 The 'Menu-aware Monitoring' tool

'Menu-aware Monitoring', or MaM, is a tool (that I co-wrote) devised to allow offline trigger monitoring configurations to be changed outside of the ATLAS offline software release cycle. The aim of MaM is to overcome the possible time delay between a signature group deciding that they want to update their offline monitoring configuration and the updated configuration being in place during reconstruction, caused by the different ATLAS software release cycles. MaM achieves this by providing the functionality to 'patch' the offline monitoring configurations with snippets of Python (patches), corresponding to the configuration changes desired. Updates can be made via MaM to any aspect of the offline monitoring configurations that are configurable via the Python configuration files. This includes list of trigger chains to be monitored, but can include any other parameters a signature group has made configurable in this way, for example, histogram axis limits. The primary use case of MaM is to facilitate fast updates to the monitoring configurations when a menu change that affects the triggers used for monitoring occurs. MaM allows for an update like this to occur in minutes (a few days once validation of the configuration change is factored in) compared to the 2 weeks it usually takes to move to a new offline software release. MaM also allows monitoring configurations to be updated at short notice for any other purpose. Ensuring that the trigger monitoring configuration is relevant for the data taking environment means that data quality can be monitored more accurately and easily. MaM is written in Python, Java, C++ and SQL.

MaM provides users with functions to create and store these patches, and allows them to be applied automatically or manually during ATLAS reconstruction. The monitoring configuration patches are stored in an SQL database, which can be updated at any time, and is not constrained by the ATLAS offline software release cycle. The schema of the database is shown as Figure 4.5. A single monitoring

configuration patch for a single signature is identified by a 'Slice Monitoring Configuration Key' (SMCK), where a 'slice' is another term for a signature. A bundle of patches to be used with a particular offline software release is identified by a Monitoring Configuration Key (MCK). MaM allows users to create links between MCKs and SMKs in the trigger database, specifying that a particular set of patches should be applied when a run has been taken with a particular SMK (which specifies the trigger configuration). In this way, a link between the offline monitoring configuration and the trigger menu is made. The MCK-SMK links can be updated when needed (though an SMK can only be linked to one MCK at any time), meaning that offline monitoring configurations can be kept in sync with the online trigger menu.

Patches are produced in the following way. Firstly, developers from the signature groups make changes to copies of the monitoring configuration files within local (away from Tier-0) copies of the offline trigger monitoring packages. MaM's Python functions are used to set up and then extract the new configurations of the tools. The ATLAS offline trigger monitoring (and reconstruction) software runs in Athena, the ATLAS offline software framework [101]. The trigger monitoring tools, like all other tools in Athena, are managed by the Tool Service (ToolSvc) and their configuration parameters are accessible via ToolSvc. Extracting configurations from tools in their running state via ToolSvc, rather than from the configuration files themselves, is necessary as there are often parameters that have their values modified during the tool setup stage. The values MaM needs to store are the final values these parameters hold, as the patches are applied subsequent to the setup stage. MaM creates patches by comparing the modified, extracted tool configurations to the default tool configurations within the same ATLAS offline software release. The default configurations can depend on parameters external to the release (such as whether the run in question is a proton-proton or heavy ion run) so the default configuration is extracted concurrently with the modified configuration to ensure these external parameters have the same value. The patches are then stored in the SQL database and assigned an ID, where they can be grouped and linked to SMKs as required. As well as the monitoring tool configurations themselves, MaM stores other information such as the name of the patch creator ('(S)MCK_CREATOR') and an optional comment ('(S)MCK_COMMENT'), in order to improve usability. Actions such as linking, grouping, duplicating and inspecting patches can be performed either via command line (through the Python-based interactive Athena environment) or via a graphical user interface (written in Java), as shown as Figure 4.6.

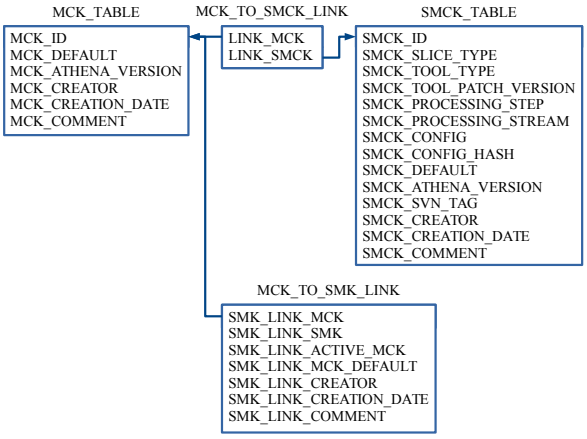


**Figure 4.5** The MaM database schema, showing the four tables and the columns they contain. An 'SMCK' is a 'Slice Monitoring Configuration Key', specifying a single monitoring configuration patch for a single signature, an 'MCK' is a 'Monitoring Configuration Key' that specifies a set of monitoring configuration patches, and an 'SMK' is the 'Super Master Key' that specifies the complete online trigger configuration. Taken from [1]

In order to automate the application of monitoring configuration patches during ATLAS offline event reconstruction, there is C++ code (that I co-wrote) within the ATLAS online software that archives the MCK that is linked to the SMK for each run. At the start of a data-taking run, this software checks the 'MCK_TO_SMK_LINK' table in the MaM database to retrieve the MCK ID, and stores it in the ATLAS Conditions Database ('COOL') [101], where details about each run are stored. This step is required for reasons of reproducibility of offline monitoring results as SMK-MCK links can be updated, but only one link to a particular SMK can exist at a given time. For example, there would be unintended consequences to the monitoring results if an SMK-MCK link changed whilst reconstruction was in progress. Storing the MCK in COOL also ensures that the correct patch is applied if the run is reconstructed again at a later date.

During reconstruction of a run, MaM checks in the COOL to find if there is an MCK stored for the run. Then, MaM checks whether the software release that the patch was created in (stored in the '(S)MCK_ATHENA_VERSION' columns) matches the software release that reconstruction is running in, and only applies the patch if these values match. From one software release to the next, the exact behaviour of each monitoring configuration parameter and the parameters themselves might change, so applying a patch from one release in another might have unintended consequences. This system of checks is designed to prevent this from occurring. In order to apply a patch to a running offline monitoring tool, it

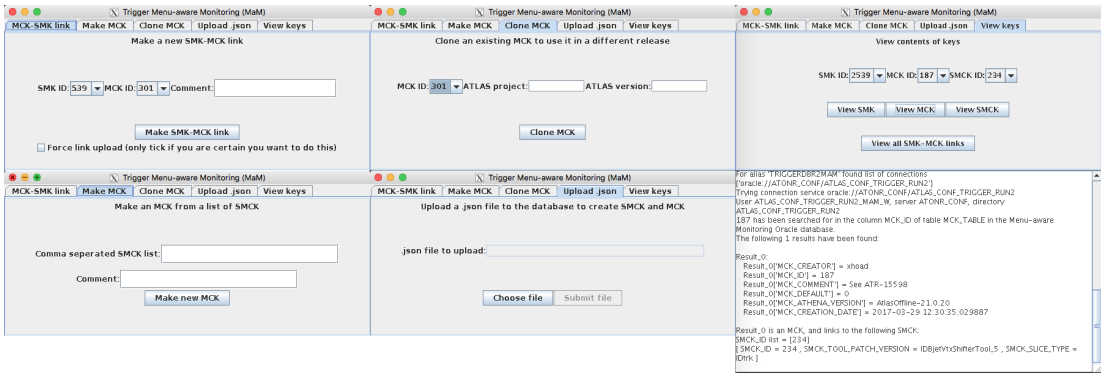


**Figure 4.6** The MaM graphical user interface, showing the various panels and range of actions that can be performed. The GUI provides a an easy to use way to complete some of the tasks that may need to be performed when using MaM to update offline trigger monitoring configurations.

is enough to overwrite the values of the configuration parameters in ToolSvc. Therefore, when asked to apply a patch, MaM checks which configuration parameters have values in the patch, checks if the relevant tool is running in ToolSvc, and if so, updates the value of each configuration parameter in ToolSvc. The offline monitoring tools then run with patched configurations and produce the histograms that are needed to monitor data quality.

MaM has been used several times during periods where the luminosity delivered to ATLAS has been increased rapidly to update monitoring configurations so they are appropriate for the trigger configuration in use. This has meant that data quality could be effectively monitored throughout these periods. MaM has also occasionally been used at other times, most notably when a faulty monitoring configuration was causing ATLAS reconstruction to crash at Tier-0. The use of MaM on this occasion allowed these crashes to be avoided and ATLAS reconstruction to continue. This resulted in a faster delivery of new, fully reconstructed datasets to analysers, compared to before the introduction of MaM when it was necessary to wait for a new offline software release to be validated and deployed.

## 4.3 Event simulation

In order to simulate a *pp* collision event, the collision itself is first simulated, followed by the ATLAS detector response to any outgoing particles. Data collected by the ATLAS detector and simulated events alike can then be

reconstructed into physics object candidates, as described in Section 4.4. In this section, some general information about how events are simulated within the ATLAS software framework is provided. Details of the simulation of the Keung-Senjanović process and of background processes can be found in Sections 4.3.1 and 4.3.2, respectively.

A $pp$ collision at a collider such as the LHC is a collision of the (real and virtual) quarks and gluons, collectively referred to as partons, that make up in the incoming protons. There are several aspects to a $pp$ collision event that must be simulated:

1. The 'hard process' is the main, high energy collision between two partons, that for most physics analyses at the ATLAS experiment is the process of interest.
2. The other remnant partons in the protons may also interact in lower momentum transfer collisions, or may continue to travel in their original flight directions, forming the 'underlying event'.
3. Gluons and photons can be radiated from the incoming partons and outgoing partons or particles, referred to as 'initial- and final-state radiation'.
4. Outgoing partons produce 'parton showers', due to their colour-charged nature.
5. As free colour-charged partons are not observed, any outgoing partons must be grouped into colourless hadrons ('hadronisation').
6. Any particles that are unstable on timescales comparable to the size of the detector must be decayed ('unstable particle decay').

Monte Carlo (MC) generators are used within ATLAS, and other collider experiments, to simulate $pp$ collisions [109]. These simulated datasets are typically referred to as MC samples. MC generators are so-called because of the probabilistic nature of how some parts of the simulations are performed, reflecting the probabilistic nature of the physics interactions to be simulated. Often, different MC generators are used to simulate different aspects the collision.

Matrix Element MC generators are used to simulate the hard process [109]. The matrix element $\mathcal{M}$, the probability amplitude for the process, is computed from theory and includes contributions from Feynman diagrams that contribute

to the process. Depending on the precision required, this calculation can be performed at leading order (LO), where only the simplest Feynman diagrams describing the process are included, next-to-leading order (NLO), where a single additional particle-antiparticle loop is added, or higher orders, where further loops are added. The matrix element, convoluted with the proton Parton Distribution Functions (PDFs)[1], gives the probability distribution for the process. This distribution is then numerically integrated over the outgoing particle energy/momentum phasespace (which is constrained by the input parton energy/momentum and energy/momentum conservation). The result of this integration is the cross section for the process. As a consequence of the Monte Carlo numerical integration method, events are randomly generated from within the probability distribution for the process.

The incoming and outgoing particles involved in the hard process may, depending on the charges, emit gluons or photons. This is referred to as initial- and final-state radiation, or ISR and FSR. Outgoing gluons, including those created via ISR, produce 'parton showers', due to the colour-charged nature of the gluons. Within parton showers, repeated splittings of partons into pairs occur, at progressively lower momentum scales. Once the momentum scale is below the hadronisation scale ($\sim$1 GeV), the showering ceases and the partons hadronise. The probability distribution for governing the energy scale at which partons split is given by the Sudakov form factor [110]. MC shower programs generate random splitting energy scale values within the probability distribution, and the splitting occurs if the scale is above the hadronisation scale. If the splitting occurs, the DGLAP splitting kernels [111, 112, 113] give the probability distributions that govern how energy is split between the two resultant partons. ISR and FSR can either be simulated by the calculation of additional matrix elemnts that include the radiated particles, or as part of the parton showering step.

Two common ways of performing hadronisation (though there are others) are the string [114, 115] and cluster [116, 117] models. In the string model, the final partons in the shower are connected with strings. Due to the characteristics of the strong force, energy can be said to build up in these strings as the partons move apart. Splitting a string creates a new particle-antiparticle pair, and the process continues until the strings separating the partons are short, meaning the final partons are confined in hadrons. In the cluster model, gluons in the shower are

[1]PDFs describe the number density of the partons within each proton as a function of the proton momentum fraction they carry, at a particular level of momentum transfer.

split into quark-antiquark pairs and then formed into colourless groups. These colourless proto-hadrons are then decayed into true hadrons. The decay to true hadrons proceeds by randomly introducing quark-antiquark pairs until a valid two-body final state is found. If the initial cluster is too massive, multiple decays can occur, in a string-like way. Clusters are also allowed to form single hadrons some proportion of the time.

The simulation of the decay of unstable hadrons and taus is an important but non-trivial step [109]. Due to incomplete knowledge of hadron properties, assumptions must be made within simulations and these are often generator specific. MC generators, or specific hadron and tau decay programs, may include matrix elements for a set of possible decays or they may calculate them on the fly. The actual decay is then randomly selected from the resultant probability distribution.

MC generators often include parameters that can be tuned to provide better agreement with data. A set of tuned parameters is referred to as a 'tune'. There are many MC tunes available, and different tunes are often used for different processes. All steps of the MC generation process can be tuned.

The underlying event, along with the effect of pile-up (see Section 3.2), is simulated within ATLAS by overlaying additional MC events, generated with minimum bias towards any particular process, onto each MC event. For the MC samples used in this thesis, the minimum-bias collisions were simulated with Pythia 8.186 [118] with the A2 tune [119] and the MSTW2008LO PDF set [120]. The pile-up simulation is described in more detail in [86, 121]. The quantity of minimum-bias events is chosen to approximately match the level of underlying event and pile-up activity seen in data, however, as the MC is often produced before the data the MC will be compared to is collected, this usually needs to be tuned if there is a difference in the level of activity. This tuning is referred to as 'pile-up reweighting' [122] and was performed for all MC datasets used in this analysis.

For the MC samples used in this thesis, the interaction of particles with the detector was simulated with a Geant 4 [123] based framework [86]. The Geant 4 simulation of the ATLAS detector includes information regarding the geometry and materials used throughout the detector, and the magnetic fields produced by the ATLAS detector magnet systems. The simulation includes the production of additional particles due to interaction of collision particles with detector material. After the behaviour of particles within the detector has been simulated, the

detector response is added. If a simulated particle is incident on a section of the detector, the response of that section of detector hardware to the resultant energy deposit is simulated by the corresponding 'digitisation simulator' for that piece of hardware. The digitisation simulators convert the energy deposits into voltages and currents, mirroring what occurs in the physical detector. During digitisation, the trigger systems are also emulated: events are not rejected from the simulation, but the trigger decision is stored. The data format obtained at the end of this process is the same as that obtained from collision data, so MC and data can be reconstructed by the same reconstruction software, and are therefore directly comparable.

### 4.3.1 Simulation of the Keung-Senjanović process

In the analysis described in this thesis, the Keung-Senjanović process was simulated using MadGraph5_aMC@NLO 2.2.2 [124, 125], using a model of the Type-I LRSM [126], produced with the Mathematica package FeynRules [127], and further modified and provided for use in this analysis by Fabrizio Nesti (IRB, Zagreb) and Miha Nemevšek (JSI, Ljubljana) [128]. Showering was then performed with Pythia 8.186 with the NNPDF2.3 PDF set [129] and the A14 parameter set [130] for shower tuning. EvtGen 1.2.0 was used to decay unstable hadrons [131]. I set up MadGraph5_aMC@NLO to produce the Keung-Senjanović process, wrote the steering code to integrate the different steps together (using MadGraphControl [132]) and performed the validation necessary to generate this MC within the ATLAS central production system.

Events were generated containing only Majorana $N_R$ neutrinos, resulting in a set of events containing 50% events with opposite-sign leptons and 50% same-sign leptons. The events containing opposite-sign leptons are reused for the Dirac $N_R$ case, with the cross section scaled to twice the original value for this subset of events. This assumes that the cross section for $N_R$ production would be unchanged between the Majorana/Dirac cases.

The following values of model parameters, introduced earlier in Section 2.3.1, were set, in order to generate events corresponding to the minimal Type-I LRSM. $g_R$, the right-handed weak coupling strength, was set equal to $g_L$, the SM weak coupling strength. The left- and right-handed coupling strengths are required to be equal to ensure that the model is invariant under parity transformations (see Section 2.3). $\kappa'$, the parameter that controls mixing between the SM $W$ and

the LRSM $W_R$, was set to zero, for simplicity. The mixing between heavy and light neutrinos was also set to zero, again for simplicity. The mixing between $N_e$, $N_\mu$ and $N_\tau$ was set to zero, so that only final states with same flavour leptons were generated. The situation where mixing between the different flavours of $N_R$ is allowed to occur is the focus of a separate ATLAS analysis. $v_R$, the VEV the Higgs triplet $\Delta_R$, $\kappa$, the non-zero VEV of $\phi$, and the couplings between the Higgs fields and the leptons and quarks, were set based on the values of chosen for $m_{W_R}$ and $m_{N_R}$ and the known masses of the other particles. The right- and left-handed Cabibbo–Kobayashi–Maskawa (CKM) matrices [133, 134] that determine the mixing between right- and left-handed quarks, were set to be equal to the SM CKM matrix, again to ensure the invariance of the model under parity transformations. More details of the model parameters can be found in [126, 128].

Signal samples were generated for a number of different $W_R$–$N_R$ mass hypotheses, covering a range in $m_{W_R}$ from 600 GeV to 5.8 TeV for $m_{N_R}$ values 50 GeV to 8 TeV. MC samples with $m_{N_R} \leq 2m_{W_R}$ were produced, but no higher in $m_{N_R}$, as the cross section for the Keung-Senjanović process drops off rapidly with increasing $N_R$ mass. The complete set of mass hypotheses considered are shown in Figure 4.7, along with the resultant cross sections. Plots of some kinematic variables for some example mass hypotheses can be found in Appendix A.

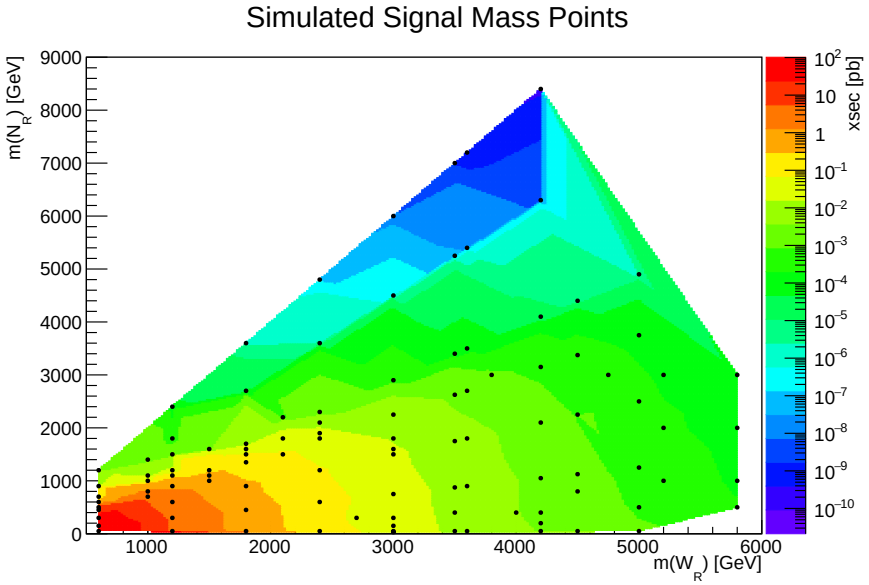


**Figure 4.7** The set of the simulated $W_R$ and $N_R$ mass points (in GeV), along with their cross sections (in pb) as calculated by MadGraph5_aMC@NLO.

All previous ATLAS and CMS searches for LRSM $W_R$ and $N_R$ participating in the Keung-Senjanović process [65, 66, 67, 68, 69] used MC samples produced using the

PYTHIA [118, 135] event generator. The PYTHIA implementation of the Keung-Senjanović process allows only the generation of mass hypotheses where $m_{W_R} > m_{N_R}$, and collapses the $N_R \to \ell_2 W_R{}^*$ and $W_R{}^* \to jj$ decays to a single vertex, as shown in Figure 4.8a. This simplification of the Keung-Senjanović decay chain in the PYTHIA implementation affects the kinematic distributions of the final state particles. When $m_{W_R} > m_{N_R}$, the on shell $W_R$ should have a Breit-Wigner [136] mass distribution, with a width ($\Gamma$) dictated by how easily it can decay, which is related to the $W_R$–$N_R$ mass difference. The off shell $W_R{}^*$, the second $W_R$ in the decay chain, should be constrained to a mass region below the peak of the Breit-Wigner mass distribution, so should have a mass distribution influenced by the tail of the Breit-Wigner. The MADGRAPH5_aMC@NLO implementation exhibits the correct behaviour, whilst the PYTHIA three-body decay implementation does not. Comparisons of generator level (with no detector simulation) mass distributions for $W_R$, $N_R$ and $W_R{}^*$ are shown for MADGRAPH5_aMC@NLO and PYTHIA for various $W_R$ and $N_R$ mass values in Figure 4.9. In regions of phase space where the $W_R$ and $N_R$ masses are highly (Figure 4.9a) or moderately (Figure 4.9b) separated, the $W_R{}^*$ mass distributions are very similar for the two generators. However, when the $W_R$ and $N_R$ masses are comparable (Figure 4.9c), there is a clear difference between the two $W_R{}^*$ mass distributions. Another consequence of the simplification of the decay chain is that the $m_{W_R} < m_{N_R}$ case cannot be implemented in PYTHIA. This is the reason why $m_{W_R} < m_{N_R}$ case has not been studied by ATLAS/CMS analyses using PYTHIA. As shown in Figure 4.10, MADGRAPH5_aMC@NLO can be used to generate MC for both the $m_{W_R} > m_{N_R}$ and $m_{N_R} > m_{W_R}$ cases.

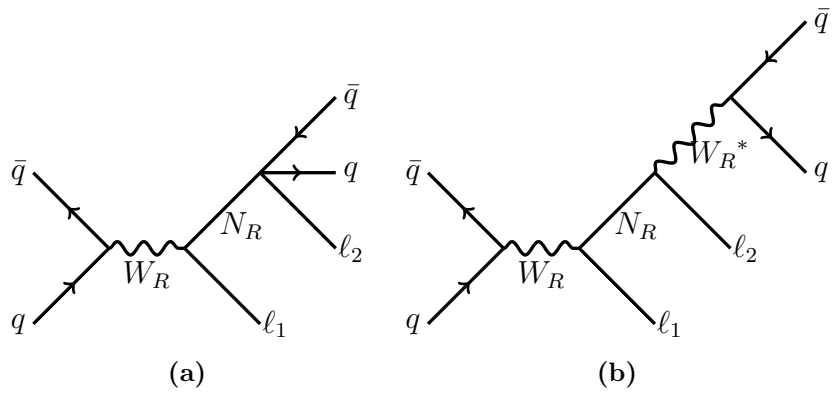


**Figure 4.8** Feynman diagrams for the Keung-Senjanović process, as implemented in (a) PYTHIA and (b) MADGRAPH5_aMC@NLO.

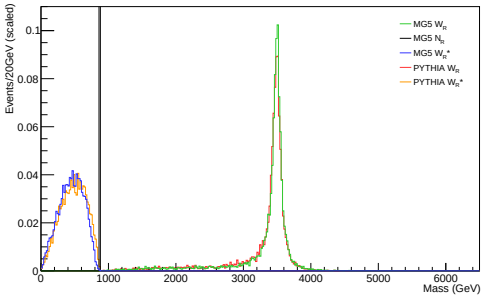


**(a)** $m_{N_R} = 875\,\text{GeV}$

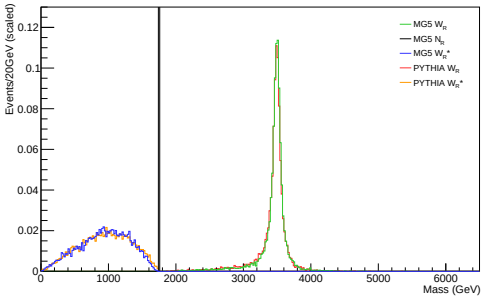


**(b)** $m_{N_R} = 1.75\,\text{TeV}$

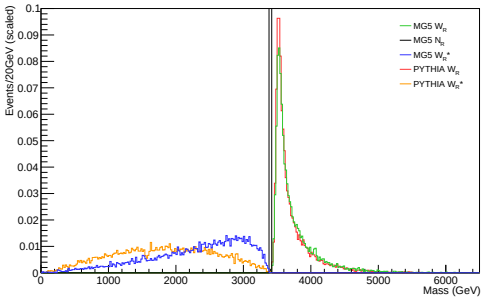


**(c)** $m_{N_R} = 3.4\,\text{TeV}$

**Figure 4.9** Comparison of generator-level $W_R$ and $W_R{}^*$ mass distributions produced with Pythia and MadGraph5_aMC@NLO, for generated mass values of $m_{W_R} = 3.5\,\text{TeV}$ and a variety of $m_{N_R}$ values, as indicated beneath each plot. The $N_R$ mass distribution produced with MadGraph5_aMC@NLO is also shown. The $W_R{}^*$ distribution is the $m_{q\bar{q}}$ distribution in the Pythia case, as there is no $W_R{}^*$ in the event record. Only the hard process was simulated.

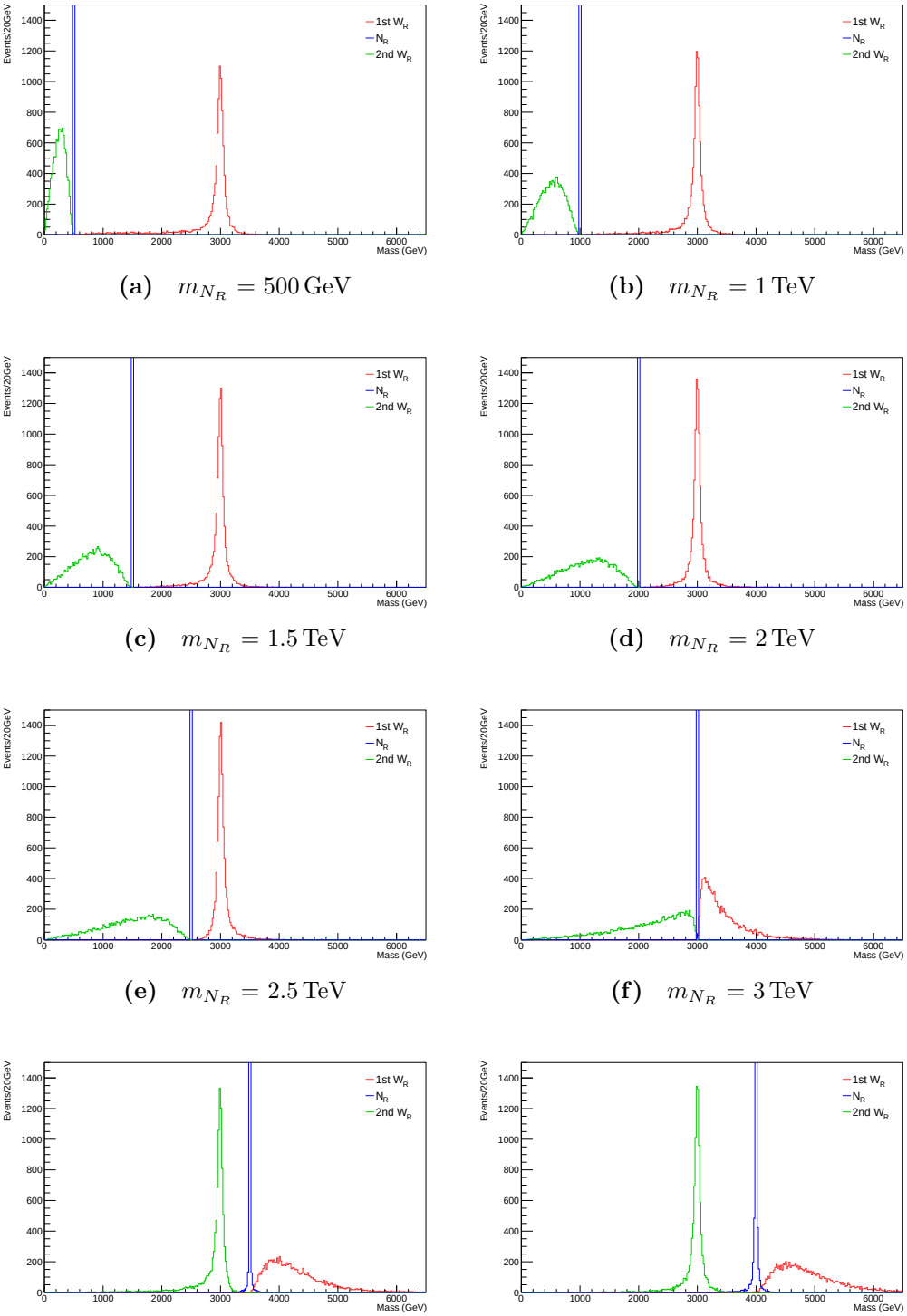


**(a)** $m_{N_R} = 500\,\text{GeV}$ **(b)** $m_{N_R} = 1\,\text{TeV}$

**(c)** $m_{N_R} = 1.5\,\text{TeV}$ **(d)** $m_{N_R} = 2\,\text{TeV}$

**(e)** $m_{N_R} = 2.5\,\text{TeV}$ **(f)** $m_{N_R} = 3\,\text{TeV}$

**(g)** $m_{N_R} = 3.5\,\text{TeV}$ **(h)** $m_{N_R} = 4\,\text{TeV}$

**Figure 4.10** Generator-level mass distributions for $W_R$ and $N_R$ decaying via the Keung-Senjanović process, for generated mass values of $m_{W_R} = 3\,\text{TeV}$ and a variety of $m_{N_R}$ values, as indicated beneath each plot, generated with MadGraph5_aMC@NLO. When $m_{W_R} > m_{N_R}$ ($m_{W_R} < m_{N_R}$), the first (second) $W_R$ in the decay chain is on shell, whereas the second (first) $W_R$ is off shell. When $m_{W_R} < m_{N_R}$ the $N_R$ mass distribution is noticeably wider than in the $m_{W_R} > m_{N_R}$ case, indicating the $N_R$ has a shorter lifetime when it can decay to an on-shell $W_R$. Only the hard process was simulated.

### 4.3.2 Simulation of background processes

There are a number of SM processes that can produce an $\ell\ell jj$ ($\ell = e, \mu$) final state with opposite-sign leptons, referred to as 'background processes'. The dominant background processes for the opposite-sign $\ell\ell jj$ final state are as follows:

- $t\bar{t} \to \ell^+\ell^- jj$ ($t\bar{t}$), see Figure 4.11a
- $Z/\gamma^*(\to \ell^+\ell^-) + jj$ ($Z+$jets), see Figure 4.11b
- $ZZ/ZW \to \ell^+\ell^- jj$ (diboson), see Figure 4.11c

The analysis strategy described in Section 5.2 is designed to accentuate the differences between the signal process, the Keung-Senjanović process, and the background processes.

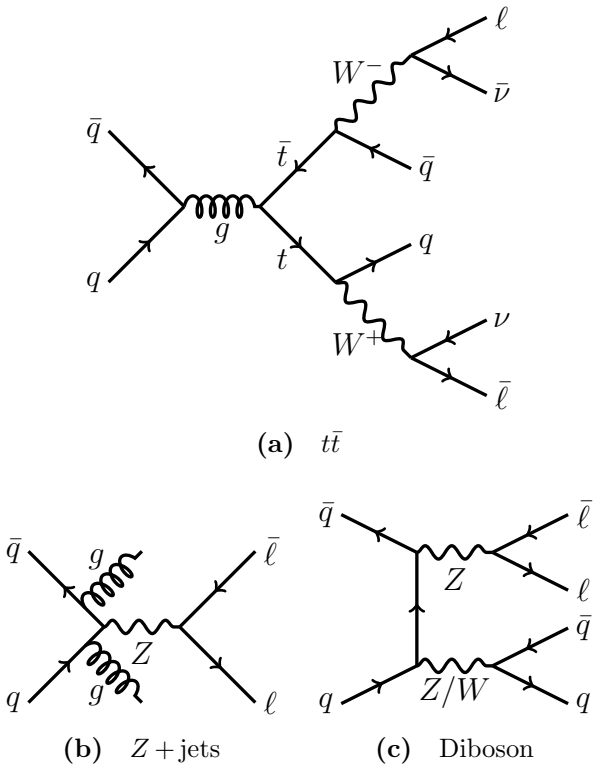


**(a)** $t\bar{t}$

**(b)** $Z+$jets **(c)** Diboson

**Figure 4.11** Example Feynman diagrams for SM backgrounds to the Keung-Senjanović process.

The background processes were simulated using a variety of different MC generators. $Z+$jets processes were modelled using Sherpa 2.2.1 [137] with the NNPDF3.0 [138] PDF set at NNLO. The matrix element was calculated for up to two partons with NLO accuracy in QCD and for up to four with LO accuracy

using Comix [139] and OpenLoops [140]. The MC samples are normalised using the NNLO cross sections specified in [141]. $W+$jets processes, which can result in an $\ell\ell jj$ final state if an additional lepton from another source is reconstructed in the event, form a minor background in this analysis and are modelled using the same setup used for $Z+$jets processes. More details of the ATLAS simulation of the $Z+$jets and $W+$jets processes can be found in [142].

For the generation of $t\bar{t}$ events, Powheg-Box 2 [143] was used with the CT10 PDF set [144] in the matrix element calculations. Single top-quark events and $Wt$ events were generated with Powheg-Box 1, with the matrix element calculation performed at NLO together with PDF set CT10f4 [144], whilst $Zt$ events were generated using MadGraph5_aMC@NLO 2.2.3 and the CTEQ6L1 PDF set [145] and the Perugia 2012 tune [146]. The parton shower, hadronisation, and the underlying event were simulated using Pythia 6.428 [135] with the CTEQ6L1 PDF set and the Perugia 2012 tune. NLO cross-sections were used to normalise these MC samples, summarised in [147]. $t\bar{t}V$ (where $V = W, Z$) processes were generated at NLO with MadGraph5_aMC@NLO 2.3.3 and the NNPDF3.0 NLO PDF set, with Pythia 8.210, and A14 tune used for showering. The $t\bar{t}WW$ and $t\bar{t}\gamma$ processes were generated at LO with MadGraph5_aMC@NLO 2.2.2 and the NNPDF2.3 LO PDF set, with Pythia 8.186 and A14 tune used for showering. EvtGen 1.2.0 was used for hadronisation. Further details of simulations of top-quark-related processes within ATLAS can be found in [148].

Diboson processes with four charged leptons ($4\ell$), three charged leptons and one neutrino ($3\ell$+$1\nu$), or two charged leptons and two neutrinos ($2\ell$+$2\nu$), and $ZZ$, $WW$ and $WZ$ processes with one boson decaying hadronically and the other one decaying leptonically, in the final state were generated using Sherpa 2.1.1 with the CT10 PDF set. The matrix elements, containing all Feynman diagrams with four electroweak vertices, were calculated for up to three partons at LO accuracy and up to one ($4\ell$, $2\ell$+$2\nu$, $ZZ$) or zero partons ($3\ell$+$1\nu$, $WW$, $WZ$) at NLO in QCD using the Comix and OpenLoops matrix element generators.

## 4.4 Physics object reconstruction

In this section, the reconstruction of physics object candidates involved in this analysis is described, as well as the track and vertex reconstruction. The same reconstruction algorithms are used for data and MC.

### 4.4.1 Tracks and vertices

Tracks, the paths taken by charged particles, are found in the Inner Detector by extrapolating outwards from a threshold number of hits in the Pixel and SCT detectors, or inwards from the TRT. The extrapolation is an iterative fitting procedure, where hits in further layers of the ID are added if they are sufficiently coincident with the predicted track. Tracks originating from pile-up or instrumental effects are reduced by rejecting the track if an expected hit in a layer is missing, and by requiring hits in the inner most layers, nearest to the beampipe. More information on track-finding within ATLAS can be found in [149, 150].

Vertex locations, points where multiple particles originate from, indicating an interaction, are found by iteratively fitting to tracks that have coincident origins within some tolerance. Tracks that are incompatible with the candidate vertex are removed from the fit, and the vertex is then refitted. Tracks that are incompatible with the found vertex become seeds for further vertices. Primary vertices, the locations of the hard scatter interactions, are identified by the large $p_{\mathrm{T}}$ of their associated tracks. Secondary vertices can originate from particles with non-negligible lifetimes travelling from the primary vertex, the underlying event, pile-up, and other effects. More information on vertex-finding within ATLAS can be found in [151, 152].

### 4.4.2 Electrons

Electron (and equivalently positron) candidates are reconstructed using information from the electromagnetic calorimeter, where they are expected to have deposited most of their energy. Total transverse energy deposits in each calorimeter tower, measuring $0.025 \times 0.025$ in $\eta \times \phi$ (see Figure 3.12a) are determined by summing the deposits in each layer within the tower, moving out from the beampipe. Towers are then algorithmically grouped in clusters which seem to originate from the same shower, using towers with high energy deposits (over 2.5 GeV) as seeds. If a cluster can be matched to a high quality track, then it is an electron candidate (otherwise, it is a photon candidate). The electron energy is derived from the calibrated energy of the matched cluster, and its $\eta$ and $\phi$ coordinates are taken from the matched track properties. Electron energies must be calibrated to correct for energy loss as the electron passes through the

detector. The energy calibration process involves deriving correction factors by comparing electron and cluster energies in simulations, and comparing energies at the $Z \to ee$ peak in data and MC [153].

Electrons are classified using a multivariate analysis (MVA) technique, and identified as 'loose', 'medium' or 'tight' electrons based on this. The identification categories move from higher to lower signal efficiency, and lower to higher background rejection, respectively. There a many electron identification quality variables (detailed in [154]), and the difference between the identification categories is the threshold required for each variable. Examples of the variables include the fraction of energy deposited in the hadronic calorimeter (lower is better), the number of hits in the inner detector (more is better), and the distance between the expolated track posistion and the cluster centre (closer is better). In order to reduce backgrounds from other charged particles being misidentified as electrons, information regarding the amount of transition radiation produced, provided by the TRT, is used. More information relating to ATLAS electron reconstruction can be found in [154, 155].

### 4.4.3 Muons

Muon (and antimuon) candidates are reconstructed using information from throughout the Inner Detector and the Muon Spectrometer, and additionally information from the calorimeters at $\eta \sim 0$, where the coverage of the Muon Spectrometer is incomplete. Tracks are reconstructed in the Muon Spectrometer from drift circles in the MDTs and energy deposits in the CSCs (see Figure 3.16). Track segments, straight lines, are formed within individual MDTs and CSCs, and tracks are fitted to these lines. Tracks in the Muon Spectrometer are extrapolated to the Inner Detector (and vice versa), and then a new track fitted, to form 'combined' muon candidates. 'Extrapolated' muon candidates are formed from well reconstructed tracks in the Muon Spectrometer that can be extrapolated to the primary vertex, but do not have a well reconstructed Inner Detector track, or originate from outside the acceptance of the Inner Detector. 'Segment-tagged' muon candidates have good tracks in some subsections of the Muon Spectrometer, and an energy deposit indicating that the muon did not exit the subdetector, which can be extrapolated to an Inner Detector track. Finally, 'calorimeter-tagged' muon candidates are found if an Inner Detector track is matched to a calorimeter cluster which indicates a minimally-ionising particle.

To correct for differences in muon momentum between data and simulation, muon momentum calibration factors are derived from comparison of data and simulation for $Z \to \mu\mu$ and $J/\Psi \to \mu\mu$ events, and applied to simulated events [156].

Muons are also identified as loose, medium or tight. Different types of muons are included in different identification categories, as well as different requirements on the number of hits in different subdetectors, and requirements on the compatibility of track segments. More information regarding ATLAS muon reconstruction can be found in [156].

### 4.4.4 Jets

The aim of jet reconstruction is to determine the characteristics of the initial parton as accurately as possible. Within ATLAS, the most frequently used jet algorithm, and the one used in this thesis, is the anti-$k_t$ sequential clustering algorithm [157, 158]. The anti-$k_t$ algorithm takes as input topologically-connected calorimeter clusters (topo-clusters), and combines them to form jets. Topo-clusters [159] are built from energy deposits in the calorimeters, starting from an initial deposit with an energy above a set threshold. The initial deposit is combined with deposits in adjacent cells if they are sufficiently large. The topo-cluster energy is then the sum of the energy deposited in the cells in the cluster.

The anti-$k_t$ algorithm makes use of the distance measures:

$$d_{ij} = \min\left(\frac{1}{{p_{Ti}}^2}, \frac{1}{{p_{Tj}}^2}\right)\frac{\Delta R_{ij}^2}{R^2}$$
$$d_{iB} = \frac{1}{{p_{Ti}}^2}$$

where $i, j$ are two input objects (initially, topo-clusters), $\Delta R_{ij}^2 = (\eta_i - \eta_j)^2 + (\phi_i - \phi_j)^2$, $d_{ij}$ is the distance measure between the two inputs, and $d_{iB}$ is the distance measure between $i$ and the beam.

The algorithm proceeds as follows:

1. The minimum $d_{ij}$ between all objects in the event is found.
2. If $d_{ij} < d_{iB}$, objects $i$ and $j$ are combined.

3. If $d_{ij} > d_{iB}$, the objects are not combined and $i$ is declared a jet, and $i$ is removed from the set of objects from which to build further jets.

4. The process is repeated until a stable set of jets have been found, and all objects are contained in jets.

The behaviour of the algorithm is such that low $p_{\mathrm{T}}$ objects combine with high $p_{\mathrm{T}}$ objects, resulting in circular jets. The parameter $R$ controls the radius of the output jets, and the minimum distance between jets, and a value of $R = 0.4$ is used in this analysis. The anti-$k_t$ algorithm is also insensitive to the collinear splitting of partons and to very soft partons ("infrared safe"), which cause issues for some jet reconstruction algorithms.

There are numerous calibrations applied to jets within ATLAS [160], some of which will be briefly described. Topo-cluster energies are calibrated to correct for the difference in calorimeter response to electromagnetic and hadronic showers (see Section 3.2.2) with a correction factor derived from data-to-simulation comparisons. This calibration involves the classification of topo-clusters by the type of shower they appear to predominantly contain, using variables relating to shower shapes, and is referred to as 'local cell weighting'. Total jet energies are further corrected, as a function of their energy and $\eta$, to correct for differences between the reconstructed energy and the true jet energy, using correction factors derived from simulations, and correction factors derived from measurements of well-measured reference jets in data. The effect of pile-up is corrected for by subtracting a fraction (proportional to the area of the jet) of the median $p_{\mathrm{T}}$ of the event, used as a proxy pile-up measurement.

### 4.4.5 Taus

Taus have short lifetimes ($\sim 290 \times 10^{-15}$ s) and decay either leptonically (with a branching fraction of 37%) or hadronically (with a branching fraction of 63%) [22], so their presence within the ATLAS detector is inferred from the detection of their decay products. Leptonic tau decays result in a lepton and two neutrino final state (for example, $\tau \to \ell \bar{\nu}_\ell \nu_\tau$ where $\ell = e, \mu$) and so cannot be precisely reconstructed due to the presence of missing energy in the final state. Hadronically-decaying taus mainly result in final states including either one or three charged pions and a tau neutrino, for example $\tau^- \to \pi^- \nu_\tau$ or $\tau^- \to \pi^- \pi^+ \pi^- \nu_\tau$ (branching ratios of 22% and 72%). The hadronic components of these states are identified using

an identification algorithm that utilises Boosted Decision Trees (BDTs) [161]. The starting point for the algorithm is jet candidates, identified with the anti-$k_t$ algorithm with $R = 0.4$, with $p_{\mathrm{T}} > 10\,\mathrm{GeV}$ and $|\eta| > 2.5$. Variables relating to tracks and electromagnetic deposits in the calorimeter within $\Delta R = 0.2$ of the jet vertex are used as input to two MC-trained BDTs, one trained tau decays to one pion and the other on tau decays to three pions. Like for electrons and muon candidates, tau candidates are identified as loose, medium or tight, with each identification level requiring different BDT scores. More information on tau reconstruction is given in [162, 163].

# Chapter 5

# Event Selection and Background Estimation

In this chapter, the event selections that are applied to the the set of data collected with the ATLAS detector in order to discriminate between the signal process (the Keung-Senjanović process) and the background processes, are described, along with the methods used to estimate the contribution of the background processes to the final dataset. I, in conjunction with other members of the small analysis team, designed the analysis strategy described in this chapter.

The initial dataset used consists of events recorded by the ATLAS detector during 2015–2016 at $\sqrt{s} = 13\,\text{TeV}$ that have been assessed as being of good quality by the ATLAS Data Quality Group (see Section 4.2), resulting in an initial dataset size of $36.1\,\text{fb}^{-1}$.

Firstly, as the reconstruction of physics object candidates may be ambiguous, a so-called 'overlap removal' is performed, as described in Section 5.1. Once this has been performed, events are selected as described in Section 5.2, forming the definition of the 'signal region' (SR). Signal regions are designed to be dominated by expected signal-like events. Data in the signal region was not viewed until the definition of the signal region was finalised, to avoid biasing the analysis. The practice of not viewing the data in the signal region is referred to as 'blinding', and the viewing of the data after the finalisation of the event selections as 'unblinding'. Further region types, 'control regions' (CR) and 'validation regions' (VR), are also defined (described in Section 5.3), and were used to improve and assess the modelling of the background processes.

## 5.1 Overlap removal

It is possible for physics object candidates to be reconstructed in an ambiguous way by the ATLAS software framework. For example, electron and muon candidates could be reconstructed using the same Inner Detector track, making it unclear which particle really is responsible for the detector hits used for the track reconstruction. To resolve these ambiguities, some objects that spatially overlap with other objects are removed following ATLAS overlap removal recomendations [164]. The overlap removal implementation is the same as in the ATLAS search for a Higgs boson decaying to two $b$-quarks in association with a leptonically-decaying $W$ or $Z$ using data from 2015–2016 [165] and is described in detail in [166].

The selections applied to the objects included in the overlap removal are outlined in Sections 5.1.1 to 5.1.4. After these selections are applied, the overlaps between selected particle candidates are resolved in the following sequence of steps [166]:

- **tau-electron:** If $\Delta R(\tau, e) < 0.2$, the $\tau$ candidate is removed (it is more likely that there is an unrelated coincident cluster that has been reconstructed, along with the electron-like track, as a tau).
- **tau-muon:** If $\Delta R(\tau, \mu) < 0.2$, the $\tau$ candidate is removed (it is more likely that there is an unrelated coincident cluster that has been reconstructed, along with the muon-like track, as a tau), with the exception that if the $\tau$ candidate has $p_{\mathrm{T}} > 50\,\mathrm{GeV}$ and the muon candidate is not a combined muon, then the $\tau$ candidate is not removed (the tau candidate is likely to be a true tau if it has high $p_{\mathrm{T}}$ and the muon is not high quality).
- **electron-muon:** If a combined muon candidate shares an Inner Detector track with an electron candidate, the electron candidate is removed (it is more likely that there is an unrelated coincident cluster rather than there are truly coincident tracks, if the muon is well reconstructed). If a calorimeter-tagged muon candidate shares an Inner Detector track with an electron candidate, the muon candidate is removed (calorimeter-tagged muons do not leave tracks in the Muon Spectrometer, so it is more likely the candidate is an electron).
- **electron-jet:** If $\Delta R(j, e) < 0.2$ the jet candidate is removed (because any calorimeter cluster will be reconstructed as a jet). For any surviving

jet candidates, if $\Delta R(j, e) < \min(0.4, 0.04 + 10\,\text{GeV}/E_T^e)$, the electron candidate is removed (because it is likely to have originated from semi-leptonic $b/c$ decays).

- **muon-jet:** If $\Delta R(j, \mu) < 0.2$ or the muon candidate Inner Detector track is ghost-associated [167] to the jet candidate[1], the jet candidate is removed (because the jet-like cluster is not substantial in relation to the muon-like track) if the jet candidate has less than three associated tracks with $p_\text{T} > 500\,\text{MeV}$ or both of the following conditions are met: the $p_\text{T}$ ratio of the muon and jet candidates is larger than 0.5 and the ratio of the muon candidate $p_\text{T}$ to the sum of $p_\text{T}$ of tracks with $p_\text{T} > 500\,\text{MeV}$ associated to the jet candidate is larger than 0.7. For any surviving jet candidates, if $\Delta R(j, \mu) < \min(0.4, 0.04 + 10\,\text{GeV}/p_T^\mu)$, the muon candidate is removed (because it is likely to have originated from semi-leptonic $b/c$ decays).

- **tau-jet:** If $\Delta R(j, \tau) < 0.2$, the jet candidate is removed (because any calorimeter cluster will be reconstructed as a jet).

### 5.1.1 Electrons

The electron candidates included in the overlap removal satisfy:

- $E_\text{T} > 7\,\text{GeV}$
- $|\eta| < 2.47$
- Reconstructed with loose electron identification criteria
- Isolated from other high $p_\text{T}$ tracks
- Origin compatible with the primary vertex

The $|\eta| < 2.47$ requirement ensures that the tracks of the selected electron candidates are within the acceptance of the Inner Detector ($|\eta| < 2.5$) and that the electromagnetic shower will be within the acceptance of the barrel electromagnetic calorimeter ($|\eta| < 2.5$).

[1]The muon candidate is normalised to have an energy of approximately zero, so as to not modify the kinematics and hard particle content of the existing set of jet candidates in the event. Jet clustering is then reperformed and if the muon candidate Inner Detector track is inside a jet candidate (rather than forming its own jet), the muon and jet candidates are ghost-associated.

The identification efficiency for loose electron candidates (the ratio of loose electron candidates to all electron candidates) is between 92–97% (increasing with inreasing $E_{\mathrm{T}}$), and the probability to reconstruct hadrons as loose electron candidates is less than 0.8%, for $20 < E_{\mathrm{T}} < 80\,\mathrm{GeV}$ [154]. The combined reconstruction and identification efficiency of loose electron candidates (the ratio of loose electron candidates to electromagnetic calorimeter clusters) with $7 < E_{\mathrm{T}} < 80\,\mathrm{GeV}$ is between 84–96% (increasing with inreasing $E_{\mathrm{T}}$) [154].

Electron candidate tracks are required to be isolated from other high $p_{\mathrm{T}}$ tracks, to reduce the background of electrons from hadron decays and light hadrons misidentified as electrons. The isolation scheme used (described in more detail as the 'LooseTrackOnly' criteria in [154]) requires that electron candidate tracks be isolated according to the relationship:

$$\frac{p_T^{\mathrm{varcone2.0}}}{E_T^e} < I(\eta, E_T^e)$$

where $E_T^e$ is the $E_{\mathrm{T}}$ of the electron candidate, and $p_T^{\mathrm{varcone2.0}}$ is the scalar sum of the $p_{\mathrm{T}}$ of all good quality tracks with $E_{\mathrm{T}} > 1\,\mathrm{GeV}$, within a cone of radius $\Delta R = \min(10\,\mathrm{GeV}/E_T^e, 0.2)$ around the electron candidate track, excluding the track associated with the electron candidate. $I(\eta, E_T^e)$ is defined so that the overall selection efficiency of the isolation (ratio of isolated electron candidates to all electron candidates) is 99% when applied to $Z \to e^+e^-$ MC [154].

To ensure compatibility with the primary vertex in the event, electron candidates are required to satisfy relevant ATLAS recommendations [168] relating to the closest distance from the track to the primary vertex in the longitudinal and transverse directions ($|z_0 \sin\theta| < 0.5\,\mathrm{mm}$ and $|d_0|/\sigma_{d_0} < 5$, where $z_0$ is the closest longitudinal distance, $d_0$ is the closest transverse distance, and $\sigma_{d_0}$ is the uncertainty on $d_0$).

### 5.1.2 Muons

The muon candidates included in the overlap removal satisfy:

- $p_{\mathrm{T}} > 7\,\mathrm{GeV}$
- $|\eta| < 2.7$
- Reconstructed with loose muon identification criteria

- Isolated from other high $p_{\mathrm{T}}$ tracks
- Origin compatible with the primary vertex

The loose identification category includes combined muons, and additionally extrapolated muons in the region $2.5 < |\eta| < 2.7$ and calorimeter-tagged and segment-tagged muons in the $|\eta| < 0.1$ region. The $2.5 < |\eta| < 2.7$ region is not covered by the acceptance of the Inner Detector, so combined muons cannot be formed in this region, whilst there is a gap in the Muon Spectrometer acceptance at $|\eta| < 0.1$. The reconstruction efficiency of loose muons candidates (ratio of loose muon candidates to well reconstructed Inner Detector tracks) with $4 < p_{\mathrm{T}} < 20\,\mathrm{GeV}$ ($20 < p_{\mathrm{T}} < 100\,\mathrm{GeV}$) in MC is more than 96% (98%), whilst the probability of misreconstructing a pion as a muon is less than 0.6% (0.8%) [156].

Muon candidate tracks are required to be isolated from other high $p_{\mathrm{T}}$ tracks, to reduce the background of muons coming from hadron decays. The isolation scheme used (the 'LooseTrackOnly' criteria in [156]) requires that muon candidate tracks be isolated according to the relationship:

$$\frac{p_T^{\mathrm{varcone3.0}}}{p_T^{\mu}} < I(\eta, p_T^{\mu})$$

where $p_T^{\mu}$ is the $p_{\mathrm{T}}$ of the muon candidate, and $p_T^{\mathrm{varcone3.0}}$ is the scalar sum of the $p_{\mathrm{T}}$ of all good quality tracks with $p_{\mathrm{T}} > 1\,\mathrm{GeV}$, within a cone of radius $\Delta R = \min(10\,\mathrm{GeV}/p_T^{\mu}, 0.3)$ around the muon candidate track, excluding the track associated with the muon candidate. $I(\eta, p_T^{\mu})$ is defined so that the overall selection efficiency in MC of the isolation (ratio of isolated muon candidates to all muon candidates) is 99%, whilst muons originating from light mesons or semileptonic decays of $b$- and $c$-quarks are suppressed by a factor of 15 [156].

Muon candidates are required to satisfy relavent ATLAS recommendations [168] relating to the closest distance from the track to the primary vertex in the longitudinal and transverse directions ($|z_0 \sin\theta| < 0.5\,\mathrm{mm}$ and $|d_0|/\sigma_{d_0} < 3$) to ensure compatibility with the primary vertex in the event.

### 5.1.3 Jets

The jet candidates included in the overlap removal satisfy:

- $p_{\mathrm{T}} > 20\,\mathrm{GeV}$ and $|\eta| < 2.5$, or $p_{\mathrm{T}} > 30\,\mathrm{GeV}$ and $2.5 \leq |\eta| < 4.5$
- Not a pile-up jet candidate
- Not a jet candidate of non-collision origin

Jets from pile-up are rejected using the Jet Vertex Tagger (JVT) discriminant [169]. The variables that enter into the discriminant are the 'jet vertex fraction', which aims to identify the vertex from which a jet originated from by comparing the scalar sum of $p_{\mathrm{T}}$ of tracks associated to a jet and a particular vertex, to the scalar sum of $p_{\mathrm{T}}$ of tracks associated to the same jet but associated to other vertices in the event (with a correction related to the number of vertices in the event), and $R_{p_T}$, which gives the ratio of the scalar sum of $p_{\mathrm{T}}$ from tracks associated to the primary hard scatter vertex to the calibrated jet $p_{\mathrm{T}}$. The discriminant is formed using a k-nearest neighbour algorithm [161, 170]: in the 2D space formed by these variables, the probability for a jet with a particular JVF and $R_{p_T}$ values to be not from pile-up is defined as the ratio of non-pile-up jets to all jets amongst the neighbourhood of that point in an MC training sample. The technique is used only on jets with $p_{\mathrm{T}} < 60\,\mathrm{GeV}$ and $|\eta| < 2.4$. The selections on the JVT discriminant provide an efficiency of ∼95% (percentage of non-pile-up jets passing the JVT selection) with a fake rate of 3% (percentage of jets passing the selection that are pile-up jets) when applied to simulated $Z \to \mu\mu$ + jet(s) events [169].

Jet candidates of non $pp$-collision origin, or 'fake' jet candidates, are rejected using the 'BadLoose' criteria described in [171]. Sources of fake jets include $pp$ beam-induced background effects, where protons escaping the beam away from the interaction point can cause cascades of secondary particles, resulting in muons that may deposit their energy in the calorimeters and be reconstructed as jet candidates. Cosmic-ray muons may also reach the ATLAS detector with the same consequences. Calorimeter noise can also be reconstructed as jet candidates. Fake jet candidates erroneously reconstructed from noise in the LAr calorimeters are rejected using variables related to signal pulse shapes in the LAr calorimeters. Fake jet candidates from the beam-induced background and those from calorimeter noise usually are more longitudinally localised in the calorimeters than real jets, so can be rejected using variables relating to the fraction of energy they deposit in different calorimeter sections/layers. Finally, real jets contain usually charged hadrons, which may be absent in a fake jet candidate, and can be rejected using track-related variables. Over 99.5% of real

jets with $p_{\mathrm{T}} > 20\,\mathrm{GeV}$ are retained after the application of the 'BadLoose' criteria MC [171].

### 5.1.4 Hadronically-decaying taus

The hadronically-decaying tau candidates included in the overlap removal satisfy:

- $p_{\mathrm{T}} > 20\,\mathrm{GeV}$
- $|\eta| < 2.5$, but not within $1.37 < |\eta| < 1.52$
- Reconstructed with medium hadronically-decaying tau identification criteria

Hadronically-decaying tau candidates falling in the $1.37 < |\eta| < 1.52$ region are excluded, as this is the transition area between the barrel and endcap regions of the calorimeter, where there is a large amount of material between the calorimeters and the beampipe (see Figure 3.11) which increases the uncertainty on calorimeter-based energy measurements. The efficiency to reconstruct and identify medium hadronically-decaying tau candidates (ratio of medium hadronically-decaying tau candidates to the total number hadronically-decaying taus in MC) is 55% (40%) for taus decaying to one charged pion (three charged pions), whilst less than 0.05% of jets are mis-identified as hadronically-decaying tau candidates [163].

## 5.2 Event selection

The event selections applied to form the signal region in the analysis are:

- Exactly two same-flavour opposite-sign lepton candidates passing the selections described in Sections 5.2.1 and 5.2.2
- At least one of the selected lepton candidates must have contributed to the acceptance of the event by the ATLAS trigger system
- Selected lepton candidate pair must have high invariant mass: $m_{\ell\ell} > 400\,\mathrm{GeV}$

- At least two jet candidates passing the selection described in Section 5.2.3
- Two highest $p_{\mathrm{T}}$ selected jet candidates must have high invariant mass ($m_{jj} > 110\,\mathrm{GeV}$) to suppress jets from $W/Z$ decays
- $\sum E_{\mathrm{T}} > 400\,\mathrm{GeV}$, summed over the two selected lepton candidates and two highest $p_{\mathrm{T}}$ selected jet candidates

As $N_e$ and $N_\mu$ are not theoretically constrained to have the same mass, following the event selections, the events are divided into two groups, those containing two electrons and those containing two muons, forming the electron and muon signal regions ($ee$ SR and $\mu\mu$ SR). One of the selected electron or muon candidates must have caused the event to pass a single lepton trigger. The single electron triggers used in this analysis had a minimum $E_{\mathrm{T}}$ threshold of 24 GeV for data taken in 2015 and 26 GeV for data taken in 2016, whilst the minimum $p_{\mathrm{T}}$ threshold for the single muon triggers was 20 GeV in 2015 and 24 GeV in 2016. Same flavour leptons are required as this analysis considers a situation where there is no mixing between $N_R$ flavours. The two selected lepton candidates and two highest-$p_{\mathrm{T}}$ selected jet candidates are collectively referred to as the signal leptons and jets, or signal particles. The signal region event selections are summarised and compared to those used in the control and validation regions in Table 5.1. Distributions of key variables in the signal regions can be seen in Figures 6.22–6.23.

Motivated by observed differences between signal and background MC in the dilepton mass spectrum, it was decided to implement a minimum dilepton mass selection in the signal region. As shown in Figures 5.1a and 5.1b, the background processes have an $m_{\ell\ell}$ distribution that tends to lower masses with respect to the signal process. To choose the $m_{\ell\ell}$ threshold value, the ratio of an estimate of analysis sensitivity ($S/\sqrt{B}$, where $S$ is the number of signal events passing all selections and $B$ is the number of background events passing all selections, predicted by MC) was found for various $m_{\ell\ell}$ threshold values with respect to our initial choice of threshold value ($m_{\ell\ell} > 110\,\mathrm{GeV}$). Figure 5.2 shows the estimated change in sensitivity achieved by the incorporation of the $m_{\ell\ell} > 400\,\mathrm{GeV}$ selection. The selection was found to result in a good improvement in sensitivity in large regions of the $m_{W_R}$–$m_{N_R}$ phase space considered in this analysis. In a region where $m_{W_R} \simeq m_{N_R}$ and $m_{W_R}$ and $m_{N_R}$ are low, where the sensitivity ratio can be seen to be less than 1 in Figure 5.2, the selection becomes harmful to the sensitivity because the two leptons in the event are less likely to have a high combined invariant mass, due to the similar masses of the $W_R$ and $N_R$. However,

the substantial benefit to the rest of the phase space led to the decision to include this selection in the analysis. The $\sum E_{\mathrm{T}} > 400\,\mathrm{GeV}$ selection was previously used in the ATLAS $\sqrt{s} = 7\,\mathrm{TeV}$ analysis [65]. Figures 5.1c and 5.1d show that the signal tends to much higher $\sum E_{\mathrm{T}}$ values than the background, so it was decided to include this selection in this analysis.

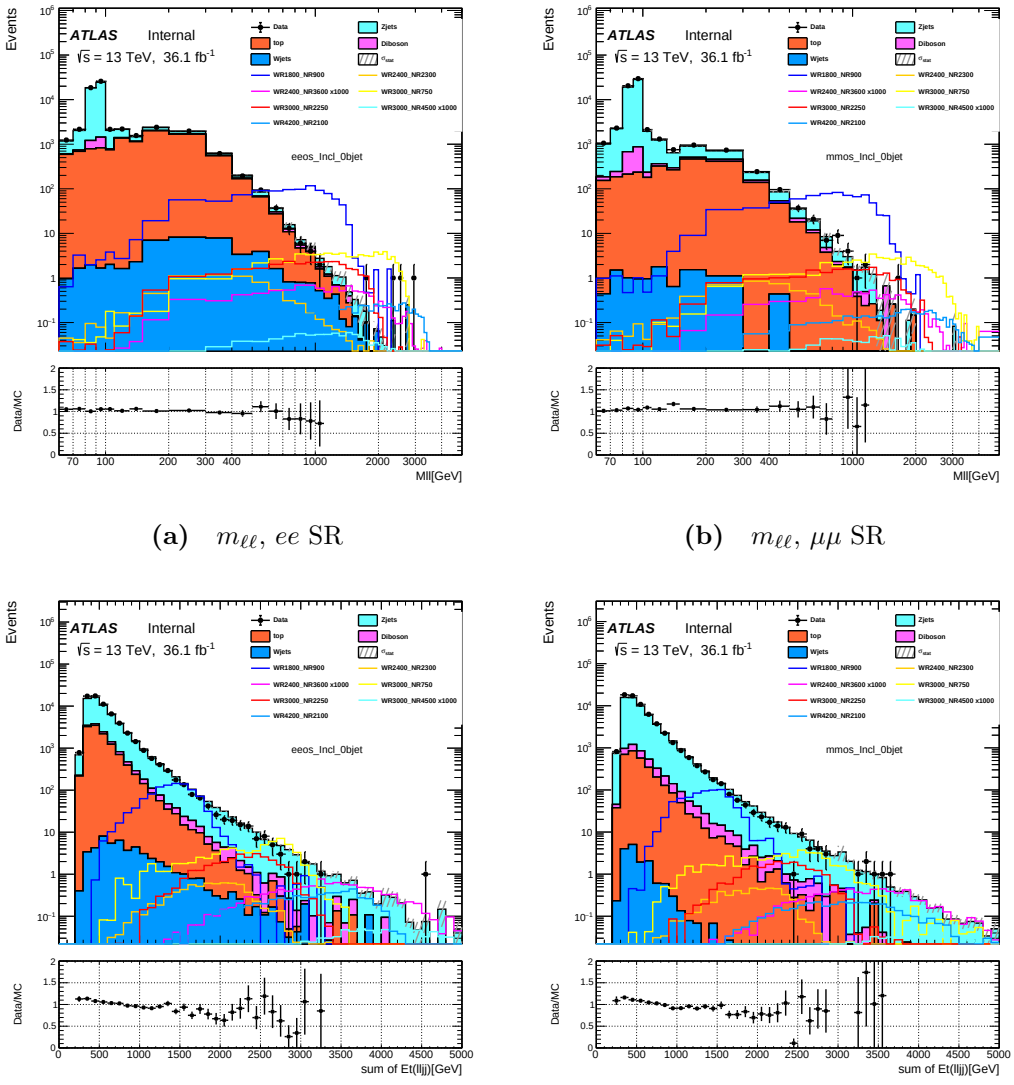


**(a)** $m_{\ell\ell}$, $ee$ SR **(b)** $m_{\ell\ell}$, $\mu\mu$ SR

**(c)** $\sum E_{\mathrm{T}}$, $ee$ SR **(d)** $\sum E_{\mathrm{T}}$, $\mu\mu$ SR

**Figure 5.1** $m_{\ell\ell}$ and $\sum E_{\mathrm{T}}$ distributions in the $ee$ and $\mu\mu$ signal regions, before applying the $m_{\ell\ell} > 400\,\mathrm{GeV}$, $m_{jj} > 110\,\mathrm{GeV}$ and $\sum E_{\mathrm{T}} > 400\,\mathrm{GeV}$ selections. Though the plots show data markers, the selections were optimised without viewing the data. Taken from [172].

Figure 5.3 shows the the combined signal acceptance and selection efficiency after all signal region selections are applied, as evaluated with simulated signal events. The combined signal acceptance and selection efficiency varies from 54% in high

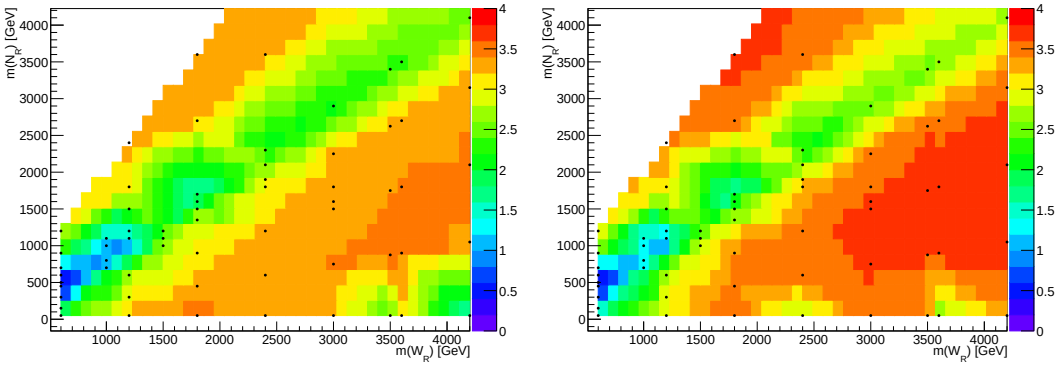


**(a)** $ee$ SR **(b)** $\mu\mu$ SR

**Figure 5.2** Ratio of estimated analysis sensitivity (using $S/\sqrt{B}$, where $S$ is the number of signal events and $B$ is the number of background events, predicted by MC) for the $m_{\ell\ell} > 400\,\text{GeV}$ selection, over the estimated sensitivity for a $m_{\ell\ell} > 110\,\text{GeV}$ selection, in the indicated regions. The black dots represent the mass hypotheses of the generated signal samples. This study was performed before the addition of the jet candidate $p_{\text{T}} > 100\,\text{GeV}$ selection (instead using a jet candidate $p_{\text{T}} > 50\,\text{GeV}$ selection).

$W_R$ and $N_R$ mass regions (areas shown in yellow), to 0.2% in low $W_R$ and $N_R$ mass regions (areas shown in dark blue) already excluded by previous LHC searches. The combined acceptance and efficiency is particularly low when $m_{W_R} \gg m_{N_R}$ because in this region of the phase space, the two jets from the $W_R$ decay tend to be merged into one jet, as shown in Figure 5.4. This is due to the high $p_{\text{T}}$ of the $W_R$ resulting from the large mass difference between the $W_R$ and $N_R$. A separate ATLAS analysis targets this region of the phase space, so, consequently, this analysis has not been optimised for the $m_{W_R} \gg m_{N_R}$ region. In the region $m_{W_R} \simeq m_{N_R}$, especially when $m_{W_R}$ and $m_{N_R}$ are low, the combined acceptance and efficiency drops because the two leptons in the event are less likely to have a high combined invariant mass, as they will be emitted from the $W_R$ or $N_R$ with lower momenta.

### 5.2.1 Electrons

Electron candidates are selected based on the following criteria:

- $E_{\text{T}} > 25\,\text{GeV}$
- $|\eta| < 2.47$, but not within $1.37 < |\eta| < 1.52$

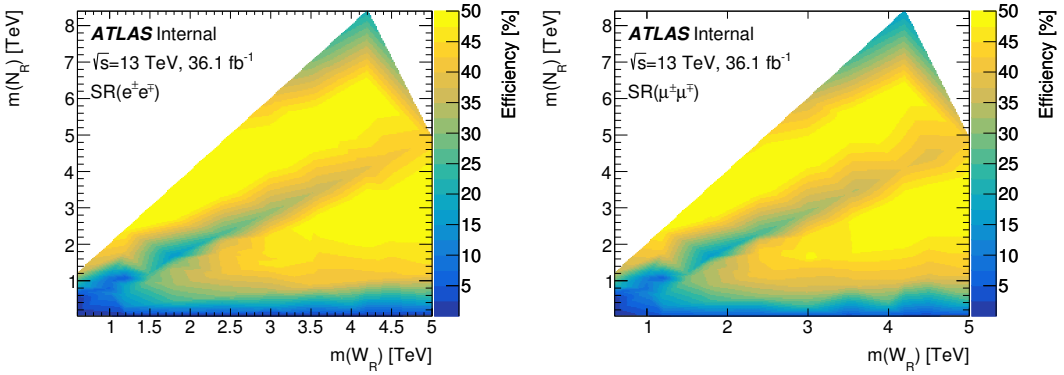


**(a)** $ee$ SR **(b)** $\mu\mu$ SR

**Figure 5.3** Combined signal acceptance and selection efficiency for signal region selections as a function of the signal $W_R$ and $N_R$ masses, from MC. The combined acceptance and selection efficiency is defined as the percentage of signal events passing the signal region selections compared to the initial number of signal events containing opposite-sign, same-flavour leptons. Taken from [172].

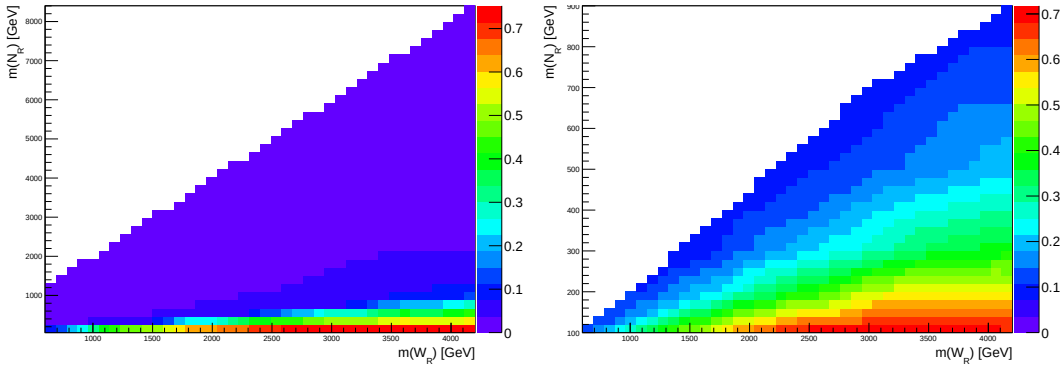


**(a)** $m_{N_R} \leq 8.4\,\text{TeV}$ **(b)** $m_{N_R} \leq 900\,\text{GeV}$

**Figure 5.4** The estimated generator-level fraction of events with merged jets originating from $W_R$ decay, for the stated $m_{N_R}$ range. The fraction of merged jets from a $W_R$ decay is estimated by using the number of events where the two jets originating from the $W_R$ are separated by less than $\Delta R = 0.4$, as this is the minimum distance between jets within the anti-$k_t$ algorithm configuration used in this analysis (see Section 4.4.4).

- Reconstructed with medium electron identification criteria
- Isolated from other high $p_{\mathrm{T}}$ tracks
- Origin compatible with the primary vertex

The $E_{\mathrm{T}} > 25\,\mathrm{GeV}$ requirement is applied because low energy electrons are not of interest in this analysis, as the search targets high mass $W_R$ and $N_R$. Electron candidates are not included in the overlap removal if they fall in the $1.37 < |\eta| < 1.52$ region, as this is the calorimeter transition region. The medium electron identification criteria (see Section 4.4.2) is used because it identifies electrons with high efficiency, with a low rate of misidentification. The reconstruction efficiency of electrons (the ratio of electron candidates to all electromagnetic clusters) is above 97% for all electrons with $E_{\mathrm{T}} > 15\,\mathrm{GeV}$, whilst the identification efficiency (ratio of medium electron candidates to all electron candidates) is between 87–95% (increasing with increasing $E_{\mathrm{T}}$). The probability to reconstruct hadrons as medium electrons candidates is less than 0.6%, for $20 < E_{\mathrm{T}} < 80\,\mathrm{GeV}$ [154].

Criteria relating to compatibility with the primary vertex and isolation criteria are unchanged from those applied to electron candidates that take part in the overlap removal.

### 5.2.2 Muons

Muon candidates are selected based on the following criteria:

- $p_{\mathrm{T}} > 25\,\mathrm{GeV}$
- $|\eta| < 2.5$
- Reconstructed with medium muon identification criteria
- Isolated from other high $p_{\mathrm{T}}$ tracks
- Origin compatible with the primary vertex

The $E_{\mathrm{T}} > 25\,\mathrm{GeV}$ requirement is applied because low energy muon are not of interest in this analysis, for the same reasons low energy electrons are not selected. The $|\eta| < 2.5$ requirement ensures that selected muon candidates are within the acceptance of the Inner Detector and Muon Spectrometer.

The medium identification criteria category (see Section 4.4.3) includes only combined muons within the $\eta$ range of the analysis, with other criteria detailed in Reference [156]. The reconstruction efficiency of medium muons (ratio of medium muon candidates to well reconstructed Inner Detector tracks) with $20 < p_{\mathrm{T}} < 100\,\mathrm{GeV}$ in MC is more than 96%, whilst the probability of misreconstructing a pion as a muon is less than 0.2% [156].

As for electron candidates, criteria relating to compatibility with the primary vertex and isolation criteria are unchanged from those applied to muon candidates that take part in the overlap removal.

### 5.2.3 Jets

Jet candidates are selected based on the following criteria:

- $p_{\mathrm{T}} > 100\,\mathrm{GeV}$
- $|\eta| < 2$
- Not a $b$-jet candidate
- Not a jet candidate of non-collision origin

These $p_{\mathrm{T}}$ and $|\eta|$ selections were found to give a large improvement in the search sensitivity (compared to previous choices of $\eta$ and $p_{\mathrm{T}}$ selections) for large regions of the phase space. Heavier $W_R$ and $N_R$ will naturally produce jets with higher $p_{\mathrm{T}}$, and it can be seen from Figure 5.6 that heavier $W_R$ generally result in more central jets (lower $|\eta|$ values), and for a given $W_R$ mass, heavier $N_R$ generally give more central jets. Figure 5.5 shows the estimated improvements in the analysis sensitivity by using these jet kinematic cuts, compared to the previous selections used in the analysis. Despite some degradation of the sensitivity for low values of $m_{W_R}$ and $m_{N_R}$, it was decided to choose these cuts because most of the affected mass points are in regions of the phase space already excluded by other analyses. Some low $m_{N_R}$ with high $m_{W_R}$ mass points are in areas not previously excluded, however it was decided to include these selections anyway due to the existence of another in-progress ATLAS analysis that specifically targets this region of the phase space.

$b$-jets, jets originating from $b$-quarks, have special characteristics that mean they can be distinguished from light jets (those originating from $u$, $d$, or $s$ quarks

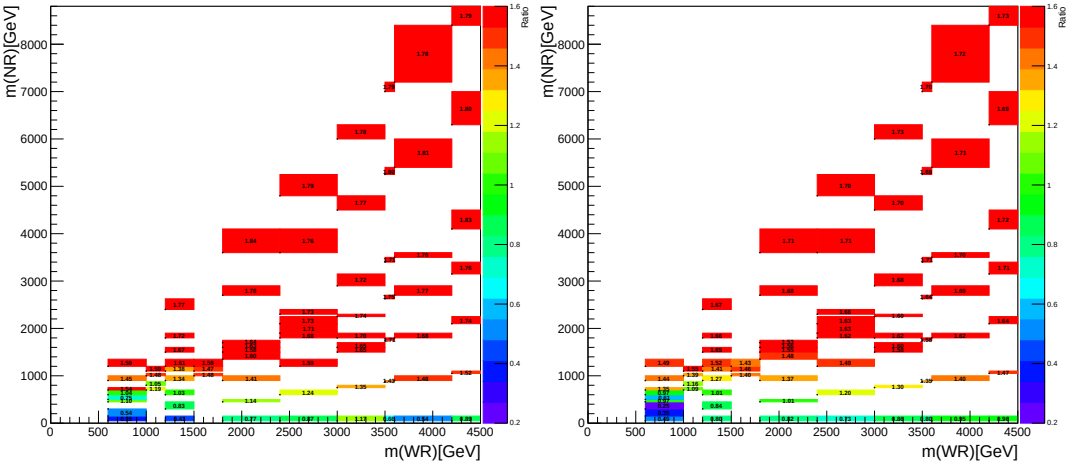


**(a)** $ee$ SR **(b)** $\mu\mu$ SR

**Figure 5.5** Ratio of estimated analysis sensitivity (using $S/\sqrt{B}$, predicted by MC) for jet candidate $|\eta| < 2$ and $p_{\mathrm{T}} > 100\,\mathrm{GeV}$ selections, over the estimated sensitivity for jet candidate $|\eta| < 2.8$ and $p_{\mathrm{T}} > 50\,\mathrm{GeV}$ selections, in the indicated regions. The black dots represent the mass hypotheses of the generated signal samples. Taken from [172].

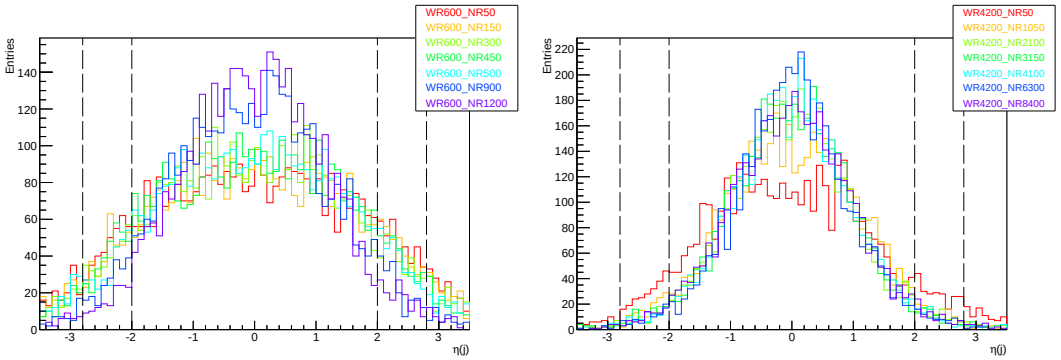


**(a)** $m_{W_R} = 600\,\mathrm{GeV}$ **(b)** $m_{W_R} = 4.2\,\mathrm{TeV}$

**Figure 5.6** Generator-level $\eta$ distributions for jets originating from $W_R$ decay, for several mass hypotheses. Heavier $W_R$ and $N_R$ generally give more central jets, motivating the choice of jet $|\eta| < 2$ selection.

or gluons). The weak decays of $b$-hadrons, formed from $b$-quarks, to lighter quarks are suppressed via the CKM matrix element factors. The result is an experimental signature in which the $b$-hadrons have a non-negligible lifetime within the ATLAS detector, especially long for their masses, resulting in the formation of a secondary vertex. $b$-hadrons often decay to $c$-hadrons, which also have non-negligible lifetimes, so a further secondary vertex may also be present. The MV2 algorithm is used within ATLAS to identify $b$-jets [173, 174], which uses a multivariate approach with variables including ones relating to secondary vertex parameters and $p_{\mathrm{T}}$, which is usually large due to the high mass of the $b$-quark. The algorithm configuration used in this analysis results in an efficiency of 70% (percentage of $b$-jets identified), with a purity of 97% (percentage of true $b$-jets in a set of $b$-jet candidates), when applied to simulated $t\bar{t}$ events [174].

$b$-jet candidates are rejected in this analysis in order to reduce the $t\bar{t}$ background relative to the number of signal events. In the form of LRSM considered in this analysis, $W_R$ decay to quarks pairs in the same manner as $W$ bosons, with the same CKM matrix elements $|V_{qq'}|$, where $q, q'$ are different quark flavours. Therefore, the branching fraction formulae of $W \to q\bar{q}'$ and $W_R \to q\bar{q}'$ have the same form:

$$\frac{\Gamma_{W\to q\bar{q}'}}{\Gamma_{W\to\mathrm{hadrons}}} = \frac{3|V_{q\bar{q}'}|^2}{\sum\limits_{q=u,d,s,c,b}\Gamma_{W\to q\bar{q}'}} \quad\longrightarrow\quad \frac{\Gamma_{W_R\to q\bar{q}'}}{\Gamma_{W_R\to\mathrm{hadrons}}} = \frac{3|V_{q\bar{q}'}|^2}{\sum\limits_{q=u,d,s,c,b,t}\Gamma_{W_R\to q\bar{q}'}}$$

In the $W$ boson case, $W \to tb$ does not occur (indicated by the lack of $t$ in the summation) because the top quark is substantially heavier than the $W$. However, the $W_R$ may be heavier than the top quark, in which case $W_R \to tb$ could occur. As the diagonal CKM matrix elements ($|V_{ud}|$, $|V_{cs}|$ and $|V_{tb}|$) are roughly $\sim$1 and the off-diagonal elements are non-zero [22], the branching fraction of $W_R \to tb$ is less than a third. On the other hand, top quarks most frequently decay to $W$ and a $b$-quark ($t \to Wb$), with a branching fraction of 91%, in relation to $t \to Wq$ where $q = (u, s, b)$ [22], so the large majority of $t\bar{t}$ decays result in one or two $b$-quarks. Therefore, the proportion of signal events rejected is less than the proportion of background events rejected, when $b$-jet events are rejected. Additionally, signal events containing $W_R \to tb$ would not be well identified by the other event selections made in this analysis, due to the possible presence of an extra lepton in the final state. Figure 5.7 shows the estimated enhancement in analysis sensitivity when rejecting $b$-jet candidates.

The same selections are using to reject jets of non-collision origin as during the

overlap removal (see Section 5.1.3). Over 99.9% of real jets with $p_{\mathrm{T}} > 100\,\mathrm{GeV}$ are retained after the application of the fake jet removal selections to MC [171].

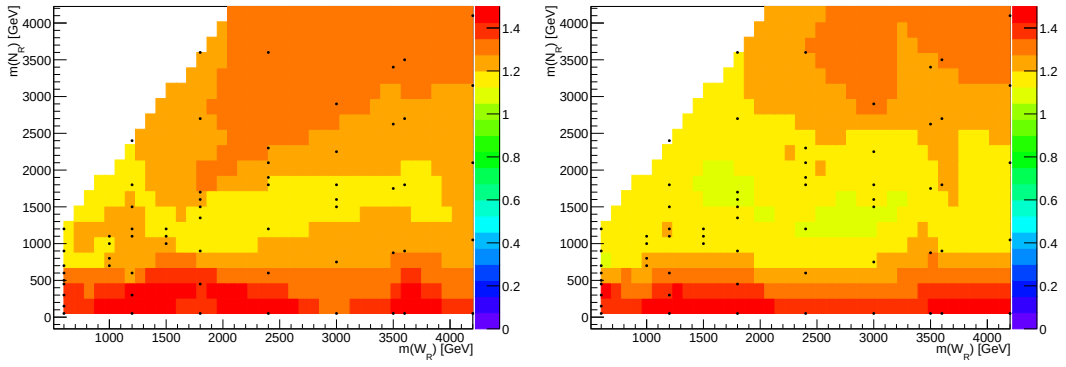


**(a)** $ee$ SR **(b)** $\mu\mu$ SR

**Figure 5.7** Ratio of estimated analysis sensitivity (using $S/\sqrt{B}$, predicted by MC) for the case where $b$-jet candidates are rejected, over the estimated sensitivity for when $b$-jet candidates are allowed, in the indicated regions. The black dots represent the mass hypotheses of the signal samples. This study was performed before the addition of the $m_{\ell\ell} > 400\,\mathrm{GeV}$ selection and jet candidate $p_{\mathrm{T}} > 100\,\mathrm{GeV}$ selection (instead using a $m_{\ell\ell} > 110\,\mathrm{GeV}$ selection and jet candidate $p_{\mathrm{T}} > 50\,\mathrm{GeV}$ selection).

## 5.3 Background estimation

The background processes considered in this analysis are modelled with MC, as discussed in Section 4.3.2. Control regions are defined with the aim of checking the modelling of background processes, and deriving data-driven normalisation factors to correct for any differences in normalisation between data and MC. Normalisation factors are extracted from the control regions by comparing the number of expected background events to the observed number of events in data. The decision to use data to derive normalisation factors requires that only a negligible amount of signal is allowed to enter into the control regions. The background predictions for normalised background process are scaled according to the relevant derived normalisation factor, in all of the analysis regions. The extraction and application of the normalisation factors occurs during fits of the signal and background MC to the data, which is the topic of Section 6.1. Validation regions (VR) are also defined, so that the effect of the normalisation factors could be checked before the signal region was unblinded.

The selections for the control and validation regions are based on identical selections to the signal region, with the exception of a particular variable that is used to define orthogonal phase space regions and which differentiates between the two. The variable used to ensure the orthogonality between the regions is $m_{\ell\ell}$, except for in the $e\mu$ CR which has the same kinematic selection as the signal regions, but requires different-flavour leptons. The event selections used in the control and validation regions are summarised and compared to those used in the signal region in Table 5.1. Distributions of key variables in the control and validation regions can be seen in Figures 6.18–6.21.

| | Control regions | | | Validation regions | | Signal regions | |
|---|---|---|---|---|---|---|---|
| Selection | $ee$ CR | $\mu\mu$ CR | $e\mu$ CR | $ee$ VR | $\mu\mu$ VR | $ee$ SR | $\mu\mu$ SR |
| $\ell\ell$ | $e^{\pm}e^{\mp}$ | $\mu^{\pm}\mu^{\mp}$ | $e^{\pm}\mu^{\mp}$ | $e^{\pm}e^{\mp}$ | $\mu^{\pm}\mu^{\mp}$ | $e^{\pm}e^{\mp}$ | $\mu^{\pm}\mu^{\mp}$ |
| $m_{\ell\ell}$ [GeV] | $[60, 110]$ | $[60, 110]$ | $> 400$ | $[110, 400]$ | $[110, 400]$ | $> 400$ | $> 400$ |
| # of jets | $\geq 2$ | $\geq 2$ | $\geq 2$ | $\geq 2$ | $\geq 2$ | $\geq 2$ | $\geq 2$ |
| $m_{jj}$ [GeV] | $> 110$ | $> 110$ | $> 110$ | $> 110$ | $> 110$ | $> 110$ | $> 110$ |
| $\sum E_{\mathrm{T}}$ [GeV] | $> 400$ | $> 400$ | $> 400$ | $> 400$ | $> 400$ | $> 400$ | $> 400$ |

**Table 5.1** Summary of all regions defined in the analysis, indicating the event selection criteria used for a given region. Pairs of values $[X, Y]$ indicate the minimum and maximum values the quantity in question may take in the analysis region in question.

For convenience, the background processes are grouped into three groups within this analysis: $Z+$jets, top-quark related processes, and diboson and $W+$jets processes. The main SM backgrounds in the signal regions are from top-quark events (mainly $t\bar{t}$) and $Z+$jets production, with contributions of ∼49% and ∼35% respectively in the $ee$ SR and ∼55% and ∼37% in the $\mu\mu$ SR. Minor contributions arise from diboson (mainly $ZW \to \ell^+\ell^- jj$ and $ZZ \to \ell^+\ell^- jj$) and $W+$jets events, with a combined contribution of ∼16% in the $ee$ SR and ∼8% in the $\mu\mu$ SR. Normalisation factors are derived only for the top-quark and $Z+$jets backgrounds, as these are the major backgrounds to the Keung-Senjanović process.

The normalisation factor for the $Z+$jets process is extracted from data in the $ee$ and $\mu\mu$ control regions, where the $60 < m_{\ell\ell} \leq 110\,\mathrm{GeV}$ selection is defined to select events with $m_{\ell\ell}$ around the $Z$ boson mass, to enhance the proportion of $Z+$jets events in these control regions. The proportion of $Z+$jets events is above 95% in both control regions. The maximum amount of signal contamination, the

percentage of predicted signal events compared to the total number of predicted events, is 4.7% in the $ee$ CR and 4.1% in the $\mu\mu$ CR, though this is for a region of phase space already excluded by previous searches. Most of the signal hypotheses considered do not enter either control region.

The $e\mu$ CR is dominated by top-quark events (80.2%), with an admixture of $W+$jets and diboson events, and thus a normalisation factor for top-quark processes is extracted from this region. The maximum amount of signal contamination is 6.7% in the $e\mu$ CR, though, as before, this is in an previously-excluded region and, and for most signal hypotheses the control region is signal free.

Top-quark decays usually give rise to $b$-quarks, as already discussed, so an alternative control region, defined by requiring $b$-jet candidates, was considered. This control region would be $\sim$ 99% pure top-quark events, but was rejected as the signal expectation was unacceptably high in comparison to the predicted background events, with signal events reaching a maximum of 74.2% of the total predicted events for $m_{W_R}$–$m_{N_R}$ combinations with high cross sections.

The generator used to simulate the $Z+$jets (and $W+$jets) background (see Section 4.3.2), does not correctly model the $m_{jj}$ spectrum, as shown in Figures 5.8a and 5.8b, an effect also observed by other in-progress ATLAS analyses. A reweighting factor is derived using events from the $ee$ and $\mu\mu$ CR (combined) and applied to the simulated $Z+$jets events in all of the analysis regions. In order to correct this mismodelling, a Novosibirsk function is fitted to the data-to-MC ratio as a function of $m_{jj}$, after subtracting the non-$Z+$jets contributions (as predicted by simulation) from both. The Novosibirsk function [175] is defined as:

$$f(m_{jj};\sigma,x_0,\Lambda) = e^{-\frac{1}{2}\frac{(\ln q_y)^2}{\Lambda^2}+\Lambda^2}$$
$$q_y(m_{jj};\sigma,x_0,\Lambda) = 1+\frac{\Lambda(m_{jj}-x_0)}{\sigma}\times\frac{\sinh(\Lambda\sqrt{\ln 4})}{\Lambda\sqrt{\ln 4}}$$

where the three free parameters, $\sigma$, $x_0$ and $\Lambda$ control the width, peak and tail of the distribution. The resulting ratio with the best fit reweighting function is shown in Figure 5.9. The reweighting factor ranges from 1.1 in the low-$m_{jj}$ region to 0.5 in the high-$m_{jj}$ region above 3 TeV. Reweighted $m_{jj}$ distributions in the $ee$ and $\mu\mu$ CRs are shown in Figures 5.8c and 5.8d.

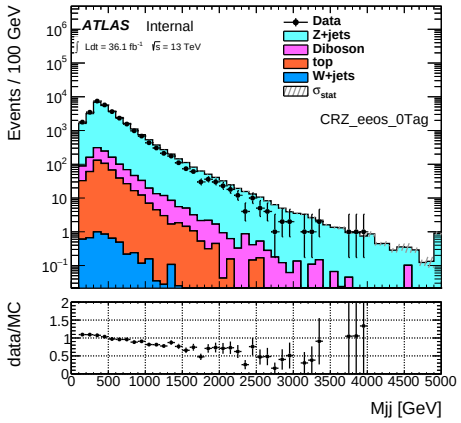


**(a)** $ee$ CR, without $m_{jj}$ reweighting

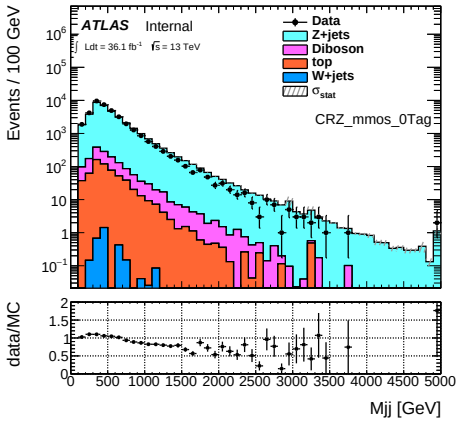


**(b)** $\mu\mu$ CR, without $m_{jj}$ reweighting

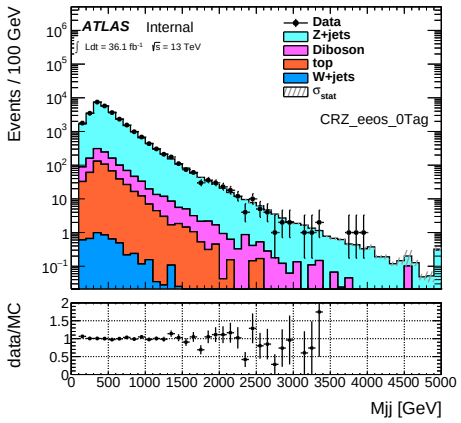


**(c)** $ee$ CR, with $m_{jj}$ reweighting

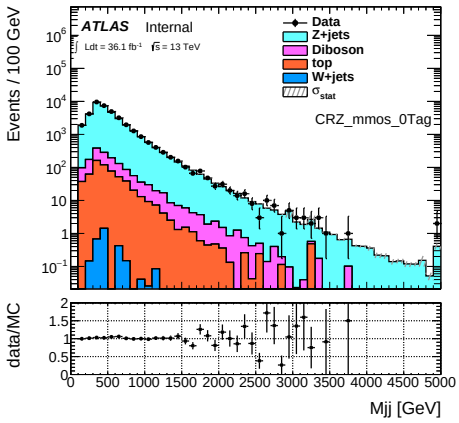


**(d)** $\mu\mu$ CR, with $m_{jj}$ reweighting

**Figure 5.8** $m_{jj}$ distributions for the $ee$ and $\mu\mu$ CRs, before and after $m_{jj}$ reweighting, as indicated. Taken from [172].

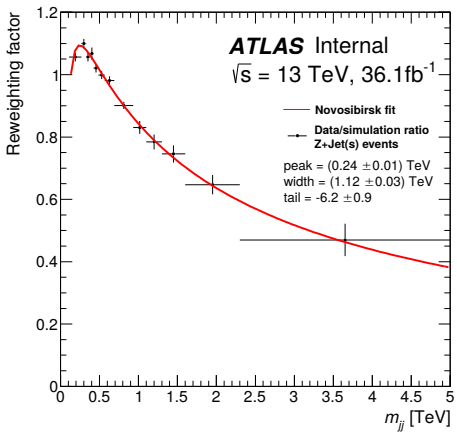


**Figure 5.9** The data-to-MC ratio, as a function of $m_{jj}$, with the result of the Novosibirsk fit superimposed, in the combined $ee$ and $\mu\mu$ CRs. The fitted values for the peak ($\sigma$), width ($x_0$) and tail ($\Lambda$) are shown. The binning was chosen such that the resulting distribution was sufficiently populated. Taken from [172].

# Chapter 6

# Statistical Analysis

This chapter describes how the final results in this analysis were obtained. The results themselves are presented in Chapter 7. The statistical analysis package HistFitter [176], which is used extensively throughout the ATLAS collaboration, was used to implement a series of binned maximum-likelihood fits to the data distributions in the control and signal regions, as described in Section 6.1. A check was then performed looking for significant deviations of data from the post-fit background distributions, described in Section 6.2, finding none that were inconsistent with SM predictions. The procedure followed to obtain exclusion limits on possible $W_R$–$N_R$ masses, as well as upper bounds on the Keung-Senjanović process cross section multiplied by the branching fraction ($\sigma \times B$) to $eejj$ or $\mu\mu jj$ as a function of the $W_R$–$N_R$ mass hypothesis, is described in Section 6.3. I, in consultation with the rest of the small analysis team, decided on and implemented the fitting strategy, generated the theory systematic variations for the signal MC, performed the check for significant deviations, and calculated the exclusion limits.

A statistical combination was also performed with a related search for the Keung-Senjanović process using same-sign leptons [177], referred to as the same-sign analysis to contrast with the opposite-sign analysis described in the rest of this thesis, in order to set improved limits on $m_{W_R}$ and $m_{N_R}$ for the Majorana $N_R$ case. The combination is described in Section 6.1.5.

## 6.1 Likelihood fits

This analysis uses a series of binned maximum-likelihood fits, in which a likelihood function, defined in Section 6.1.1, is maximised in order to find the best-fit values of some parameters within the model encapsulated by the function. The free parameters in the likelihood function include the signal strength parameter $\mu_{\mathrm{S}}$, which scales the signal prediction, and normalisation factors for the $Z+\mathrm{jets}$ and top-quark processes. Statistical and systematic uncertainties are also implemented in the fit as so-called nuisance parameters (NPs), which can alter the shape and normalisation of both the signal and background predictions. Section 6.1.2 details the uncertainties included in the fit as nuisance parameters. The various control and signal regions are used simultaneously to fit most of the free parameters in order to maximise the likelihood. The exceptions are the normalisation factors of the $Z+\mathrm{jets}$ and top-quark backgrounds, which are determined by comparing data to MC in dedicated control regions. As a cross-check of the fitting procedure, the post-fit values of the free parameters were applied in the validation regions so that the compatibility between the data and the prediction can be inspected.

The fit inputs passed to HistFitter are histograms of $m_{\ell\ell jj}$ or $m_{jj}$ distributions in each signal and control region, with the exception of the $ee$ and $\mu\mu$ control regions, where only the yield in the region is used. $m_{\ell\ell jj}$ or $m_{jj}$ distributions are used as inputs to the fit, depending on whether we are considering a signal mass point in the $m_{W_R} > m_{N_R}$ or $m_{W_R} < m_{N_R}$ phase space region. The pre-fit distributions in Figures 6.18–6.23 are examples of input distributions used in the fit. For each background and signal sample, the nominal histograms and histograms showing the effect of $\pm 1\sigma$ variations of each systematic uncertainty are included.

### 6.1.1 Likelihood function definition

The likelihood function used in this analysis is defined as follows [176]:

$$\mathcal{L}(\mu_{\mathrm{S}}, \boldsymbol{\mu_{\mathbf{B}}}, \boldsymbol{\theta}) = \prod_{i}^{\text{bins}} \mathcal{P}(n_i \,|\, S_i(\mu_{\mathrm{S}}, \boldsymbol{\theta}) + B_i(\boldsymbol{\mu_{\mathbf{B}}}, \boldsymbol{\theta})) \times \prod_{j}^{\text{NPs}} \mathcal{F}_j(\tilde{\theta_j} \,|\, \theta_j)$$

The first term contains a product (over all bins in the analysis regions) of Poisson distributions $\mathcal{P}$, which have form:

$$\mathcal{P}(n \,|\, \lambda) = \frac{e^{-\lambda}\lambda^n}{n!}$$

which gives the probability of observing $n$ events in data, assuming a combined signal and background prediction of $\lambda$. The predicted signal and background yields, $S(\mu_{\mathrm{S}}, \boldsymbol{\theta})$ and $B(\boldsymbol{\mu_{\mathbf{B}}}, \boldsymbol{\theta})$, are functions of $\boldsymbol{\theta}$, the set of nuisance parameters (NPs), and the signal strength and the set of background normalisation parameters, $\mu_{\mathrm{S}}$ and $\boldsymbol{\mu_{\mathbf{B}}}$. $\mu_{\mathrm{S}}$ scales the predicted signal yield relative to the initial prediction. $\mu_{\mathrm{S}} = 1$ corresponds to the nominal MC prediction, and so corresponds to the Majorana $N_R$ hypothesis, whilst $\mu_{\mathrm{S}} = 0$ gives the SM prediction. Additionally, $\mu_{\mathrm{S}} = 2$ corresponds to the Dirac $N_R$ hypothesis. This is because, under the Dirac $N_R$ hypothesis, the cross section multiplied by the branching fraction of the Keung-Senjanović process to opposite sign leptons is twice that for the Majorana $N_R$ case. The $\boldsymbol{\mu_{\mathbf{B}}}$ consists of $\mu_{\mathrm{Z}}$ and $\mu_{\mathrm{top}}$, the $Z+\text{jets}$ and top-quark background normalisation factors, which scale the background predictions. These normalisation factors are set during the fit so that the total background yield matches the observed data yield in the $ee$, $\mu\mu$ and $e\mu$ CRs.

The second term is a product (over NPs) of auxiliary functions $\mathcal{F}$, which constrain the values of the nuisance parameters. The auxiliary functions for most NPs take the form of either a Poisson distribution, as above, or a Gaussian, given by:

$$\mathcal{G}(\tilde{\theta} \,|\, \theta, \sigma) = \frac{1}{\sqrt{2\pi\sigma^2}} e^{-\frac{(\tilde{\theta}-\theta)^2}{2\sigma^2}}$$

depending on the uncertainty under consideration. The central value of the NP before the fit, $\tilde{\theta}$, is zero and the standard deviation, $\sigma$, is one, because the NPs have units of standard deviation and because they parametrise changes to the

signal and background yields.

The dependences of the signal and background predictions on the NPs take the forms:

$$S_i(\mu_{\mathrm{S}}, \boldsymbol{\theta}) = \mu_{\mathrm{S}} S_i^{\mathrm{nom}} (1 + \sum_{j}^{\mathrm{NPs}} \Delta_{ij}(\theta_j))$$

$$B_i(\boldsymbol{\mu_{\mathrm{B}}}, \boldsymbol{\theta}) = \sum_{b}^{\mathrm{bkgs}} \mu_{\mathrm{B}b} B_{bi}^{\mathrm{nom}} (1 + \sum_{j}^{\mathrm{NPs}} \Delta_{bij}(\theta_j))$$

where $S_i^{\mathrm{nom}}$ is the nominal signal prediction in bin $i$ and $B_{bi}^{\mathrm{nom}}$ is the nominal background prediction for background $b$ in bin $i$. $\Delta_{ij}(\theta_j)$ and $\Delta_{bij}(\theta_j)$ are response functions that encode the change in signal and background $b$ yields due to systematic $j$ in bin $i$, as a function of the NP value. For each background and signal sample in a bin, the nominal yield and the yield corresponding to the $\pm 1\sigma$ variation of each systematic uncertainty are input into the fit, from which the changes in yield for an arbitrary value of $\theta$ are found from a 6th order polynomial interpolation between $\pm 1\sigma$ and exponential extrapolation outside of this range (see [178]).

### 6.1.2 Treatment of uncertainties

This section summarises the uncertainties considered in this analysis. Experimental systematic uncertainties are discussed in Section 6.1.2.1, whilst systematic uncertainties relating to MC predictions, referred to as theory uncertainties, are discussed in Section 6.1.2.2. Both experimental and theory uncertainties use auxiliary functions with Gaussian forms. Additionally, the statistical uncertainty on the number of signal and background events in each bin is taken in account using one NP per bin per sample, with auxiliary functions with Poissonian forms. However, the statistical error is neglected for bins and processes where the relative statistical error is under 5%.

The effect of these uncertainties on the $m_{\ell\ell jj}$ and $m_{jj}$ distributions are included in the fit as NPs, with response functions that may vary the overall normalisation and/or per-bin normalisations of the signal and backgrounds yields. An NP for a particular uncertainty is correlated across processes and analysis regions, but all NPs are treated as fully uncorrelated from each other. Figure 6.9 shows the sources of uncertainty on the post-fit background yields in all the analysis regions.

For any systematic uncertainties applied to the $Z+$jets and top-quark background processes, any contribution of the uncertainty on the total yield of the process is absorbed into the $\mu_{\mathrm{Z}}$ and $\mu_{\mathrm{top}}$ normalisation factors. The per-bin response functions of these systematic uncertainties are therefore correlated so as to not affect the overall yield of the process. However, in Figure 6.9, the contributions of $Z+$jets and top-quark uncertainties to the total yield are kept separate from the normalisation factors, so that the full effect of the uncertainties can be seen. The total uncertainty is the same in both cases due to correlations and anti-correlations between the uncertainties.

#### 6.1.2.1 Experimental uncertainties

Per-event scale factors are applied to MC events in this analysis to correct for differences in physics object reconstruction, identification, isolation and trigger efficiencies between data and MC. These scale factors, derived and provided by the ATLAS Combined Performance (CP) groups, change the relative weighting of MC events in order to reproduce the efficiencies seen in data. Whenever scale factors are applied on an event-by-event basis, there are uncertainties in the overall rate of a process, and also in the shape of any output distributions. Uncertainties relating to the derivation of the scale factors are assessed by the ATLAS CP groups, and propagated to this analysis by the provision of $\pm1\sigma$ scale factor variations. The $\pm1\sigma$ scale factor variations are then applied to the MC datasets used in the analysis, separately for each uncertainty. The resultant distributions are input into the likelihood fit, allowing the response functions to be formed. Procedures used to determine physics object energy and momentum scales, described in Section 4.4, also have associated uncertainties. $\pm1\sigma$ variations of the object energy and momentum scales, once again centrally provided by the ATLAS CP groups, are also applied and propagated to the likelihood fit.

Table 6.1 lists the electron, muon, jet and jet flavour identification related uncertainty sources considered in this analysis. The uncertainty in the combined 2015 and 2016 integrated luminosity is also included. It has a size of 2.1%, and is derived, following a methodology similar to that detailed in [179], from a calibration of the luminosity scale using $x$–$y$ beam-separation scans performed in August 2015 and May 2016. The uncertainty on luminosity scales the process yields in a coherent way for all processes and bins. The impact of all considered experimental uncertainties sources on the per-bin background process yields is

shown in Figure 6.1 for $Z+$jets, Figure 6.2 for top-quark process, and Figure 6.3 for the combined $W+$jets and diboson processes. The dominant uncertainty category varies depending on the process and $m_{\ell\ell jj}$ or $m_{jj}$ mass range. The individual uncertainties in each category are treated as uncorrelated.

| Electron related | # NPs | Ref. |
|---|---|---|
| Energy scale and resolution | 2 | [154] |
| Reconstruction and identification efficiency | 2 | [154] |
| Isolation efficiency | 1 | [154] |
| Trigger efficiency | 1 | [154] |
| **Muon related** | **# NPs** | **Ref.** |
| Momentum scale and resolution | 3 | [156] |
| Reconstruction and identification efficiency | 2 | [156] |
| Isolation efficiency | 2 | [156] |
| Trigger efficiency | 2 | [156] |
| Track-to-vertex association efficiency | 2 | [180] |
| **Jet related** | **# NPs** | **Ref.** |
| Energy scale and resolution | 5 | [160] |
| Jet flavour (inc. $b$-jet) identification | 13 | [174] |

**Table 6.1** Experimental systematic uncertainty sources, along with the number of associated nuisance parameters (NPs), and a reference to the ATLAS CP group publication covering the derivation of the scale factor and calibration, along with the sources of uncertainty.

#### 6.1.2.2 Theory uncertainties

Theory uncertainties, systematic uncertainties associated with the choice of theory parameters or the choice of software used when generating MC datasets, are assessed by producing datasets with alternative theory parameter values, or by using different software, and comparing these datasets to the nominal datasets (detailed in Section 4.3.2). Alternative approach used for some uncertainties is to reweight the events in an existing MC dataset to produce different distributions to emulate the use of different theory parameter values.

Theory uncertainties for the signal process were evaluated by varying the QCD renormalisation and factorisation scale factors, $\mu_{\mathrm{R}}$ and $\mu_{\mathrm{F}}$, and by using alternative PDF sets, CTEQ6L1 and MSTW2008LO. The QCD scale uncertainty was estimated by varying the nominal values of $\mu_{\mathrm{R}}$ and $\mu_{\mathrm{F}}$ by factors of 0.5 and

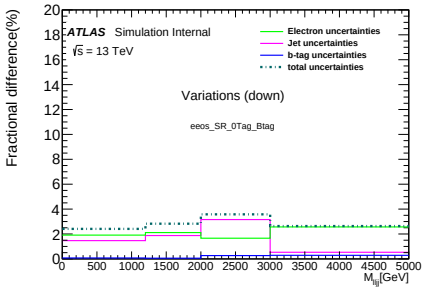


**(a)** $ee$ SR, $m_{\ell\ell jj}$, $-1\sigma$ variation

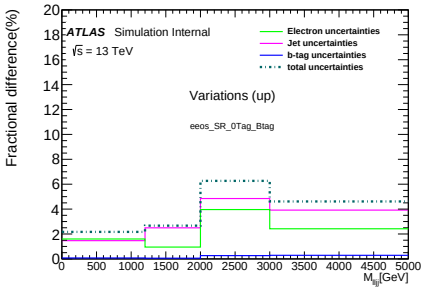


**(b)** $ee$ SR, $m_{\ell\ell jj}$, $+1\sigma$ variation

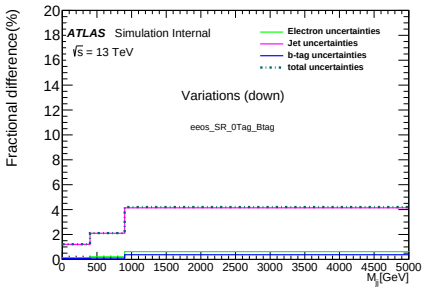


**(c)** $ee$ SR, $m_{jj}$, $-1\sigma$ variation

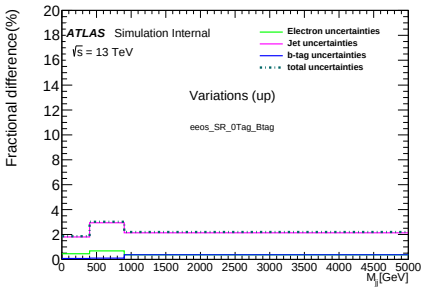


**(d)** $ee$ SR, $m_{jj}$, $+1\sigma$ variation

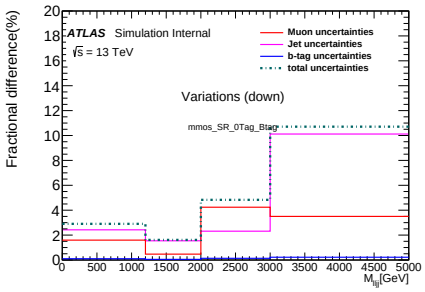


**(e)** $\mu\mu$ SR, $m_{\ell\ell jj}$, $-1\sigma$ variation

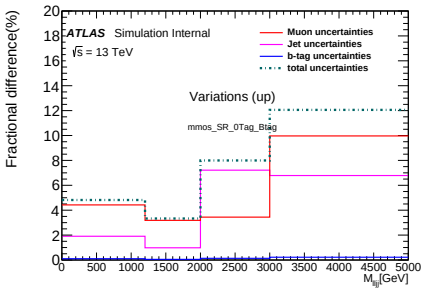


**(f)** $\mu\mu$ SR, $m_{\ell\ell jj}$, $-1\sigma$ variation

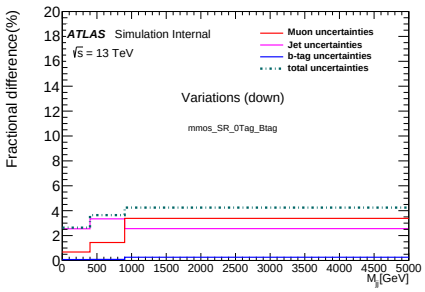


**(g)** $\mu\mu$ SR, $m_{jj}$, $-1\sigma$ variation

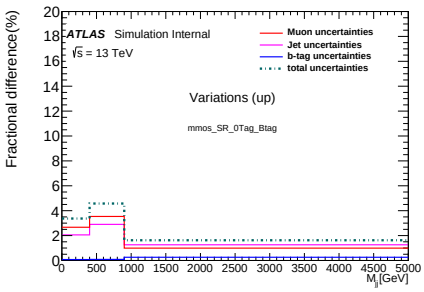


**(h)** $\mu\mu$ SR, $m_{jj}$, $-1\sigma$ variation

**Figure 6.1** Effect of experimental uncertainties in the $ee$ and $\mu\mu$ SRs on the $Z+$jets background $m_{\ell\ell jj}$ and $m_{jj}$ distributions, for the indicated region and discriminant. Contributions from each source are treated as uncorrelated. '$b$-tagging uncertainties' refers to jet flavour identification uncertainties. Taken from [172].

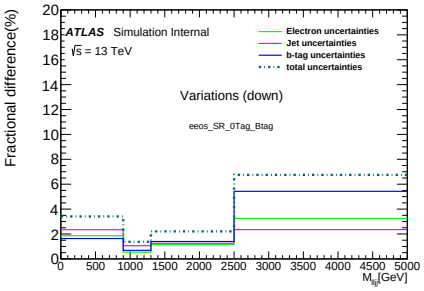


**(a)** $ee$ SR, $m_{\ell\ell jj}$, $-1\sigma$ variation

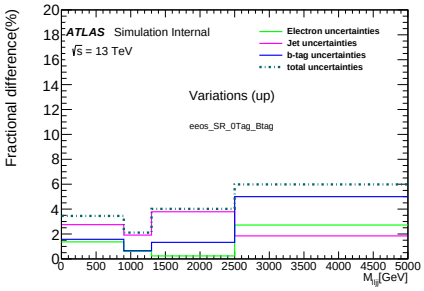


**(b)** $ee$ SR, $m_{\ell\ell jj}$, $+1\sigma$ variation

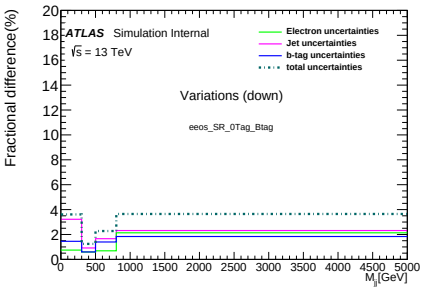


**(c)** $ee$ SR, $m_{jj}$, $-1\sigma$ variation

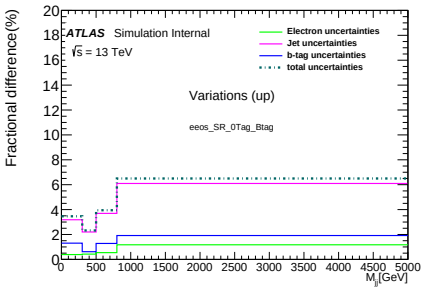


**(d)** $ee$ SR, $m_{jj}$, $+1\sigma$ variation

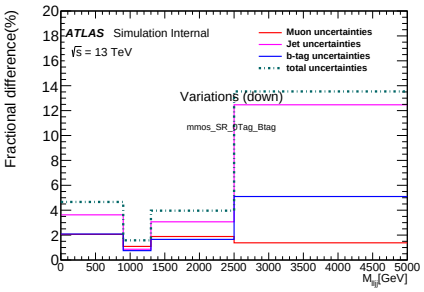


**(e)** $\mu\mu$ SR, $m_{\ell\ell jj}$, $-1\sigma$ variation

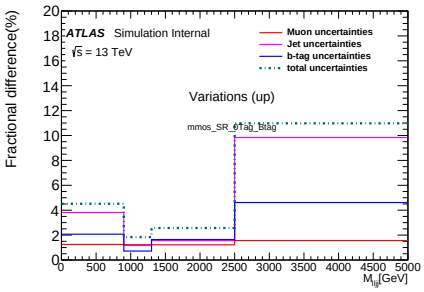


**(f)** $\mu\mu$ SR, $m_{\ell\ell jj}$, $-1\sigma$ variation

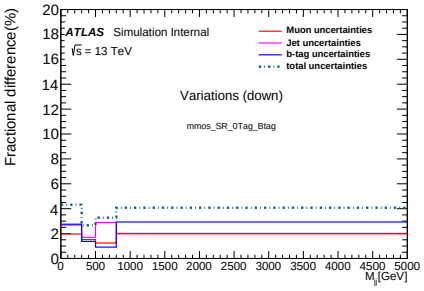


**(g)** $\mu\mu$ SR, $m_{jj}$, $-1\sigma$ variation

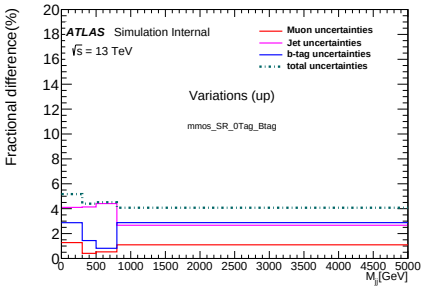


**(h)** $\mu\mu$ SR, $m_{jj}$, $-1\sigma$ variation

**Figure 6.2** Effect of experimental uncertainties in the $ee$ and $\mu\mu$ SRs on the top-quark process background $m_{\ell\ell jj}$ and $m_{jj}$ distributions, for the indicated region and discriminant. Contributions from each source are treated as uncorrelated. '$b$-tagging uncertainties' refers to jet flavour identification uncertainties. Taken from [172].

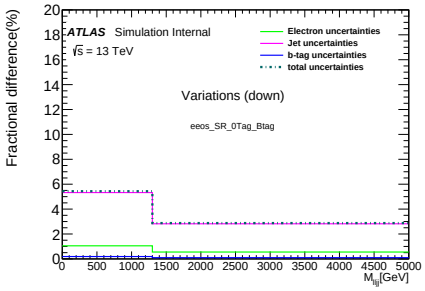


**(a)** $ee$ SR, $m_{\ell\ell jj}$, $-1\sigma$ variation

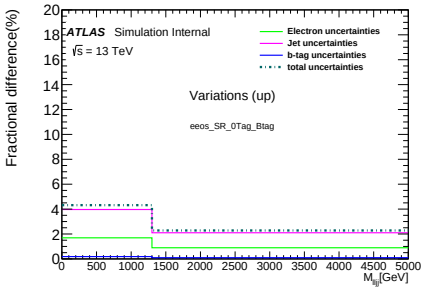


**(b)** $ee$ SR, $m_{\ell\ell jj}$, $+1\sigma$ variation

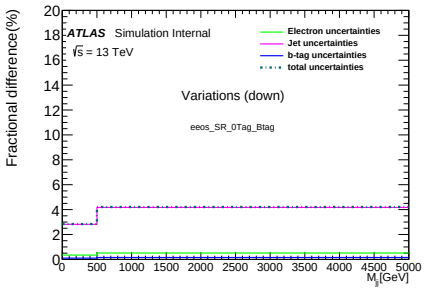


**(c)** $ee$ SR, $m_{jj}$, $-1\sigma$ variation

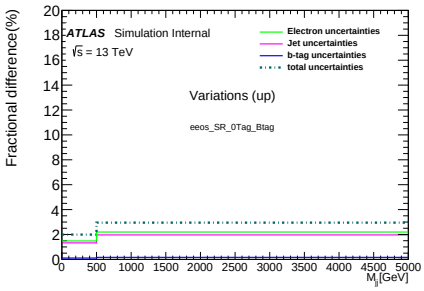


**(d)** $ee$ SR, $m_{jj}$, $+1\sigma$ variation

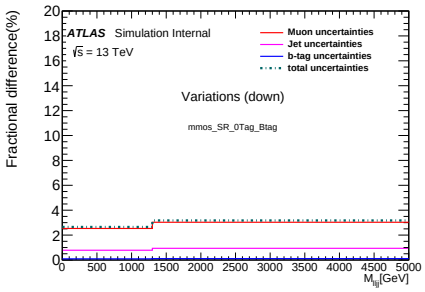


**(e)** $\mu\mu$ SR, $m_{\ell\ell jj}$, $-1\sigma$ variation

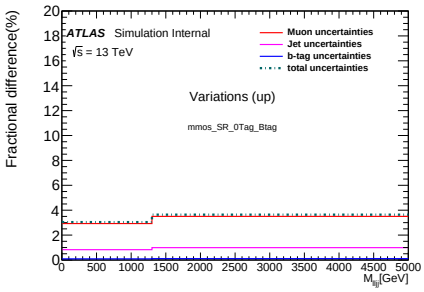


**(f)** $\mu\mu$ SR, $m_{\ell\ell jj}$, $+1\sigma$ variation

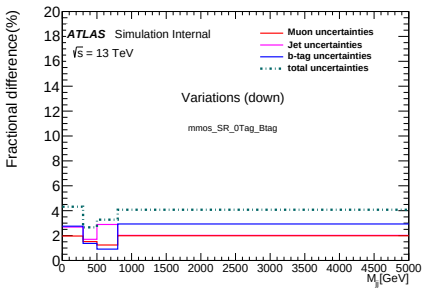


**(g)** $\mu\mu$ SR, $m_{jj}$, $-1\sigma$ variation

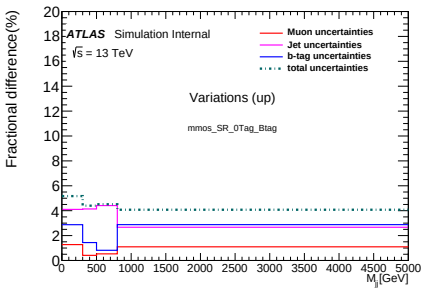


**(h)** $\mu\mu$ SR, $m_{jj}$, $+1\sigma$ variation

**Figure 6.3** Effect of experimental uncertainties in the $ee$ and $\mu\mu$ SRs on the combined $W$+jets and diboson background $m_{\ell\ell jj}$ and $m_{jj}$ distributions, for the indicated region and discriminant. Contributions from each source are treated as uncorrelated. '$b$-tagging uncertainties' refers to jet flavour identification uncertainties. Taken from [172].

2.0, and taking the envelope of these variations as the uncertainty. The value of strong coupling constant, $\alpha_S$, was also varied to half and twice the nominal value. The variations were performed using SysCalc [181], which provides event weights so the existing generator level datasets could be reweighted and the change to the signal yield in the signal region could be studied. The result of this procedure is shown in Figure 6.4. The $\alpha_S$ scale variation has no effect because, at LO hard process generation level, the Keung-Senjanović process only includes weak vertices. The $\mu_R$ variation also has no effect because it serves to vary the energy scale of $\alpha_S$. The uncertainty is dominated by the variation in factorisation scale, which changes the energy scale of the PDF used by the MC generator. A conservative uncertainty of $\pm 10\%$ yield variation was used in the fit, to include the envelope of the considered uncertainties.

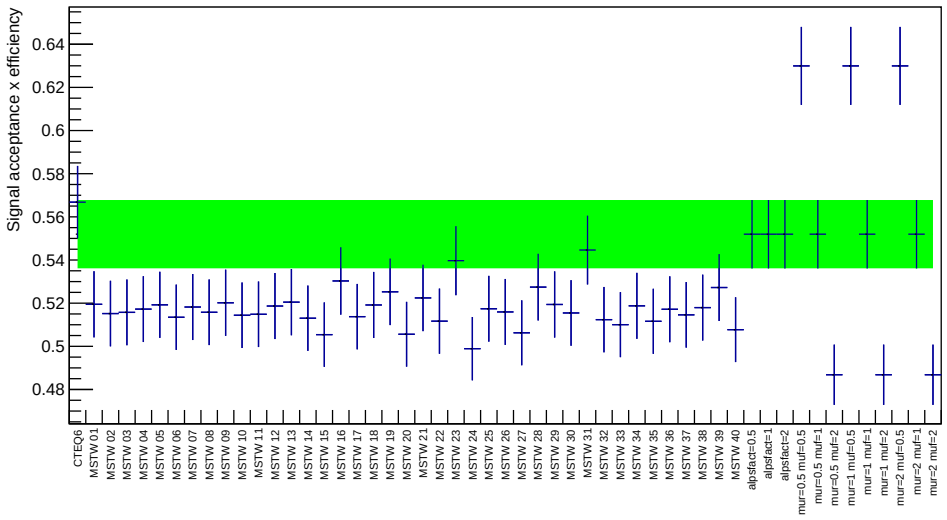


**Figure 6.4** Variation of the product of the signal acceptance and selection efficiency for an example signal mass hypothesis ($m_{W_R} = 4.2\,\text{TeV}$, $m_{N_R} = 2.1\,\text{TeV}$) with the generated event weight varied corresponding to the named theoretical uncertainties. CTEQ6 and MSTWxx variations refer to different PDF choices; 'alps', 'mur', and 'muf' variations refer to the $\alpha_S$ emission scale factor, and the renormalisation and factorisation scales ($\mu_R$ and $\mu_F$), respectively. The green band indicates the nominal weight (uncertainties arising from statistical uncertainty in a 2000 event test sample). Taken from [172].

The theory uncertainties included for the $Z+\text{jets}$ background processes include the choice of QCD scale variations (varied as described above), choice of the PDF set, the value used for $\alpha_S$, and the PDF uncertainty. The PDF uncertainty covers experimental uncertainties entering the datasets used in the PDF fits and the uncertainty on the functional form used in the PDF fits, and was estimated using the envelope of the NNPDF3.0 PDF set, as recommended in [182]. The MMHT2014 [183] and CT14NNLO [184] PDF sets were used to

generate alternative $Z+$jets MC in order to estimate the uncertainty due to the choice of PDF. The uncertainty due to the value of $\alpha_S$ was evaluated by varying the nominal value used when generating the MC of 0.118 (at $m_Z$) by $\pm 0.001$. The largest theory uncertainty generally originates from the QCD scale variations, and is between 20% and 40%, depending on the simulated process and the invariant mass of the $\ell\ell jj$ system (and similar for the $m_{jj}$ distribution). The effect of QCD scale variation on the $m_{\ell\ell jj}$ distribution in signal regions for the $Z+$jets background is shown in Figure 6.5.

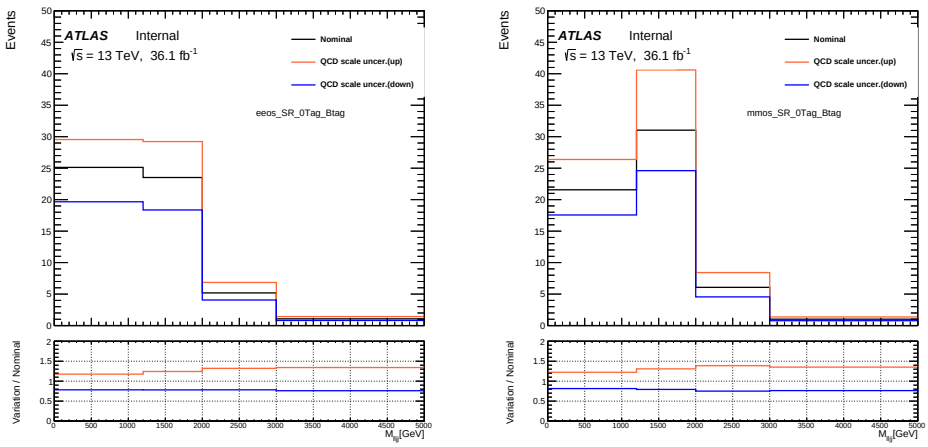


**(a)** $ee$ SR **(b)** $\mu\mu$ SR

**Figure 6.5** Effect of QCD scale variation in the $ee$ and $\mu\mu$ SRs on the $Z+$jets background $m_{\ell\ell jj}$ distribution, for the indicated region. Taken from [172].

The uncertainty arising from the $m_{jj}$ reweighting procedure (see Section 5.3) is derived by comparing the reweighted background with the data in the combined $ee$ and $\mu\mu$ VR, and then taking their difference as the systematic uncertainty. The shape difference between data and background in the combined $ee$ and $\mu\mu$ VR, and the resultant uncertainty is shown in Figure 6.6 for the $m_{jj}$ discriminant. The same process is used for the $m_{\ell\ell jj}$ discriminant. The uncertainty by varying parameters of reweighting function is considered to be covered by statistical error, thus not included separately. The reweighting is only applied to the $Z+$jets MC, so the uncertainty is also only assessed for this process.

Theory uncertainties were also evaluated for the $t\bar{t}$ process. An uncertainty relating to the generation of the hard process was evaluated by comparing alternative samples generated with the Powheg-Box and MadGraph5_aMC@NLO generators, both interfaced to Pythia 8 for parton showering, as recommended in [182]. An uncertainty due to the hadronisation model used when generating

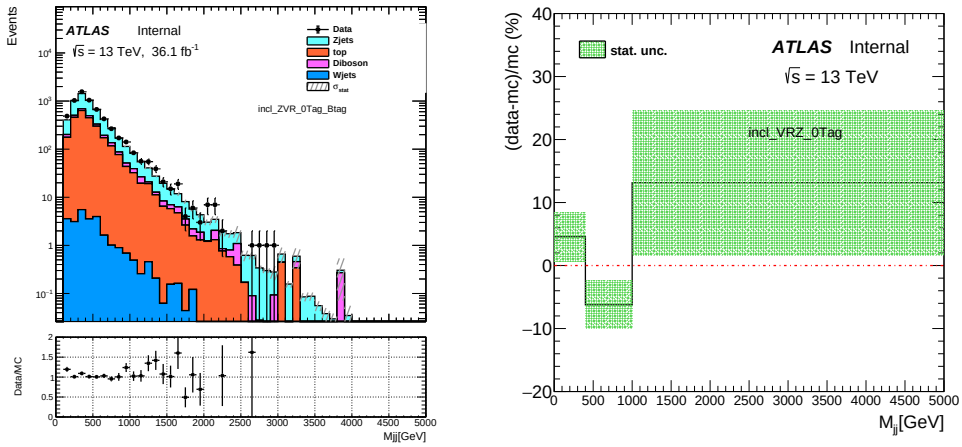


**(a)** **(b)**

**Figure 6.6** (a): The data and $m_{jj}$ reweighted background $m_{jj}$ distribution in the combined $ee$ and $\mu\mu$ VR (see Section 5.3), and (b): the difference in shape between data and reweighted background the combined $ee$ and $\mu\mu$ VR, used as the $m_{jj}$ reweighting uncertainty. Taken from [172].

the MC was evaluated by comparing the nominal Powheg-Box and Pythia 8 generated sample with the one generated by Powheg-Box and Herwig 7 [185]. An uncertainty related to the amount of initial- and final-state radiation was assessed by varying parton shower-related settings, including those relating to $\mu_{\mathrm{R}}$ and $\mu_{\mathrm{F}}$. Figure 6.7 shows the effect of all considered $t\bar{t}$ theory uncertainties on the top-quark background. Theory uncertainties for other top-quark processes were not included, due to their small contributions (less than 5% in the SRs) to the background compared to the $t\bar{t}$ process. Theory uncertainties on the diboson and $W+$jets processes are also not included due to the small contribution of these processes to the total background yield (see Section 5.3).

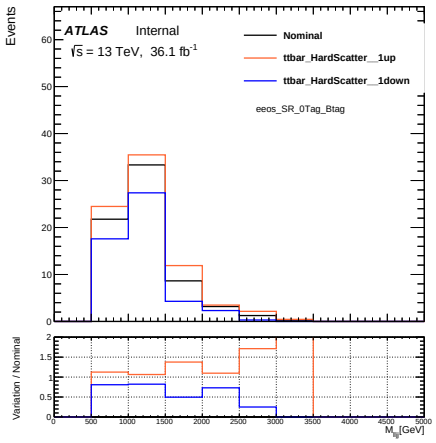


**(a)** *ee* SR, hard process

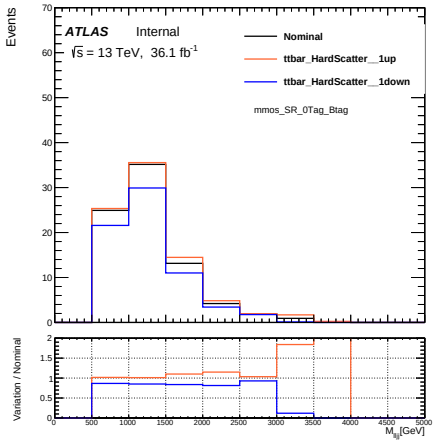


**(b)** $\mu\mu$ SR, hard process

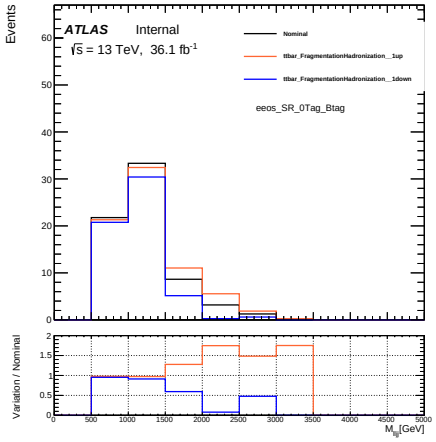


**(c)** *ee* SR, hadronisation

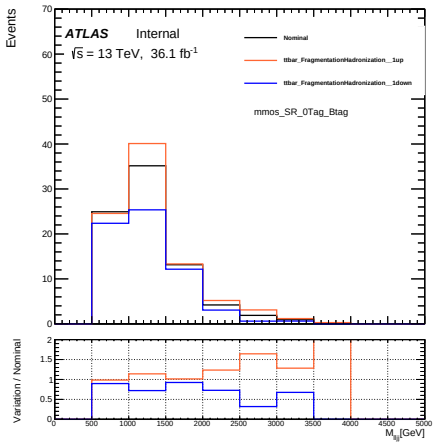


**(d)** $\mu\mu$ SR, hadronisation

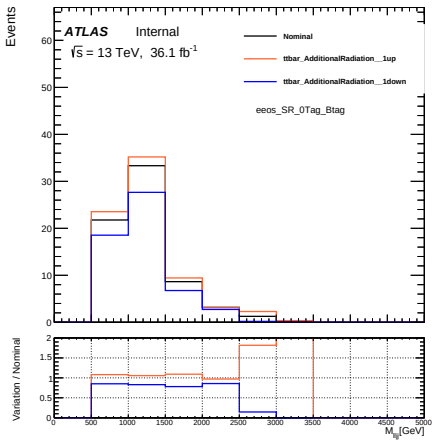


**(e)** *ee* SR, ISR/FSR

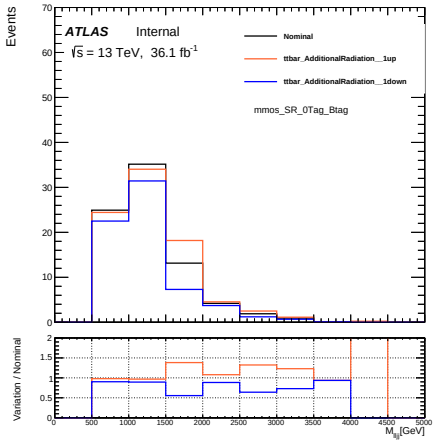


**(f)** $\mu\mu$ SR, ISR/FSR

**Figure 6.7** Effect of $t\bar{t}$ theory uncertainties in the *ee* and $\mu\mu$ SRs on the top-quark background $m_{\ell\ell jj}$ distribution, for the indicated region and theory variation. Orange indicates the $+1\sigma$ variation, blue indicates the $-1\sigma$ variation. Taken from [172].

### 6.1.3 Background-only fits

In order to perform a check for significant data-deviations from the background prediction (see Section 6.2), a pair of background-only fits (one for each of the $m_{\ell\ell jj}$ and $m_{jj}$ discriminants) were performed, with the constraint that $\mu_S = 0$. Neither of the $ee$ and $\mu\mu$ SRs were included in the fits, however the post-fit distributions in the SRs were produced, using the values of the fit parameters found during the fit. The SRs were not included so as not to assume the absence of a signal. The VRs are also not included in the fits, but the post-fit values of the likelihood function parameters were applied in the VRs in order to observe the fit performance. The resultant yields in the analysis regions from these background-only fits are given in Figure 6.8, and a breakdown of the sources of uncertainty on the post-fit background yields in each analysis region can be found in Figure 6.9. Pre- and post-fit distributions in the analysis regions are shown in Figures 6.10–6.15, with the exception of the single-bin $ee$ and $\mu\mu$ CRs. The lack of significant deivations in the data from the post-fit background prediction in the SRs (as determined in Section 6.2) indicates that the data is consistent with the background hypotheses.

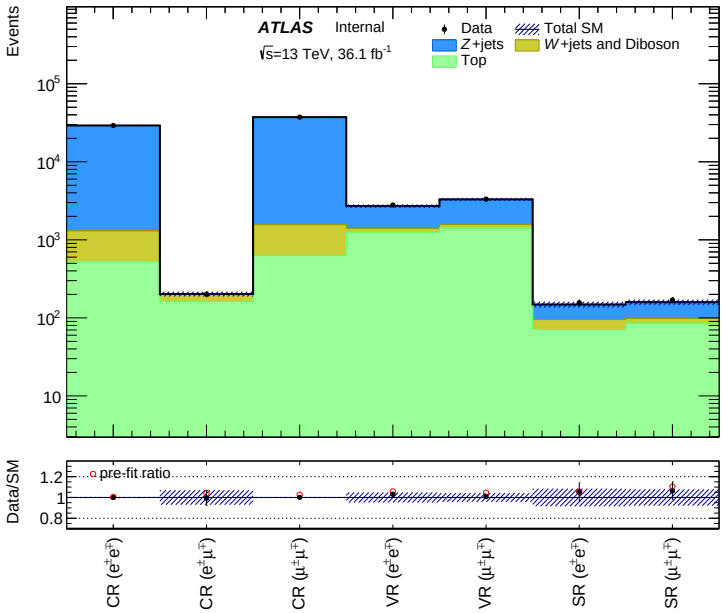


**(a)** $m_{\ell\ell jj}$ background-only fit

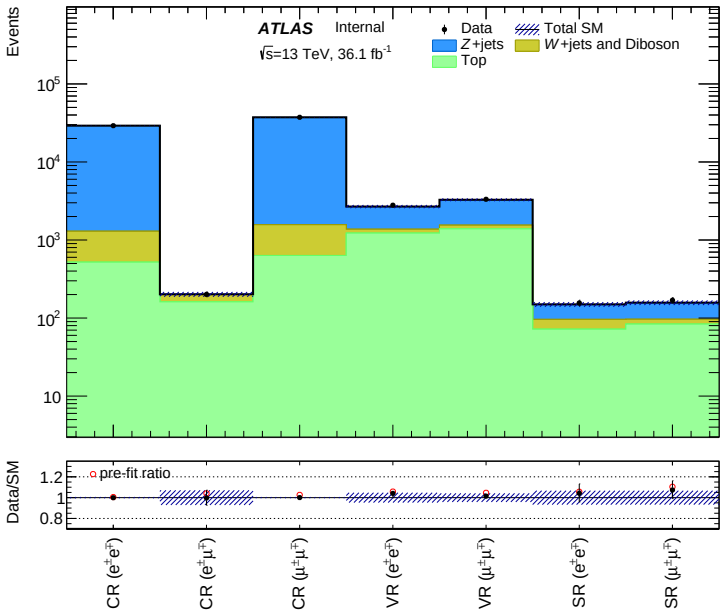


**(b)** $m_{jj}$ background-only fit

**Figure 6.8** Pre- and post-fit $m_{\ell\ell jj}$ or $m_{jj}$ background-only fit yields in all analysis regions. Events with $m_{\ell\ell jj}$ ($m_{jj}$) $< 9\,\text{TeV}$ are included for the $m_{\ell\ell jj}$ ($m_{jj}$) fit (no data events are seen above this value). The pre-fit ratios are the same in both plots because the same selections are applied for both discriminants.

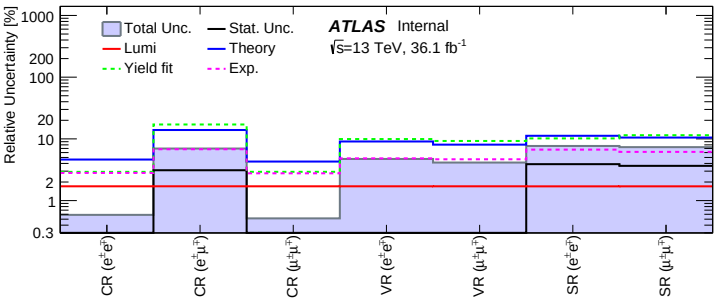


**(a)** $m_{\ell\ell jj}$ background-only fit

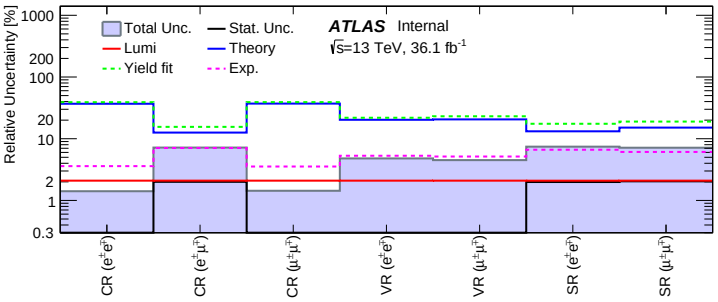


**(b)** $m_{jj}$ background-only fit

**Figure 6.9** Relative uncertainties on the total background yield estimation in each analysis region after the $m_{\ell\ell jj}$ and $m_{jj}$ background-only fits. "Yield fit" corresponds to the uncertainty from the background normalisation from the fit. "Luminosity" corresponds to the luminosity uncertainty. "Theory" and "Exp." indicate respectively the total theoretical and experimental uncertainties. These sources of uncertainty are described in more detail in Section 6.1.2. They are calculated individually by shifting in turn only one nuisance parameter from the post-fit value by one standard deviation, keeping all the other parameters at their post-fit values, and comparing the resulting event yield to the nominal yield. Due to correlations among uncertainties after the fit, the individual components do not necessarily add in quadrature to the total uncertainty, indicated by "Total Unc.".

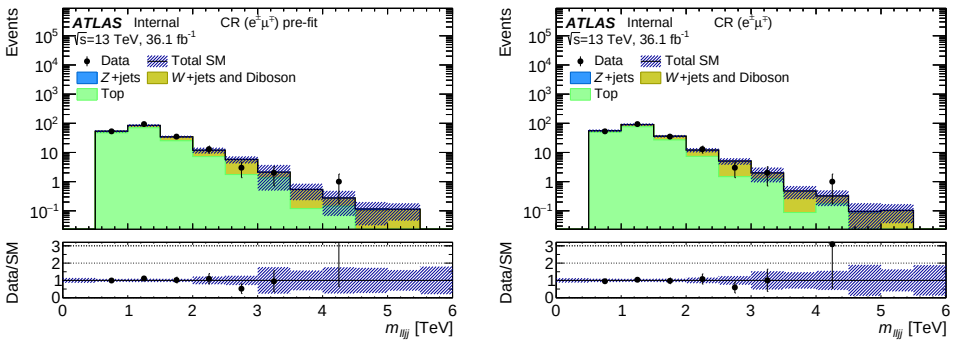


**(a)** pre-fit **(b)** post-fit

**Figure 6.10** Pre- and post-fit $m_{\ell\ell jj}$ distributions in the $e\mu$ control region for the $m_{\ell\ell jj}$ background-only fit.

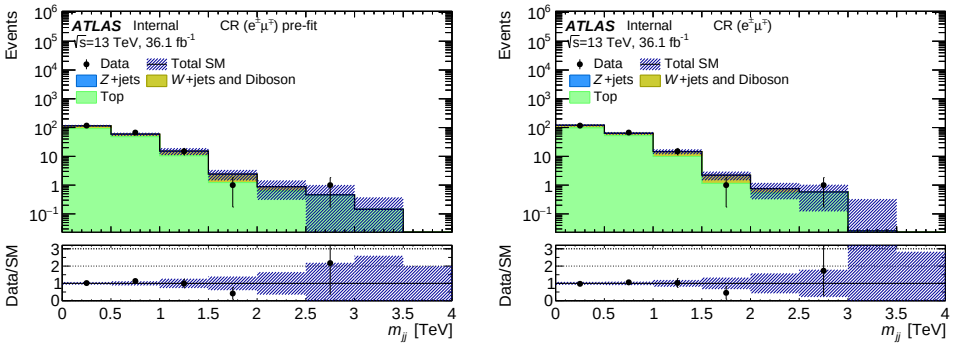


**(a)** pre-fit **(b)** post-fit

**Figure 6.11** Pre- and post-fit $m_{jj}$ distributions in the $e\mu$ control region for the $m_{jj}$ background-only fit.

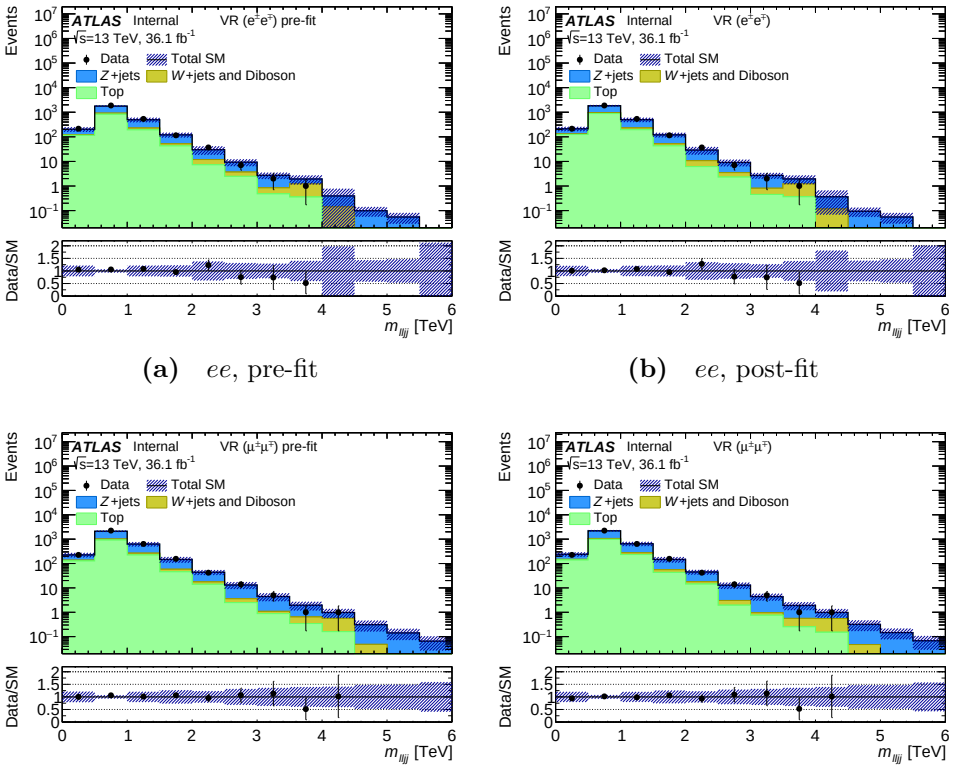


**(a)** $ee$, pre-fit **(b)** $ee$, post-fit

**(c)** $\mu\mu$, pre-fit **(d)** $\mu\mu$, post-fit

**Figure 6.12** Pre- and post-fit $m_{\ell\ell jj}$ distributions in the $ee$ and $\mu\mu$ validation regions for the $m_{\ell\ell jj}$ background-only fit.

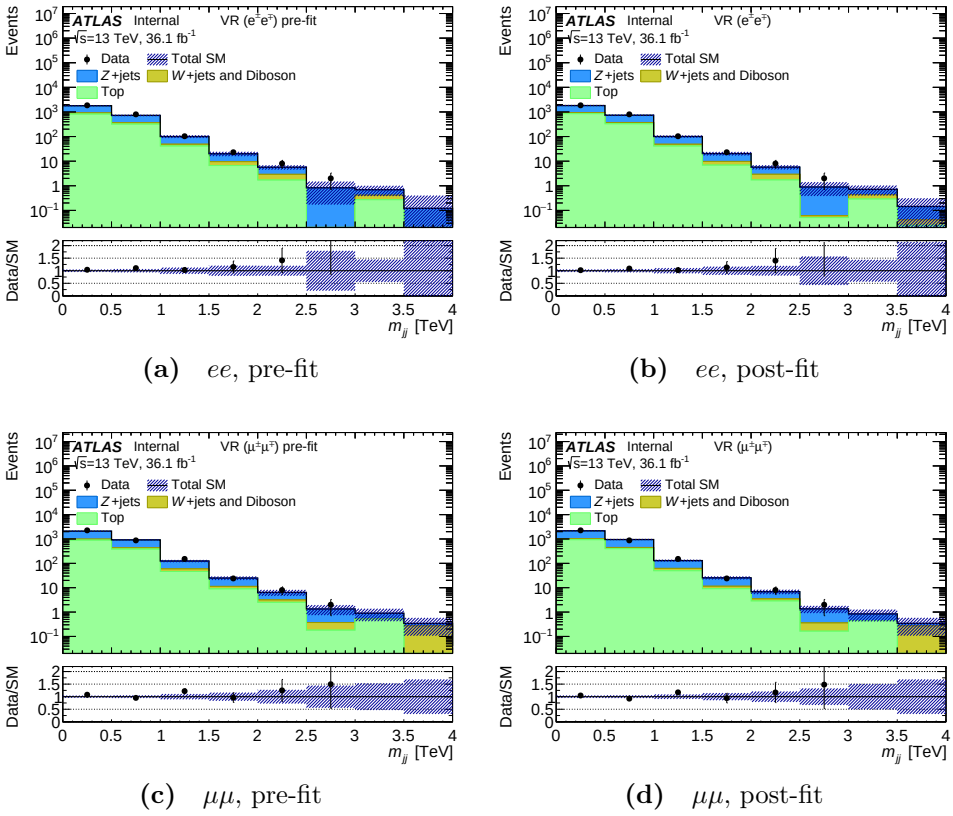


**(a)** $ee$, pre-fit **(b)** $ee$, post-fit

**(c)** $\mu\mu$, pre-fit **(d)** $\mu\mu$, post-fit

**Figure 6.13** Pre- and post-fit $m_{jj}$ distributions in the $ee$ and $\mu\mu$ validation regions for the $m_{jj}$ background-only fit.

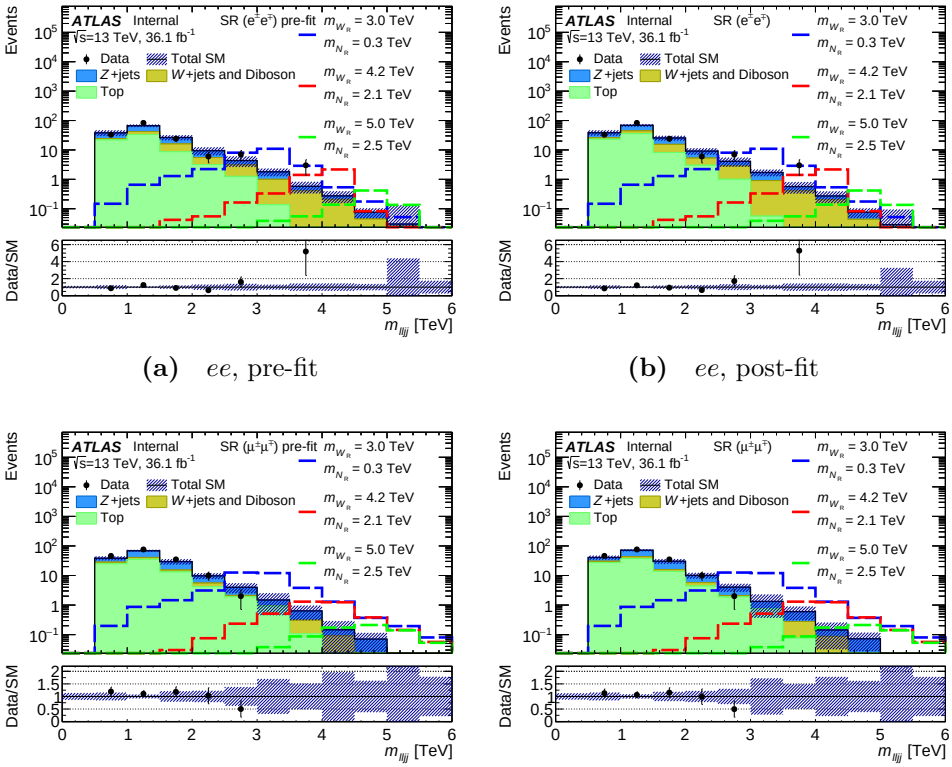


**(a)** $ee$, pre-fit **(b)** $ee$, post-fit

**(c)** $\mu\mu$, pre-fit **(d)** $\mu\mu$, post-fit

**Figure 6.14** Pre- and post-fit $m_{\ell\ell jj}$ distributions in the $ee$ and $\mu\mu$ signal regions for the $m_{\ell\ell jj}$ background-only fit. Post-fit values of the fit parameters were extrapolated to the SRs to make these plots, which were not included in the fit. Predicted signal distributions for several mass hypotheses are overlaid for illustrative purposes, and were not input to the fit.

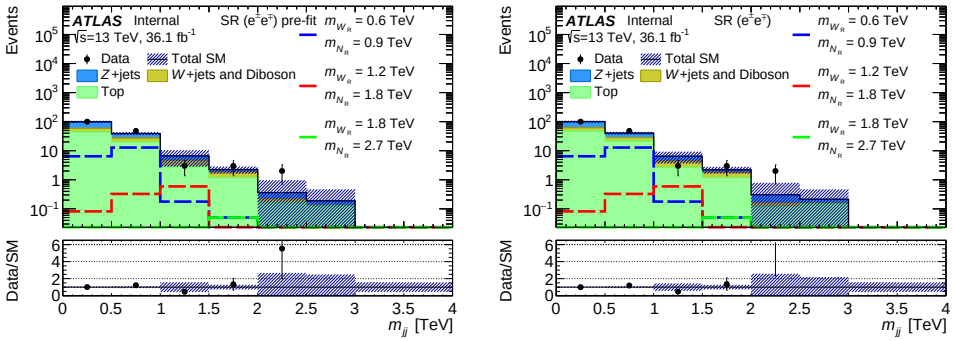


**(a)** $ee$, pre-fit




**(b)** $ee$, post-fit

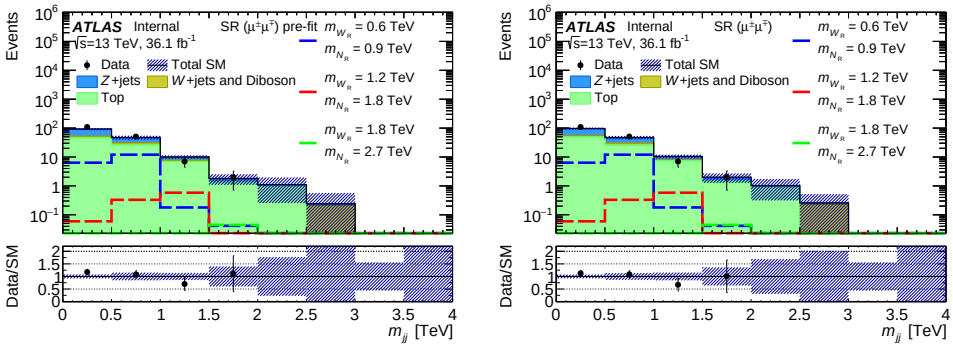


**(c)** $\mu\mu$, pre-fit




**(d)** $\mu\mu$, post-fit

**Figure 6.15** Pre- and post-fit $m_{jj}$ distributions in the $ee$ and $\mu\mu$ signal regions for the $m_{jj}$ background-only fit. Post-fit values of the fit parameters were extrapolated to the SRs to make these plots, which were not included in the fit. Predicted signal distributions for several mass hypotheses are overlaid for illustrative purposes, and were not input to the fit.

### 6.1.4 Signal fits

Fits with $\mu_{\mathrm{S}}$ unconstrained are utilised in order to exclude $m_{W_R}$–$m_{N_R}$ hypotheses and set upper limits on the Keung-Senjanović process $\sigma \times B$ to $eejj$ or $\mu\mu jj$ (see Section 6.3). As $N_e$ and $N_\mu$ are not theoretically constrained to have the same mass, two different fit channels are defined, one targeted at $N_e$ (the $ee$ channel) and one at $N_\mu$ (the $\mu\mu$ channel). The $ee$ ($\mu\mu$) signal region is only included in the $ee$ ($\mu\mu$) channel fit. In the $ee$ ($\mu\mu$) channel fit, no signal prediction is included in the $\mu\mu$ ($ee$) control region, as doing so would assume identical masses for $N_e$ and $N_\mu$. No signal prediction is included in the $e\mu$ CR, as events within our signal samples that enter into this region are from $N_\tau$ events, which we do not target in this analysis, and including them would also assume the equivalence of the $N_\tau$ mass with the $N_e$ or $N_\mu$ mass. Electron (muon) systematic uncertainties are considered only in the in $ee$ ($\mu\mu$) control, signal and validation regions, whilst both electron and muon systematic uncertainties are considered in the $e\mu$ control region. The VRs are not included in the fits, but the post-fit values of the likelihood function parameters were applied in the VRs in order to observe the fit performance. Pre- and post-fit yields for two example likelihood fits (for the $m_{W_R} = 4.2\,\mathrm{TeV}$, $m_{N_R} = 1.05\,\mathrm{TeV}$ and $m_{W_R} = 600\,\mathrm{GeV}$, $m_{N_R} = 700\,\mathrm{GeV}$ hypotheses) are shown in Figures 6.16 and 6.17. Pre- and post-fit distributions in the analysis regions are shown in Figures 6.18–6.23, with the exception of the single-bin $ee$ and $\mu\mu$ CRs.

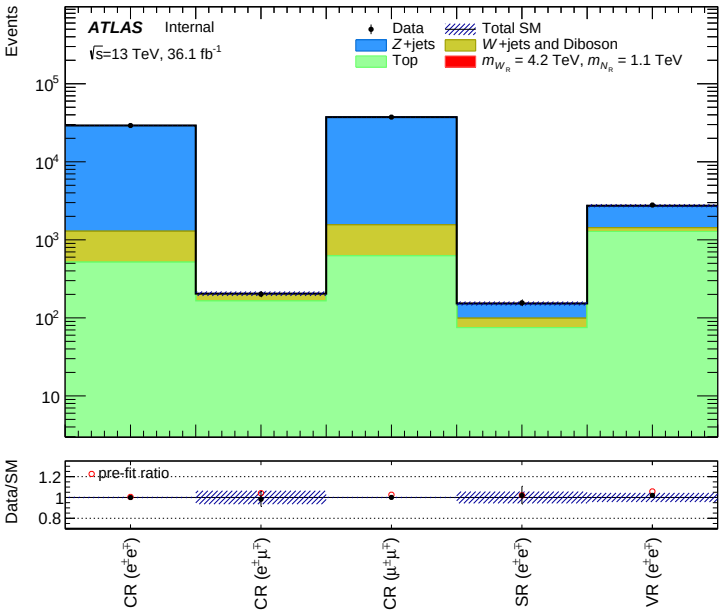


**(a)** $ee$ signal fit

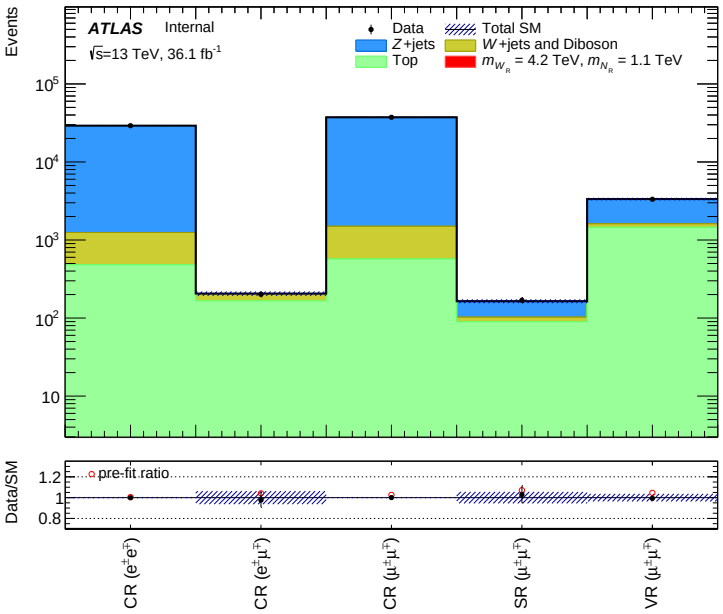


**(b)** $\mu\mu$ signal fit

**Figure 6.16** Pre- and post-fit yields in all analysis regions for the $ee$ channel fit or $\mu\mu$ channel fit, as indicated, for the $m_{W_R} = 4.2\,\text{TeV}$, $m_{N_R} = 1.05\,\text{TeV}$ hypothesis. Events with $m_{\ell\ell jj} < 9\,\text{TeV}$ are included (no data events are seen above this value).

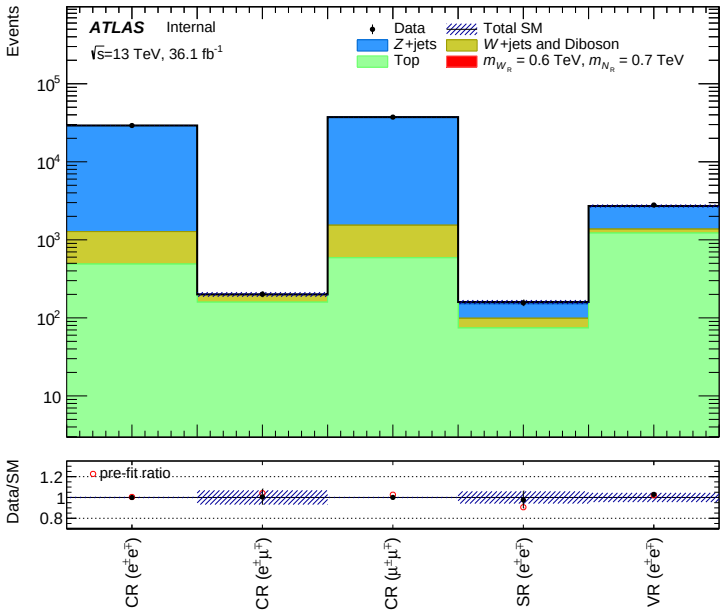


**(a)** $ee$ signal fit

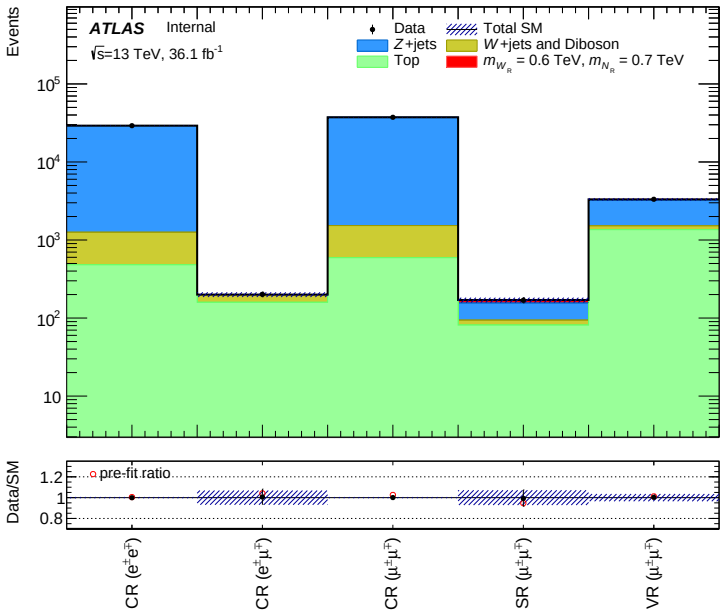


**(b)** $\mu\mu$ signal fit

**Figure 6.17** Pre- and post-fit yields in all analysis regions for the $ee$ channel fit or $\mu\mu$ channel fit, as indicated, for the $m_{W_R} = 600\,\text{GeV}$, $m_{N_R} = 700\,\text{GeV}$ hypothesis. Events with $m_{jj} < 9\,\text{TeV}$ are included (no data events are seen above this value).

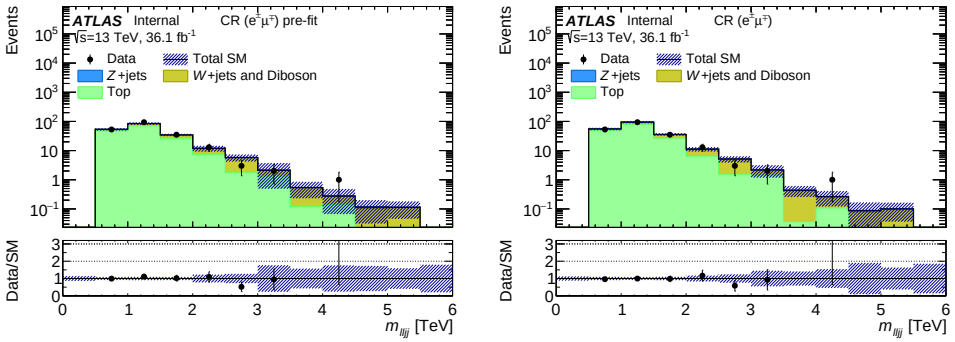


**(a)** $ee$, pre-fit




**(b)** $ee$, post-fit

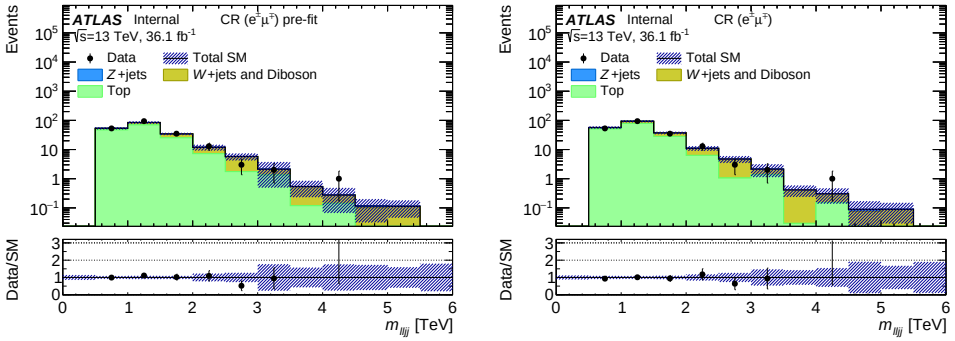


**(c)** $\mu\mu$, pre-fit




**(d)** $\mu\mu$, post-fit

**Figure 6.18** Pre- and post-fit $m_{\ell\ell jj}$ distributions in the $e\mu$ control region for the $ee$ channel fit or $\mu\mu$ channel fit, as indicated, for the $m_{W_R} = 4.2\,\text{TeV}$, $m_{N_R} = 1.05\,\text{TeV}$ hypothesis.

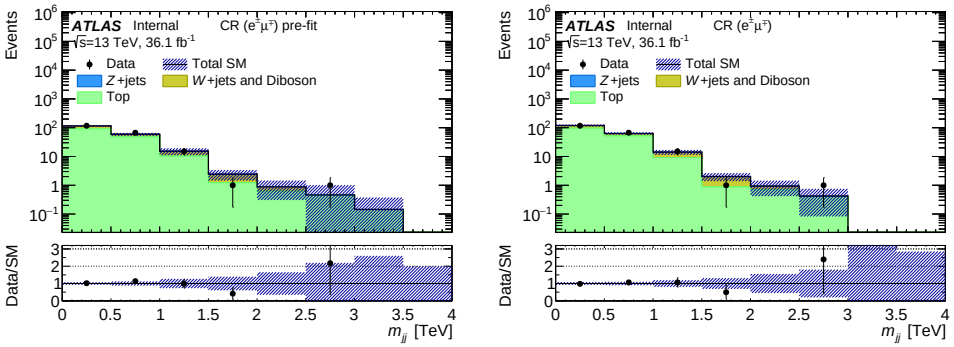


**(a)** $ee$, pre-fit **(b)** $ee$, post-fit

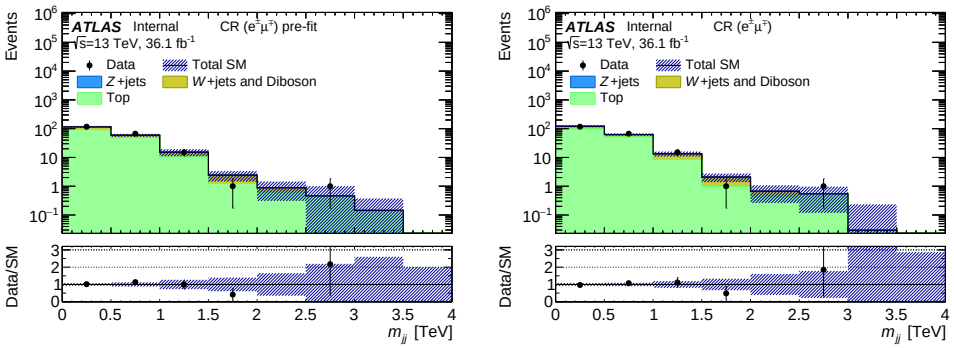


**(c)** $\mu\mu$, pre-fit **(d)** $\mu\mu$, post-fit

**Figure 6.19** Pre- and post-fit $m_{jj}$ distributions in the $e\mu$ control region for the $ee$ channel fit or $\mu\mu$ channel fit, as indicated, for the $m_{W_R} = 600\,\text{GeV}$, $m_{N_R} = 700\,\text{GeV}$ hypothesis.

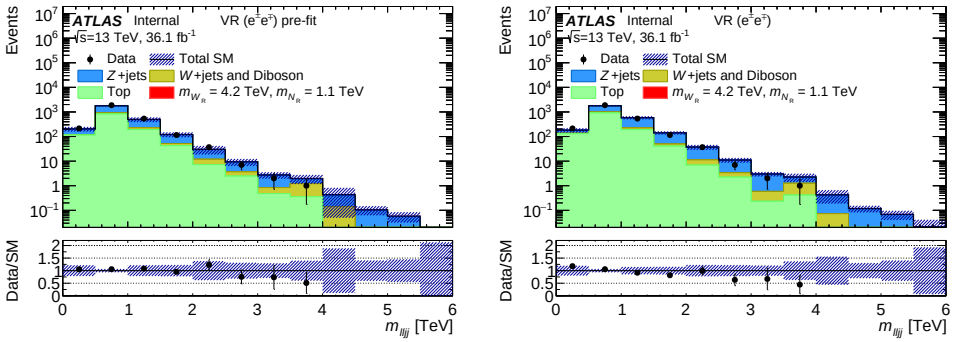


**(a)** $ee$, pre-fit




**(b)** $ee$, post-fit

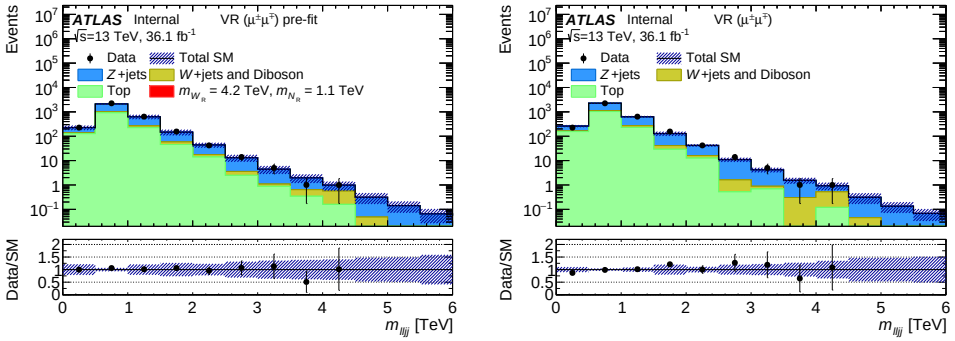


**(c)** $\mu\mu$, pre-fit




**(d)** $\mu\mu$, post-fit

**Figure 6.20** Pre- and post-fit $m_{\ell\ell jj}$ distributions in the $ee$ and $\mu\mu$ validation regions for the $ee$ channel fit ($ee$ VR) or $\mu\mu$ channel fit ($\mu\mu$ VR), as indicated, for the $m_{W_R} = 4.2\,\text{TeV}$, $m_{N_R} = 1.05\,\text{TeV}$ hypothesis.

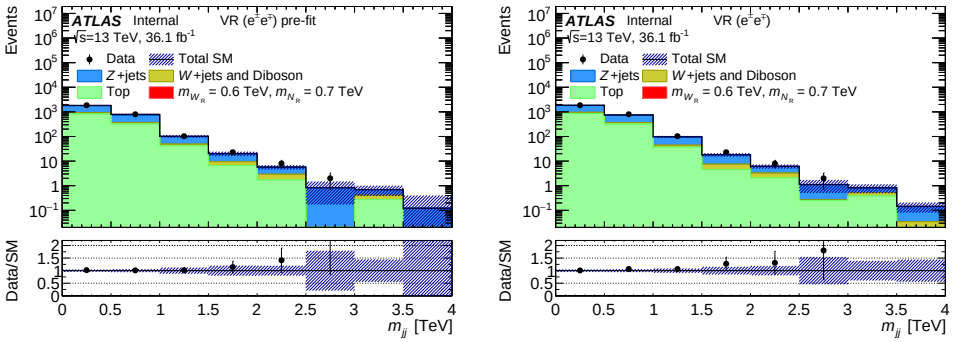


**(a)** $ee$, pre-fit **(b)** $ee$, post-fit

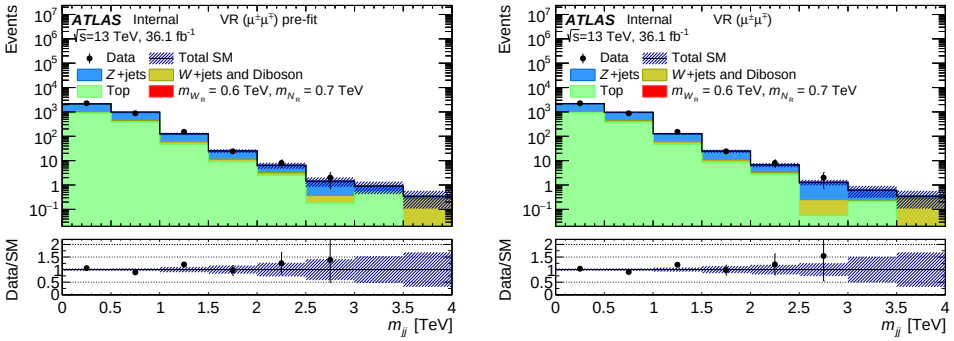


**(c)** $\mu\mu$, pre-fit **(d)** $\mu\mu$, post-fit

**Figure 6.21** Pre- and post-fit $m_{jj}$ distributions in the $ee$ and $\mu\mu$ validation regions for the $ee$ channel fit ($ee$ VR) or $\mu\mu$ channel fit ($\mu\mu$ VR), as indicated, for the $m_{W_R} = 600\,\text{GeV}$, $m_{N_R} = 700\,\text{GeV}$ hypothesis.

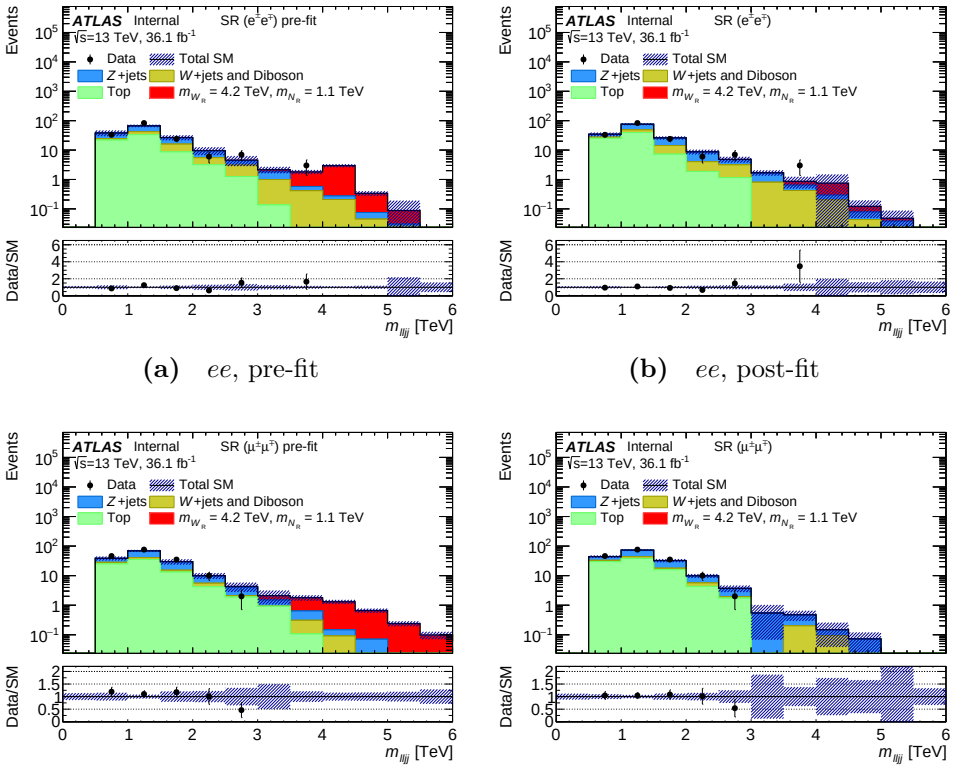


**(a)** $ee$, pre-fit **(b)** $ee$, post-fit

**(c)** $\mu\mu$, pre-fit **(d)** $\mu\mu$, post-fit

**Figure 6.22** Pre- and post-fit $m_{\ell\ell jj}$ distributions in the $ee$ and $\mu\mu$ signal regions for the $ee$ channel fit ($ee$ SR) or $\mu\mu$ channel fit ($\mu\mu$ SR), as indicated, for the $m_{W_R} = 4.2\,\text{TeV}$, $m_{N_R} = 1.05\,\text{TeV}$ hypothesis.

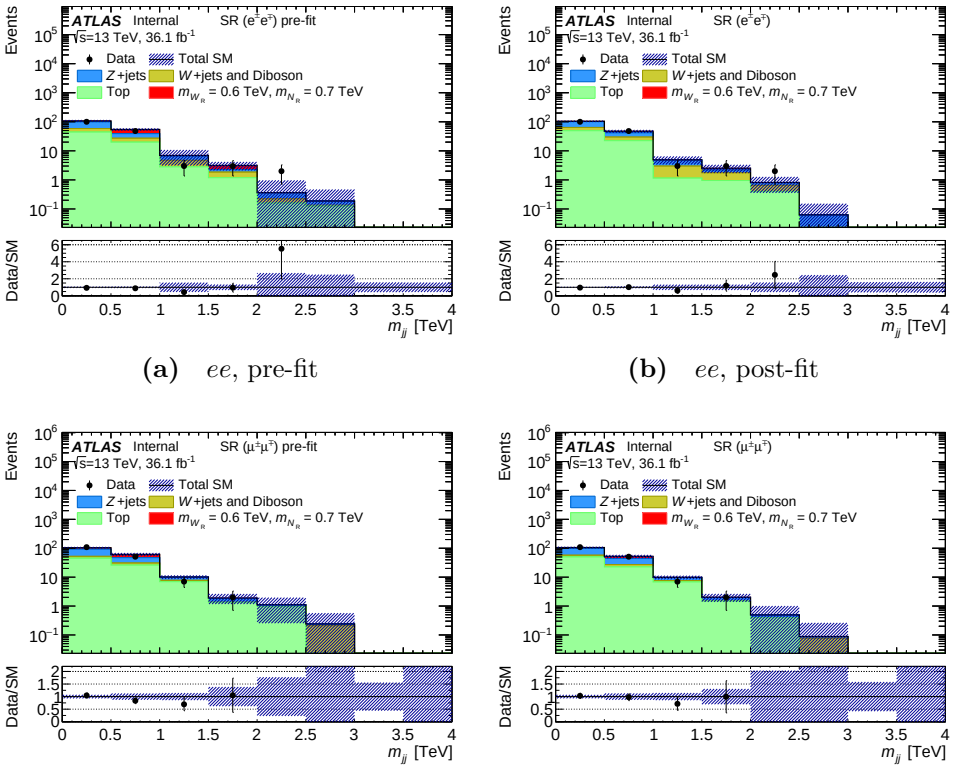


**(a)** $ee$, pre-fit **(b)** $ee$, post-fit

**(c)** $\mu\mu$, pre-fit **(d)** $\mu\mu$, post-fit

**Figure 6.23** Pre- and post-fit $m_{jj}$ distributions in the $ee$ and $\mu\mu$ signal regions for the $ee$ channel fit ($ee$ SR) or $\mu\mu$ channel fit ($\mu\mu$ SR), as indicated, for the $m_{W_R} = 600\,\text{GeV}$, $m_{N_R} = 700\,\text{GeV}$ hypothesis.

### 6.1.5 Combination with same-sign analysis

This section describes the statistical combination of the analysis described in this thesis with another ATLAS search for $W_R$ and $N_R$ participating in the Keung-Senjanović process, but focused on final states with same-sign leptons [2, 177]. I did not work on the same-sign analysis, but did contribute to the statistical combination strategy.

The two analyses were combined in such a way as to preserve their original, independent, fit setups, but with a single (joint) signal strength parameter. It was necessary to perform the fit in this way, due to the following differences in analysis strategy:

- A different overlap removal scheme was used compared to the opposite-sign analysis.
- Electron candidates were also required to have isolated calorimeter deposits, as well as isolated tracks (the 'Loose' criteria in [154]), whilst a different track isolation criteria (the 'FixedCutTightTrackOnly' criteria in [156]) is used for muon candidates.
- $E_{\mathrm{T}}$ and $p_{\mathrm{T}}$ thresholds of 30 GeV were used for electron and muon candidates.
- A different $b$-jet candidate identification algorithm configuration was used, with an identification efficiency of 77% (at the expense of lower background rejection power) [174].
- For some background process common to both the opposite-sign and same-sign analyses, different MC generators or generator versions were used.
- Different sets of NPs were used for some sources of uncertainty.

Separate same-sign signal, control and validation regions are used in the combined fit, as defined in Table 6.2, alongside the previously defined opposite-sign analysis regions. From this point onwards in this thesis, opposite-sign analysis regions names are modified to show the lepton charges (for example $ee$ SR becomes $e^{\pm}e^{\mp}$ SR). Separate nuisance parameters are used for all sources of uncertainty, and separate normalisation factors are also used for opposite-sign and same-sign backgrounds. The full set of opposite-sign and same-sign normalisation factors are summarised in Table 6.3. The same-sign diboson normalisation was constrained

using the two same-sign CRs, the $e^{\pm}e^{\pm}$ and $\mu^{\pm}\mu^{\pm}$ CRs. The same-sign $Z+$jets normalisation was determined using the $e^{\pm}e^{\pm}$ CR only, as the contribution in the $\mu^{\pm}\mu^{\pm}$ CR is negligible. For the same-sign regions, the $\sum E_{\mathrm{T}}$ (also referred to as $H_{\mathrm{T}}$) variable of the selected two charged leptons and two jets is used as the discriminant in the fit. Events with misidentified or non-prompt electrons and muons (collectively called 'fakes'), which form the largest contribution to the same-sign background (∼53% in the $e^{\pm}e^{\pm}$ SR and ∼60% in the $\mu^{\pm}\mu^{\pm}$ SR) [1], was assessed using a data-driven method (described in more detail in [2]) and therefore does not have a normalisation factor in the fit.

Like in the opposite-sign analysis, two fit channels are defined targeting $N_e$ and $N_\mu$. The $e^{\pm}e^{\pm}$ ($\mu^{\pm}\mu^{\pm}$) signal region is only included in the $ee$ ($\mu\mu$) channel fit, and no signal prediction is included in the $\mu^{\pm}\mu^{\pm}$ ($e^{\pm}e^{\pm}$) control region, as doing so would assume identical masses for $N_e$ and $N_\mu$.

| | Control regions | | Validation regions | | Signal regions | |
|---|---|---|---|---|---|---|
| Selection | $e^{\pm}e^{\pm}$ CR | $\mu^{\pm}\mu^{\pm}$ CR | $e^{\pm}e^{\pm}$ VR | $\mu^{\pm}\mu^{\pm}$ VR | $e^{\pm}e^{\pm}$ SR | $\mu^{\pm}\mu^{\pm}$ SR |
| $\ell\ell$ | $e^{\pm}e^{\pm}$ | $\mu^{\pm}\mu^{\pm}$ | $e^{\pm}e^{\pm}$ | $\mu^{\pm}\mu^{\pm}$ | $e^{\pm}e^{\pm}$ | $\mu^{\pm}\mu^{\pm}$ |
| $m_{\ell\ell}$ [GeV] | $[110, 300]$ | $[60, 300]$ | $[300, 400]$ | $[300, 400]$ | $> 400$ | $> 400$ |
| # of jets | $\geq 2$ | $\geq 2$ | $\geq 2$ | $\geq 2$ | $\geq 2$ | $\geq 2$ |
| jet $p_{\mathrm{T}}$ [GeV] | $> 50$ | $> 50$ | $> 50$ | $> 50$ | $> 100$ | $> 100$ |
| $m_{jj}$ [GeV] | — | — | — | — | $> 110$ | $> 110$ |
| $\sum E_{\mathrm{T}}$ [GeV] | — | — | — | — | $> 400$ | $> 400$ |

**Table 6.2** Summary of all regions defined in the same-sign analysis, indicating the event selection criteria used for a given region. Pairs of values $[X, Y]$ indicate the minimum and maximum values in GeV that $m_{\ell\ell}$ may take in the analysis region in question.

[1] The fake lepton yield was estimated in the opposite-sign analysis regions by the same-sign analysis team and found to be negligible [186].

| SM background yield | $e^{\pm}e^{\mp}$ CR | $e^{\pm}\mu^{\mp}$ CR | $\mu^{\pm}\mu^{\mp}$ CR | $e^{\pm}e^{\pm}$ CR | $\mu^{\pm}\mu^{\pm}$ CR |
|---|---|---|---|---|---|
| OS $Z$ + jets | ✓ | – | ✓ | – | – |
| SS $Z$ + jets | – | – | – | ✓ | – |
| OS top | – | ✓ | – | – | – |
| SS diboson | – | – | – | ✓ | ✓ |

**Table 6.3** Summary of the control regions used to fit the yields of the largest SM background predictions. Control regions used to fit a certain SM prediction yield are marked with a check-mark (✓) and control regions not used for this SM prediction are marked with a dash (–).

## 6.2 Check for significant deviations

Post-fit background distributions resultant from the opposite-sign background-only fits (see Section 6.1.3) were scanned using the BumpHunter [187, 188] algorithm in order to identify the most significant deviations of the data from the background predictions. Each of the four signal region distributions ($m_{\ell\ell jj}$ and $m_{jj}$ in the $e^{\pm}e^{\mp}$ and $\mu^{\pm}\mu^{\mp}$ SRs) were checked. Additionally, post-fit background distributions for the opposite-sign and same-sign SRs, produced by a background-only fit performed for the combination, were checked. As the only common parameter between the opposite-sign and same-sign regions in the combination, $\mu_{\mathrm{S}}$, is constrained to zero during background-only fits, the background-only opposite-sign post-fit distributions are the same when output from the combined fit as when output from the opposite-sign fit, and are therefore only presented once.

The BumpHunter algorithm scans through the bins of an input distribution using windows of sizes ranging from a single bin to the full set of bins, and compares the data yield in the window to the expected background yield. The number of data events observed in a window $w$ is denoted $n_w$, whilst the background prediction, under the background-only hypothesis B ($\mu_{\mathrm{S}} = 0$), in the window is denoted $B_w$. The BumpHunter algorithm calculates a p-value in each window: the probability that a number of events, $d$, which deviates from $B_w$ at least as much (or more) than $n_w$, would be observed. The probability of a deviation exceeding $n_w$, used if $n_w > B_w$, is given by:

$$p_w = P(d \geq n_w \,|\, \mathrm{B}) = \sum_{d=n_w}^{\infty} \mathcal{P}(d \,|\, B_w)$$

whilst if a deficit is observed, $n_w < B_w$, the $p$-value calculated is:

$$p_w = P(d < n_w \,|\, \mathrm{B}) = \sum_{d=0}^{n_w} \mathcal{P}(d \,|\, B_w)$$

Equivalently, $p_w$ can be written as a significance, from:

$$Z = \Phi^{-1}(1-p) = \sqrt{2}\,\mathrm{erf}^{-1}(1-2p)$$

where $\Phi^{-1}$ is the inverse cumulative distribution function, and erf is the error function:

$$\mathrm{erf}(x) = \frac{2}{\sqrt{\pi}} \int_0^x e^{-t^2}\, dt$$

The lowest $p_w$ found in the distribution is used to define the BumpHunter test statistic:

$$t = -\log p_w^{\min}$$

The observed BumpHunter test statistic $t_o$ is found for the real data and the background prediction from the background-only fit. The probability that a value of $t$ as high as (or higher than) the observed value $t_o$ could be found in a distribution compatible with the background-only hypothesis is found by generating pseudo-data distributions that are compatible with the background prediction (within the statistical uncertainty associated with each bin). The BumpHunter algorithm is then run on the set pseudo-data distributions, and the fraction that have $t \geq t_o$ is calculated. Only the statistical uncertainty on the background was taken into account when running the BumpHunter algorithm.

The results of these checks for significant deviations with BumpHunter are shown in Figure 6.24 for the opposite-sign SRs and Figure 6.25 for the same-sign SRs. The most significant local excess is observed in the $m_{\ell\ell jj}$ spectrum in the $e^{\pm}e^{\mp}$ SR, where a $\sim$2.05$\sigma$ local excess is observed between 3.5–4 TeV. The $p$-value of a deviation occurring in a distribution statistically compatible with the background prediction is 0.151, corresponding to a 1.03$\sigma$ effect. It cannot be rejected that the deviation could be caused by a fluctuation of the SM background, so the deviation is therefore not viewed as significant.

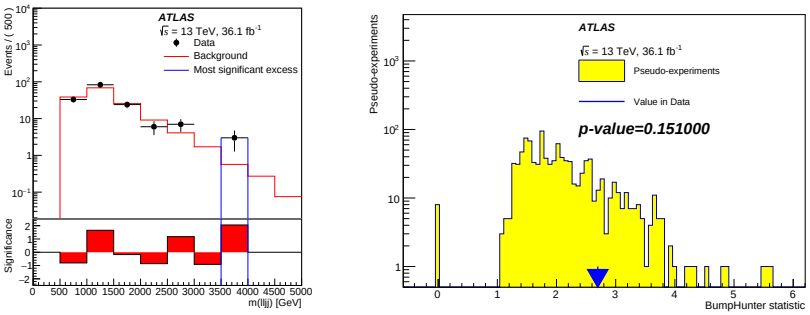


**(a)** $e^{\pm}e^{\mp}$ SR, $m_{\ell\ell jj}$

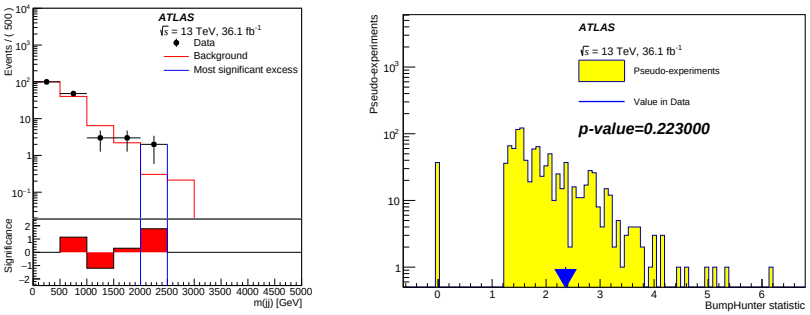


**(b)** $e^{\pm}e^{\mp}$ SR, $m_{jj}$

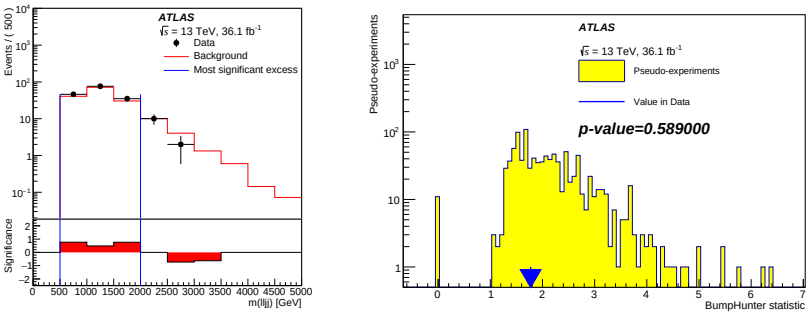


**(c)** $\mu^{\pm}\mu^{\mp}$ SR, $m_{\ell\ell jj}$

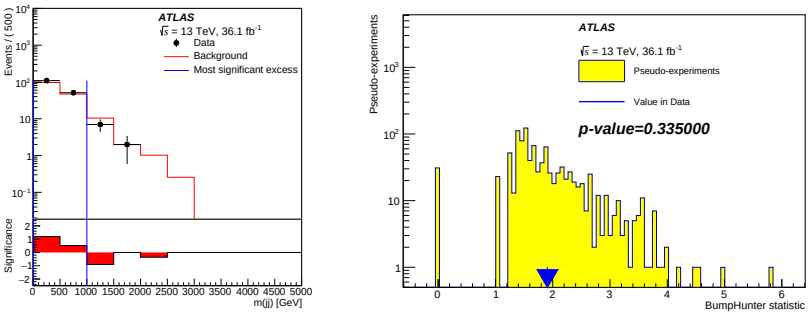


**(d)** $\mu^{\pm}\mu^{\mp}$ SR, $m_{jj}$

**Figure 6.24** Scans for significant deviations produced with BumpHunter (left); and the distributions of the BumpHunter test statistic $t$ from pseudo-data, the value $t_o$ observed in real data, and the $p$-value for that value of $t_o$ (right), for $m_{\ell\ell jj}$ or $m_{jj}$ distributions in the $e^{\pm}e^{\mp}$ and $\mu^{\pm}\mu^{\mp}$ SRs, as indicated.

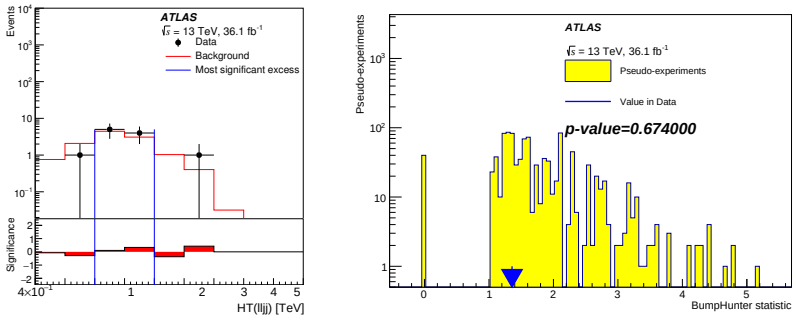


**(a)** $e^{\pm}e^{\pm}$ SR, $\sum E_{\mathrm{T}}$

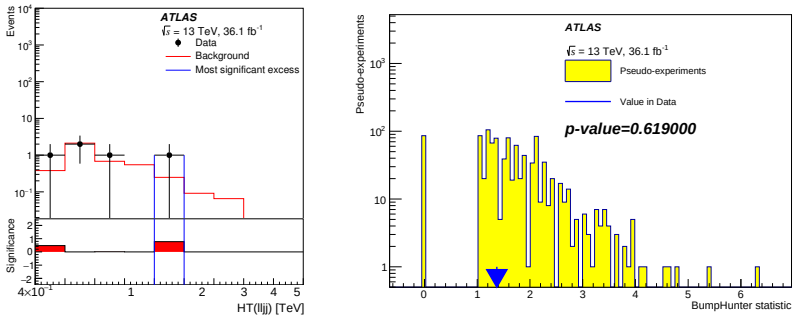


**(b)** $\mu^{\pm}\mu^{\pm}$ SR, $\sum E_{\mathrm{T}}$

**Figure 6.25** Scans for significant deviations produced with BumpHunter (left); and the distributions of the BumpHunter test statistic $t$ from pseudo-data, the value $t_o$ observed in real data, and the $p$-value for that value of $t_o$ (right), for the indicated region and distribution, for $\sum E_{\mathrm{T}}$ distributions in the $e^{\pm}e^{\pm}$ and $\mu^{\pm}\mu^{\pm}$ SRs, as indicated.

## 6.3 Limit setting procedure

The profile likelihood ratio test statistic, $q_\mu$, was used in order to discriminate between signal-like and background-like data distributions, defined as [189]:

$$q_\mu = -2\ln\left(\frac{\mathcal{L}(\mu_\mathrm{S}, \hat{\hat{\boldsymbol{\mu}}}_{\mathbf{B}\mu_\mathrm{S}}, \hat{\hat{\boldsymbol{\theta}}}_{\mu_\mathrm{S}})}{\mathcal{L}(\hat{\mu_\mathrm{S}}, \hat{\boldsymbol{\mu}}_{\mathbf{B}}, \hat{\boldsymbol{\theta}})}\right)$$

where the denominator of the fraction is the the so-called unconditional likelihood, where the likelihood function is maximised with $\mu_\mathrm{S}$, $\boldsymbol{\mu}_\mathbf{B}$ and $\boldsymbol{\theta}$ all allowed to vary, and the numerator is the so-called conditional likelihood, where the likelihood is maximised for a fixed value of $\mu_\mathrm{S}$. Higher values of $q_\mu$ corresponding to increasing disagreement between the chosen value of $\mu_\mathrm{S}$ and the data, whereas lower values of $q_\mu$ indicate better compatibility between data and the chosen value of $\mu_\mathrm{S}$.

The probability $p_{S+B}$ that a signal plus background (S+B) hypothesis (for example, $\mu_\mathrm{S} = 1$ for Majorana $N_R$ and $\mu_\mathrm{S} = 2$ for Dirac $N_R$ with the nominal Keung-Senjanović cross section) gives a test statistic above a reference value $q_\mu^\mathrm{ref}$, or the probability $p_B$ that a background-only hypothesis ($\mu_\mathrm{S} = 0$) gives a test statistic below $q_\mu^\mathrm{ref}$, are defined as [190]:

$$\begin{aligned} p_\mathrm{B} = P(q_\mu < q_\mu^\mathrm{ref} \,|\, \mathrm{B}) \quad &= \int_{-\infty}^{q_\mu^\mathrm{ref}} f(q_\mu \,|\, \mathrm{B})\, dq_\mu \quad \equiv 1 - \mathrm{CL_b} \\ p_\mathrm{S+B} = P(q_\mu > q_\mu^\mathrm{ref} \,|\, \mathrm{S+B}) &= \int_{q_\mu^\mathrm{ref}}^{\infty} f(q_\mu \,|\, \mathrm{S+B})\, dq_\mu \equiv \mathrm{CL_{s+b}} \end{aligned}$$

When calculating the observed limits from the real dataset, $q_\mu^\mathrm{ref}$ is the value of $q_\mu$ extracted from the fit to the observed data. For expected limits, $q_\mu^\mathrm{ref}$ is taken to be the median, $\pm 1\sigma$ and $\pm 2\sigma$ of $q_\mu$ extracted from a fit to a dataset that is generated to match the background prediction [189]. The probability density function (PDF) of the test statistic under a particular signal hypothesis, $f(q_\mu \,|\, \mathrm{hyp})$, is found using an asymptotic approximation [176, 189]. A value of $\mu_\mathrm{S}$ is said to be excluded at 95% CL (confidence level) if it fulfils the following requirement [190]:

$$\mathrm{CL_s} \equiv \frac{p_\mathrm{S+B}}{1 - p_\mathrm{B}} = \frac{\mathrm{CL_{s+b}}}{\mathrm{CL_b}} \leq 5\%$$

The upper limit on the value of $\mu_\mathrm{S}$ is the highest value of $\mu_\mathrm{S}$ that cannot be

excluded at 95% CL. To determine the upper limit on $\mu_S$ for each $m_{W_R}$–$m_{N_R}$ hypotheses, $CL_s$ values were calculated for a range of $\mu_S$ values, in order to obtain a distribution of $\mu_S$ vs. $CL_s$. An example of an upper limit scan is shown as Figure 6.26. These upper limits on $\mu_S$ were then converted to an upper limits on the $\sigma \times B$ to $eejj$ or $\mu\mu jj$ by multiplying each upper limit on $\mu_S$ by the $\sigma \times B$ to $eejj$ or $\mu\mu jj$ (for lepton pairs of any sign) of the signal mass hypothesis under consideration. When upper limits on $\sigma \times B$ are calculated for the Dirac hypothesis, the fact that $\mu_S$ represents the Majorana hypothesis signal strength is taken in account by the addition of a factor of a half.

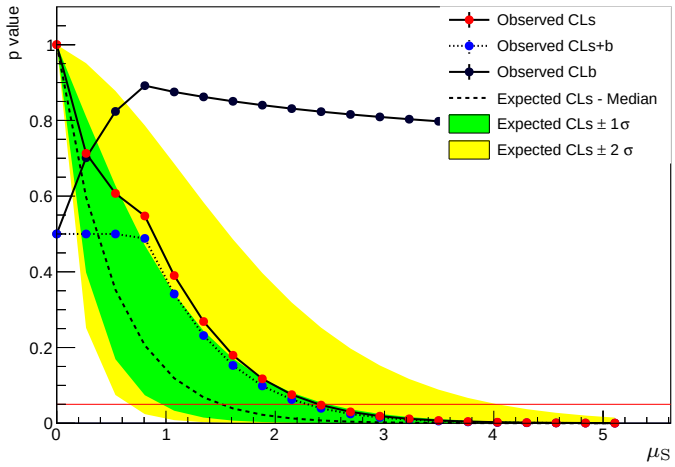


**Figure 6.26** Upper limit scan on $\mu_S$ for the $m_{W_R} = 3.8\,\text{TeV}$, $m_{N_R} = 3\,\text{TeV}$ hypothesis, opposite-sign analysis, $ee$ channel. The observed upper limit (where the observed $CL_s$ line falls below 0.05) is higher than the expected upper limit (where the expected $CL_s$ line falls below 0.05) due to the presence of $\sim 2.05\sigma$ local excess between 3.5–4 TeV (see Section 6.2).

The 95% CL excluded region of $m_{W_R}$–$m_{N_R}$ phase space is the area in which the upper limit on $\mu_S$ is less than 1 (for the Majorana $N_R$ case) or less than 2 (for the Dirac $N_R$ case). The extent of this area was found using SCIPY [191] to interpolate the upper limit on $\mu_S$ values throughout the $m_{W_R}$–$m_{N_R}$ space using a sum of multiquadric radial basis functions [192, 193] with weights $w_i$:

$$y(\boldsymbol{x}) = \sum_{i=1}^{N} w_i \phi(||\boldsymbol{x} - \boldsymbol{x_i}||) \quad \text{where} \quad \phi(||\boldsymbol{x} - \boldsymbol{x_i}||) = \sqrt{\left(\frac{||\boldsymbol{x} - \boldsymbol{x_i}||}{\epsilon}\right)^2 + 1}$$

where $\boldsymbol{x}$ is an arbitrary $(m_{W_R}, m_{N_R})$ coordinate, the $\boldsymbol{x_i}$ are $(m_{W_R}, m_{N_R})$ coordinates where an upper limit on $\mu_S$ has been set, $N$ is the number of $\boldsymbol{x_i}$, and $\epsilon$ is the average distance between $\boldsymbol{x_i}$.

Additional mass hypotheses were also added by interpolating the discriminating

distributions obtained for existing signal hypotheses using a moment morphing technique [194]. The same upper limit setting procedure was then performed in these interpolated points, in order to reduce artefacts in the final limit plots due to the choice of signal hypotheses. Cross sections for these interpolated points were found by generating 100 events with MadGraph5_aMC@NLO, in the same manner described in Section 4.3.1. Table 6.4 summarises the interpolated mass hypotheses and cross sections.

| $m_{W_R}$ [GeV] | $m_{N_R}$ [GeV] | $\sigma$ [nb] |
|---|---|---|
| 2100 | 1700 | $4.335 \times 10^{-5}$ |
| 2400 | 200 | $1.076 \times 10^{-4}$ |
| 2400 | 400 | $9.782 \times 10^{-5}$ |
| 3000 | 2100 | $1.046 \times 10^{-5}$ |
| 3000 | 2500 | $4.147 \times 10^{-6}$ |
| 3500 | 200 | $1.028 \times 10^{-5}$ |
| 3500 | 300 | $1.008 \times 10^{-5}$ |

**Table 6.4** Interpolated signal mass hypotheses, and their cross sections found using MadGraph5_aMC@NLO.

# Chapter 7

# Results

In this chapter, the final results obtained in the analysis described in this thesis are presented. Results from the opposite-sign analysis are presented in Section 7.1. Results obtained via the combination of the opposite-sign analysis with the same-sign analysis are presented in Section 7.2. Both sets of results are discussed in Section 7.3.

## 7.1 Opposite-sign analysis

Exclusion limits on $W_R$ and $N_R$ mass are presented in Figure 7.1. Limits on the Keung-Senjanović process $\sigma \times B$ to $eejj$ or $\mu\mu jj$ are presented as a function of $m_{W_R}$–$m_{N_R}$ in Figure 7.2, and as a function of $m_{W_R}$ for various $m_{W_R}/m_{N_R}$ ratios in Figures 7.3–7.6. Limits are set for both Majorana and Dirac $N_R$ hypotheses. The limits on $\sigma \times B$ calculated are for branching fractions to lepton pairs of any sign. The theoretical Keung-Senjanović process cross sections ($\sigma_{\mathrm{KS}}$) are also multiplied by branching fractions to lepton pairs of any sign in Figures 7.3–7.6, and therefore $\sigma_{\mathrm{KS}} \times B$ for a particular mass hypothesis is same irrespective of the Majorana or Dirac $N_R$ hypothesis considered.

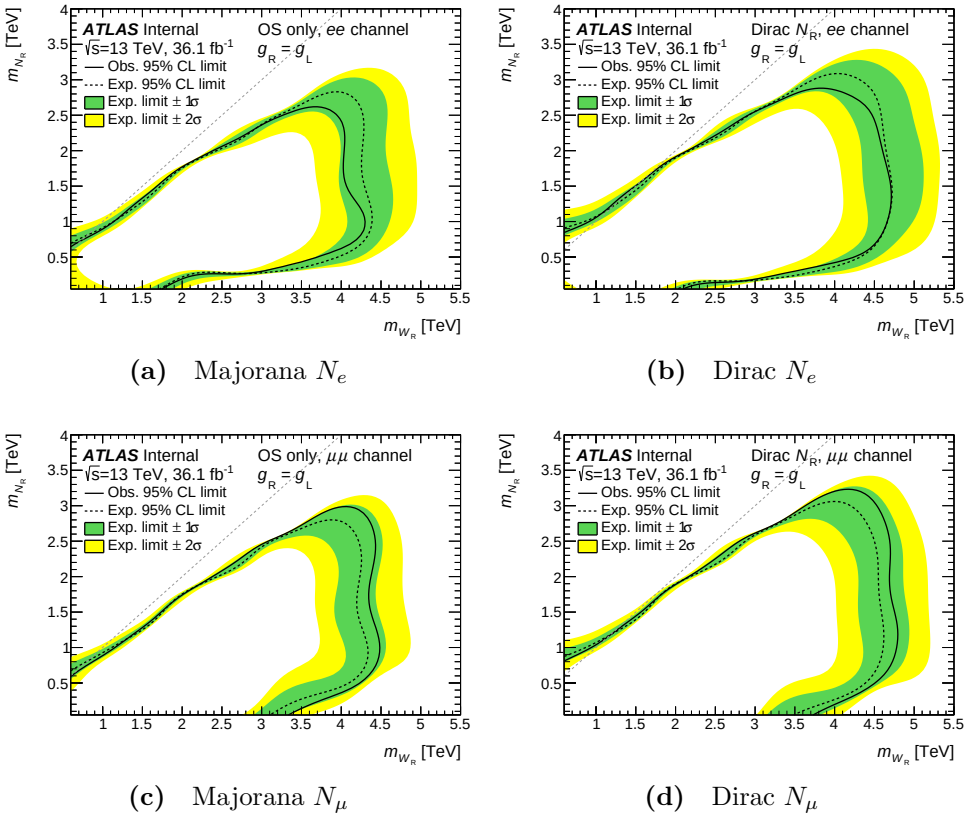


**(a)** Majorana $N_e$ **(b)** Dirac $N_e$

**(c)** Majorana $N_\mu$ **(d)** Dirac $N_\mu$

**Figure 7.1** $m_{W_R}$–$m_{N_R}$ hypotheses excluded by the opposite-sign analysis, for the Majorana (left) or Dirac (right) $N_R$ hypotheses, for the $ee$ (top) and $\mu\mu$ (bottom) channels. The diagonal line indicates $m_{W_R} = m_{N_R}$.

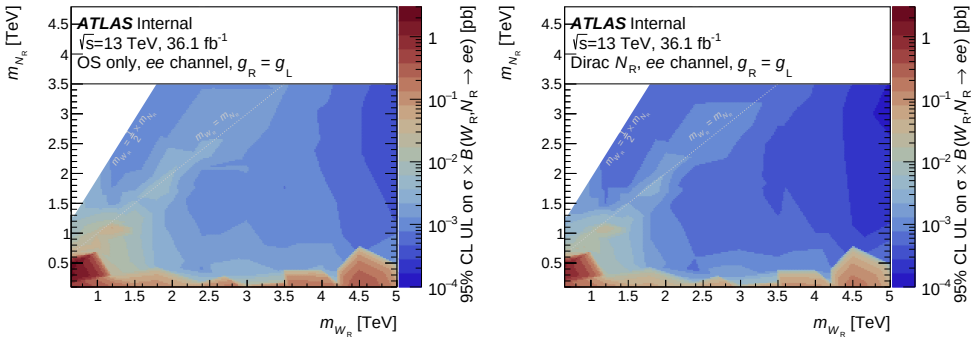


**(a)** Majorana $N_e$ **(b)** Dirac $N_e$

**(c)** Majorana $N_\mu$ **(d)** Dirac $N_\mu$

**Figure 7.2** Upper limits on $\sigma \times B$ as a function of $m_{W_R}$ and $m_{N_R}$ from the opposite-sign analysis, for the Majorana (left) or Dirac (right) $N_R$ hypotheses, for the $ee$ (top) and $\mu\mu$ (bottom) channels.

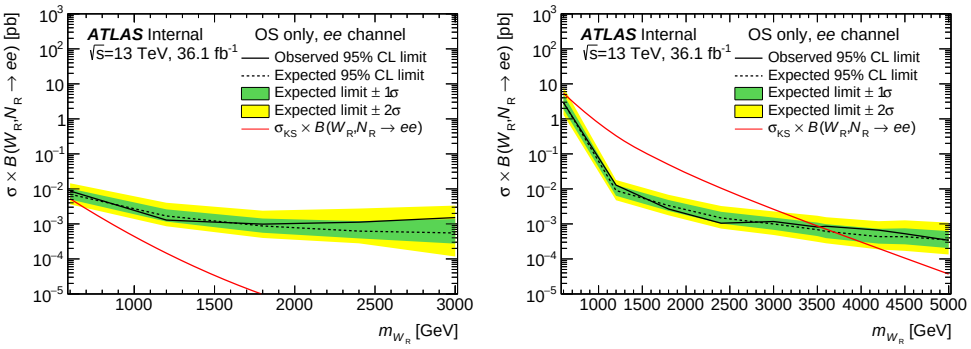


**(a)** $m_{W_R} = 2/3 \times m_{N_R}$ **(b)** $m_{W_R} = 4/3 \times m_{N_R}$

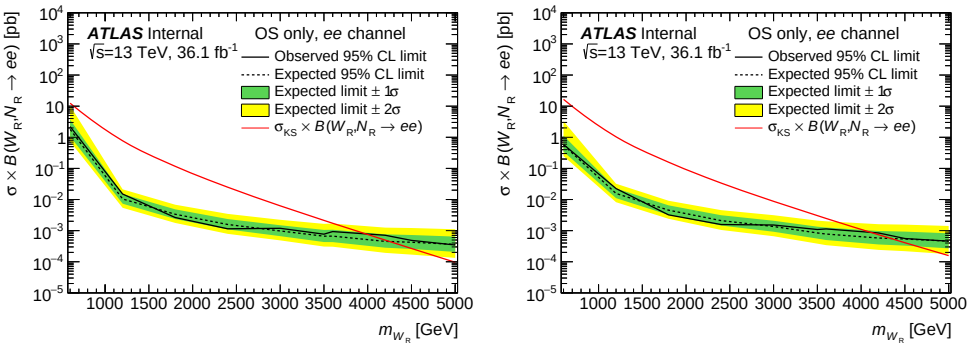


**(c)** $m_{W_R} = 2 \times m_{N_R}$ **(d)** $m_{W_R} = 4 \times m_{N_R}$

**Figure 7.3** Upper limits on $\sigma \times B$ for Majorana $N_e$, for various $m_{W_R}/m_{N_R}$ ratios, as indicated. $\sigma_{\mathrm{KS}} \times B$ is the theory prediction for the Keung-Senjanović process. Results are shown for the opposite-sign analysis.

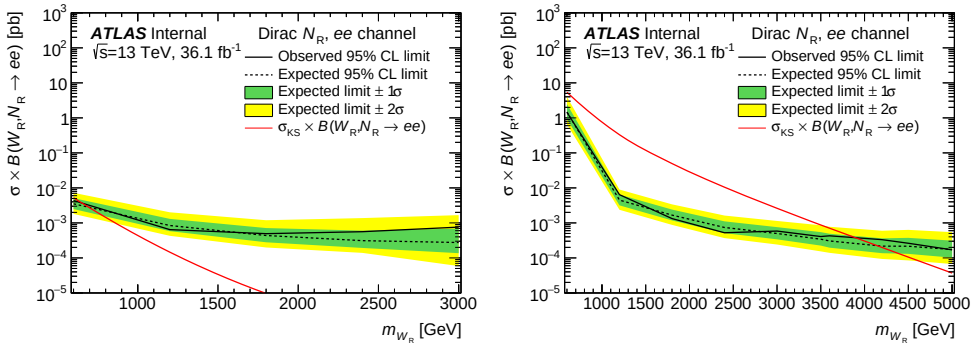


**(a)** $m_{W_R} = 2/3 \times m_{N_R}$ **(b)** $m_{W_R} = 4/3 \times m_{N_R}$

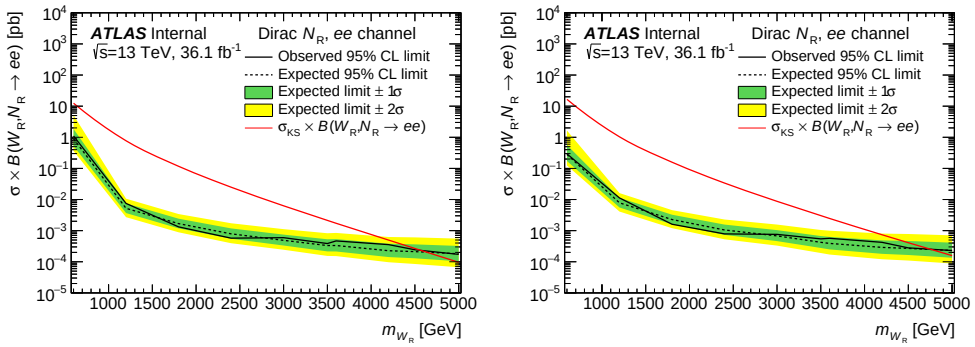


**(c)** $m_{W_R} = 2 \times m_{N_R}$ **(d)** $m_{W_R} = 4 \times m_{N_R}$

**Figure 7.4** Upper limits on $\sigma \times B$ for Dirac $N_e$, for various $m_{W_R}/m_{N_R}$ ratios, as indicated. $\sigma_{\mathrm{KS}} \times B$ is the theory prediction for the Keung-Senjanović process. Results are shown for the opposite-sign analysis.

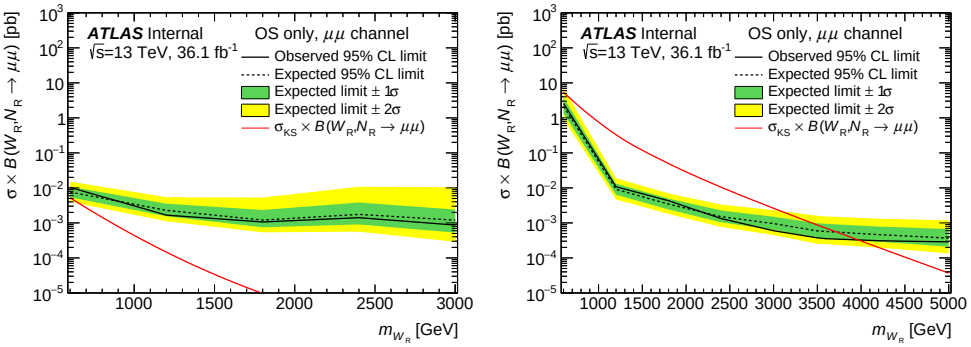


**(a)** $m_{W_R} = 2/3 \times m_{N_R}$ **(b)** $m_{W_R} = 4/3 \times m_{N_R}$

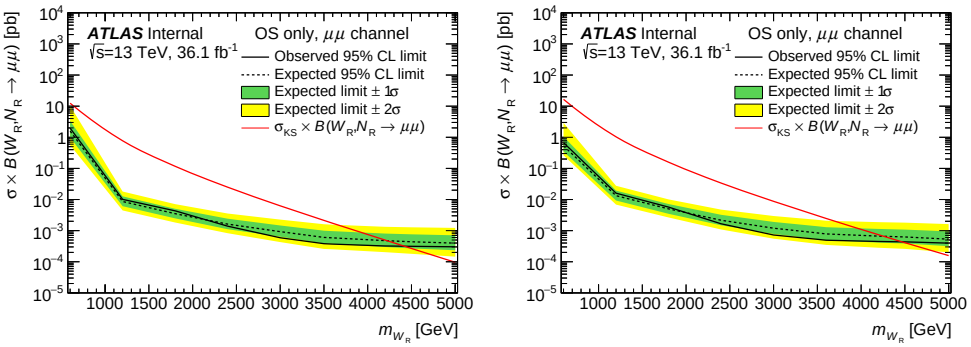


**(c)** $m_{W_R} = 2 \times m_{N_R}$ **(d)** $m_{W_R} = 4 \times m_{N_R}$

**Figure 7.5** Upper limits on $\sigma \times B$ for Majorana $N_\mu$, for various $m_{W_R}/m_{N_R}$ ratios, as indicated. $\sigma_{\mathrm{KS}} \times B$ is the theory prediction for the Keung-Senjanović process. Results are shown for the opposite-sign analysis.

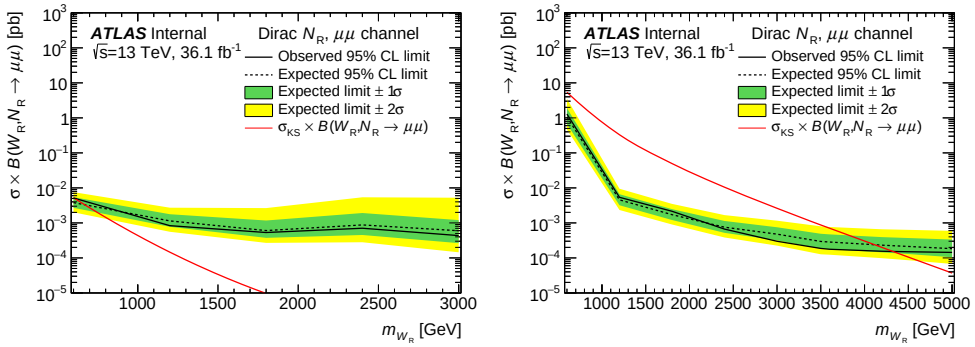


**(a)** $m_{W_R} = 2/3 \times m_{N_R}$ **(b)** $m_{W_R} = 4/3 \times m_{N_R}$

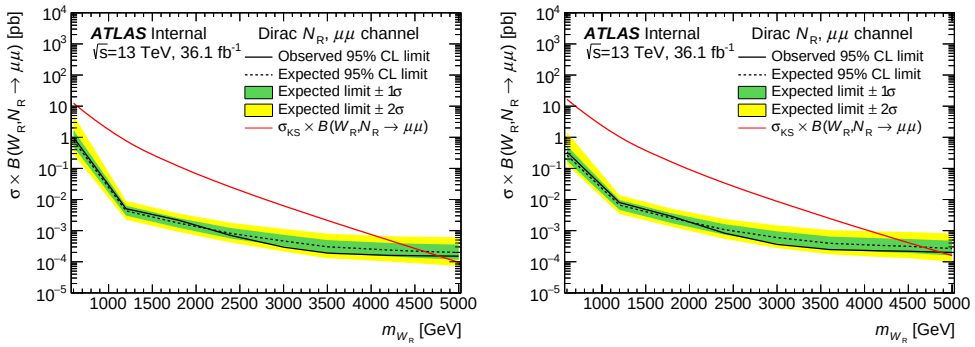


**(c)** $m_{W_R} = 2 \times m_{N_R}$ **(d)** $m_{W_R} = 4 \times m_{N_R}$

**Figure 7.6** Upper limits on $\sigma \times B$ for Dirac $N_\mu$, for various $m_{W_R}/m_{N_R}$ ratios, as indicated. $\sigma_{\mathrm{KS}} \times B$ is the theory prediction for the Keung-Senjanović process. Results are shown for the opposite-sign analysis.

## 7.2 Combination

Improved limits for the Majorana $N_R$ hypothesis obtained by combining the opposite-sign and same-sign analyses (see Section 6.1.5) are presented in Figure 7.7 for $m_{W_R}$–$m_{N_R}$ exclusion limits and Figure 7.8 for upper limits on $\sigma \times B$ to $eejj$ or $\mu\mu jj$.

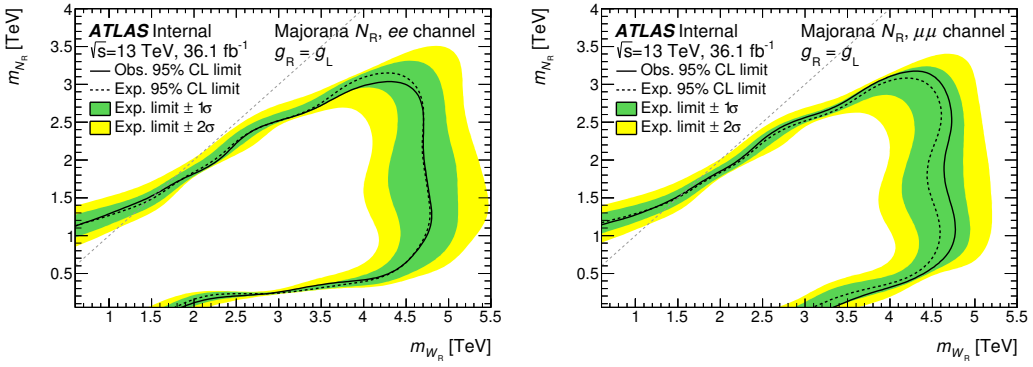


**(a)** Majorana $N_e$ **(b)** Majorana $N_\mu$

**Figure 7.7** $m_{W_R}$–$m_{N_R}$ hypotheses excluded by the combination of the opposite-sign and same-sign analyses, for the Majorana hypothesis, for the $ee$ (left) and $\mu\mu$ (right) channels. The diagonal line indicates $m_{W_R} = m_{N_R}$. Taken from [2].

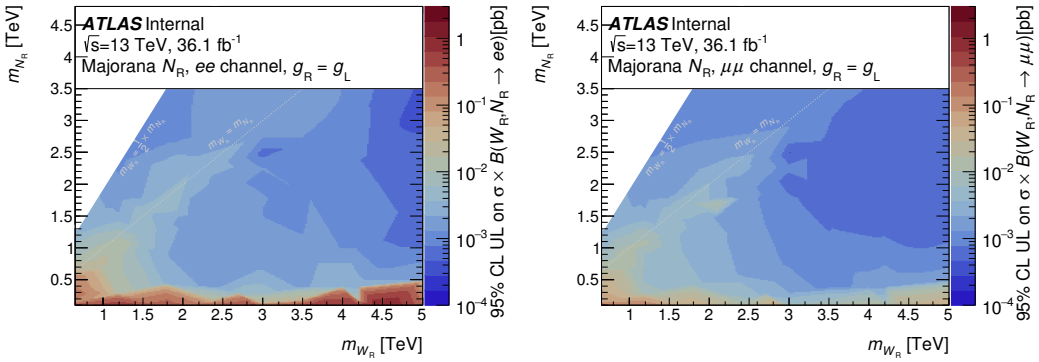


**(a)** Majorana $N_e$ **(b)** Majorana $N_\mu$

**Figure 7.8** Upper limits on $\sigma \times B$ as a function of $m_{W_R}$ and $m_{N_R}$ from the combination of the opposite-sign and same-sign analyses, for the Majorana hypothesis, for the $ee$ (left) and $\mu\mu$ (right) channels. Taken from [2].

## 7.3 Discussion

No evidence for the existence of $W_R$ and $N_R$ has been found. For both the Majorana and Dirac $N_R$ hypotheses, $W_R$ masses up to 4.7 TeV are excluded at 95% CL, for $N_R$ masses between ∼500 GeV and ∼3 TeV. The best result for the Majorana $N_R$ hypothesis comes from the combined opposite-sign and same-sign limits, which are more stringent than the opposite-sign limits, as expected. Figure 7.9 shows the exclusion limits separately for the opposite-sign and same-sign analyses. The two analyses generally exhibit a similar sensitivity across the two-dimensional mass plane, however, the same-sign analysis is more sensitive under the $m_{N_R} > m_{W_R}$ hypothesis due to the lower expected background.

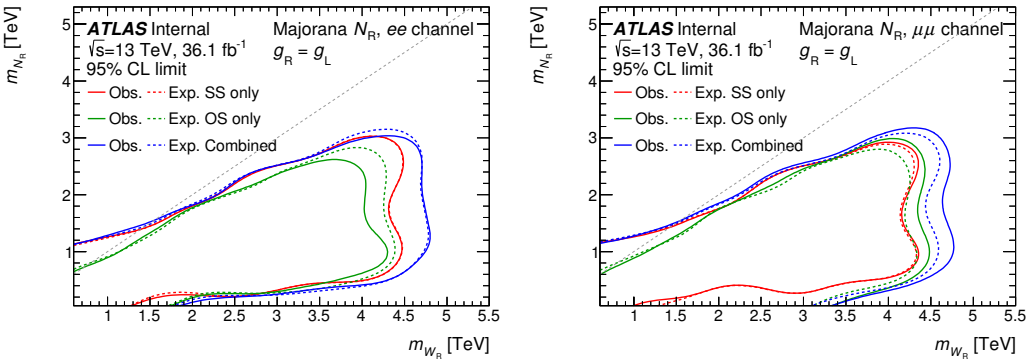


**(a)** Majorana $N_e$ **(b)** Majorana $N_\mu$

**Figure 7.9** $m_{W_R}$–$m_{N_R}$ hypotheses excluded by the combination of the opposite-sign and same-sign analyses, and also for the opposite-sign and same-sign analyses seperately, for the Majorana hypothesis, for the $ee$ (left) and $\mu\mu$ (right) channels. The diagonal line indicates $m_{W_R} = m_{N_R}$. Taken from [2].

In the opposite-sign analysis $ee$ channel, the observed limits around $m_{W_R}$ ∼4.2 TeV and $m_{N_R}$ ∼3 TeV are weaker than the expected limits due to the presence of ∼2.05$\sigma$ local excess between 3.5–4 TeV in the opposite-sign analysis (see Section 6.2). The effect is most dramatic for the Majorana $N_R$ limits. There is a smaller effect in the Dirac $N_R$ and combined Majorana $N_R$ cases as the excess is less significant compared to the higher expected number of signal events. Stronger limits are observed than expected in the opposite-sign $\mu\mu$ channel, because no events are observed in bins where $m_{\ell\ell jj} > 3$ TeV (see Figure 6.14).

The combination limits are more stringent than the previous best limits on $W_R$ and Majorana $N_R$ mass, found by the CMS collaboration at $\sqrt{s} = 13$ TeV [69]. The regions excluded by the CMS collaboration excluded to $m_{W_R}$ ∼4.4 TeV for

$N_R$ masses between ∼1–2.3 TeV. The limits in the Dirac $N_R$ case far exceed the previous best limits, set by the ATLAS collaboration at $\sqrt{s} = 7$ TeV [65], which extended to just over $m_{W_R}$ ∼2.4 TeV, and to $m_{N_R}$ ∼1.5 TeV. The limits on $W_R$ mass presented in this thesis also exceed the limit of $m_{W_R}$ ∼3.7 TeV from the ATLAS $W' \to jj$ search at $\sqrt{s} = 13$ TeV [74].

Exclusion limits presented in this thesis extend into the $m_{N_R} > m_{W_R}$ region for the first time for an LHC Keung-Senjanović process analysis, made possible by the use of a different generator to produce signal MC datasets, as discussed in Section 4.3.1. The excluded region for the $m_{N_R} > m_{W_R}$ case is small for a number of reasons. Firstly, the Keung-Senjanović production cross section, for a given value of $m_{W_R}$, decreases as $m_{N_R}$ increases (see Figure 4.7). In phase space regions where the Keung-Senjanović production cross section is not prohibitively low, the $W_R$ mass is low so separation between signal and background is poor (see Figure 6.23). Additionally, the opposite-sign selections result in low sensitivity to the Keung-Senjanović process when $m_{W_R}$ and $m_{N_R}$ are similar (see Figure 5.3).

Upper limits on $\sigma \times B$ to $eejj$ or $\mu\mu jj$ are also presented, including in the $m_{N_R} > m_{W_R}$ region for the first time. The Majorana $N_R$ upper limits on $\sigma \times B$ to $eejj$ or $\mu\mu jj$ can not be compared to the CMS $\sqrt{s} = 13$ TeV results at this time, because inconsistent results are presented within the relevant paper [69]. More details regarding the previous best limits can be found in Section 2.4.1.

# Chapter 8

# Conclusion

Left-Right Symmetric Models are a promising class of extensions to the Standard Model of particle physics. By introducing a right-handed component to the weak force, LRSMs can restore the parity symmetry to the SM, and provide a viable mechanism for generating the small masses of the known neutrinos. Two forms of LRSM were considered in this thesis, which predict the existence of heavy right-handed $W$ bosons, $W_R$, and either Majorana or Dirac heavy right-handed neutrinos, $N_R$.

An analysis searching for LRSM $W_R$ and $N_R$ in final states with two opposite-sign electrons or muons has been performed, focusing on the Keung-Senjanović process. $36.1\,\text{fb}^{-1}$ of $pp$ good quality collision data recorded during 2015–2016 at $\sqrt{s} = 13\,\text{TeV}$ by the ATLAS experiment was analysed. Monte Carlo datasets were used to model the signal and SM background processes. The MC modelling of the Keung-Senjanović process was improved in this analysis with respect to past LHC searches. Various selections were applied in order to enhance the sensitivity of the analysis. The data was found to be compatible with the SM prediction and exclusion limits were set on the possible masses of the $W_R$ and $N_R$, and upper limits on the Keung-Senjanović process cross section multiplied by the branching fraction to $eejj$ or $\mu\mu jj$. A statistical combination was performed with a related Keung-Senjanović process analysis to same-sign electrons or muons to produce improved limits for the Majorana $N_R$. The limits found are the current most stringent on $m_{W_R}$ and $m_{N_R}$, reaching $W_R$ masses up to $4.7\,\text{TeV}$ for $N_R$ masses between $\sim$500 GeV and $\sim$3 TeV. The $m_{N_R} > m_{W_R}$ phase space region was considered for the first time by an LHC Keung-Senjanović process analysis.

# Appendix A

# Kinematics plots for the Keung-Senjanović process

In this appendix, plots of various kinematic quantities are shown, at generator level, for the Keung-Senjanović process. For more details on the MC samples, see Section 4.3.1. The labelling used to refer to the particles produced by the Keung-Senjanović process is demonstrated in Figure A.1. Plots for the first $W_R$ in the event are not included because:

1. The $p_{\mathrm{T}}$ of the first $W_R$ is strictly zero at generator level
2. $\eta$ of the first $W_R$ is strictly maximal at generator level (along the LHC beampipe)
3. The first $W_R$ are quantised in $\phi$, which is an artificial feature of the event generation.

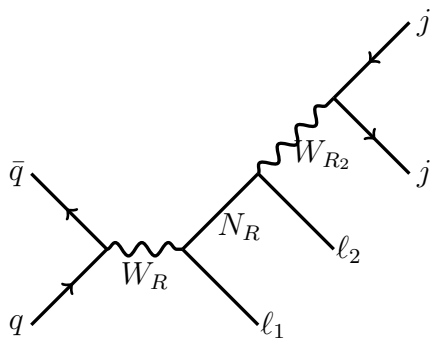


**Figure A.1** The Feynman diagram for the Keung-Senjanović process, demonstrating the labelling scheme used throughout this appendix.

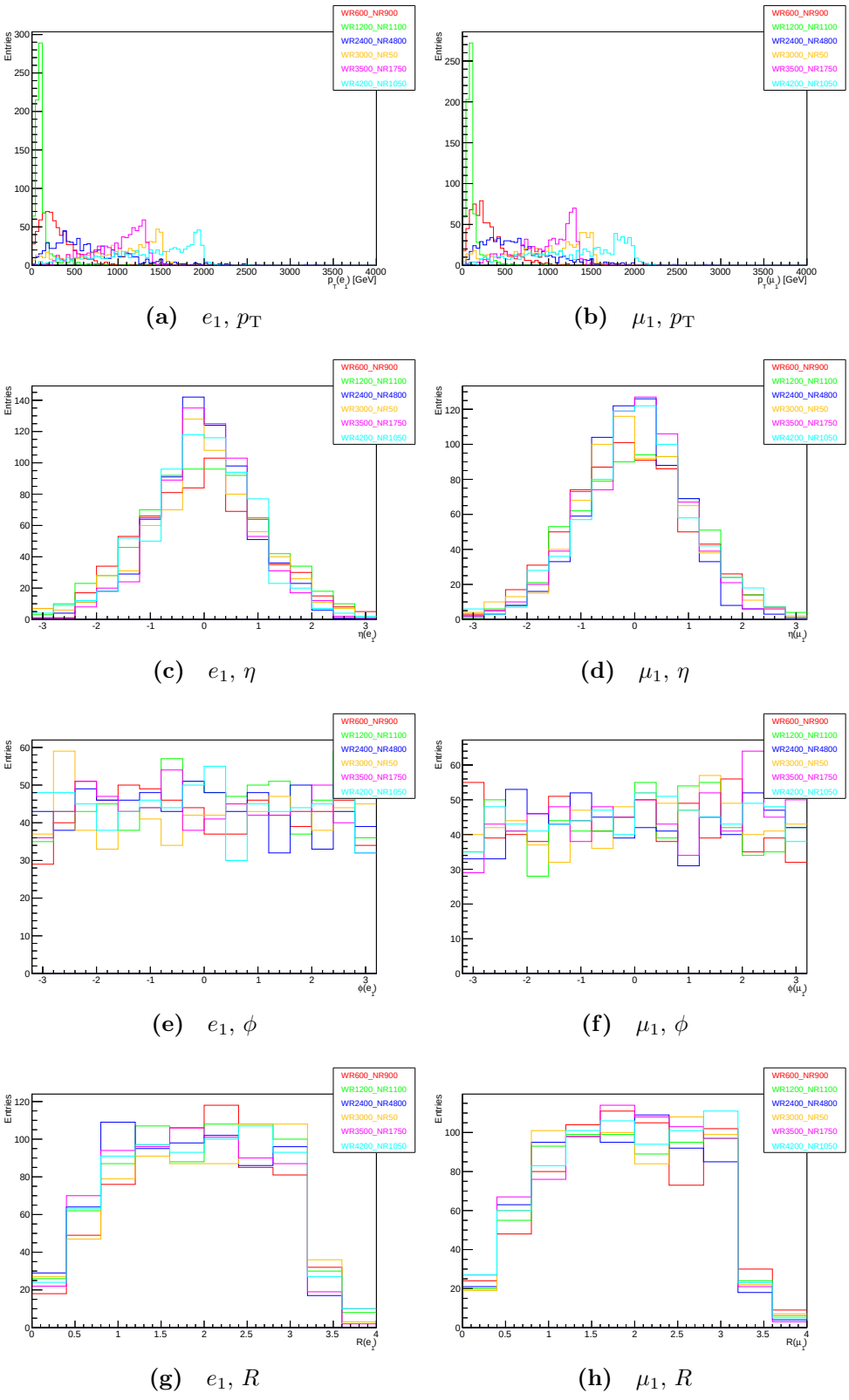


**(a)** $e_1$, $p_{\mathrm{T}}$ **(b)** $\mu_1$, $p_{\mathrm{T}}$

**(c)** $e_1$, $\eta$ **(d)** $\mu_1$, $\eta$

**(e)** $e_1$, $\phi$ **(f)** $\mu_1$, $\phi$

**(g)** $e_1$, $R$ **(h)** $\mu_1$, $R$

**Figure A.2** Generator-level kinematic distributions for the first lepton emitted during the Keung-Senjanović process, for a range of generated $W_R$ and $N_R$ mass values (in GeV), generated with MadGraph5_aMC@NLO. Only the hard process was simulated.

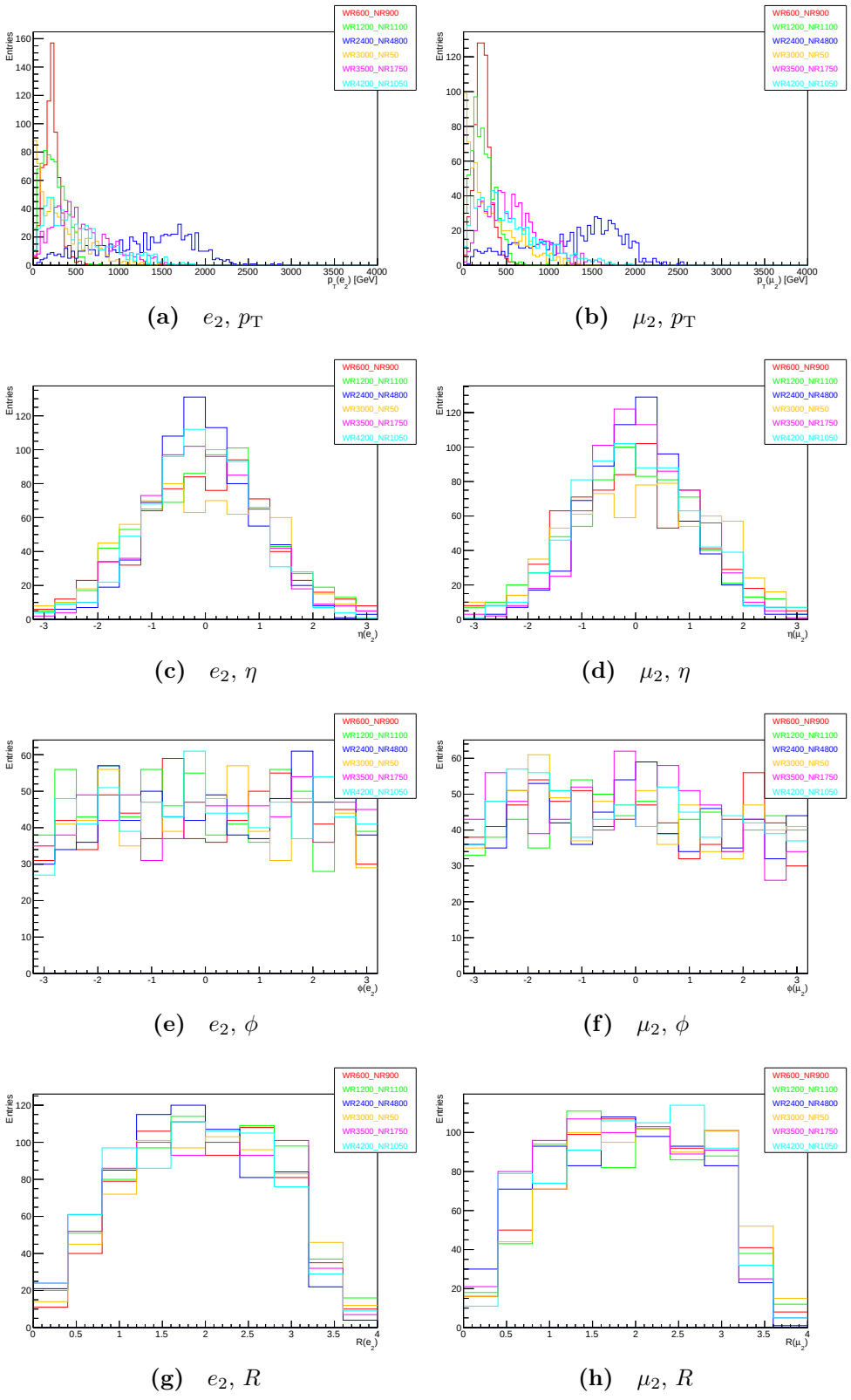


**(a)** $e_2$, $p_{\mathrm{T}}$ **(b)** $\mu_2$, $p_{\mathrm{T}}$

**(c)** $e_2$, $\eta$ **(d)** $\mu_2$, $\eta$

**(e)** $e_2$, $\phi$ **(f)** $\mu_2$, $\phi$

**(g)** $e_2$, $R$ **(h)** $\mu_2$, $R$

**Figure A.3** Generator-level kinematic distributions for the second lepton emitted during the Keung-Senjanović process, for a range of generated $W_R$ and $N_R$ mass values (in GeV), generated with MadGraph5_aMC@NLO. Only the hard process was simulated.

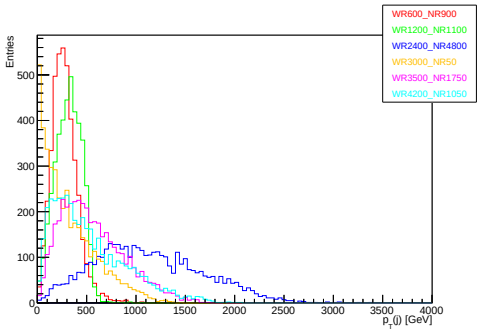


**(a)** $j$, $p_{\mathrm{T}}$

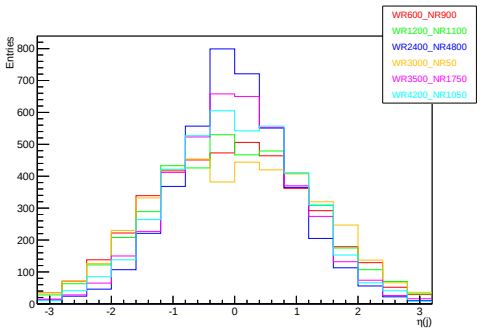


**(b)** $j$, $\eta$

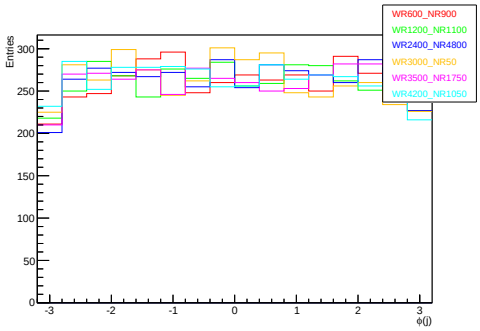


**(c)** $j$, $\phi$

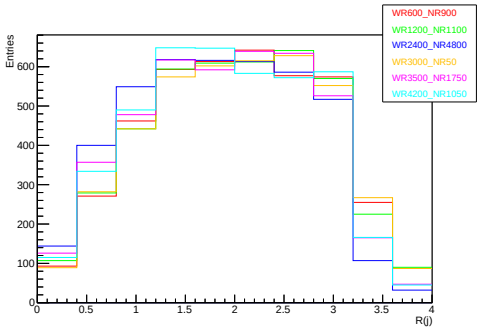


**(d)** $j$, $R$

**Figure A.4** Generator-level kinematic distributions for jets emitted during the Keung-Senjanović process, for a range of generated $W_R$ and $N_R$ mass values (in GeV), generated with MadGraph5_aMC@NLO. Only the hard process was simulated.

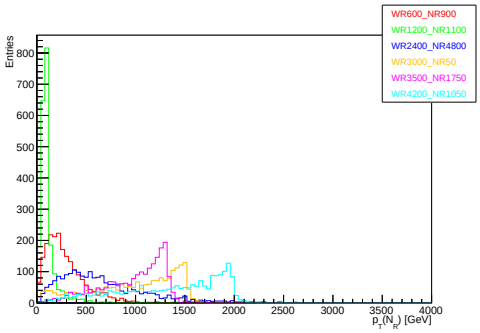


**(a)** $N_R$, $p_{\mathrm{T}}$

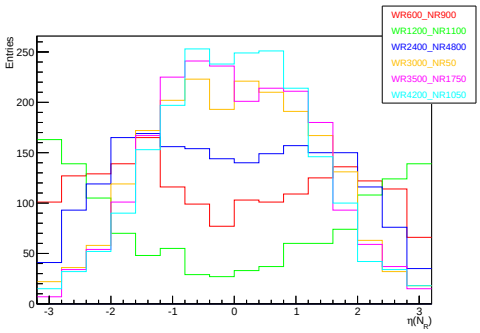


**(b)** $N_R$, $\eta$

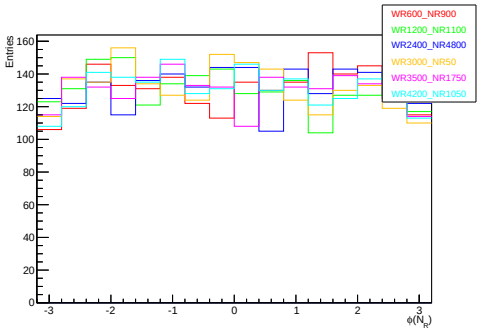


**(c)** $N_R$, $\phi$

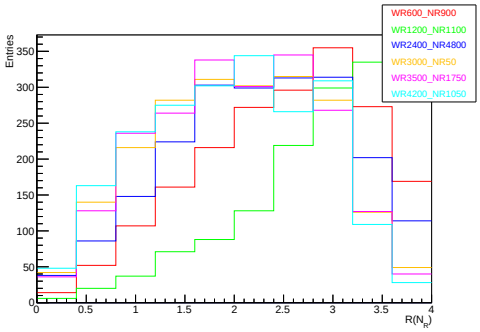


**(d)** $N_R$, $R$

**Figure A.5** Generator-level kinematic distributions for $N_R$ produced during the Keung-Senjanović process, for a range of generated $W_R$ and $N_R$ mass values (in GeV), generated with MadGraph5_aMC@NLO. Only the hard process was simulated.

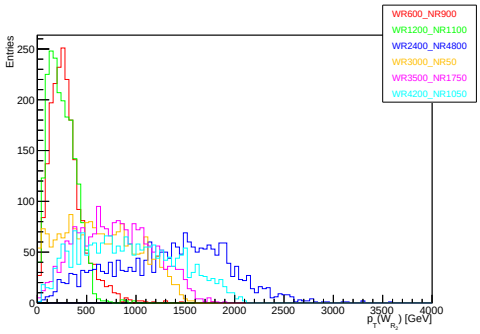


**(a)** $W_{R_2}$, $p_{\mathrm{T}}$

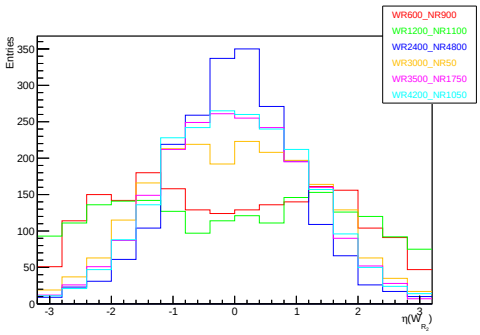


**(b)** $W_{R_2}$, $\eta$

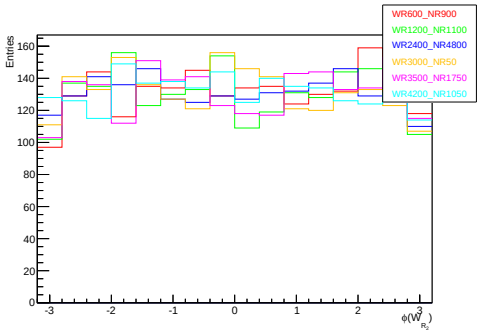


**(c)** $W_{R_2}$, $\phi$

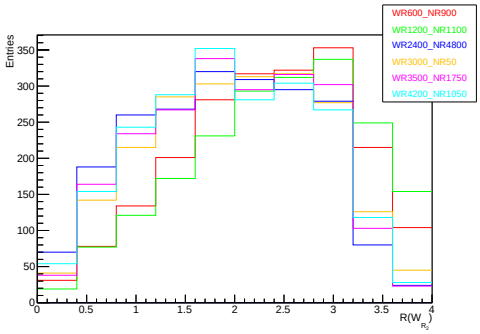


**(d)** $W_{R_2}$, $R$

**Figure A.6** Generator-level kinematic distributions for the second $W_R$ produced during the Keung-Senjanović process, for a range of generated $W_R$ and $N_R$ mass values (in GeV), generated with MadGraph5_aMC@NLO. Only the hard process was simulated.

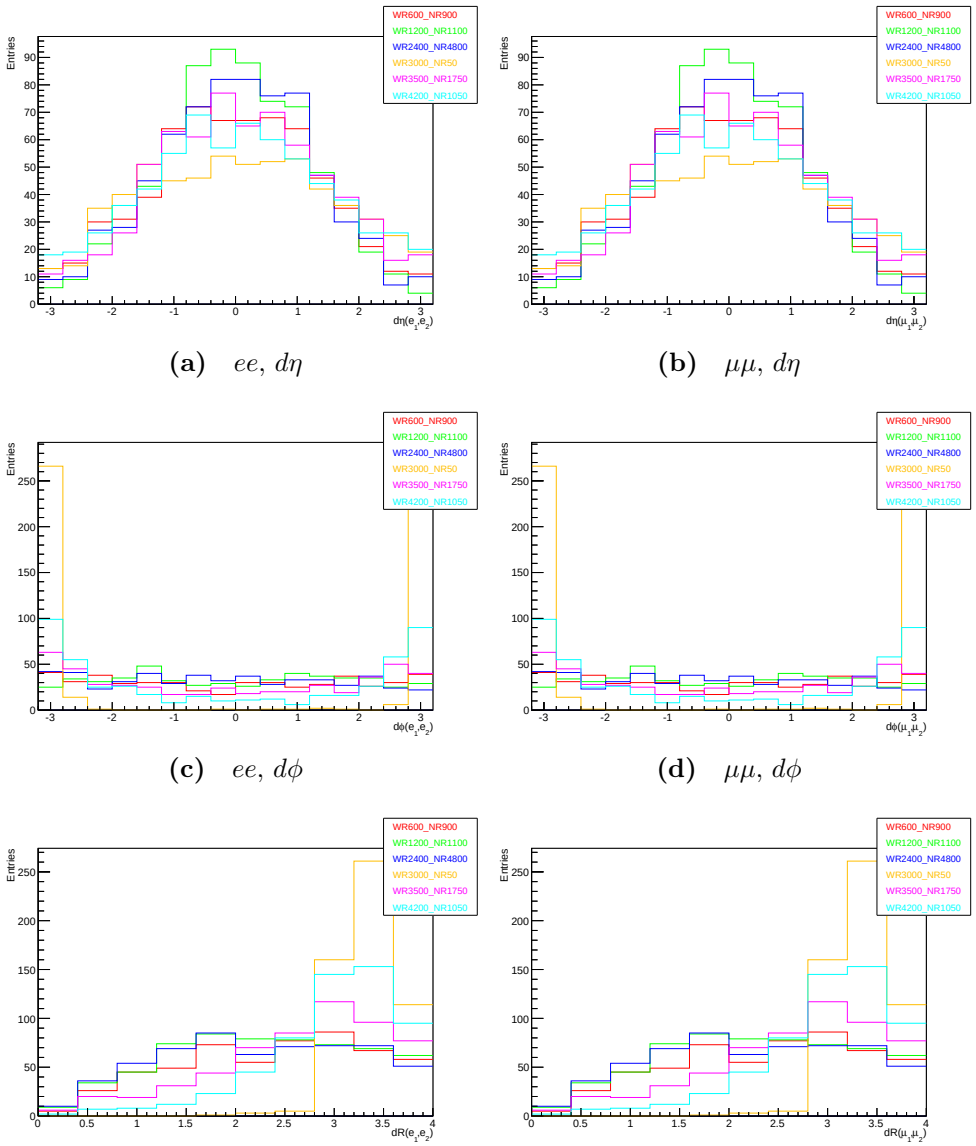


**(a)** $ee$, $d\eta$ **(b)** $\mu\mu$, $d\eta$

**(c)** $ee$, $d\phi$ **(d)** $\mu\mu$, $d\phi$

**(e)** $ee$, $dR$ **(f)** $\mu\mu$, $dR$

**Figure A.7** Generator-level angular relationships between leptons produced during the Keung-Senjanović process, for a range of generated $W_R$ and $N_R$ mass values (in GeV), generated with MadGraph5_aMC@NLO. Only the hard process was simulated.

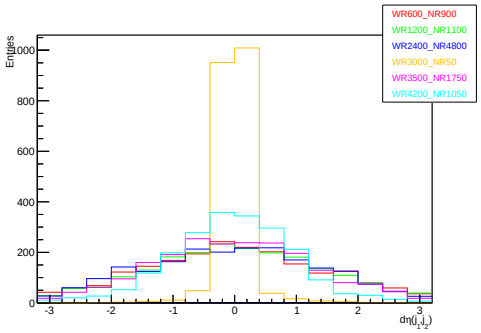


**(a)** $jj$, $d\eta$

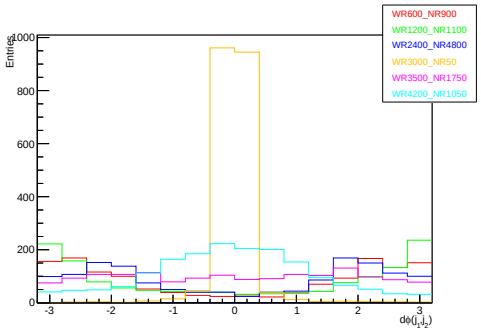


**(b)** $jj$, $d\phi$

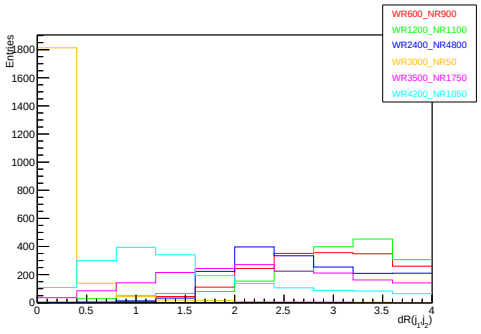


**(c)** $jj$, $dR$

**Figure A.8** Generator-level angular relationships between jets produced during the Keung-Senjanović process, for a range of generated $W_R$ and $N_R$ mass values (in GeV), generated with MadGraph5_aMC@NLO. Only the hard process was simulated.

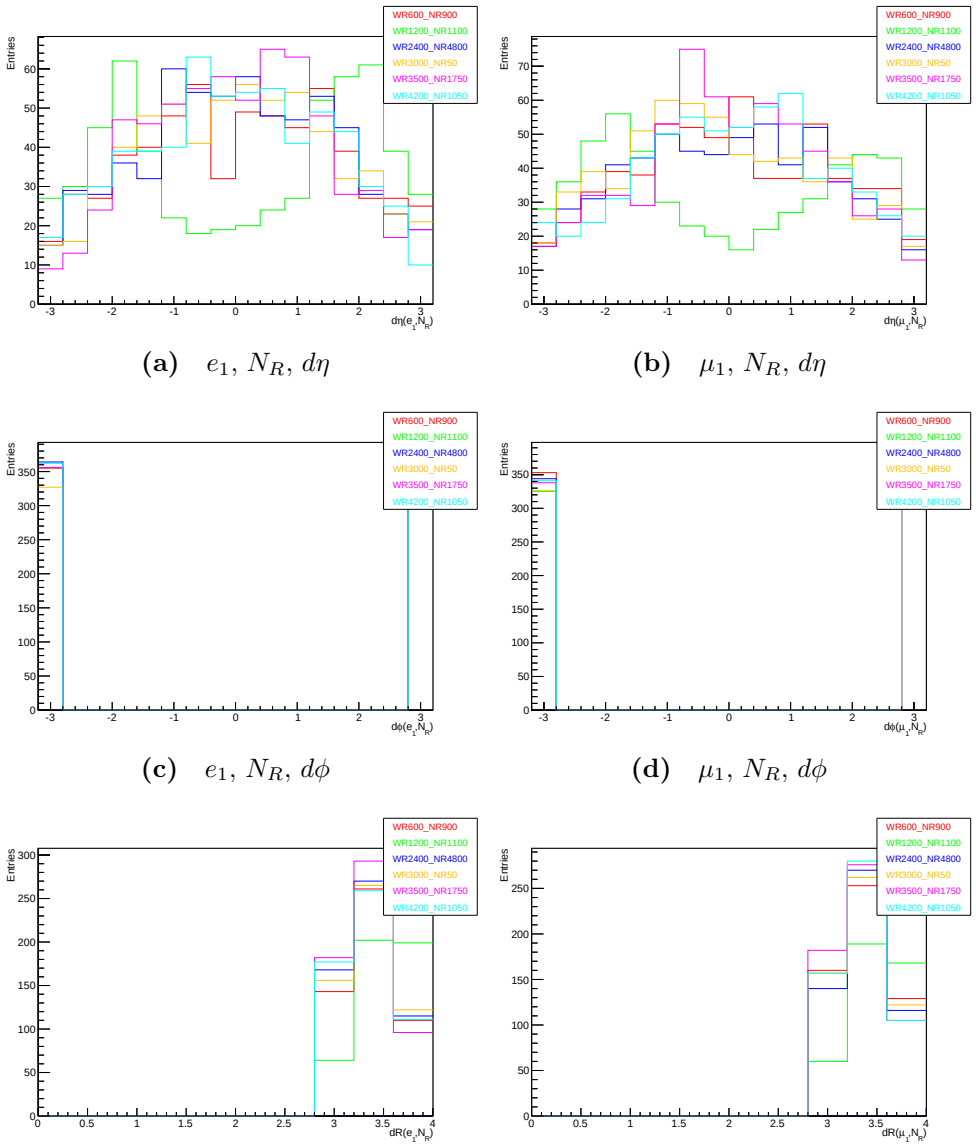


**(a)** $e_1$, $N_R$, $d\eta$ **(b)** $\mu_1$, $N_R$, $d\eta$

**(c)** $e_1$, $N_R$, $d\phi$ **(d)** $\mu_1$, $N_R$, $d\phi$

**(e)** $e_1$, $N_R$, $dR$ **(f)** $\mu_1$, $N_R$, $dR$

**Figure A.9** Generator-level angular relationships between the first lepton and $N_R$ produced during the Keung-Senjanović process, for a range of generated $W_R$ and $N_R$ mass values (in GeV), generated with MadGraph5_aMC@NLO. Only the hard process was simulated.

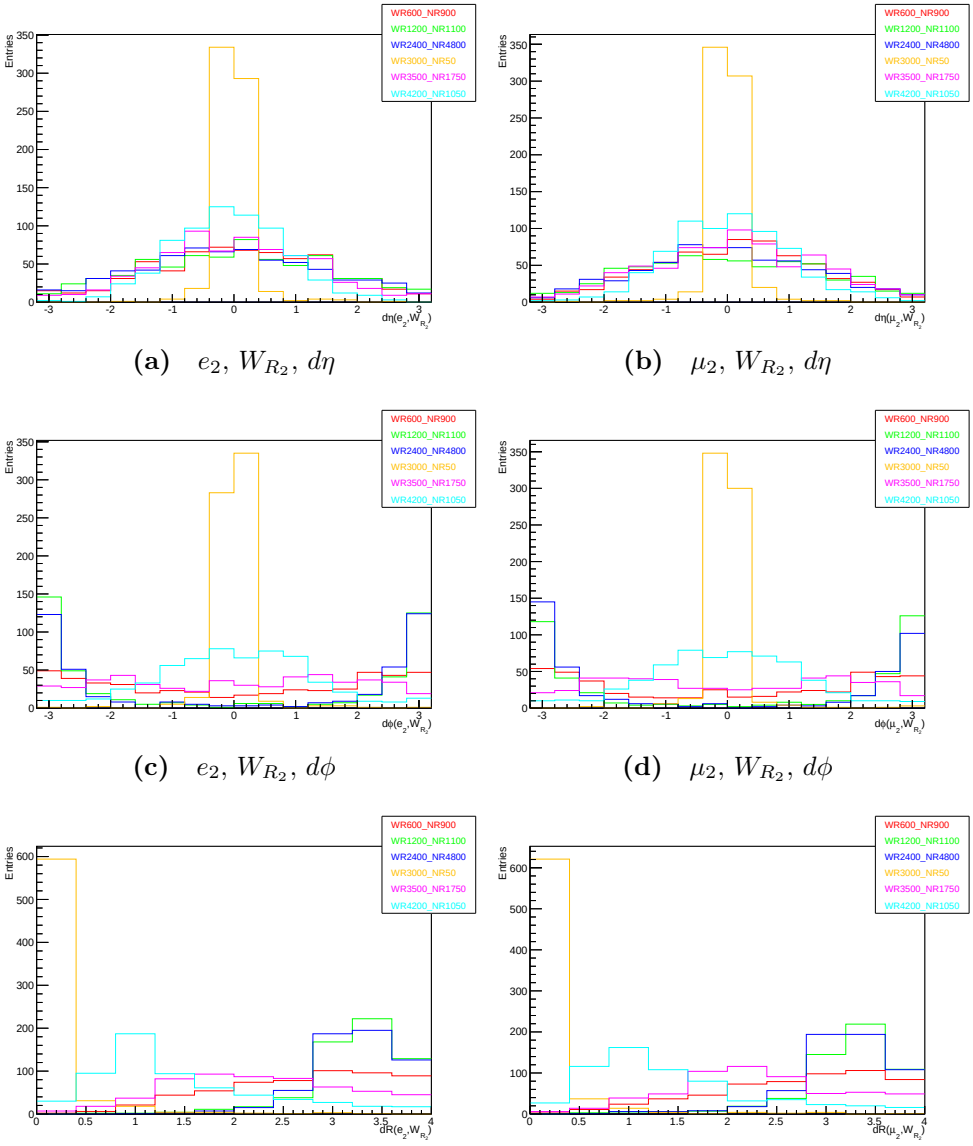


**(a)** $e_2$, $W_{R_2}$, $d\eta$ **(b)** $\mu_2$, $W_{R_2}$, $d\eta$

**(c)** $e_2$, $W_{R_2}$, $d\phi$ **(d)** $\mu_2$, $W_{R_2}$, $d\phi$

**(e)** $e_2$, $W_{R_2}$, $dR$ **(f)** $\mu_2$, $W_{R_2}$, $dR$

**Figure A.10** Generator-level angular relationships between the second lepton and the second $W_R$ produced during the Keung-Senjanović process, for a range of generated $W_R$ and $N_R$ mass values (in GeV), generated with MadGraph5_aMC@NLO. Only the hard process was simulated.

# Bibliography


[1] ATLAS Collaboration, X. Hoad, *Trigger Menu-aware Monitoring for the ATLAS experiment*, J. Phys. Conf. Ser. **898** (2017) 092007. (Cited on pages v, 55, and 58.)

[2] ATLAS Collaboration, *Search for heavy Majorana or Dirac neutrinos and right-handed $W$ gauge bosons in final states with two charged leptons and two jets at $\sqrt{s}$ = 13 TeV with the ATLAS detector*, JHEP **01** (2019) 016, `arXiv:1809.11105 [hep-ex]`. (Cited on pages v, 124, 125, 140, and 141.)

[3] S. L. Glashow, *Partial Symmetries of Weak Interactions*, Nucl. Phys. **22** (1961) 579–588. (Cited on page 3.)

[4] A. Salam and J. C. Ward, *Electromagnetic and weak interactions*, Phys. Lett. **13** (1964) 168–171. (Cited on page 3.)

[5] S. Weinberg, *A Model of Leptons*, Phys. Rev. Lett. **19** (1967) 1264–1266. (Cited on page 3.)

[6] A. Salam, *Weak and Electromagnetic Interactions*, Conf. Proc. **C680519** (1968) 367–377. (Cited on page 3.)

[7] F. Englert and R. Brout, *Broken Symmetry and the Mass of Gauge Vector Mesons*, Phys. Rev. Lett. **13** (1964) 321–323, [,157(1964)]. (Cited on pages 3 and 8.)

[8] P. W. Higgs, *Broken Symmetries and the Masses of Gauge Bosons*, Phys. Rev. Lett. **13** (1964) 508–509, [,160(1964)]. (Cited on pages 3 and 8.)

[9] G. S. Guralnik, C. R. Hagen and T. W. B. Kibble, *Global Conservation Laws and Massless Particles*, Phys. Rev. Lett. **13** (1964) 585–587, [,162(1964)]. (Cited on pages 3 and 8.)

[10] H. Fritzsch, M. Gell-Mann and H. Leutwyler, *Advantages of the Color Octet Gluon Picture*, Phys. Lett. **47B** (1973) 365–368. (Cited on page 3.)

[11] D. J. Gross and F. Wilczek, *Ultraviolet Behavior of Nonabelian Gauge Theories*, Phys. Rev. Lett. **30** (1973) 1343–1346, [,271(1973)]. (Cited on page 3.)

[12] H. D. Politzer, *Reliable Perturbative Results for Strong Interactions?*, Phys. Rev. Lett. **30** (1973) 1346–1349, [,274(1973)]. (Cited on page 3.)

[13] ATLAS Collaboration, *Observation of a new particle in the search for the Standard Model Higgs boson with the ATLAS detector at the LHC*, Phys. Lett. B **716** (2012) 1, arXiv:1207.7214 [hep-ex]. (Cited on page 4.)

[14] CMS Collaboration, *Observation of a new boson at a mass of 125 GeV with the CMS experiment at the LHC*, Phys. Lett. B **716** (2012) 30, arXiv:1207.7235 [hep-ex]. (Cited on page 4.)

[15] Latham Boyle, *Standard Model Of Particle Physics–Most Complete Diagram*, 2014, https://commons.wikimedia.org/wiki/File:Standard_Model_Of_Particle_Physics--Most_Complete_Diagram.png, (accessed 08/06/18). (Cited on page 5.)

[16] ATLAS Collaboration, *Summary plots from the ATLAS Standard Model physics group*, 2018, https://atlas.web.cern.ch/Atlas/GROUPS/PHYSICS/CombinedSummaryPlots/SM/, (accessed 08/06/18). (Cited on page 6.)

[17] E. Noether, *Invariant Variation Problems*, Gott. Nachr. **1918** (1918) 235–257, arXiv:physics/0503066 [physics], [Transp. Theory Statist. Phys.1,186(1971)]. (Cited on page 4.)

[18] W. Chinowsky and J. Steinberger, *Absorption of Negative Pions in Deuterium: Parity of the Pion*, Phys. Rev. **95** (1954) 1561–1564. (Cited on page 7.)

[19] T. D. Lee and C.-N. Yang, *Question of Parity Conservation in Weak Interactions*, Phys. Rev. **104** (1956) 254–258. (Cited on page 7.)

[20] C. S. Wu, E. Ambler, R. W. Hayward, D. D. Hoppes and R. P. Hudson, *Experimental Test of Parity Conservation in Beta Decay*, Phys. Rev. **105** (1957) 1413–1414. (Cited on page 7.)

[21] R. L. Garwin, L. M. Lederman and M. Weinrich, *Observations of the Failure of Conservation of Parity and Charge Conjugation in Meson Decays: The Magnetic Moment of the Free Muon*, Phys. Rev. **105** (1957) 1415–1417. (Cited on page 7.)

[22] Particle Data Group Collaboration, C. Patrignani et al., *Review of Particle Physics*, Chin. Phys. **C40** (2016) 100001. (Cited on pages 7, 11, 37, 73, and 89.)

[23] H. Yukawa, *On the Interaction of Elementary Particles I*, Proc. Phys. Math. Soc. Jap. **17** (1935) 48–57, [Prog. Theor. Phys. Suppl.1,1(1935)]. (Cited on page 8.)

[24] P. A. M. Dirac, *The quantum theory of the electron*, Proc. Roy. Soc. Lond. **A117** (1928) 610–624. (Cited on page 8.)

[25] A. Salam, *On parity conservation and neutrino mass*, Nuovo Cim. **5** (1957) 299–301. (Cited on page 8.)

[26] T. D. Lee and C.-N. Yang, *Parity Nonconservation and a Two Component Theory of the Neutrino*, Phys. Rev. **105** (1957) 1671–1675, [,245(1957)]. (Cited on page 8.)

[27] L. D. Landau, *On the conservation laws for weak interactions*, Nucl. Phys. **3** (1957) 127–131. (Cited on page 8.)

[28] M. Goldhaber, L. Grodzins and A. W. Sunyar, *Helicity of Neutrinos*, Phys. Rev. **109** (1958) 1015–1017. (Cited on page 8.)

[29] E. Majorana, *Teoria simmetrica dell'elettrone e del positrone*, Nuovo Cim. **14** (1937) 171–184. (Cited on page 8.)

[30] B. Pontecorvo, *Mesonium and anti-mesonium*, Sov. Phys. JETP **6** (1957) 429, [Zh. Eksp. Teor. Fiz.33,549(1957)]. (Cited on page 10.)

[31] B. Pontecorvo, *Inverse beta processes and nonconservation of lepton charge*, Sov. Phys. JETP **7** (1958) 172–173, [Zh. Eksp. Teor. Fiz.34,247(1957)]. (Cited on page 10.)

[32] Z. Maki, M. Nakagawa and S. Sakata, *Remarks on the unified model of elementary particles*, Prog. Theor. Phys. **28** (1962) 870–880, [,34(1962)]. (Cited on page 10.)

[33] B. Pontecorvo, *Neutrino Experiments and the Problem of Conservation of Leptonic Charge*, Sov. Phys. JETP **26** (1968) 984–988, [Zh. Eksp. Teor. Fiz.53,1717(1967)]. (Cited on page 10.)

[34] B. T. Cleveland, T. Daily, R. Davis, Jr., J. R. Distel, K. Lande et al., *Measurement of the solar electron neutrino flux with the Homestake chlorine detector*, Astrophys. J. **496** (1998) 505–526. (Cited on page 11.)

[35] S. M. Bilenky and B. Pontecorvo, *Lepton Mixing and the Solar Neutrino Puzzle*, Comments Nucl. Part. Phys. **7** (1977) 149–152. (Cited on page 11.)

[36] SNO Collaboration, *Measurement of the rate of $\nu_e + d \to p + p + e^-$ interactions produced by $^8B$ solar neutrinos at the Sudbury Neutrino Observatory*, Phys. Rev. Lett. **87** (2001) 071301, `arXiv:nucl-ex/0106015 [nucl-ex]`. (Cited on page 11.)

[37] Troitsk Collaboration, V. N. Aseev et al., *An upper limit on electron antineutrino mass from Troitsk experiment*, Phys. Rev. **D84** (2011) 112003, `arXiv:1108.5034 [hep-ex]`. (Cited on page 11.)

[38] K. Assamagan et al., *Upper limit of the muon-neutrino mass and charged pion mass from momentum analysis of a surface muon beam*, Phys. Rev. **D53** (1996) 6065–6077. (Cited on page 11.)

[39] ALEPH Collaboration, *An Upper limit on the tau-neutrino mass from three-prong and five-prong tau decays*, Eur. Phys. J. **C2** (1998) 395–406. (Cited on page 11.)

[40] R. N. Mohapatra and P. B. Pal, *Massive neutrinos in physics and astrophysics*, World Sci. Lect. Notes Phys. **41** (1991) 1–318. (Cited on pages 11, 12, 14, and 15.)

[41] J. C. Pati and A. Salam, *Lepton Number as the Fourth Color*, Phys. Rev. **D10** (1974) 275–289, [Erratum: Phys. Rev.D11,703(1975)]. (Cited on page 12.)

[42] R. N. Mohapatra and J. C. Pati, *Left-Right Gauge Symmetry and an Isoconjugate Model of CP Violation*, Phys. Rev. **D11** (1975) 566–571. (Cited on pages 12 and 14.)

[43] R. N. Mohapatra and J. C. Pati, *A Natural Left-Right Symmetry*, Phys. Rev. **D11** (1975) 2558. (Cited on page 12.)

[44] G. Senjanović and R. N. Mohapatra, *Exact Left-Right Symmetry and Spontaneous Violation of Parity*, Phys. Rev. **D12** (1975) 1502. (Cited on page 12.)

[45] G. Senjanović, *Spontaneous Breakdown of Parity in a Class of Gauge Theories*, Nucl. Phys. **B153** (1979) 334–364. (Cited on pages 12 and 15.)

[46] P. Minkowski, $\mu \to e\gamma$ *at a Rate of One Out of* $10^9$ *Muon Decays?*, Phys. Lett. **67B** (1977) 421–428. (Cited on page 12.)

[47] R. N. Mohapatra and G. Senjanović, *Neutrino Mass and Spontaneous Parity Violation*, Phys. Rev. Lett. **44** (1980) 912. (Cited on pages 12 and 16.)

[48] R. E. Marshak and R. N. Mohapatra, *Quark - Lepton Symmetry and B-L as the U(1) Generator of the Electroweak Symmetry Group*, Phys. Lett. **91B** (1980) 222–224. (Cited on page 12.)

[49] R. N. Mohapatra and R. E. Marshak, *Local B-L Symmetry of Electroweak Interactions, Majorana Neutrinos and Neutron Oscillations*, Phys. Rev. Lett. **44** (1980) 1316–1319, [Erratum: Phys. Rev. Lett.44,1643(1980)]. (Cited on pages 12 and 15.)

[50] R. N. Mohapatra, *Mechanism for Understanding Small Neutrino Mass in Superstring Theories*, Phys. Rev. Lett. **56** (1986) 561–563. (Cited on pages 12 and 18.)

[51] R. N. Mohapatra and J. W. F. Valle, *Neutrino Mass and Baryon Number Nonconservation in Superstring Models*, Phys. Rev. **D34** (1986) 1642. (Cited on pages 12 and 18.)

[52] C.-Y. Chen and P. S. B. Dev, *Multi-Lepton Collider Signatures of Heavy Dirac and Majorana Neutrinos*, Phys. Rev. **D85** (2012) 093018, arXiv:1112.6419 [hep-ph]. (Cited on pages 12, 18, 19, and 20.)

[53] P. S. Bhupal Dev and R. N. Mohapatra, *Unified explanation of the eejj, diboson and dijet resonances at the LHC*, Phys. Rev. Lett. **115** (2015) 181803, arXiv:1508.02277 [hep-ph]. (Cited on pages 12 and 18.)

[54] C. Hati, S. Patra, P. Pritimita and U. Sarkar, *Neutrino Masses and Leptogenesis in Left–Right Symmetric Models: A Review From a Model Building Perspective*, Front.in Phys. **6** (2018) 19. (Cited on pages 12 and 18.)

[55] J. Schechter and J. W. F. Valle, *Neutrino Masses in SU(2) x U(1) Theories*, Phys. Rev. **D22** (1980) 2227. (Cited on page 12.)

[56] M. Drewes et al., *A White Paper on keV Sterile Neutrino Dark Matter*, JCAP **1701** (2017) 025, arXiv:1602.04816 [hep-ph]. (Cited on page 13.)

[57] B. Audren, J. Lesgourgues, G. Mangano, P. D. Serpico and T. Tram, *Strongest model-independent bound on the lifetime of Dark Matter*, JCAP **1412** (2014) 028, arXiv:1407.2418 [astro-ph.CO]. (Cited on page 13.)

[58] M. Nemevsek, G. Senjanović and Y. Zhang, *Warm Dark Matter in Low Scale Left-Right Theory*, JCAP **1207** (2012) 006, arXiv:1205.0844 [hep-ph]. (Cited on page 13.)

[59] R. N. Mohapatra and G. Senjanović, *Neutrino Masses and Mixings in Gauge Models with Spontaneous Parity Violation*, Phys. Rev. **D23** (1981) 165. (Cited on pages 15 and 16.)

[60] N. G. Deshpande, J. F. Gunion, B. Kayser and F. I. Olness, *Left-right symmetric electroweak models with triplet Higgs*, Phys. Rev. **D44** (1991) 837–858. (Cited on page 15.)

[61] S. M. Bilenky and S. T. Petcov, *Massive Neutrinos and Neutrino Oscillations*, Rev. Mod. Phys. **59** (1987) 671, [Erratum: Rev. Mod. Phys.60,575(1988)]. (Cited on page 16.)

[62] L. Wolfenstein, *Different Varieties of Massive Dirac Neutrinos*, Nucl. Phys. **B186** (1981) 147–152. (Cited on page 19.)

[63] A. Das, P. S. B. Dev and R. N. Mohapatra, *Same Sign versus Opposite Sign Dileptons as a Probe of Low Scale Seesaw Mechanisms*, Phys. Rev. **D97** (2018) 015018, arXiv:1709.06553 [hep-ph]. (Cited on pages 19 and 20.)

[64] W.-Y. Keung and G. Senjanović, *Majorana Neutrinos and the Production of the Right-handed Charged Gauge Boson*, Phys. Rev. Lett. **50** (1983) 1427. (Cited on page 19.)

[65] ATLAS Collaboration, *Search for heavy neutrinos and right-handed W bosons in events with two leptons and jets in pp collisions at $\sqrt{s} = 7$ TeV with the ATLAS detector*, Eur. Phys. J. C **72** (2012) 2056, arXiv:1203.5420 [hep-ex]. (Cited on pages 21, 23, 64, 83, and 142.)

[66] CMS Collaboration, *Search for heavy neutrinos and $W_R$ bosons with right-handed couplings in a left-right symmetric model in pp collisions at $\sqrt{s} = 7$ TeV*, Phys. Rev. Lett. **109** (2012) 261802, arXiv:1210.2402 [hep-ex]. (Cited on pages 21 and 64.)

[67] ATLAS Collaboration, *Search for heavy Majorana neutrinos with the ATLAS detector in pp collisions at $\sqrt{s} = 8$ TeV*, JHEP **07** (2015) 162, arXiv:1506.06020 [hep-ex]. (Cited on pages 21 and 64.)

[68] CMS Collaboration, *Search for heavy neutrinos and W bosons with right-handed couplings in proton–proton collisions at $\sqrt{s} = 8$ TeV*, Eur. Phys. J. C **74** (2014) 3149, arXiv:1407.3683 [hep-ex]. (Cited on pages 21 and 64.)

[69] CMS Collaboration, *Search for a heavy right-handed W boson and a heavy neutrino in events with two same-flavor leptons and two jets at $\sqrt{s} = 13$ TeV*, arXiv:1803.11116 [hep-ex]. (Cited on pages 21, 22, 64, 141, and 142.)

[70] CMS Collaboration, *Search for heavy neutrinos or third-generation leptoquarks in final states with two hadronically decaying $\tau$ leptons and two jets in proton–proton collisions at $\sqrt{s} = 13$ TeV*, JHEP **03** (2017) 077, arXiv:1612.01190 [hep-ex]. (Cited on page 21.)

[71] CMS Collaboration, *Search for third-generation scalar leptoquarks and heavy right-handed neutrinos in final states with two tau leptons and two jets in proton–proton collisions at $\sqrt{s} = 13$ TeV*, JHEP **07** (2017) 121, arXiv:1703.03995 [hep-ex]. (Cited on page 21.)

[72] GERDA Collaboration, *Results on Neutrinoless Double-$\beta$ Decay of $^{76}Ge$ from Phase I of the GERDA Experiment*, Phys. Rev. Lett. **111** (2013) 122503, arXiv:1307.4720 [nucl-ex]. (Cited on page 21.)

[73] KamLAND-Zen Collaboration, *Search for Majorana Neutrinos near the Inverted Mass Hierarchy Region with KamLAND-Zen*, Phys. Rev. Lett. **117** (2016) 082503, arXiv:1605.02889 [hep-ex], [Addendum: Phys. Rev. Lett.117,no.10,109903(2016)]. (Cited on page 21.)

[74] ATLAS Collaboration, *Search for new phenomena in dijet events using 37 $fb^{-1}$ of pp collision data collected at $\sqrt{s} = 13$ TeV with the ATLAS detector*, Phys. Rev. D **96** (2017) 052004, arXiv:1703.09127 [hep-ex]. (Cited on pages 21 and 142.)

[75] ATLAS Collaboration, *Search for long-lived, massive particles in events with displaced vertices and missing transverse momentum in* $\sqrt{s} = 13$ *TeV pp collisions with the ATLAS detector*, Phys. Rev. D **97** (2018) 052012, arXiv:1710.04901 [hep-ex]. (Cited on page 21.)

[76] M. Lindner, F. S. Queiroz, W. Rodejohann and C. E. Yaguna, *Left-Right Symmetry and Lepton Number Violation at the Large Hadron Electron Collider*, JHEP **06** (2016) 140, arXiv:1604.08596 [hep-ph]. (Cited on page 21.)

[77] M. Nemevsek, F. Nesti and G. Popara, *Keung-Senjanović process at the LHC: From lepton number violation to displaced vertices to invisible decays*, Phys. Rev. **D97** (2018) 115018, arXiv:1801.05813 [hep-ph]. (Cited on pages 21 and 23.)

[78] O. Brüning, P. Collier, P. Lebrun, S. Myers, R. Ostojic et al., *LHC Design Report Vol.1: The LHC main ring*, 2004, http://cds.cern.ch/record/782076. (Cited on page 25.)

[79] O. Brüning, P. Collier, P. Lebrun, S. Myers, R. Ostojic et al., *LHC Design Report Vol.2: The LHC infrastructure and general services*, 2004, http://cds.cern.ch/record/815187. (Cited on page 25.)

[80] M. Benedikt, P. Collier, V. Mertens, J. Poole and K. Schindl, *LHC Design Report Vol.3: The LHC injector chain*, 2004, http://cds.cern.ch/record/823808. (Cited on page 25.)

[81] ATLAS Collaboration, *The ATLAS Experiment at the CERN Large Hadron Collider*, JINST **3** (2008) S08003. (Cited on pages 25, 39, 40, 41, 44, 48, and 53.)

[82] C. Lefévre, *The CERN accelerator complex. Complexe des accélérateurs du CERN*, Dec, 2008, https://cds.cern.ch/record/1260465. (Cited on page 26.)

[83] AC Team, *Diagram of an LHC dipole magnet. Schéma d'un aimant dipôle du LHC*, Jun, 1999, https://cds.cern.ch/record/40524. (Cited on page 28.)

[84] J. Pequenao and P. Schaffner, *A computer generated image representing how ATLAS detects particles*, Jan, 2013, https://cds.cern.ch/record/1505342. (Cited on page 29.)

[85] J. Pequenao, *Computer generated image of the whole ATLAS detector*, Mar, 2008, https://cds.cern.ch/record/1095924. (Cited on page 30.)

[86] ATLAS Collaboration, *The ATLAS Simulation Infrastructure*, Eur. Phys. J. C **70** (2010) 823, arXiv:1005.4568 [physics.ins-det]. (Cited on pages 29 and 62.)

[87] ATLAS Collaboration, *Event Displays from Run 2 physics analyses* , 2018, https://twiki.cern.ch/twiki/bin/view/AtlasPublic/EventDisplayRun2Physics, (accessed 27/06/18). (Cited on page 31.)

[88] ATLAS IBL Collaboration, *Production and Integration of the ATLAS Insertable B-Layer*, 2018, arXiv:1803.00844 [physics.ins-det]. (Cited on pages 30 and 33.)

[89] J. Pequenao, *Computer generated image of the ATLAS inner detector*, Mar, 2008, https://cds.cern.ch/record/1095926. (Cited on page 32.)

[90] K. Lantzsch, *Status and performance of the ATLAS Pixel Detector at the LHC after three years of operation*, Geneva, Jan, 2014, https://cds.cern.ch/record/1643938. (Cited on page 34.)

[91] ATLAS Collaboration, *$dE/dx$ measurement in the ATLAS Pixel Detector and its use for particle identification*, ATLAS-CONF-2011-016, 2011, https://cds.cern.ch/record/1336519. (Cited on page 34.)

[92] ATLAS Collaboration, *Calibration of the ATLAS Transition Radiation Tracker*, ATLAS-CONF-2011-006, 2011, https://cds.cern.ch/record/1330712. (Cited on pages 35 and 36.)

[93] ATLAS Collaboration, B. Mindur, *ATLAS Transition Radiation Tracker (TRT): Straw tubes for tracking and particle identification at the Large Hadron Collider*, Nucl. Instrum. Meth. **A845** (2017) 257–261. (Cited on page 35.)

[94] ATLAS Collaboration, *Particle Identification Performance of the ATLAS Transition Radiation Tracker*, ATLAS-CONF-2011-128, 2011, https://cds.cern.ch/record/1383793. (Cited on page 36.)

[95] J. Pequenao, *Computer Generated image of the ATLAS calorimeter*, Mar, 2008, https://cds.cern.ch/record/1095927. (Cited on page 38.)

[96] P. Loïez, *The first CERN-built module of the barrel section of ATLAS's electromagnetic calorimeter. Premier module du tonneau du calorimètre electromagnétique d'ATLAS*, Apr, 2001, https://cds.cern.ch/record/42207. (Cited on page 40.)

[97] J. Pequenao, *Computer generated image of the ATLAS Muons subsystem*, Mar, 2008, https://cds.cern.ch/record/1095929. (Cited on page 42.)

[98] ATLAS Collaboration, *Expected Performance of the ATLAS Experiment - Detector, Trigger and Physics*, 2009, arXiv:0901.0512 [hep-ex], https://cds.cern.ch/record/1125884. (Cited on page 43.)

[99] P. Bagnaia et al., *Calibration model for the MDT chambers of the ATLAS muon spectrometer*, 2008, http://cds.cern.ch/record/1089868. (Cited on page 43.)

[100] D. S. Levin et al., *Drift time spectrum and gas monitoring in the ATLAS Muon Spectrometer precision chambers*, Nucl. Instrum. Meth. **A588** (2008) 347–358. (Cited on page 43.)

[101] ATLAS Collaboration, G. Duckeck, D. Barberis, R. Hawkings, R. Jones, N. McCubbin et al., *ATLAS computing: Technical design report*, `https://cds.cern.ch/record/837738`. (Cited on pages 47, 57, and 58.)

[102] ATLAS Collaboration, *2015 start-up trigger menu and initial performance assessment of the ATLAS trigger using Run-2 data*, ATL-DAQ-PUB-2016-001, 2016, `https://cds.cern.ch/record/2136007`. (Cited on pages 48 and 49.)

[103] ATLAS Collaboration, *Performance of the ATLAS Trigger System in 2015*, Eur. Phys. J. C **77** (2017) 317, `arXiv:1611.09661 [hep-ex]`. (Cited on pages 48, 49, 52, and 54.)

[104] ATLAS Collaboration, *ATLAS first level trigger: Technical design report*, 1998, `https://cds.cern.ch/record/381429`. (Cited on page 48.)

[105] ATLAS Collaboration, *ATLAS high-level trigger, data acquisition and controls: Technical design report*, 2003, `https://cds.cern.ch/record/616089`. (Cited on page 48.)

[106] ATLAS Collaboration, *Trigger Operation Public Results*, 2018, `https://twiki.cern.ch/twiki/bin/view/AtlasPublic/TriggerOperationPublicResults`, (accessed 24/05/18). (Cited on page 50.)

[107] C. Cuenca Almenar et al., *ATLAS online data quality monitoring*, Nucl. Phys. Proc. Suppl. **215** (2011) 304–306. (Cited on page 54.)

[108] J. Adelman et al., *ATLAS offline data quality monitoring*, J. Phys. Conf. Ser. **219** (2010) 042018. (Cited on page 54.)

[109] A. Buckley et al., *General-purpose event generators for LHC physics*, Phys. Rept. **504** (2011) 145–233, `arXiv:1101.2599 [hep-ph]`. (Cited on pages 60 and 62.)

[110] V. V. Sudakov, *Vertex parts at very high-energies in quantum electrodynamics*, Sov. Phys. JETP **3** (1956) 65–71, [Zh. Eksp. Teor. Fiz.30,87(1956)]. (Cited on page 61.)

[111] V. N. Gribov and L. N. Lipatov, *Deep inelastic e p scattering in perturbation theory*, Sov. J. Nucl. Phys. **15** (1972) 438–450, [Yad. Fiz.15,781(1972)]. (Cited on page 61.)

[112] Y. L. Dokshitzer, *Calculation of the Structure Functions for Deep Inelastic Scattering and e+ e- Annihilation by Perturbation Theory in Quantum Chromodynamics.*, Sov. Phys. JETP **46** (1977) 641–653, [Zh. Eksp. Teor. Fiz.73,1216(1977)]. (Cited on page 61.)

[113] G. Altarelli and G. Parisi, *Asymptotic Freedom in Parton Language*, Nucl. Phys. **B126** (1977) 298–318. (Cited on page 61.)

[114] B. Andersson, G. Gustafson, G. Ingelman and T. Sjostrand, *Parton Fragmentation and String Dynamics*, Phys. Rept. **97** (1983) 31–145. (Cited on page 61.)

[115] B. Andersson, *The Lund model*, Camb. Monogr. Part. Phys. Nucl. Phys. Cosmol. **7** (1997) 1–471. (Cited on page 61.)

[116] B. R. Webber, *A QCD Model for Jet Fragmentation Including Soft Gluon Interference*, Nucl. Phys. **B238** (1984) 492–528. (Cited on page 61.)

[117] J.-C. Winter, F. Krauss and G. Soff, *A Modified cluster hadronization model*, Eur. Phys. J. **C36** (2004) 381–395, arXiv:hep-ph/0311085 [hep-ph]. (Cited on page 61.)

[118] T. Sjostrand, S. Mrenna and P. Z. Skands, *A Brief Introduction to PYTHIA 8.1*, Comput. Phys. Commun. **178** (2008) 852–867, arXiv:0710.3820 [hep-ph]. (Cited on pages 62 and 65.)

[119] ATLAS Collaboration, *Summary of ATLAS Pythia 8 tunes*, ATL-PHYS-PUB-2012-003, 2012, https://cds.cern.ch/record/1474107. (Cited on page 62.)

[120] A. D. Martin, W. J. Stirling, R. S. Thorne and G. Watt, *Parton distributions for the LHC*, Eur. Phys. J. C **63** (2009) 189–285, arXiv:0901.0002 [hep-ph]. (Cited on page 62.)

[121] ATLAS Collaboration, Z. Marshall, *Simulation of Pile-up in the ATLAS Experiment*, J. Phys. Conf. Ser. **513** (2014) 022024. (Cited on page 62.)

[122] W. Buttinger, *Using Event Weights to account for differences in Instantaneous Luminosity and Trigger Prescale in Monte Carlo and Data*, Tech. Rep. ATL-COM-SOFT-2015-119, CERN, Geneva, May, 2015. https://cds.cern.ch/record/2014726. ATLAS internal. (Cited on page 62.)

[123] GEANT4 Collaboration, S. Agostinelli et al., *GEANT4: A Simulation toolkit*, Nucl. Instrum. Meth. A **506** (2003) 250. (Cited on page 62.)

[124] J. Alwall, M. Herquet, F. Maltoni, O. Mattelaer and T. Stelzer, *MadGraph 5 : Going Beyond*, JHEP **06** (2011) 128, arXiv:1106.0522 [hep-ph]. (Cited on page 63.)

[125] J. Alwall, R. Frederix, S. Frixione, V. Hirschi, F. Maltoni et al., *The automated computation of tree-level and next-to-leading order differential cross sections, and their matching to parton shower simulations*, JHEP **07** (2014) 079, arXiv:1405.0301 [hep-ph]. (Cited on page 63.)

[126] A. Roitgrund, G. Eilam and S. Bar-Shalom, *Implementation of the left-right symmetric model in FeynRules*, Comput. Phys. Commun. **203** (2016) 18–44, arXiv:1401.3345 [hep-ph]. (Cited on pages 63 and 64.)

[127] A. Alloul, N. D. Christensen, C. Degrande, C. Duhr and B. Fuks, *FeynRules 2.0 - A complete toolbox for tree-level phenomenology*, Comput. Phys. Commun. **185** (2014) 2250–2300, arXiv:1310.1921 [hep-ph]. (Cited on page 63.)

[128] X. Hoad, *Summary of LRSM model updates by F. Nesti and M. Nemevšek*, 2016, https://indico.cern.ch/event/570893/contributions/2309254/attachments/1341184/2019971/20160922Modelling.pdf, ATLAS internal (accessed 26/06/18). (Cited on pages 63 and 64.)

[129] R. D. Ball et al., *Parton distributions with LHC data*, Nucl. Phys. **B867** (2013) 244–289, arXiv:1207.1303 [hep-ph]. (Cited on page 63.)

[130] ATLAS Collaboration, *ATLAS Pythia 8 tunes to 7 TeV data*, ATL-PHYS-PUB-2014-021, 2014, https://cds.cern.ch/record/1966419. (Cited on page 63.)

[131] D. J. Lange, *The EvtGen particle decay simulation package*, Nucl. Instrum. Meth. **A462** (2001) 152–155. (Cited on page 63.)

[132] Z. Marshall, J. McFayden, S. von Buddenbrock and H. Mildner, *MadGraph5_aMC@NLO for ATLAS*, 2018, https://twiki.cern.ch/twiki/bin/viewauth/AtlasProtected/MadGraph5aMCatNLOForAtlas, ATLAS internal (accessed 26/06/18). (Cited on page 63.)

[133] N. Cabibbo, *Unitary Symmetry and Leptonic Decays*, Phys. Rev. Lett. **10** (1963) 531–533, [,648(1963)]. (Cited on page 64.)

[134] M. Kobayashi and T. Maskawa, *CP Violation in the Renormalizable Theory of Weak Interaction*, Prog. Theor. Phys. **49** (1973) 652–657. (Cited on page 64.)

[135] T. Sjostrand, S. Mrenna and P. Z. Skands, *PYTHIA 6.4 Physics and Manual*, JHEP **05** (2006) 026, arXiv:hep-ph/0603175 [hep-ph]. (Cited on pages 65 and 69.)

[136] G. Breit and E. Wigner, *Capture of Slow Neutrons*, Phys. Rev. **49** (1936) 519–531. (Cited on page 65.)

[137] T. Gleisberg, S. Höche, F. Krauss, M. Schönherr, S. Schumann et al., *Event generation with SHERPA 1.1*, JHEP **02** (2009) 007, arXiv:0811.4622 [hep-ph]. (Cited on page 68.)

[138] NNPDF Collaboration, R. D. Ball et al., *Parton distributions for the LHC Run II*, JHEP **04** (2015) 040, arXiv:1410.8849 [hep-ph]. (Cited on page 68.)

[139] T. Gleisberg and S. Höche, *Comix, a new matrix element generator*, JHEP **12** (2008) 039, arXiv:0808.3674 [hep-ph]. (Cited on page 69.)

[140] F. Cascioli, P. Maierhofer and S. Pozzorini, *Scattering Amplitudes with Open Loops*, Phys. Rev. Lett. **108** (2012) 111601, arXiv:1111.5206 [hep-ph]. (Cited on page 69.)

[141] J. Butterworth, E. Dobson, U. Klein, B. Mellado Garcia, T. Nunnemann et al., *Single Boson and Diboson Production Cross Sections in pp Collisions at sqrts=7 TeV*, Tech. Rep. ATL-COM-PHYS-2010-695, CERN, Geneva, Aug, 2010. https://cds.cern.ch/record/1287902. (Cited on page 69.)

[142] ATLAS Collaboration, *Monte Carlo Generators for the Production of a $W$ or $Z/\gamma^*$ Boson in Association with Jets at ATLAS in Run 2*, ATL-PHYS-PUB-2016-003, 2016, https://cds.cern.ch/record/2120133. (Cited on page 69.)

[143] S. Alioli, P. Nason, C. Oleari and E. Re, *A general framework for implementing NLO calculations in shower Monte Carlo programs: the POWHEG BOX*, JHEP **06** (2010) 043, arXiv:1002.2581 [hep-ph]. (Cited on page 69.)

[144] H.-L. Lai et al., *New parton distributions for collider physics*, Phys. Rev. D **82** (2010) 074024, arXiv:1007.2241 [hep-ph]. (Cited on page 69.)

[145] J. Pumplin, D. R. Stump, J. Huston, H. L. Lai, P. M. Nadolsky et al., *New generation of parton distributions with uncertainties from global QCD analysis*, JHEP **07** (2002) 012, arXiv:hep-ph/0201195 [hep-ph]. (Cited on page 69.)

[146] P. Z. Skands, *Tuning Monte Carlo generators: The Perugia tunes*, Phys. Rev. D **82** (2010) 074018, arXiv:1005.3457 [hep-ph]. (Cited on page 69.)

[147] N. Kidonakis, *Theoretical results for electroweak-boson and single-top production*, PoS **DIS2015** (2015) 170, arXiv:1506.04072 [hep-ph]. (Cited on page 69.)

[148] ATLAS Collaboration, *Simulation of top-quark production for the ATLAS experiment at $\sqrt{s} = 13$ TeV*, ATL-PHYS-PUB-2016-004, 2016, https://cds.cern.ch/record/2120417. (Cited on page 69.)

[149] ATLAS Collaboration, *Performance of the ATLAS track reconstruction algorithms in dense environments in LHC Run 2*, Eur. Phys. J. C **77** (2017) 673, arXiv:1704.07983 [hep-ex]. (Cited on page 70.)

[150] ATLAS Collaboration, *Early Inner Detector Tracking Performance in the 2015 Data at $\sqrt{s} = 13$ TeV*, ATL-PHYS-PUB-2015-051, 2015, https://cds.cern.ch/record/2110140. (Cited on page 70.)

[151] ATLAS Collaboration, *Reconstruction of primary vertices at the ATLAS experiment in Run 1 proton–proton collisions at the LHC*, Eur. Phys. J. C **77** (2017) 332, arXiv:1611.10235 [hep-ex]. (Cited on page 70.)

[152] ATLAS Collaboration, *Vertex Reconstruction Performance of the ATLAS Detector at* $\sqrt{s} = 13$ *TeV*, ATL-PHYS-PUB-2015-026, 2015, https://cds.cern.ch/record/2037717. (Cited on page 70.)

[153] ATLAS Collaboration, *Electron and photon energy calibration with the ATLAS detector using LHC Run 1 data*, Eur. Phys. J. C **74** (2014) 3071, arXiv:1407.5063 [hep-ex]. (Cited on page 71.)

[154] ATLAS Collaboration, *Electron efficiency measurements with the ATLAS detector using the 2015 LHC proton–proton collision data*, ATLAS-CONF-2016-024, 2016, https://cds.cern.ch/record/2157687. (Cited on pages 71, 78, 86, 100, and 124.)

[155] ATLAS Collaboration, *Electron efficiency measurements with the ATLAS detector using 2012 LHC proton–proton collision data*, Eur. Phys. J. C **77** (2017) 195, arXiv:1612.01456 [hep-ex]. (Cited on page 71.)

[156] ATLAS Collaboration, *Muon reconstruction performance of the ATLAS detector in proton–proton collision data at* $\sqrt{s} = 13$ *TeV*, Eur. Phys. J. C **76** (2016) 292, arXiv:1603.05598 [hep-ex]. (Cited on pages 72, 79, 87, 100, and 124.)

[157] M. Cacciari, G. P. Salam and G. Soyez, *The Anti-k(t) jet clustering algorithm*, JHEP **04** (2008) 063, arXiv:0802.1189 [hep-ph]. (Cited on page 72.)

[158] M. Cacciari, G. P. Salam and G. Soyez, *FastJet User Manual*, Eur. Phys. J. **C72** (2012) 1896, arXiv:1111.6097 [hep-ph]. (Cited on page 72.)

[159] ATLAS Collaboration, *Topological cell clustering in the ATLAS calorimeters and its performance in LHC Run 1*, Eur. Phys. J. C **77** (2017) 490, arXiv:1603.02934 [hep-ex]. (Cited on page 72.)

[160] ATLAS Collaboration, *Jet energy scale measurements and their systematic uncertainties in proton–proton collisions at* $\sqrt{s} = 13$ *TeV with the ATLAS detector*, Phys. Rev. D **96** (2017) 072002, arXiv:1703.09665 [hep-ex]. (Cited on pages 73 and 100.)

[161] A. Hocker et al., *TMVA - Toolkit for Multivariate Data Analysis*, PoS **ACAT** (2007) 040, arXiv:physics/0703039 [PHYSICS]. (Cited on pages 74 and 80.)

[162] ATLAS Collaboration, *Measurement of the tau lepton reconstruction and identification performance in the ATLAS experiment using pp collisions at* $\sqrt{s} = 13$ *TeV*, ATLAS-CONF-2017-029, 2017, https://cds.cern.ch/record/2261772. (Cited on page 74.)

[163] ATLAS Collaboration, *Reconstruction, Energy Calibration, and Identification of Hadronically Decaying Tau Leptons in the ATLAS Experiment for Run-2 of the LHC*, ATL-PHYS-PUB-2015-045, 2015, https://cds.cern.ch/record/2064383. (Cited on pages 74 and 81.)

[164] D. Adams, C. Anastopoulos, A. Andreazza, M. Aoki, L. Asquith et al., *Recommendations of the Physics Objects and Analysis Harmonisation Study Groups 2014*, Tech. Rep. ATL-PHYS-INT-2014-018, CERN, Geneva, Jul, 2014. https://cds.cern.ch/record/1743654. ATLAS internal. (Cited on page 76.)

[165] ATLAS Collaboration, *Evidence for the $H \to b\bar{b}$ decay with the ATLAS detector*, JHEP **12** (2017) 024, arXiv:1708.03299 [hep-ex]. (Cited on page 76.)

[166] A. Buzatu and W. Wang, *Object selections for SM Higgs boson produced in association with a vector boson in which $H \to b\bar{b}$ and V decays leptonically with Run-2 data: Object support note for VH(bb) 2015+2016 dataset publication*, Tech. Rep. ATL-COM-PHYS-2016-1674, CERN, Geneva, Nov, 2016. https://cds.cern.ch/record/2233686. ATLAS internal. (Cited on page 76.)

[167] M. Cacciari, G. P. Salam and G. Soyez, *The Catchment Area of Jets*, JHEP **04** (2008) 005, arXiv:0802.1188 [hep-ph]. (Cited on page 77.)

[168] ATLAS collaboration, *Tracking CP Pre-Recommendations for 2017 Winter Conferences, 2015+2016/20.7*, 2017, https://twiki.cern.ch/twiki/bin/view/AtlasProtected/TrackingCPMoriond2017, ATLAS internal (accessed 09/07/18). (Cited on pages 78 and 79.)

[169] ATLAS Collaboration, *Performance of pile-up mitigation techniques for jets in pp collisions at $\sqrt{s} = 8$ TeV using the ATLAS detector*, Eur. Phys. J. C **76** (2016) 581, arXiv:1510.03823 [hep-ex]. (Cited on page 80.)

[170] E. Fix and J. L. Hodges, *Discriminatory Analysis. Nonparametric Discrimination: Consistency Properties*, International Statistical Review / Revue Internationale de Statistique **57** (1989) 238–247, http://www.jstor.org/stable/1403797. (Cited on page 80.)

[171] ATLAS Collaboration, *Selection of jets produced in* 13 *TeV proton–proton collisions with the ATLAS detector*, ATLAS-CONF-2015-029, 2015, https://cds.cern.ch/record/2037702. (Cited on pages 80, 81, and 90.)

[172] X. Hoad, S. Hou, C. Leonidopoulos, B. Li, E. Carquin et al., *Search for heavy Majorana or Dirac neutrinos and right-handed W gauge bosons in final states with two charged leptons and two jets at $\sqrt{s}$=13 TeV with the ATLAS collaboration*, Tech. Rep. ATL-COM-PHYS-2017-704, CERN, Geneva, Jun, 2017. https://cds.cern.ch/record/2267874. ATLAS internal. (Cited on pages 83, 85, 88, 93, 94, 101, 102, 103, 104, 105, 106, and 107.)

[173] ATLAS Collaboration, *Performance of b-jet identification in the ATLAS experiment*, JINST **11** (2016) P04008, arXiv:1512.01094 [hep-ex]. (Cited on page 89.)

[174] ATLAS Collaboration, *Optimisation of the ATLAS b-tagging performance for the 2016 LHC Run*, ATL-PHYS-PUB-2016-012, 2016, https://cds.cern.ch/record/2160731. (Cited on pages 89, 100, and 124.)

[175] Belle Collaboration, H. Ikeda et al., *A detailed test of the CsI(Tl) calorimeter for BELLE with photon beams of energy between 20-MeV and 5.4-GeV*, Nucl. Instrum. Meth. **A441** (2000) 401–426. (Cited on page 92.)

[176] M. Baak, G. J. Besjes, D. Côte, A. Koutsman, J. Lorenz et al., *HistFitter software framework for statistical data analysis*, Eur. Phys. J. **C75** (2015) 153, arXiv:1410.1280 [hep-ex]. (Cited on pages 95, 97, and 130.)

[177] M. Muškinja, T. Novak, F. Scutti, M. Sioli, A. Gorisek et al., *Search for heavy neutrinos and right-handed W bosons in final states with two same-charge leptons and two jets with the ATLAS detector using proton–proton collisions at $\sqrt{s}$ = 13 TeV*, Tech. Rep. ATL-COM-PHYS-2017-1345, CERN, Geneva, Sep, 2017. https://cds.cern.ch/record/2282048. ATLAS internal. (Cited on pages 95 and 124.)

[178] ROOT Collaboration, K. Cranmer, G. Lewis, L. Moneta, A. Shibata and W. Verkerke, *HistFactory: A tool for creating statistical models for use with RooFit and RooStats*, https://cds.cern.ch/record/1456844. (Cited on page 98.)

[179] ATLAS Collaboration, *Luminosity determination in pp collisions at $\sqrt{s} = 8$ TeV using the ATLAS detector at the LHC*, Eur. Phys. J. C **76** (2016) 653, arXiv:1608.03953 [hep-ex]. (Cited on page 99.)

[180] ATLAS Muon CP Group, *Muon Combined Performance Group Guidelines 2015–2016*, 2016, https://twiki.cern.ch/twiki/bin/view/AtlasProtected/MCPAnalysisGuidelinesMC15, ATLAS internal (accessed 06/08/18). (Cited on page 100.)

[181] A. Kalogeropoulos and J. Alwall, *The SysCalc code: A tool to derive theoretical systematic uncertainties*, arXiv:1801.08401 [hep-ph]. (Cited on page 104.)

[182] M. Botje et al., *The PDF4LHC Working Group Interim Recommendations*, arXiv:1101.0538 [hep-ph]. (Cited on pages 104 and 105.)

[183] L. A. Harland-Lang, A. D. Martin, P. Motylinski and R. S. Thorne, *Parton distributions in the LHC era: MMHT 2014 PDFs*, Eur. Phys. J. **C75** (2015) 204, arXiv:1412.3989 [hep-ph]. (Cited on page 104.)

[184] S. Dulat, T.-J. Hou, J. Gao, M. Guzzi, J. Huston et al., *New parton distribution functions from a global analysis of quantum chromodynamics*, Phys. Rev. **D93** (2016) 033006, arXiv:1506.07443 [hep-ph]. (Cited on page 104.)

[185] M. Bahr et al., *Herwig++ Physics and Manual*, Eur. Phys. J. **C58** (2008) 639–707, arXiv:0803.0883 [hep-ph]. (Cited on page 106.)

[186] M. Muškinja, *Study of the amount of fakes in opposite-sign regions*, 2017, https://indico.cern.ch/event/722788/contributions/2972259/attachments/1642284/2623321/16.Avg.2017.HNMeeting.OSMee.pdf, ATLAS internal (accessed 19/08/18). (Cited on page 125.)

[187] CDF Collaboration, *Global Search for New Physics with 2.0 $fb^{-1}$ at CDF*, Phys. Rev. **D79** (2009) 011101, arXiv:0809.3781 [hep-ex]. (Cited on page 126.)

[188] G. Choudalakis, *On hypothesis testing, trials factor, hypertests and the BumpHunter*, in *Proceedings, PHYSTAT 2011 Workshop on Statistical Issues Related to Discovery Claims in Search Experiments and Unfolding, CERN, Geneva, Switzerland 17-20 January 2011*. 2011. arXiv:1101.0390 [physics.data-an]. (Cited on page 126.)

[189] G. Cowan, K. Cranmer, E. Gross and O. Vitells, *Asymptotic formulae for likelihood-based tests of new physics*, Eur. Phys. J. **C71** (2011) 1554, arXiv:1007.1727 [physics.data-an], [Erratum: Eur. Phys. J.C73,2501(2013)]. (Cited on page 130.)

[190] A. L. Read, *Presentation of search results: The CL(s) technique*, J. Phys. **G28** (2002) 2693–2704, [,11(2002)]. (Cited on page 130.)

[191] E. Jones, T. Oliphant, P. Peterson et al., *SciPy: Open source scientific tools for Python*, http://www.scipy.org/, (accessed 04/08/18). (Cited on page 131.)

[192] M. J. D. Powell, *Restart procedures for the conjugate gradient method*, Mathematical Programming **12** (1977) 241–254, https://doi.org/10.1007/BF01593790. (Cited on page 131.)

[193] D. S. Broomhead and D. Lowe, *Multivariable Functional Interpolation and Adaptive Networks*, Complex Systems **2** (1988) 321–355, https://www.complex-systems.com/abstracts/v02_i03_a05/. (Cited on page 131.)

[194] M. Baak, S. Gadatsch, R. Harrington and W. Verkerke, *Interpolation between multi-dimensional histograms using a new non-linear moment morphing method*, Nucl. Instrum. Meth. **A771** (2015) 39–48, arXiv:1410.7388 [physics.data-an]. (Cited on page 132.)